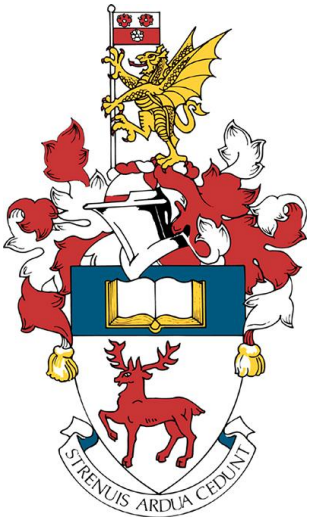

UNIVERSITY OF SOUTHAMPTON

FACULTY OF NATURAL AND ENVIRONMENTAL SCIENCES
SCHOOL OF OCEAN AND EARTH SCIENCES

An Investigation into the Variability of Ferromanganese Crusts in the NE Atlantic

by

Sarah Atinta Howarth

A thesis for the degree of
Doctor of Philosophy

March 2022

University of Southampton

Abstract

Faculty of Natural and Environmental Sciences
School of Ocean and Earth Sciences

Doctor of Philosophy

An Investigation into the Variability of Ferromanganese Crusts in the NE Atlantic

by Sarah Atinta Howarth

With the growth of renewable technologies, patterns in the demand for mineral resources required have shifted, with increasing demand for emerging technologies and a growing reliance on a wider suite of elements. Given their extreme enrichment in many of these critical elements, ferromanganese (FeMn) crust deposits have the potential to be an important future resource but the variability at the scale of a prospective exploration site remains poorly understood. This problem is acute for FeMn crust understanding in the Atlantic Ocean where fewer in-depth studies have been carried out to date. This study provides a systematic investigation into the distribution of FeMn crusts and the variation in texture and composition at the scale of an individual seamount in the NE Atlantic. Relationships with environmental factors are investigated to provide an improved understanding of the formation, distribution and preservation processes that influence FeMn crust characteristics at this local scale. Ferromanganese crusts from Tropic Seamount were observed across a range of water depths and environments, and distribution modelling predicted highest presence probabilities in summit and flank regions. The distribution of FeMn crusts at this scale is driven by both the substrate characteristics and interactions of local topography and current regimes which exert fundamental controls on the distribution of exposed hard surface and the period of exposure for FeMn crust precipitation. Concentrations of Co (mean of 0.5 wt%) and Te (mean of 51 ppm) in Tropic Seamount FeMn crusts showed the highest concentrations in summit regions, and coincide with regions of active surface erosion. Significant variability in composition was observed across the seamount. Statistical analyses of composition, alongside element mapping and textural studies, showed that the high variability in FeMn crust composition is affected by local scale topography. Combined with the interaction with local current regimes, this can play a key role in determining the flux of detrital material to FeMn crusts and associated dilution of hydrogenetic FeMn phases.

Contents

List of Figures

List of Tables

List of Additional Material

DIGITAL MATERIAL 1 - Full ICP-QQQ geochemical results for samples analysed in Chapter 5

DIGITAL MATERIAL 2 - Full ICP-QQQ geochemical results for surface scrape material analysed in Chapter 6

DIGITAL MATERIAL 3 - Full ICP-QQQ geochemical results for targeted horizon samples analysed in Chapter 6

DIGITAL MATERIAL 4 - Correlation matrix for upper surface scrape materials in Chapter 6

DIGITAL MATERIAL 5 - Compiled Pb LA ICP-MS data used for horizon correlation in Chapter 6

Declaration of Authorship

I declare that this thesis and the work presented in it is my own and has been generated by me as the result of my own original research.

I confirm that:

1. This work was done wholly or mainly while in candidature for a research degree at this University;
2. Where any part of this thesis has previously been submitted for a degree or any other qualification at this University or any other institution, this has been clearly stated;
3. Where I have consulted the published work of others, this is always clearly attributed;
4. Where I have quoted from the work of others, the source is always given. With the exception of such quotations, this thesis is entirely my own work;
5. I have acknowledged all main sources of help;
6. Where the thesis is based on work done by myself jointly with others, I have made clear exactly what was done by others and what I have contributed myself;
7. Parts of this work have been published as:
   I. A. Yeo, K. Dobson, P. Josso, R. B. Pearce, S. A. Howarth, P. A. J. Lusty, T. P. Le Bas, and B. J. Murton. Assessment of the Mineral Resource Potential of Atlantic Ferromanganese Crusts Based on Their Growth History, Microstructure, and Texture. *Minerals*, 8(8), 2018a
   B. J. Murton and shipboard scientific party. JC142 Cruise Report, MarineE-Tech Project to map the cobalt-rich Ferromanganese crusts of Tropic Seamount, NE Atlantic Ocean, RSS James Cook. Cruise Report, 2016

Signed:..... Date:.....

Acknowledgements

I would like to thank my main supervisor, Prof. Bramley J. Murton at National Oceanography Centre Southampton, for all of his support and advice during my PhD. I am particularly grateful for all of the seagoing opportunities he gave me and fieldwork he encouraged me to go on which has been my chance to see the world (mostly ocean). A huge thanks goes to my second supervisor Prof. Rachael James, for her insight and expertise and I would also like to thank my third supervisor Dr. Christopher Pearce for all of his support and belief in me through my PhD journey. And thank you to my supervisor at the BGS Paul Lusty, for his insight and feedback. I would also like to thank all of those who have supported me through the scientific process, particularly Dr. Matt Cooper, Dr Richard Pearce and the BGS labs for their assistance through the analytical process. And thank you to my two examiners, Prof. Andy Cundy and Dr. Matthias Haeckel, for the interesting discussion that made my viva so enjoyable and all of the valuable feedback that has improved this thesis.

A special thanks to my shipmates! Including all of the seagoing teams from MarineE-Tech and beyond across JC142, DY094 and RGR1. Dr. Isobel Yeo, thank you for helping me to survive the many night-shifts, taking me under your wing and keeping everything afloat - couldn't have done it without you. I would also like to thank Dr. Berit Lehrmann and my office-mates, Dr. Adeline Dutrieux and Dr. Iain Stobbs, for making my time at NOC a special one as part of the deep-sea mineral gang and Dr. Pierre Josso for his scientific insight. And last but not least, thanks to my family and friends who have kept me laughing. I am very grateful to so many of my fellow PhD students for making my time in Southampton the best years possible – I am sure I have laughed enough for a lifetime. Special thanks go to Dr. Rachael Shuttleworth, my long-suffering flatmate who is an inspiration, to my partner Dr. Sam Ellis for keeping me alive and fed during the long PhD months, and to my parents and brother for their unconditional support, patience, and regular BBQs.

This work was funded by a NERC SPITFIRE DTP studentship (NE/L002531/1) and under the NERC MarineE-Tech project (NE/M011186/1, awarded to Prof. Bramley J. Murton, and NE/M011151/1, awarded to Paul Lusty) within SoS Minerals. A grant from the NERC Isotope Geosciences Facilities Steering Committee for a collaborative study (IP-1860-118) allocated to Prof. Bramley J. Murton supported the Pb LA ICP-MS work.

Abbreviations and Definitions

AUV	Autonomous underwater vehicle
BGS	British Geological Survey
BODC	British Oceanographic Data Centre
BOSCORF	British Ocean Sediment Core Research Facility
CFA	Carbonate fluorite apatite phases
CISP	Canary Island Seamount Province
CRM	Certified Reference Material
FeMn	Ferromanganese
GAM	Generalised additive model
HREE	Heavy rare earth elements (Tb, Dy, Er, Ho, Tm, Yb, Lu)
HRM	House Reference Material
ICP-MS	Inductively coupled plasma mass spectrometry
ICP-QQQ	Triple quadrupole inductively coupled plasma mass spectrometry
ISA	International Seabed Authority
LA ICP-MS	Laser ablation inductively coupled mass spectrometry
LREE	Light rare earth elements (La, Ce, Pr, Nd)
Ma	Million years ago
Myr	Million years
NERC	National Environmental Research Council
NOCS	National Oceanography Centre Southampton
OMZ	Oxygen minimum zone
PCZ	Prime Crust Zone
REE	Rare earth elements
REY	Rare earth elements and yttrium
RF	Random Forest
ROV	Remotely operated vehicle
RRS	Royal research ship
RSD	Relative standard deviation
SD	Standard deviation
SEM	Scanning electron microscopy
UNCLOS	United Nations Convention of the Law of the Sea
USGS	The United States Geological Survey

Chapter 1

Introduction

The resource potential of marine ferromanganese (FeMn) crust deposits has been extensively discussed since the 1980s, following the interest generated by research into the economic prospects of FeMn nodules (e.g. Mero, 1965). Initial focus on elemental enrichments within these deposits that drew attention in the 1980s has now shifted, largely due to technological advances that are driving changes in resource demands. Ferromanganese crusts present a highly enriched source of elements including manganese (Mn), cobalt (Co), platinum (Pt), the rare earth elements (REE, with yttrium, REY) and tellurium (Te), all of which have been identified as important raw materials for numerous emerging technologies.

While FeMn crusts have been widely sampled across all major ocean basins, there remains a gap in the understanding of the scale of occurrence and compositional variability. Characterising this variability and developing an understanding of the impact of different environmental drivers on formation and metal concentrations is a vital step towards improving the understanding of FeMn crusts as a potential mineral resource and for the effective management of environmental impacts. This study provides a detailed characterisation and investigation of spatial trends in FeMn crust distribution, preservation and composition at an individual seamount to improve understanding of the dominant controls on variability at this scale.

1.1 Critical Elements

The definition of "critical metals" has developed over time with changes in demand and supply of raw materials, and the specific elements deemed critical can vary between regions, with the USA and EU defining critical elements since the 1970s (e.g. Graedel et al., 2014). Critical elements are those that are vital for the production of numerous technologies but also have a high risk of supply shortages, which mean

potentially large economic impacts when compared to other raw materials (European Commission, 2017, Figure 1.1).

There is growing demand for many of these critical elements due to expanding global populations, emergent technologies and increasing demand for high-tech products. In particular, the transition to non-renewable energy sources to support this global growth means a growing reliance on a wider suite of elements, which can lead to increased sensitivity of economies to the supply of these elements (e.g European Commission, 2017). There are numerous factors that can contribute to an increased risk to the supply of a raw material. According to the European Commission, these fall into two main categories. The first describes the risk to supply of an element, which considers the geographical spread of reserves and production, the political and economic stability of the producing country, the ability for substitution for other elements in technologies and potential element recycling. The second category considers the extraction processes in different producing countries, with negative environmental practices endangering supply to the EU due to environmental regulations on imports (European Commission, 2017). A key factor that can feed into supply risk is if an element is critical in the manufacturing of new technologies but that are currently extracted as by-products from the mining of other metals. This can change over time with technological advancements, both in terms of shifts in demand patterns for different raw materials to build new technologies and potential advancements in the exploration and extraction of deposits.

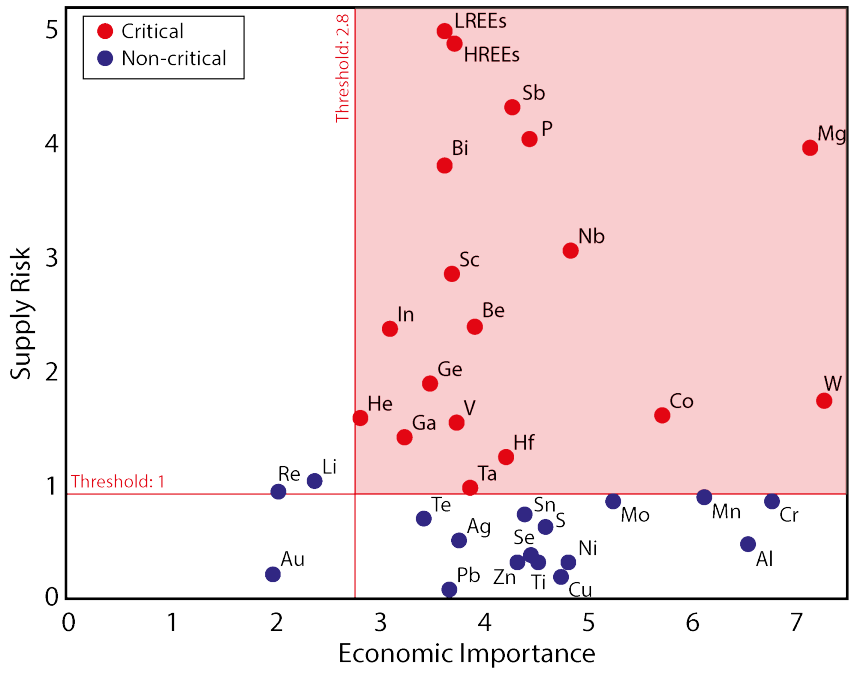

FIGURE 1.1: Schematic showing element criticality according to the EU Critical Elements report (adapted from European Commission, 2010).

One example of an element deemed critical by both the USA and EU is cobalt. Cobalt is widely used in superalloys and is a key constituent of lithium-ion batteries where it is used to improve battery performance by improving efficiencies and stability through repeated charge cycling (e.g. Li and Lu, 2020). Currently, the Democratic Republic of Congo leads the world's sources of cobalt production (e.g. Nassar et al., 2012). Most cobalt is also mined as a byproduct of copper or nickel and so production is reliant on demand for these base metals. In 2010, the European Commission identified cobalt as a critical metal due these combined factors, with limited options for substitution in technologies and high dependence of worldwide production from few sources (European Commission, 2010). Another example critical element is tellurium, which is used in solar energy technologies within cadmium-telluride photovoltaic cells (Zweibel, 2010). Almost all tellurium used today is mined as a byproduct of other base metal ores, largely recovered through the refining of copper (e.g. Nassar et al., 2012; Mudd et al., 2017).

The rare earth elements are a group of 17 elements, including 15 lanthanides (from lanthanum through to lutetium), scandium and yttrium (REY). This group is commonly split into subgroups following similar chemical behaviours dictated by their atomic weights. The atomically lighter group, from lanthanum through to europium, are known as the light rare earth elements (LREE) and the heavier group, from gadolinium through to lutetium and yttrium, are called the heavy rare earth elements (HREE). They are widely used across a range of new technologies, including in magnets and metal alloys (Castor and Hedrick, 2006). A large risk to their supply security is due to the concentration of production in one country, with the proportion of global REE production in China peaking at 97.1% in 2006 and falling to current levels of over 60% in 2019 (Weng et al., 2015). One of the key challenges in sourcing REE isn't just the total REE grade of the deposit, but the relative proportions of the individual REE and processing of complex ores. In general, in the Earth's crust, LREEs are more abundant than the HREEs and this has been mirrored in the relative resource estimates of LREE in comparison to HREE (Weng et al., 2015).

Given the growing competition for the resources needed to manufacture new technologies for expanding populations, marine mineral deposits that are enriched in critical elements are being explored for their potential to supplement to raw material demands in the future (Ragnarsdottir, 2008; Hein et al., 2013). The initial economic interest in FeMn crust deposits in the 1980s was driven by the high concentrations of cobalt, copper and nickel (Aplin and Cronan, 1985). Following the decline of base metal commodity prices and remaining challenges in implementing deep sea mining, marine mineral deposits fell out of favour until the start of the 21st century. The renewal of interest in marine minerals has been driven by their polymetallic composition and their enrichment in numerous critical elements (e.g European Commission, 2017).

1.2 Deep sea mineral deposits: an overview of exploration and exploitation

While oceans cover a greater proportion of the Earth's surface than land, currently the majority of mineral resources are sourced from terrestrial deposits. Mining of marine mineral resources has been limited to shallow-water, near-shore deposits on the continental shelf such as industrial aggregates and precious metal placer deposits, which have a long and well-established history of extraction (e.g. Rona, 2008). Deep marine mineral deposits, in the form of ferromanganese nodules, were first sampled during the scientific expeditions of the HMS Challenger from 1873 to 1876 (Murray and Renard, 1891). The interest in economic potential of the deep marine realm was galvanised in the 1970s by the discussions on the resource potential of ferromanganese nodule deposits (e.g. Mero, 1965) and subsequent discoveries of hydrothermal vent sites and the associated seafloor massive sulphide deposits (Corliss et al., 1979).

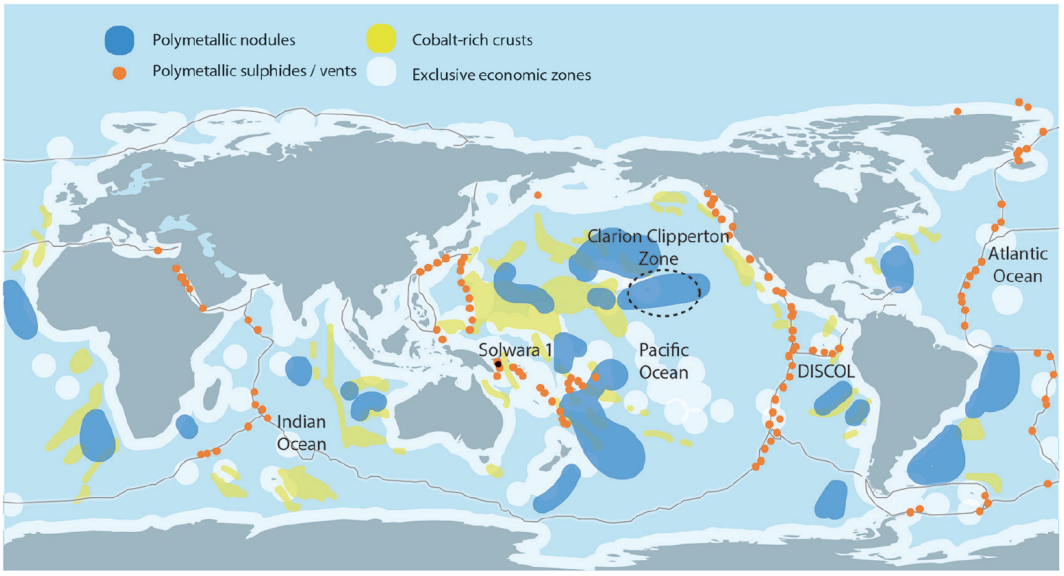

FIGURE 1.2: World map showing key locations of the three main marine mineral deposit types, including areas of interest and exploration; polymetallic nodules, polymetallic sulphides and cobalt-rich crusts, from Miller et al. (2018).

While research on deep sea mineral deposits continued throughout the 20th century, there has been a renewal of interest in the resource potential of marine mineral deposits since the start of the 21st century. One reason for this is to meet growing demand for the materials required to manufacture emerging and disruptive technologies. For example, as societies move to increase the proportion of energy consumption from renewable sources and work towards decarbonisation goals there has been growth in the demand for green energy technologies, such as wind turbines, and expansion to new technologies, such as improving battery technologies for electric vehicles. Many of the trace elements needed for these technologies have high risk to their supply security (Ragnarsdottir, 2008). This can be due to a range of factors, from national monopolies

on element supply to dependence on extraction as by-products rather than primary commodity. As terrestrial deposits trend towards lower grades and more challenging operational environments, marine mineral deposits present opportunities for high grade deposits (Hein et al., 2010; Calas, 2017).

The potential benefits of deep marine FeMn deposits include their polymetallic nature, lack of significant overburden for mining and relative ease of processing (e.g. Hein et al., 2013). Despite these factors, the largest barriers to exploitation of marine minerals remain the economic, technological and environmental factors that make drafting exploitation regulations difficult (Lodge and Verlaan, 2018). The fluctuating nature of metal markets makes ventures into new environments such as the deep sea challenging and such deposits will only be fully considered once potential commodities are comparable.

The regulation of activities in the oceans beyond regions of national jurisdiction, known as the "Area", falls under the 1982 United Nations Convention of the Law of the Sea (UNCLOS) and is enacted by the International Seabed Authority (ISA). The ISA was established by UNCLOS in 1994 to build a regulatory framework in order to organise and control activities related to deep-sea mining in the Area, following principles of the "common heritage of mankind" (Lodge and Verlaan, 2018). This principle includes concepts of ensuring shared benefits from the outcomes of seabed mining and the consideration of conservation and preservation alongside resource exploitation (e.g. Jaeckel et al., 2017). The drafting of regulations for the exploration and exploitation of deep sea minerals, known as the "Mining Code" are still underway, with significant focus on how environmental conservation can be integrated into exploitation. Another key factor that is required before the exploitation of deep sea minerals occurs is an understanding of mineral resource assessments and estimated reserves. The ISA follows the resource classification scheme defined by the 2013 Committee for Mineral Reserves International Reporting Standards (CRIRSCO). A mineral resource is defined by the ISA as a "concentration or occurrence of solid material of economic interest in or on the Earth's crust in such form, grade or quality that there are reasonable prospects for economic extraction" (ISA/21/LTC/15/Annex V), and does not consider feasibility of exploitation. The level of uncertainty in mineral resource estimates defines whether a mineral resource is inferred, indicated or measured. A mineral reserve is a resource that has been evaluated so that abundances and volumes are known within acceptable limits of uncertainty and which is economically and technically feasible to exploit. Only indicated or measured resources can be converted into mineral reserves following evaluations of viability. This means that before exploitation of a marine mineral deposit can be considered, extensive exploration is first required to characterise a deposit. As of 2020, the ISA had approved 30 contracts for exploration in the Area with 22 countries and covering an area of 0.7% of the Earth's seabed. Of these 30 contracts, 18 are for FeMn nodules, seven for polymetallic sulphides and five are for FeMn crusts

(Figure 1.2). From the five FeMn crust exploration contracts, four are for areas in the W Pacific and one is in the SE Atlantic. The proportion of exploration contracts issued for different marine mineral resources and different regions reflects a range of factors, such as the history of exploration in an area and ease of extraction of the resource. Ferromanganese crust resources, particularly in the Atlantic Ocean, have some of the greatest uncertainties around resource potential and estimation due to uncertainties in variability in occurrence, composition and thickness.

1.3 Ferromanganese crust deposits

Hydrogenetic FeMn crusts form from the precipitation of Fe-oxyhydroxides and Mn-oxides directly from seawater onto hard rock substrates, to form pavements and encrustations. Very slow formation rates, between 1 – 10 mm/Myr, combined with high specific surface areas of 325 m^2g^{-1} support the enrichment of many elements above continental crustal mean concentrations (e.g. Hein et al., 2000). Figure 1.3 shows the enrichment of key target elements relative to elemental concentrations in seawater and continental crust and highlights the significant enrichment of elements such as cobalt (Co), platinum (Pt), tellurium (Te) and the rare earth elements (with yttrium, REY). These high concentrations highlight the main research topics of FeMn crusts, primarily as a potential resource of economically important elements, such as Co and Pt. Particular focus in recent years has been on the growing demand for "green" energy technologies such as photo-voltaic cells and electric cars (see Section 1.1). The growth in this industry has led to shifts in demand patterns for raw materials, with some of the elements that are vital to the production of these technologies highly concentrated in FeMn crusts (Hein et al., 2010, 2013). One such element is Te, which is enriched in FeMn crusts by a factor of 10^4 relative to continental crustal concentrations (Figure 1.3). Secondly, due to the nature of FeMn crust formation from seawater and the high enrichments of some elements in FeMn crusts relative to seawater concentrations, FeMn crusts could play a significant role in the ocean geochemical cycling of these elements (Hein et al., 2003). Ferromanganese crusts have also been extensively studied in palaeoceanography (Koschinsky et al., 1996; Ling et al., 1997; Abouchami et al., 1997; Claude-Ivanaj et al., 2001; van de Flierdt et al., 2002). As hydrogenetic FeMn crusts precipitate from ambient seawater over geological timescales they can provide an important record of Cenozoic palaeoceanography and ocean chemistry.

Hydrogenetic FeMn crust mineralogy is dominated by Fe-oxyhydroxides and Mn-oxides. The most common minerals include an Fe-rich δ-MnO_2 (ferruginous vernadite; Bolton et al., 1988; Koschinsky and Halbach, 1995) and an amorphous Mn-bearing Fe-oxyhydroxide (Mn-feroxyhyte; Varentsov et al., 1991; Hein and Koschinsky, 2014; Marino et al., 2017). Common impurities within crusts include quartz and feldspar, often as grains within the ferromanganese layers, and carbonate-fluorite-apatite phases

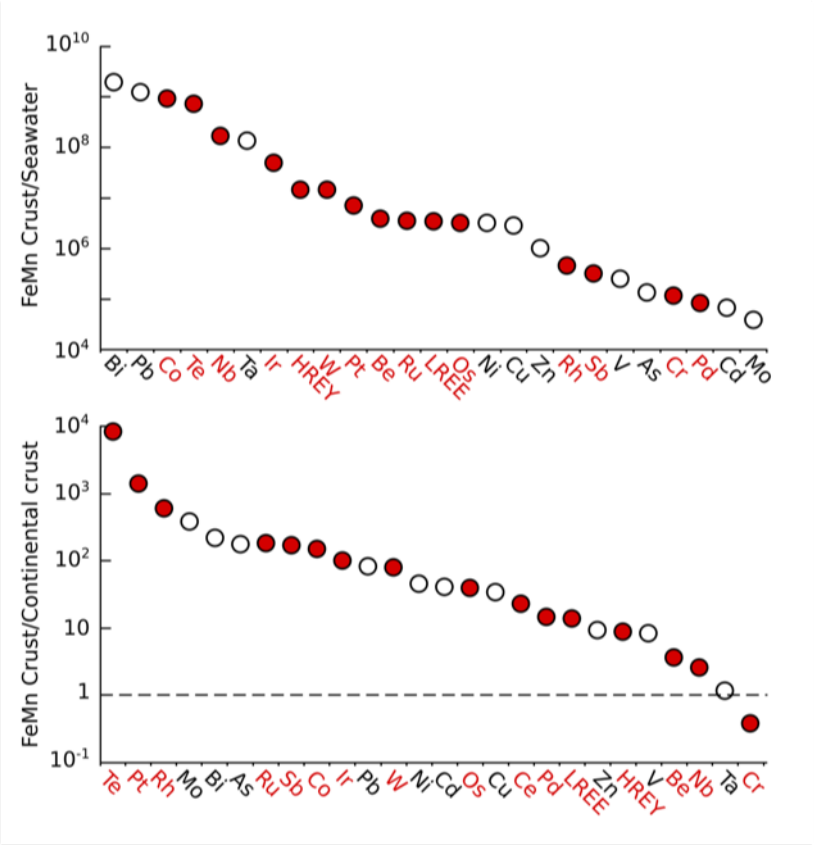

FIGURE 1.3: Graph to show the enrichment of selected elements in FeMn crusts with respect to seawater (top) and continental crust concentrations (bottom) (adapted from Hein et al., 2010). Elements highlighted in red are those that have been identified as critical (European Commission, 2010, 2017).

(CFAs) as diagenetic horizons or clasts. The mineralogy of crusts can be altered by secondary processes, including redissolution and enrichment processes (e.g. Koschinsky et al., 1997).

Common alteration minerals include minor goethite, from the recrystallization of ferroxyhyte, and todorokite, from the recrystallization of vernadite under lower oxic conditions (Hein and Koschinsky, 2014). The geochemistry of crusts varies on a range of scales, from intra-basin down to individual layers. This breadth of variation can capture contrasting processes, from changes in palaeoceanography and palaeoredox through to the site-specific surface chemistry of different Mn-oxide polymorphs.

1.3.1 Formation mechanisms

Ferromanganese crust formation is stipulated to have four pre-requisites (Hein et al., 2013). Firstly, the precipitation of crusts requires a supply of the main constituent elements, Mn and Fe (Halbach and Manheim, 1982). In the marine environment, the main sources of Mn are terrestrial inputs, seafloor hydrothermal fluids and diagenetic pore

fluids from ocean basin and continental shelf sediments (Elderfield, 1972; Heggie et al., 1987). Iron fluxes to oceans are dominated by atmospheric dust inputs but also include rivers carrying continental runoff and groundwaters, hydrothermal fluids and diagenetic sediment pore fluids (e.g. Duce and Tindale, 1991; Johnson et al., 1997; Archer and Johnson, 2000; Elrod et al., 2004; Windom et al., 2006). Secondly, crust formation requires oxidized waters to trigger the oxidation of aqueous $Fe(OH)_3$ and Mn^{2+} to form Fe-oxyhydroxide and Mn-oxide species (Koschinsky and Halbach, 1995). Thirdly, crusts require a sediment-free hard substrate on which to form (Halbach and Puteanus, 1983). Hence areas with elevated flow speeds, such as turbulent flows around seafloor obstructions, promote crust precipitation. Finally, this substrate needs to be a stable surface to allow for the accretion of slow growing Mn-oxides and Fe-oxyhydroxides (Hein et al., 1988). Many of these assumed pre-requisites are fulfilled by seamount and guyot environments, where FeMn crusts have been widely observed and studies have used models of global seamount coverage to estimate FeMn crust reserves (Manheim, 1986; Hein et al., 2009a, 2013). Preferential formation on seamounts, in conjunction with leaching experiments, have supported the development of the widely applied colloid-chemistry model for the formation of hydrogenetic FeMn crusts (Halbach, 1986; Koschinsky and Halbach, 1995). Their formation has been linked to the concentration of reduced manganese, Mn^{2+}, at the oxygen minimum zone (OMZ) (Johnson et al., 1996). Seafloor protrusions allow for upwelling and turbulent mixing of more oxygenated bottom waters, allowing Mn^{2+} to be oxidized and form oxide- and hydroxide-colloids. The mixed colloid species form due to the interaction of opposing surface charges between a central Mn- or Fe- core and other oxide and hydroxide elements (Koschinsky and Halbach, 1995). Trace metals can then be scavenged from the water column and adsorbed onto colloid surfaces of opposite charge (Figure 1.4). Sequential leaching experiments show distinct elemental associations between Mn- and Fe-species (Koschinsky and Halbach, 1995). Metal cations such as Co^{2+} and Ni^{2+} (manganophiles) form colloid complexes with MnO_2-colloids and anions such as MoO_4^{2-} are associated with Fe-oxyhydroxide colloid complexes. These associations are supported by investigations into the crystal structure and bonding environments of different metal ions using spectroscopic analyses, such as X-ray absorption spectroscopy (e.g. Takahashi et al., 2007; Kashiwabara et al., 2014; Manceau et al., 1992) The type of bonding mechanisms for different metal ions and their position in specific polymorphs of different Mn-oxides and Fe-oxyhydroxides has been shown to drive the relative enrichments of different elements (see Section 1.3.3).

1.3.2 Occurrence

Ferromanganese crusts have been most commonly observed on the flanks of seafloor topographic highs, including guyots, seamounts, ridges and plateaus (e.g. Bonatti,

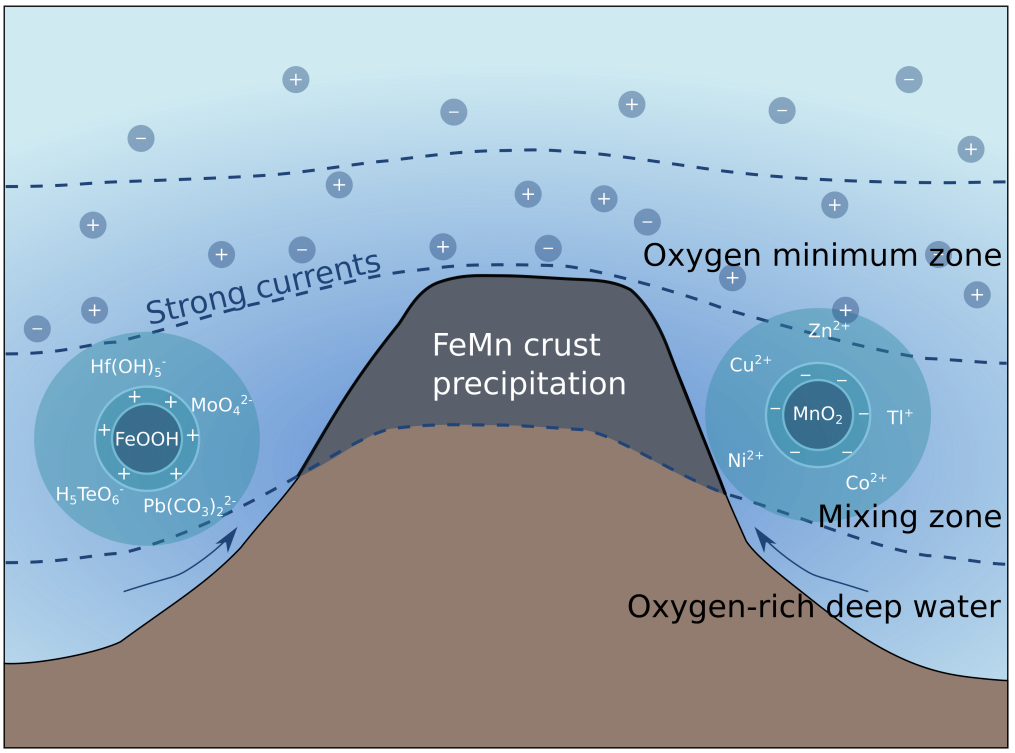

FIGURE 1.4: Schematic diagram showing the formation mechanism for FeMn crusts on seamounts (adapted from Koschinsky and Halbach, 1995).

1972; Roden, 1987) and have been sampled across all major ocean basin, most extensively in the Pacific Ocean (Figure 1.2). The association of FeMn crust formation processes with seafloor obstructions means that seamount distribution has been used to estimate likely FeMn crust occurrence at the ocean basin scale (e.g. Hein et al., 2009a), but the controls on the distribution of crusts at the scale of individual seamounts requires further investigation. Seamount mapping using satellite altimetry have registered over 13,000 seamounts with heights over 1500 m, and modelling has predicted over 100,000 seamounts taller than 1000 m are still to be charted (Wessel et al., 2010). Estimates of seamount numbers from 30 arc-second bathymetry suggest that the Pacific Ocean has the greatest proportion of seamounts over 1000 m in height (57% of total), with 20% in the Atlantic Ocean and 12% in the Indian Ocean (Yesson et al., 2011). While the bulk of research focusses on FeMn crusts from the open ocean on seamounts, they have been reported across a wide range of ocean basin settings, including within restricted ocean basins and on continental margins (Conrad et al., 2017), as well as encrusting fossil material such as whale bones and corals (e.g. Nozaki et al., 2017). While this study focusses on oceanic ferromanganese crusts, they have also been reported in terrestrial basin environments, such as in Lake Baikal in Siberia (Granina, 1991). Ferromanganese crusts have been reported across a wide range of water depths, between 400 – 7000 m (e.g. Hein et al., 2009a; Hein and Koschinsky, 2014). As hydrogenetic, diagenetic and hydrothermal crust horizons can occur within samples depending on the local conditions

at the time of formation, the distribution of these genetic types isn't reported individually, except for ferromanganese crusts dominated by hydrothermal phases. These are limited to regions of near to high seafloor heat flow, such as along mid-ocean ridges (e.g. Dubinin et al., 2018), in island arc settings (e.g. Usui et al., 1986), in back-arc basins (e.g. Eckhardt et al., 1997) and near hot spots (e.g. Scholten et al., 2004).

The bulk of research focus has been on the Pacific Ocean, with intensive sampling of ferromanganese crusts in the 1980s (e.g. Halbach et al., 1983; Halbach and Manheim, 1982), and Pacific FeMn crusts became "model sites" for theories on formation (e.g. Halbach and Puteanus, 1983). Given the association between the occurrence of seafloor obstructions and FeMn crusts, the Pacific Ocean is considered to host the greatest proportion of oceanic FeMn crusts. Highly prospective crusts are also associated with the hydrogenous formation of deep ocean basin FeMn crusts (see Section 1.3.3), with fewer terrigenous inputs and spreading centres that can dilute the concentrations of economic target elements (Hein and Koschinsky, 2014). In particular, the Prime Crust Zone in the NE Pacific Ocean has been extensively studied, principally from a resource perspective, due to a combination of the density of seamount structures and the potential for prospective resource grades and has been estimated to host over 7500 million dry metric tonnes of FeMn crust (Hein and Koschinsky, 2014). While most studies have relied on dredging for crust sampling, advances in autonomous underwater vehicle (AUV) and remotely operated vehicle (ROV) technology in recent years has improved capability for FeMn crust observation at the scale of individual seamounts (e.g. Templeton et al., 2009; Schlacher et al., 2014). In the Pacific Ocean, the Takuyo-Daigo seamount in the northwest Pacific is one of the few structures systematically mapped for ferromanganese crusts at high spatial resolutions using these techniques, across five research expeditions from 2009 – 2016 (Usui et al., 2011, 2013, 2017).

Within the Indian Ocean basin, there are fewer studies on the presence of FeMn crusts due to the smaller basin size, with fewer estimated seamounts and the significant dilution of economic target elements (Hein and Koschinsky, 2014). This is due to substantial detrital inputs in the northern Indian Ocean and hydrothermal influence from the three spreading centres and volcanic arcs in the basin. Crusts have been reported in the Central Indian basin (e.g. Banakar and Borole, 1991; Nath et al., 1992), on the Afanasiy-Nikitin seamount complex (e.g. Rajani et al., 2005; Banakar et al., 2007), on the Ninetyeast Ridge (Hein et al., 2016) and on the Perth Abyssal Plain (Zawadzki et al., 2018). The best studied Indian Ocean FeMn crusts are from the Afanasiy-Nikitin seamount, which is the largest seamount in the Indian Ocean and has minimal inputs from these sources of hydrogenetic dilution (e.g. Rajani et al., 2005; Glasby et al., 2010).

While the number of studies on the ferromanganese crusts of the Atlantic Ocean are still dwarfed by those of the Pacific Ocean, there have been numerous studies in recent years on the occurrence, composition and resource potential of FeMn crust deposits in the Atlantic Ocean (see Section 1.4). Ferromanganese crusts have been sampled across

the Atlantic Ocean basin but studies have largely focussed on a few key regions; FeMn crusts of the Canary Island Seamount Province and Saharan Seamount chain in the NE Atlantic (e.g. Koschinsky et al., 1996; Muinos et al., 2008; Marino et al., 2017; Yeo et al., 2018a), the Rio Grande Rise in the SW Atlantic (e.g. Goto et al., 2017; Jovane et al., 2019; Benites et al., 2020), the New England Seamounts in the NW Atlantic (e.g. Reynolds et al., 1999) (e.g. Reynolds et al., 1999), the Mid-Atlantic Ridge (e.g. Dubinin et al., 2018; Mills et al., 2001) and in the Angola and Cape basins in the SE Atlantic (e.g. Berezhnaya et al., 2018).

1.3.3 Composition

Numerous processes have been postulated to affect the chemical and mineralogical composition of FeMn crusts. The characteristics of the ambient seawater, such as chemical composition, oxygen content, pH and age, exert the fundamental controls on hydrogenetic FeMn crust composition (e.g. Piper, 1974; Aplin and Cronan, 1985; Hodkinson and Cronan, 1991; Hein et al., 2016). These characteristics can be altered through changing productivity, lysocline depth and rate of carbonate dissolution, and current speeds (e.g. Halbach and Puteanus, 1984; Claude et al., 2005). Furthermore, the composition reflects the degree of dilution from detrital and diagenetic phases. Increased detrital inputs at basin peripheries causes continental margin FeMn crusts to show higher Fe/Mn ratios and higher proportions of Si, Al and Cr compared to open basin crusts (e.g. Koschinsky et al., 1996; Hein et al., 2017, 2016; Conrad et al., 2017). The geochemical characteristics may also be further imprinted by proximal hydrothermal fluids, showing elevated Li, Cd, Zn, Mo and Ba, low REEs and generally higher proportions of todorokite (a 10 Å manganate) and goethite (e.g. Michard and Albarede, 1986; Bau, 1991). At the basin-scale, the role of redox processes can be difficult to discriminate due to the local effects of upwelling around individual seamounts and seafloor obstructions.

Elevated concentrations of Ca and P are usually associated with phosphatization events. Central Pacific Ocean FeMn crusts show distinct phosphatization events that correlate across multiple seamounts (Hein et al., 1985; Glasby et al., 2007; Hyeong et al., 2013). These phosphatization horizons commonly mark a two-stage separation in the geochemistry of crusts from the Pacific which also coincide with changes in mineralogy and morphology (e.g. Debaar et al., 1985; Halbach et al., 1989; Usui et al., 2017). Distinct, basin-wide phosphatization events within Atlantic FeMn crusts have not been widely documented. For example, Marino et al. (2017) documented both phosphatized and non-phosphatized crusts for the Canary Island Seamount Province (CISP) and Tropic seamount, supported by observations made in this study, while Muinos et al. (2013) observed large variations in phosphatization for NE Atlantic crusts. Phosphatization events have been attributed to a range of factors. Hein et al. (1993) linked

phosphatization events to the upwelling of P-rich waters at seamounts, with changes in ocean circulation reinvigorating slow circulation of P-rich waters that are derived from intense chemical weathering of continental crust. Halbach et al. (1982) suggested that episodes of high surface-productivity drive the expansion of the OMZs, preventing the precipitation of FeMn crusts and allowing the suboxic, P-rich waters to permeate pre-existing FeMn crusts. Phosphatization is thought to be one of the major secondary diagenetic processes that affect FeMn crust chemistry. Comparisons between phosphatized and non-phosphatized crusts have shown redistribution for a range of elements (Koschinsky et al., 1997). In particular, phosphatized crusts have shown a depletion in Fe and Fe-associated elements as well as remobilization of Cu, Ni, Co and Pt (Koschinsky et al., 1997; Marino et al., 2017). For other geochemical systems, phosphatization has been observed to have little effect, for example for Hf and Pb isotopes (Lee et al., 1999; Koschinsky et al., 1997; Abouchami et al., 1999).

Another factor that can influence FeMn crust composition is the crystal structure of the Mn-oxides and Fe-oxyhydroxides minerals (Prakash et al., 2012; Peacock and Moon, 2012; Hein and Koschinsky, 2014). For example, different Mn-oxide polymorphs have displayed different sorption characteristics for Ni and REE and have been shown to drive stable isotope fractionation, such as is observed for Tl (Peacock and Moon, 2012; Atkins et al., 2016). Diversity in the atomic structures of different Mn-oxides, from tunnel-like to layered, and variations within these end-members allow for a wide range of metal ions to be associated with different Mn-oxides and Mn-oxide mineral proportions play a significant role in crust metal compositions (Post, 1999). The highest metal contents are observed in hydrogenetic FeMn crusts, whose mineralogy is dominated by an Fe-rich vernadite that can attribute more than 90% of the crystalline mineral phases (Hein et al., 2000). Numerous studies have shown an association of Co with this Fe-rich vernadite phase in hydrogenetic FeMn crusts (e.g. Hein et al., 1986; Koschinsky and Hein, 2003). This enrichment is in part due to surface oxidation to Co from Co^{2+} to Co^{3+}, a process that is also observed for Tl (e.g. Burns, 1976; Hem, 1978; Murray and Dillard, 1979; Peacock and Moon, 2012). Tellurium is another critical element that shows extreme enrichment in FeMn crusts when compared to average concentrations in the continental crust (Hein et al., 2003), as seen in Figure 1.3. The extreme enrichment of Te in FeMn crusts is thought to be due to differing mechanisms of incorporation, whereby Te(VI) is coprecipitated with the Fe-oxyhydroxides and not just adsorbed (Hein et al., 2003; Kashiwabara et al., 2014). Adsorption is a process involving a surface reaction on the solid, whereas coprecipitation involves incorporation within the 3D structure when precipitates are formed. This mechanism has been used to explain the large contrast in concentrations between Te and Se despite similar chemical properties (Kashiwabara et al., 2014). The differences in phase associations and uptake efficiency between different mechanisms can be used to explain observed variations in degrees of enrichment relative to seawater concentrations.

1.3.4 Resource potential

The resource potential of FeMn crusts has been widely discussed since the 1980s, following initial interest in the economic potential of FeMn nodules (e.g. Mero, 1965; Halbach et al., 1982; Aplin and Cronan, 1985; Manheim, 1986). Estimates on global resources have developed through time with improvements in the understanding of the controls on FeMn crust formation and mapping techniques, alongside changes in technological mining constraints and metals of interest. A number of assumptions are commonly applied in resources estimate studies. Firstly, studies base FeMn site prospectivity on economic element grade (for example for Co, Ni and Cu content) and estimated crust tonnages. Economic grades are generally estimated using regional-scale studies, as overall the global distribution in FeMn crust sampling is relatively sparse and the focus of the majority of studies is on Pacific Ocean samples (Hein and Koschinsky, 2014). For example, the highest Co concentrations measured so far have been within the Prime Crust Zone of the Pacific Ocean (0.67 wt%, 362 crust samples) whereas Atlantic crusts have lower average Co concentrations (0.36 wt%, 43 crust samples) (Hein and Koschinsky, 2014). These grades are reported to also vary with age and water depth (e.g. Hodkinson and Cronan, 1991; Hein et al., 2000). These patterns have been applied to some mine site models in order to target the most promising crust horizons (Hein et al., 2009a). Estimating crust tonnages remains a major challenge in FeMn resource modelling. Most models rely on the use of bathymetric maps to calculate the approximate number and surface area of seamounts and guyots to give a maximum surface area for crust coverage. This area is then refined using assumptions of optimum depths for crust formation and composition and technological constraints for mining, generally for water depths shallower than 2500 m (Hein et al., 2009a; Muinos et al., 2013; Petersen et al., 2016).

The most significant unknowns in tonnage estimates are crust distribution and thickness variation. Crust distribution has been proposed to depend on a number of variables discussed in Section 1.3.1, such as water depth and sediment cover. Factors such as seamount age have been used to estimate crust formation and preservation, with older seamounts suggested to provide more stable substrates that allow for thicker crusts to grow (Hein et al., 1988). Modelling crust distribution based on the theoretical conditions of formation has been limited by the low spatial resolution of samples collected by dredging, which has been the dominant method of FeMn crust sampling. Detailed investigation of crust thickness distribution on seamounts has as of yet only been described in one study, with Usui et al. (2017) noting significant variation in crust thickness even down to local scales. Recent studies have also used statistical space interpolation to estimate regional FeMn crust resources (Du et al., 2017). Du et al. (2017) discusses a potential method for evaluating resources at the scale of individual seamounts, but they highlight the need for a greater understanding of the fundamental assumptions applied to models at this scale. Sato and Usui (2018) apply a different

technique for modelling crust grades, using estimates of metal fluxes per unit area. This method means that deposit tonnages are not included within the model and so thicknesses, bulk crust composition and physical properties such as density are not required. Such a method could be used on a regional scale to determine key prospective areas for targeted sampling but requires further ground-truthing and relies on accurate estimates of metal fluxes to oceans, which remains debated for many regions.

Currently the abundance of deep sea resources is inadequately quantified. A key reason for this is the paucity of data on proven FeMn crust coverage and high density geochemical data. In particular, global estimates of FeMn crust resources have been hindered by an insufficient understanding of the controls on crust distribution and geochemistry at the scale of the mine-site. The development of ROV and AUV technologies have facilitated high resolution studies of in-situ FeMn crust distribution and well spatially constrained sampling campaigns(Usui et al., 2017; Teague et al., 2018). Usui and Okamoto (2010) further describe lower cost techniques that allow for seamount-scale mapping of FeMn crusts, including towed camera surveys and geophysical mapping using acoustic backscatter. There remains a need to understand the sampling resolution required to fully encapsulate the variance of FeMn crust deposits and how sparse or localized datasets can be best interpreted and interpolated to predict deposit potentials in unexplored regions.

1.4 Atlantic Ocean Ferromanganese Crusts: Previous Work

The first studies dedicated to the research of FeMn crust deposits in the Atlantic focussed on the FeMn crusts of the W Atlantic margin, on the Blake Plateau and New England Seamounts (Manheim et al., 1982; Goddard et al., 1987). Seafloor photographs and early dives of the Alvin research submersible documented highly variable ferromanganese deposit morphologies and outcrop on these structures (Aumento et al., 1968; Goddard et al., 1987). Early sampling and observations of these crusts and those in the Cape Verde Basin in the SW Atlantic showed generally uneven crust coverage and thinner FeMn encrustations than those in the Pacific Ocean, although some crusts of up to 10 cm thick were sampled on Krylov Seamount (e.g. Varentsov et al., 1991). Following the assumptions of ideal conditions for the formation of thick, prospective FeMn crusts, such as stable seamount structures with limited detrital inputs in open ocean basins, the Atlantic basin is predicted to host fewer high grade and tonnage FeMn crust deposits than the Pacific Ocean (Hein et al., 2000; Hein and Koschinsky, 2014). It wasn't until the 1990s that FeMn crust of similar coverage and thickness to Pacific deposits were discovered in the NE Atlantic off the Iberian peninsula during the SO 83 cruise (Koschinsky et al., 1995). Sampling of FeMn crusts from Lion and Tropic seamounts suggested significant deposits of crusts up to 10 cm thick, but with slightly lower average concentrations of Co (average of 0.55 wt%) when compared to

Pacific crusts (0.87 wt%) (Koschinsky and Halbach, 1995). The potential resources of this region were re-evaluated in recent years following the renewed focus on critical metals and the polymetallic nature of FeMn resources (e.g Muinos et al., 2013; Marino et al., 2017, 2019; Yeo et al., 2018a, 2019). For example, the average Te and REY concentrations for Atlantic and Pacific FeMn crusts are comparable Hein et al. (2013). The 2011 DRAGO051 cruise found FeMn crusts in this region of the NE Atlantic up to 250 mm thick and Co up to 7169 μg/g (Marino et al., 2017, 2019). Predicted tonnages of ore given mean thicknesses, average resource grade and estimated coverage given seamount surface area for four seamounts in the NE Atlantic suggested comparable resources to regions of the central Pacific Ocean (Muinos et al., 2013). While the FeMn crusts of the NE Atlantic are fairly well characterised for bulk composition, there remains a need to improve understanding of the seamount-scale variation in both crust occurrence and geochemical changes in order to reduce uncertainty in resource modelling.

Of the four exploration contracts for FeMn crusts granted since 2013 the only one in the Atlantic Ocean is the Brazilian contract region on the Rio Grande Rise in the SW Atlantic (Petersen et al., 2016), while the other three are in the Prime Crust Zone of the W Pacific. The recognition of thick FeMn crusts in this region were first noted in the 1970s following studies on sedimentation on the Rio Grande Rise (Melguen and Thiede, 1974). Limited work on the FeMn crusts of the region has been published, but there is significant interest in fully characterising the nature of the FeMn deposits in this region given the signing of a 15-year exploration contract by the Companhia de Pesquisa de Recursos Minerais (CPRM) of Brazil with the ISA (Jovane et al., 2019; Benites et al., 2020).

1.5 Thesis Outline

The main body of this thesis is structured as three scientific chapters that have been produced as independent manuscripts to be submitted for publication and so each chapter can be read independently of the others. This chapter (Chapter 1) provides an overarching introduction to the themes discussed in the following chapters. Chapter 2 presents the regional geological and oceanography setting of the study area, Tropic Seamount in the NE Atlantic Ocean. Chapter 3 describes the sampling procedures undertaken during the research expedition JC142 on board the RRS James Cook in 2016, and the analytical methods used to obtain the data contained within this study.

Chapter 4 describes the outcomes of high-resolution mapping of FeMn crust distributions at Tropic Seamount from observational data. This is used to build robust models of FeMn crust occurrence. The aim of this chapter is to investigate the applicability of

distribution modelling techniques to quantify FeMn crust distribution and to assess the controls on FeMn crust presence and absence at the scale of an individual seamount.

Chapter 5 presents the results from textural and geochemical analyses of FeMn crusts around Tropic Seamount. This chapter discusses both the physical and chemical processes affecting the accumulation of FeMn crust and investigates the trends and relationships between in growth rates, erosive patterns and composition.

Chapter 6 presents the results of geochemical and statistical analyses of FeMn crust compositions. The focus of this chapter is the variability in the geochemistry of preserved recent growth surfaces and contemporaneous growth horizons, to build an understanding of the local scale environmental controls on composition.

Chapter 7 synthesises the findings of this study in the context of the overarching aim of this thesis, to improve the understanding of key processes affecting the formation, distribution, texture, preservation and composition of FeMn crusts at the scale of an individual seamount. In addition, it poses some further areas of research that have arisen from this work and should be addressed in the future.

Chapter 2

Study Area

2.1 Regional Setting of Tropic Seamount, North East Atlantic

The study area that is the focus of this thesis is Tropic Seamount in the NE Atlantic. High concentrations of key target elements, such as Co, and significant FeMn crust thicknesses have been recorded at Tropic Seamount, making it a key prospective site for exploration and potential exploitation in the Atlantic, as discussed in Section 1.4. Further detailed characterisation and improved understanding on the key controls on FeMn crust formation is required to complement the environmental studies that have been conducted in the area (e.g. Ramiro-Sánchez et al., 2019), at a comparable resolution, to better understand the potential implications of exploration and exploitation. A number of features also make Tropic Seamount a favourable site in which to explore controls on FeMn crust distribution, preservation and composition at the seamount scale. As an isolated, stable seamount with a relatively simple symmetrical structure, Tropic Seamount provides an interesting baseline study for FeMn crusts in the Atlantic Ocean basin that have a long history of dominantly hydrogenetic deposition, to investigate the interaction between local environment and FeMn crust formational processes. The following sections detail the regional geology and oceanography that is pertinent to the area.

2.1.1 Regional Geology

Tropic Seamount is an isolated submarine guyot in the NE Atlantic, 470 km off the West African coastline at 23°N 21°W, south of the CISP and Saharan Seamount chain.

The structure is that of a star-shaped, flat-topped guyot that has four spurs separated by curved landslide scars formed by flank collapse (Palomino et al., 2016). The flank morphology is dominated by incisive gullies. Tropic Seamount extends from 4200m

water depths up to the summit that sits between 950 – 1000 m water depths and covers a total seamount surface area of 1530 km^2 (Marino et al., 2017). The average slope across the summit is low, between 0.5 – 4 degrees, but small cones are observed in the southern and eastern quadrants (Palomino et al., 2016; Yeo et al., 2019). This flat top was likely formed during wave-cut action, supported by the presence of beach conglomerate deposits sampled from the summit, which suggests that Tropic Seamount was an oceanic island that was eroded at sea level and subsequently subsided to its current depth (Schmincke et al., 2000; Palomino et al., 2016). Seafloor palaeomagnetic anomalies show that Tropic Seamount lies on some of the oldest oceanic crust in the Atlantic basin, on 155 Myr old crust (Blum et al., 1996). Petrographic studies suggest that the seamount basement consists of alkaline ocean island basalts and petrogenically has been grouped with the CISP, although this petrogenesis remains debated (Van Den Bogaard, 2013; Blum et al., 1996; Patriat and Labails, 2006). $^{40}Ar/^{39}Ar$ dating of feldspars have indicated potential initial eruption ages from 119 – 114 Ma, with late stage eruptions until 60 Ma (Van Den Bogaard, 2013; Blum et al., 1996). Palomino et al. (2016) reported limited sedimentation over the seamount, with mixed sediment accumulation attributed to either insufficient time to establish a stable pelagic cap or from erosion by increase water currents over seamount summits (Pearson; Rihm et al., 1998).

Previous work on Tropic Seamount has centred around FeMn crust samples collected by dredging on two research cruises; cruise SO83 on the RV Sonne in 1992, and the DRAGO0511 cruise in 2011 on board the R/V Miguel Oliver. The first cruise was used as part of baseline studies on resource estimates for Atlantic FeMn crust deposits as well as numerous palaeoceanographic studies (Schmidt et al., 2014; Klemm et al., 2008; Claude et al., 2005; Reynolds et al., 1999; Claude-Ivanaj et al., 2001; Abouchami et al., 1999; Koschinsky et al., 1995, 1996) The DRAGO0511 cruise and subsequent work has focussed on FeMn crusts as a source of strategic elements (Marino et al., 2017).

2.1.2 Regional Oceanography

Modern circulation in this region has been characterised using physical and chemical properties of the water column and through modelling of mass transport processes (Ganachaud, 2003; Stramma et al., 2005; Voelker et al., 2015; Poehle and Koschinsky, 2017). Figure 2.1 shows the schematic circulation patterns in the Atlantic Ocean. At water depths of over 4000 m, dense Antarctic Bottom Waters (AABW) travel northwards. Above this, Eastern North Atlantic Deep Water (ENADW) dominates the deep waters, travelling south to north between 1500 – 4000 m (Voelker et al., 2015). At intermediate water depths, Antarctic Intermediate Water (AAIW) is observed at approximately 1000 m and is overlain by South Atlantic Central Water (SACW) travelling from south to north at 700 m and North Atlantic Central Water (NACW) flowing in the opposite direction (Stramma et al., 2005; Zieringer et al., 2019). Mediterranean Outflow Water

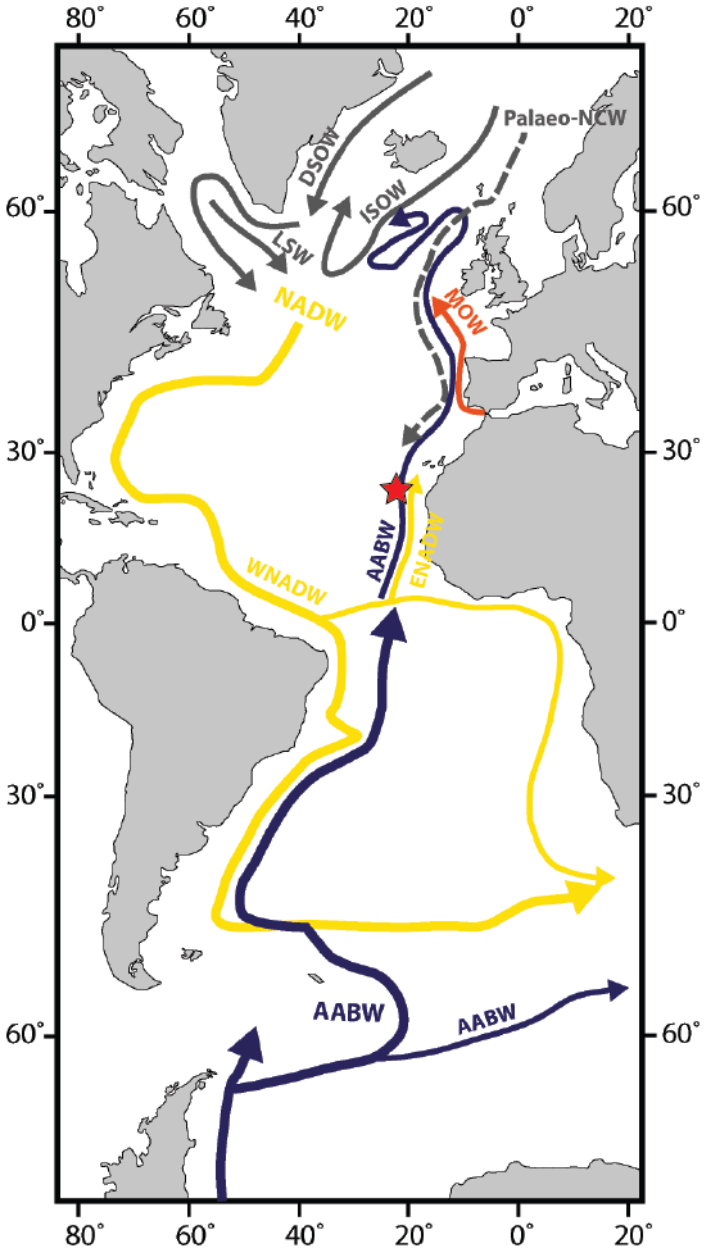

FIGURE 2.1: Schematic showing simplified modern oceanographic circulation in the Atlantic Ocean of the main intermediate and deep water masses: Denmark Strait Overflow Water – DSOW; Iceland Scotland Overflow Water – ISOW; Labrador Sea Water – LSW; North Atlantic Deep Water – NADW; Antarctic Bottom Water – AABW; Mediterranean Overflow Waters – MOW; Northern Component Waters – NCW. Based on Muinos et al. (2008) and Marino et al. (2017).

(MOW) flows into the NE Atlantic through the Strait of Gibraltar and contributes to increased salinities in this region at intermediate water depths (Machin and Pelegri, 2006; Hernandez-Guerra et al., 2014). Above these water masses, the Canary Current are observed in the CISP region further north but its extent to the south is not well quantified (e.g. Poehle and Koschinsky, 2017; Marino et al., 2017). Flow patterns are particularly complex in the region due to the interaction of the both the Canary Islands and NW African margins with water mass movement and can lead to complex eddy and upwelling patterns (Knoll et al., 2002; Barton et al., 2004).

Reconstructions of palaeocirculation over the past 15 Ma in this region have been built using high precision Pb and Nd isotope data (Abouchami et al., 1999; Reynolds et al., 1999; Claude-Ivanaj et al., 2001; Muinos et al., 2008). Prior to the adaption of LA-ICP-MS for Pb and Nd isotopic studies (Foster and Vance, 2006), the analyses relied on manual sampling at temporal resolutions of approximately 500 kyr which limited studies to million-year timescales (Ling et al., 1997; Burton et al., 1997; Frank et al., 2002). Radiogenic isotope systems such as Nd and Pb can be used as palaeoceanographic water mass tracers, as the measured isotopic ratios are dependent on the mixing of different geochemical reservoirs, and hence can be used to "fingerprint" different water masses (Frank, 2002). The crustal rocks from which aeolian, riverine and hydrothermal fluxes are sourced have different isotopic ratios due to differing ages and parent-daughter isotopic abundances. Both Nd and Pb tracer systems depend largely on aeolian and riverine inputs from the erosion of continental crust, but the shorter residence times of ^{204}Pb and the fractionation of Pb isotopes during weathering mean that local variations can play a significant role in the measured isotopic signal. The role of aeolian dust inputs can affect the geochemical and isotopic compositions within FeMn crusts, in particular for REE and Pb (Abouchami et al., 1997, 1999; Claude-Ivanaj et al., 2001; Bayon et al., 2004; Muinos et al., 2008). At Tropic Seamount, influxes of Saharan dust are likely significant due to its position within the path of the Saharan air layer (Chiapello et al., 1995).

Overall, studies that have aimed to reconstruct changes in past seawater chemistry using FeMn crusts on the basin-wide scale have been hindered by geochemical signals that are not resolvable from local-influences (Frank et al., 1999). A better understanding of the role of local processes on FeMn crust geochemistry will help to unravel the complex geochemical variations observed in basin-wide studies.

Chapter 3

Methods

The data and samples analysed in this study were collected during a multidisciplinary oceanographic expedition on RRS James Cook (JC142) between 29th October – 8th December 2016. The expedition to Tropic Seamount formed part of the MarineE-Tech project, one of four consortium projects of National Environmental Research Council's (NERC) 'SoS Minerals' research programme. The SoS Minerals, Security of Supply of Mineral Resources Research Programme, aimed to understand the cycling and concentration of E-Tech elements in natural systems and how the environmental impacts of extraction of these elements could be mitigated. The MarineE-Tech project focusses on the cycling of these elements in the marine environment and the potential impacts of seafloor mineral deposit recovery. The project also had an expedition on RRS Discovery (DY094) to Rio Grande Rise in the SW Atlantic between 16th October – 9th November 2018. In both expeditions, I participated in the recovery and processing of geological samples and observational data as part of the Geology Team.

The following sections outline the analytical methods undertaken for the production of this thesis. I conducted outcrop mapping and modelling from video survey data acquired by ROV. I conducted sample preparation, including sample powder preparation and acid digestion, and participated in the data collection and reduction of samples for geochemical analysis by inductively coupled plasma-mass spectrometry (ICP-MS) and triple quadrupole ICP-MS (ICP-QQQ). Sample digestions at the British Geological Survey Keyworth (BGS) were conducted with the help and guidance of Dr Simon Chenery, Amanda Gardner and Elliot Hamilton who also conducted the sample analysis by ICP-QQQ. Sample digestion at the University of Southampton and the National Oceanography Centre Southampton (NOCS) was conducted under the guidance of Dr Matthew Cooper who also performed the analysis by ICP-MS. Sample thin- and thick- sections were prepared at the University of Southampton by Daniel Doran and Matthew Beverley-Smith. High-resolution scanning electron microscopy (SEM) data was collected with the help of Dr Richard Pearce at the University of Southampton SEM facility and FeMn crust surface imagery was collected by myself and Dr Isobel Yeo at

the British Ocean Sediment Core Research Facility (BOSCORF) NOCS. Lead laser ablation (LA) ICP-MS analyses were conducted by Dr Matthew Horstwood and Dr Pierre Josso at Environmental Science Centre, BGS following successful application to NERC Isotope Geosciences Facilities Steering Committee for a collaborative study (IP-1860-118).

The data collected during the JC142 expedition is used within the study to: (1) Understand the controls on FeMn crust distributions; (2) assess the preservation of FeMn crusts; and (3) explore the controls on the composition of FeMn crusts, all at the scale of an individual seamount. This study aims to shed light on the local-scale processes that operate to affect FeMn crust deposits in the NE Atlantic, as part of the first detailed systematic high-resolution study of FeMn crusts in this region.

All the data that was obtained for this thesis is available within the contained chapters, appendices and electronic appendices. The full cruise report (Murton and scientific party, 2016) and published data libraries for geophysical and camera data (Yeo et al., 2018b) and TELEMAC-3D numerical model of hydrography at Tropic Seamount conducted by HR Wallingford (Murton et al., 2020) are available at the National Oceanography Centre British Oceanographic Data Centre (BODC).

3.1 Geological Sample Recovery

Over 240 ferromanganese crust and substrate samples were collected using the ROV ISIS during research expedition JC142 in 2016 to Tropic Seamount, located in the NE Atlantic approximately 650 km south of the Canary Islands (Figure 3.1). Samples span depths from 970 m at the summit of the guyot to maximum depths of 3894 m off the flanks. The use of the ROV allowed for highly constrained positional information for the samples to be recorded. Once retrieved from the seafloor, the samples were processed on board by labelling sample orientation (using ROV footage and textural indicators) and photographed. Most samples were then cut into sections onboard, to allow for inspection of internal textures and measurement of FeMn crust thickness to be made, and geological descriptions conducted before being stored for onshore analysis.

3.2 Outcrop and Environmental mapping

In order to discern the many different features observed in FeMn crusts from Tropic Seamount and understand the drivers in this variance, the FeMn crusts were mapped for numerous characteristic features. At the scale of the seamount, outcrop morphology and FeMn crust environment were mapped from over 300 hours of ROV dive footage collected over 27 ROV dives. The ROV Isis (operated by the NOCS) video footage

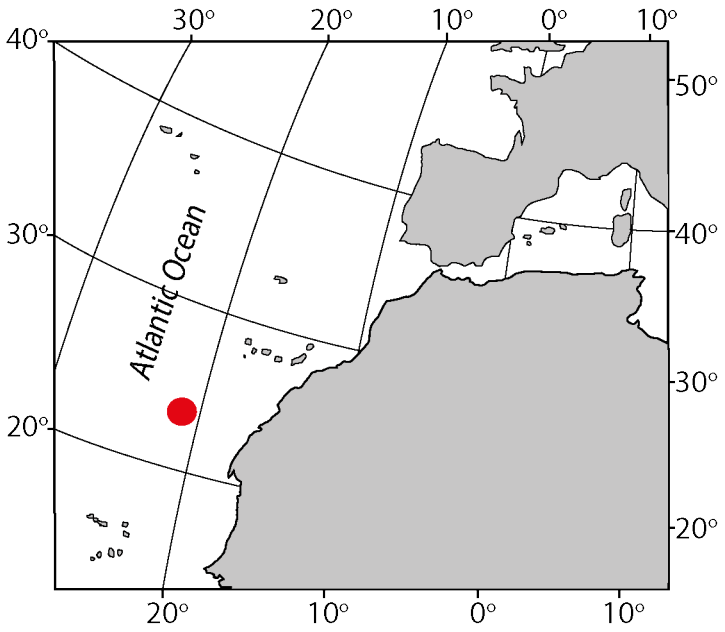

FIGURE 3.1: Schematic map to show the location of Tropic Seamount in the NE Atlantic Ocean basin

was collected during JC142 using a mini Zeus HD video and SCORPIO camera. The focus of the ROV surveys were the eastern, southern and western spurs and summit regions of Tropic Seamount. Surveys aimed to maintain a constant altitude of between 2 – 3 m above the seafloor surface to regulate the field of view, particularly for quantitative surveys. Outcrop mapping was conducted at two scales in order to generate appropriate data resolutions for seamount-scale mapping and statistical analyses. For seamount-scale mapping, lithologies were mapped to 10 m intervals, with lithological changes smaller than 10 m mapped as the dominant lithology for that interval. To facilitate statistical analyses, image captures were generated from video footage, at a rate of one still per minute of survey time. A total of 19654 stills were generated using this process. These stills were processed to remove duplicates and stills with incomplete survey data, after which 10300 stills were maintained for environmental observation and 18288 stills for the presence and absence modelling detailed in Chapter 4. For the purposes of mapping, six main environmental "type" environments were identified and used to categorise outcrop observations. These included sand plains (planar or rippled); FeMn encrusted debris fields; FeMn encrusted lobate fields; FeMn nodular and micronodular fields; FeMn crust pavements; FeMn encrusted carbonate platforms; and FeMn micronodule fields. Sand plains are regions with extensive sediment coverage, in most cases of unconsolidated sediments at the seabed surface. Observations of sediment push cores, gravity cores and ROV investigation show that these sand plains consist of pelagic silts and sands with largely uniform internal structures lacking in distinct sedimentary structures (Murton and scientific party, 2016). The encrusted debris environments have been used to classify the highly variable and chaotic debris flows observed at Tropic Seamount. They can consist of various FeMn encrusted material,

from corals to boulders, that appear to be broken and ex-situ with angular morphologies and a discontinuous in nature or chaotic regions with loose cover and encrusted mass flows. Encrusted lobate fields display a more uniform, continuous outcrop texture with smooth rounded outcrop morphologies. Nodular and micronodular regions show rounded morphologies, up to 10 cm in axis length, and are referred to in terms of morphology to remove reference to potential modes of growth that cannot be determined from video observation. Nodular and micronodular environmental observations were combined under the "Nodular field" type for distribution modelling. Pavement regions show distinct, continuous regions of FeMn encrustation that are typically flat, uniform and spatially extensive and can give limited indication of the underlying substrate morphology. Encrusted carbonate facies show distinct morphologies at Tropic Seamount, of more resistant FeMn crust that protrudes over the carbonate substrate that has been preferentially eroded to give the cross-sectional appearance of a platform. The carbonate lithology of the substrate was corroborated using ROV samples.

3.2.1 Environmental variables

A range of environmental variables were used to investigate patterns in FeMn crust distribution and composition with local topographic and oceanographic features. Bathymetric and backscatter data were collected during JC142 for the whole seamount using the shipboard EM120 multibeam echosounder system and were processed to a final grid spacing of 50 m using Caris Hips and Sips, QPS Fledermaus and FM Geocoder Toolbox v7.6.3 by Yeo et al. (2018b) and Murton and scientific party (2016). Further terrain derivatives were generated from this bathymetric data to provide a set of quantitative seafloor descriptor variables for model building using the Benthic Terrain Modeller tool (version 3.0, Walbridge et al., 2018) in ArcGIS 10.7.1. The terrain derivatives used were Aspect, Bathymetric Position Index (BPI), slope and terrain ruggedness. Aspect, measured in northness or eastness, refers to the orientation of the maximum slope. The BPI describes the location of a feature in relation to its surroundings. Positive values describe features that are elevated above their surrounding regions while negative values are features that are lower. BPI values near zero indicate regions of either zero or constant slope. The BPI value can be considered according to different neighbourhood sizes, described by a ratio that describes the inner and outer radius of a ring surrounding a location, to investigate features of different scales. In this research, both a fine (3/25 radius) and broad (25/250 radius) BPI measure were used. Slope describes the change in the elevation and three related derivatives can be used to describe the convexity or concavity of a slope. These include curvature, curve and profile. Terrain ruggedness, also known as terrain rugosity or roughness and measured as vector ruggedness measure (VRM), describes the three-dimensional orientation of the grid cells within a specific sized neighbourhood. The VRM discussed in this study is a ratio of the surface

area of a cell to its planar area, describing the variation in slope and aspect. For example, a value of 1 would indicate total terrain variation and a value of 0 would indicate no variation.

3.3 Geochemical analytical methods

3.3.1 Sample Preparation and Dissolution

Three sets of sample dissolution were carried out, two at the BGS and one at the University of Southampton (NOCS). In all cases, de-ionized, 18 MΩ-grade water from a Millipore system was used for rinsing and dilution (henceforth referred to as MQ water). All acids were distilled in quartz or Teflon sub-boiling distillation systems and all Savillex Teflon digestion vessels were acid cleaned.

At the BGS, the Tropic bulk FeMn crust and surface scrape samples were digested and analysed. Bulk geochemical characteristics are defined in this sample set using agate-milled powders from the upper 10 mm of the 100 FeMn crusts. For the Tropic bulk FeMn crust powders, approximately 250 mg of sample powder was pre-digested using 3 mL 5 % HNO_3 + 2 mL concentrated HCl + 1 mL concentrated HNO_3. This solution was evaporated at 80°C for 14 hours and then allowed to cool. An acid digestion mixture of 0.5 mL concentrated $HClO_4$ + 1.5 mL concentrated HF and 3.5 mL concentrated HNO_3 was then added and evaporated using a heating scheme of increasing temperatures from 80 °C to 160 °C over an 18-hour period. When dry, the samples were cooled to 50°C and 2.5 mL of 1:1 HNO_3:HCl mixture was added and heated for 30 minutes. After cooling to 30 °C 10 mL MQ water + 2.5 mL H_2O_2 was added and heated at 30 °C for 15 minutes. The final stage of digestion is diluting the mixture to a final acid concentration of 5% with 10 mL of MQ water.

For the preparation of the surface sample scrapes, 100 FeMn crusts were sampled using a ceramic blade to remove 1 g of material from the uppermost 1 mm of FeMn crust surface. This material was oven dried at 60 °C for 24 hours and homogenized using an agate pestle and mortar before analysis using the scheme described above, with reagent volumes scaled to account for the lower sample mass.

Sample preparation and digestion of subsampled Tropic Seamount FeMn crust horizons for comparative chemostratigraphy was conducted at the University of Southampton (NOCS). For the subsampled Tropic Seamount crusts, 5 – 10 mg of micro-drilled material was collected using a 500 μm drill bit. The micro-drill material was pre-digested in 1 mL of aqua regia (3:1 ratio of concentrated HCl to HNO_3). This material was left at room temperature for 12 hours and then evaporated to dry at 80 °C. Once cool, 0.5 mL HNO_3 and 1.5 mL of HF were added, heated at 130 °C for 12 hours and then evaporated until dry using a scheme of increasing temperatures from 130 °C to 180 °C. Once

dry, samples were cooled and 2.5 mL of 6 M HCl was added and samples heated to 130 °C for 12 hours. Samples were then dried, 2.5 mL of 6 M HCl added and the samples were heating again to 130 °C for 12 hours. Samples were then made up to 30 mL 3 M HCl solutions for storage and subsampling. For analysis of trace elements, 2 mL of this solution was sub-sampled and dried down at 130 °C and then made up to 20 mL with a running solution of 3% HNO_3 with an internal spike of 20 ppm Be and 5 ppm Re and In. For the analysis of major elements, 0.5 mL of the trace element solution was sub-sampled, dried down and made up to 5 mL with the above running solution.

3.3.2 Inductively-coupled plasma mass spectroscopy

Geochemical analyses for Tropic Seamount bulk FeMn crusts and surface scrape material were conducted at the BGS with the help of Simon Chenery, Amanda Gardner and Elliott Hamilton. Measurements were carried out using the Agilent 8900 ICP-QQQ. The ICP-QQQ can be run in He collision cell mode and three reaction cell gas modes (H, O or ammonia) which allows for improved resolving of interferences, for example from overlaps with double charged ions or isobaric interferences. The measurement of Te is facilitated by improved sensitivities and lower detection limits. Traditionally Te poses challenges during measurement due to its high ionization energies and 8 isotopes which causes reduced signal intensities. The data reduction process corrects for the machine run blank values, interferences (if not removed by different gas modes then through the analysis of single element solutions e.g. LREE oxides on HREE), reagent blanks, dilution and digestion blanks to give solid sample concentrations. Reagent blank values from both runs were used to determine machine detection limits, as the 3 standard deviation (SD) values for 8 blank measurements. Three different internal standard solutions, selected for different elemental contents (As, Ge, In solutions), were run at regular intervals to monitor instrumental drift and sample duplicates were run every 15 samples. Analyses were calibrated against the artificial element standard solutions and then the calibration was validated against two certified reference materials (CRM); Nod-A1 and Nod-P1. These FeMn nodule reference materials were chosen due to their similarities in composition and matrix, as no FeMn crust-specific reference material has yet been set. The United States Geological Survey (USGS) standard materials are NOD-A1, an Atlantic Ocean hydrogenetic FeMn nodule collected from 788 m water depths from the Blake Plateau and NOD-P1, a Pacific Ocean mixed-type FeMn nodule from 4340 m water depths (Flanagan and Gottfried, 1980). A Geological Survey of Japan (GSJ) standard JMn-1, collected from the Central Pacific Basin from 5200 m water depths, was also used (Terashima et al., 1988). Replicate measurements of standards were run alongside an in-house reference material (HRM, sample JC142_112_003) which is currently being developed to facilitate crust studies.

The analytical precision (% relative standard deviation, %RSD), a measure of the agreement between the results of an analysis, was determined by repeat analyses of the internal standards described above using the following formula:

$$\%\ \text{relative standard deviation} = 100 \times \frac{\text{absolute standard deviation}}{\text{standard average}} \tag{3.1}$$

The accuracy of the analyses, a measure of the agreement between the analytical result and the true value, was determined using the matrix-matched CRM values using the following formula:

$$\%\ \text{relative error} = 100 \times \frac{\text{absolute error}}{\text{true CRM value}} \tag{3.2}$$

For ICP-QQQ analyses, after correction for instrumental drift, blank values and dilution weights, the replicate measurements of internal standard solutions gave precisions of $\leq$5% RSD for P, S, K, Ca, Ti, V, Cr, Co, Ni, Cu, Zn, Ge, Se, Rb, Zr, Nb, Ag, Cd, In, Sn, Sb, Te, Cs, Ba, the REEs, Hf, Ta, W, Tl, Pb, Th and U. Precisions of $\leq$10% RSD were measured for Li, Be, Na, Mg, Al, Mn, Fe, As, Y, Sr, and Mo. Measured values for the three reference materials shows good correlation with reported values for most of the measured elements (see Appendix A.1 and Appendix A.2 for full details). Noted exceptions to this are for Ge, Se, Ag, In, Sn and Tb. Arsenic, Ge, and In are usually used as internal standards for ICP-QQQ analyses at BGS Keyworth. One reason for discrepancies with expected values could be due to elemental and polyatomic interferences, such as the doubly-charged REE on Se and In, which are difficult to correct for without multiple-mode analyses. The discrepancies between measured and expected values for these elements were considered during data interpretation.

Analyses of subsampled Tropic Seamount FeMn crust horizons were conducted at the University of Southampton (NOCS). Elemental concentrations were determined by Thermo Scientific X-Series III ICP-MS. Analyses were calibrated following standard laboratory procedures using certified rock standard reference materials and accuracy was assessed against multiple runs of NodA-1 and NodP-1 reference materials that were run as unknowns alongside samples. Reagent blank values were used to determine machine detection limits. Internal standard solutions (Be, Re and In) were run at regular intervals (every 10 samples) to monitor instrumental drift and sample duplicates were run every 15 samples.

For Tropic Seamount FeMn crust horizons, internal sample precision was $\leq$5% RSD for Ca, To, V, Mn, Fe, Co, Ni, Zn, Sr, Y, Ba, La, Ce, Pr, Nd, W, Pb. T, U, Cu, Zr, Nb, Mo and REE. Precisions of $\leq$10% RSD were measured for Sn and the REE and $>$10% for Li, Sc, Cr, Rb, Cs. Differences in the internal sample precision were observed between the two days over which the samples were analysed. Overall, the precision was better

on the second day of analysis, suggesting more stable ICP-MS performance. Measured values showed lower correlations with reported values for NodA-1 and NodP-1 (see Appendix A.3 for full details) This is likely due to the much smaller sample weights analysed for subsampled horizons and these reference materials (5 – 10 mg) and reported heterogeneities in reference materials potentially related to poor homogenisation processes (Josso et al., 2021).

3.3.3 Scanning electron microscopy

A range of SEM techniques were applied for the different focussed investigations of FeMn crusts according to required study resolutions. For imaging of Tropic Seamount FeMn crust surface morphology and texture, a Hitachi TM-1000 at BOSCORF NOCS was used. No sample preparation is required for this technique, which facilitates efficient analytical throughput, and images of sample surfaces were generated at 250 X and 800 X magnifications for classification.

For the higher-resolution SEM imaging and characterisation, polished sample sections were prepared to provide a level analytical surface and then subsequently analysed at the University of Southampton. Ferromanganese crust samples were prepared for SEM analysis by impregnating with epoxy resin, splitting longer sections on an oblique angle to layering to allow for analytical continuity through the sample, and then grinding and polishing samples into 100 µm thick polished sections. Prior to analysis, sections were carbon-coated. Analyses were conducted at the University of Southampton with a LEO1450 Variable Pressure SEM and an Oxford Instruments X-Act 10 mm^2 area semi-quantitative energy dispersive X-ray (EDS) detector with Silicon Drift detector (SDD) using Aztec Energy software. Elemental mapping was conducted at a resolution of 512 X 384 pixels with an accelerating voltage of 20 kV and dwell time of 305 μs per pixel with 11% overlap and a working distance of 19 mm.

3.3.4 Laser ablation inductively coupled plasma mass spectroscopy

Lead LA ICP-MS analyses were carried out by Environmental Science Centre, BGS following methods described by Bauer and Horstwood (2018) and Josso et al. (2020a). Sample analyses were conducted using Elemental Scientific Lasers NWR193UC LA system with TV2 two volume ablation cell coupled to a ThermoScientific Neptune Plus MC ICP-MS. Thick-sections were analysed using a rectangular 15x150 μm ablation spot at 10 μm/s above the sample surface, on a continuous time-resolved basis. The same reference materials were used as the dissolution analyses; NodA-1, NodP-1, JMn-1 CRMs and the HRM. Reference material sections were made to improve data quality and consistency by mixing reference powers with resin, mounting on glass slides and polishing to produce even surfaces for laser ablation. Lead isotope ratios were measured every

0.265 s and normalised using standard sample bracketing against the NodA-1 and validated against NodP-1, JMn-1 and the HRM, with further processing using Iolite (v3.65) data reduction software (Paton et al., 2011).

3.4 Modelling methods

3.4.1 Factor analyses and statistical methods

Statistical analyses of the geochemical data were conducted to investigate trends in elemental behaviour. To quantify and compare the variance in sample compositions, some basic parameters including the sample range, mean, standard deviation and relative standard deviation were calculated as for sample concentrations (X) as follows:

$$\text{Range} = X_{max} – X_{min} \tag{3.3}$$

$$\text{Mean} = \frac{\text{Sum of sample concentrations}}{\text{Number of samples}} \tag{3.4}$$

$$\text{Standard deviation} = \sqrt{\frac{\sum (\text{Concentration} – \text{Mean})^2}{\text{Number of samples}}} \tag{3.5}$$

$$\text{Relative standard deviation} = \frac{\text{Standard deviation}}{\text{Mean}} \tag{3.6}$$

Pearson's correlation coefficient matrices and Q-mode factor analyses were also conducted in R using the R Stats Package for statistical computing using a range of packages including "caret", "corrplot", "Hmisc", "factoextra", and "psych" packages (Kuhn, 2020; Kassambara and Mundt, 2020; Wei and Simko, 2017; Revelle, 2020). Raw data was normalised by mean-centering and scaling prior to correlation and factor analyses, to ensure equal weightings to different scale values. Factor analyses were derived from Varimax-rotated orthogonal principal factors (Kaiser, 1958). Correlations were deemed to be statistically significant if they had confidence levels of 95%, also referred to in-text as p-values <0.05, or greater.

3.4.2 Distribution modelling

Distribution modelling of FeMn crusts was conducted using R using the following packages for dataset processing, statistical analysis and distribution modelling; "raster" (Hijmans, 2021), "sf" (Pebesma, 2004), "sp", "mgcv" (Wood, 2015), "randomForest"

(Liaw and Wiener, 2002), "maxnet" implemented using "glmnet" for model fitting (Phillips, 2017) and "biomod2" (Thuiller et al., 2020). Prior to modelling, data exploration and cleaning processes were used following Zuur et al. (2010) to ensure robust statistical modelling and assumptions of variable independence. Three different modelling algorithms were used; a general additive model (GAM), random forest (RF) and maximum entropy methods (Maxent). The specifics of the model setting and validation processes used during analysis are described in more detail in Chapter 4.

Chapter 4

FeMn crust distribution modelling at Tropic Seamount, NE Atlantic

The outcrop mapping component of this study has been published in Yeo et al. (2019), on which I am declared a co-author, but the data analysis and results presented in this chapter pertain entirely to my own work. The current model described in 4.4.3 was conducted by HR Wallingford (Cooper and Spearman, 2017; Spearman et al., 2020; Murton et al., 2020).

4.1 Abstract

The expansion in renewable energy technologies is increasing demand for numerous elements, known as E-tech elements, such as cobalt (Co) and tellurium (Te). This is driving research into alternative sources of metal supply. Ferromanganese (FeMn) crusts present a potentially important future source of E-tech elements. There remains a need to understand the controls on FeMn crust distribution at the sub-basin scale. Here, we focus on the seamount-scale processes controlling FeMn crust occurrence at Tropic Seamount, in the NE Atlantic. Outcrop mapping based on high-definition videos show that FeMn crust morphologies on the seamount can be related to a series of "type" environments. These have been combined with maps showing the presence or absence of FeMn crust within a distribution model to assess trends in crust distribution. At Tropic Seamount, distribution modelling predicts high probability of FeMn crust presence focussed around the summit rims and along the flanks of the structure. At this local scale, it is found that the main drivers of crust presence on seamounts are likely attributed to the characteristics of the substrate and the interaction between local topography and local current regimes. These factors combine to determine the availability of exposed surface to encrust and the sustained exposure of that surface to allow for the accumulation of FeMn growth. Building predictive models using empirical data

allow for assumptions on the controls of crust formation to be tested at the scale of the individual seamount. Understanding the controls on FeMn crust abundance is key to developing appropriate economic assessments alongside potentially targeted mining strategies that can be used to better assess environmental impacts.

4.2 Introduction

Marine ferromanganese (FeMn) crust deposits have been observed in all ocean basins, across a range of water depths from 400 – 7000 m (Hein et al., 2013; Hein and Koschinsky, 2014). They are iron (Fe) and manganese (Mn) -rich precipitates that are commonly observed on submarine structures such as seamounts, ridges and plateaus (Bonatti, 1972). The formation of hydrogenetic FeMn crusts has been suggested to have four requirements (Hein and Koschinsky, 2014; Koschinsky and Halbach, 1995); a supply of the main constituent elements, Mn and Fe; the right conditions within the water column to allow for the accumulation of dissolved metal species and then subsequent precipitation; a sediment-free substrate for FeMn crust to precipitate onto; and a long-live, stable substrate that allows for the accretion of very slow FeMn crust growth. Many of these requirements are met by bathymetric highs such as seamounts. The resource potential of FeMn crusts has been widely discussed since the 1980s, following initial interest in the economic potential of FeMn nodules (Mero, 1965; Halbach et al., 1982; Aplin and Cronan, 1985; Manheim, 1986).

In recent years, the potential of FeMn crusts as a source of elements for green energy technologies has renewed interest in these deposits (e.g. Hein et al., 2010, 2013; Muinos et al., 2013; Kashiwabara et al., 2014). Estimates of global resources have developed through time with improvements in the understanding of the controls on FeMn crust formation and mapping techniques, alongside changes in technological mining constraints and metals of interest. A number of assumptions are commonly applied in resources estimate studies. Most models rely on the use of bathymetric maps to calculate the approximate number and surface area of seamounts and guyots to give a maximum surface area for crust coverage. Factors such as seamount age have been used to estimate crust formation and preservation potential (Hein et al., 1986). Prospective basin-scale studies are then refined using assumptions of optimum depths for crust formation and composition and technological constraints for mining, generally for water depths shallower than 2500 m (Hein et al., 2009a; Muinos et al., 2013). However, one of the most significant unknowns in resource estimates for FeMn crusts is the estimated tonnage of deposits, as few studies have had access to high-resolution maps of in-situ FeMn crust distribution (Petersen et al., 2016). Crust distribution at this scale is proposed to depend on a number of environmental variables, such as water depth and sediment cover, but remains poorly quantified. Modelling crust distribution based on the theoretical conditions of formation is limited by the low spatial resolution of

samples collected by dredging, which has been the dominant method of FeMn crust sampling (Usui and Okamoto, 2010). Detailed investigation of crust distribution on seamounts has as of yet only been described in two studies, with Usui et al. (2017) noting significant variation in crust thickness even down to the local, metre-scale and Yeo et al. (2018a) discussing the optimal considerations for resource potential at Tropic Seamount.

Currently, the magnitude of deep-sea resources is highly uncertain. In particular, global estimates on FeMn crust resources have been hindered by an insufficient understanding of the controls on crust distribution at the local-scale of an individual prospective mine-site. The development of remotely operated underwater vehicle (ROV) and autonomous underwater vehicle (AUV) technologies have facilitated high resolution studies of in-situ FeMn crust distribution and well spatially constrained sampling campaigns (e.g. Usui et al., 2017; Teague et al., 2018; Yeo et al., 2018a). In order to understand the controls on FeMn crust abundance and formation, more studies are required at this spatial scale (Hein et al., 2000; Glasby et al., 2007). In this study, high resolution occurrence maps are built of Tropic Seamount and patterns in FeMn distribution and morphology are compared with environmental variables. A seamount-scale distribution model is built to estimate the variability in predicted probability of FeMn crust presence and absences, in order to better understand the drivers behind local-scale patterns on occurrence on seamount structures.

4.3 Geological setting

Tropic Seamount is an isolated submarine volcano in the NE Atlantic, 470 km off the West African coastline, at 23°N 21°W, south of the Canary Island Seamount Province (CISP) and Saharan Seamount chains (Figure 4.1). The region hosts the oldest hotspot-related seamount tracks in the Atlantic (the CISP) and has displayed sustained volcanic activity since 140 Ma (Van Den Bogaard, 2013). The structure is that of a flat-topped guyot that extends from 1000 m at its summit down to 4000 m water depths at its base. The guyot has a distinctive star-shape, define by four spurs to the north, east, south and west separated by collapsed flanks. The seamount is proposed to have been a subaerial oceanic island that has subsequently been eroded and subsided to its current depth (Palomino et al., 2016). Petrographic studies suggest the seamount is based upon alkaline ocean island basalts and petrogenically has been grouped with the CISP, although this petrogenesis remains debated (e.g. Van Den Bogaard, 2013; Patriat and Labails, 2006). $^{40}Ar/^{39}Ar$ dating of feldspars indicates potential initial eruption ages from 119 – 114 Ma, with late-stage eruptions until 60 Ma (Van Den Bogaard, 2013). A high-resolution age model for Tropic Seamount based on an FeMn core dates the earliest FeMn crust precipitation between 77 – 73 Ma (Josso et al., 2019).

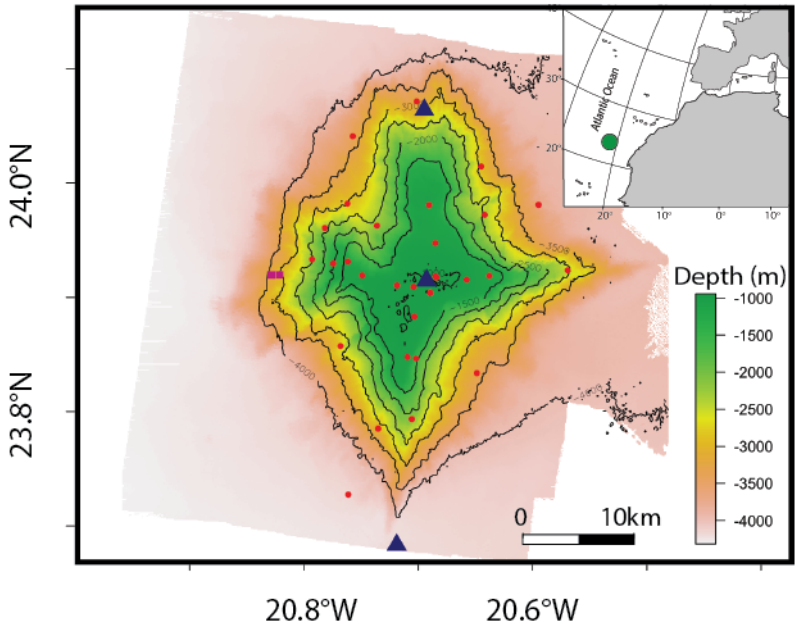

FIGURE 4.1: Map of Tropic Seamount and sampling locations. Inset shows the location of Tropic Seamount in the NE Atlantic. The main map shows the bathymetry of Tropic Seamount, with 500 m contours. For sampling sites; mooring locations (blue triangles), CTD casts (red circles), FeMn crust samples from Figure 4.5 (purple squares).

4.4 Methods

4.4.1 Data Collection

The following data were collected during research expedition JC142 on the RSS James Cook as part of the MarineE-tech project that forms part of the UK's Natural Environmental Research Council (NERC) SoS Minerals research program. Between 29th October to 8th December 2016, Tropic Seamount was surveyed and investigated using a large range of equipment including those described below (Murton and scientific party, 2016).

4.4.2 Environmental variables

Bathymetric and backscatter data was collected for the whole seamount using the ship's EM120 multibeam echosounder system. This data was processed using Caris Hips and Sips, QPS Fledermaus and FM Geocoder Toolbox v7.6.3 (Murton and scientific party, 2016; Yeo et al., 2018b). A grid spacing of 50 m was produced for the final grids and mosaics. This resolution was used within the distribution model for all of the environmental variables used in this analysis, with resampling to match this 50 m resolution

if necessary. All environmental layers were limited to the same extent for use in distribution modelling (Figure 4.2). Further terrain derivatives were generated from the bathymetric data to provide a set of quantitative seafloor descriptor variables for model building using the Benthic Terrain Modeller tool (version 3.0, Walbridge et al., 2018) in ArcGIS 10.7.1. The terrain derivatives used were Aspect, Bathymetric Position Index (BPI), slope and terrain ruggedness. Aspect refers to the orientation of the maximum slope, which is converted into a measure of northness or eastness. The BPI describes the location of a feature in respect to its surrounding features. Positive values describe features that are higher than their surrounding regions, such as ridges, negative values are features that are lower and values near zero indicate areas where the slope is either zero or constant. The BPI can be considered according to different neighbourhood sizes across the whole grid. The neighbourhood size is described by a ring of a specified size around a location and is quoted as the ratio of the inner radius to the outer radius of that ring. In this study, a fine (3/25 radius) and broad (25/250 radius) BPI measure were used. Slope is a measure of the change in the elevation and was used to generate three further derivatives that describe the convexity or concavity of a slope. These were the curvature, the curve and the profile of the slope. Terrain ruggedness, also known as terrain rugosity or roughness, conveys the three-dimensional orientation of the grid cells within a neighbourhood of specified size. The vector ruggedness measure (VRM) discussed in this study is a value that relates the ratio of the surface area of a cell to its planar area and describes the variation in both slope and aspect. A value of 1 would indicate total terrain variation and a value of 0 would indicate no variation.

4.4.3 Current modelling

Mooring and CTD data were used to build a TELEMAC flow model of the current regime around Tropic Seamount (Cooper and Spearman, 2017; Spearman et al., 2020; Murton et al., 2020). Three moorings were deployed (Figure 4.3) with a range of equipment for between 30 – 31 days. All moorings had a Nortek Aquadrop DW Current Meter to measure current velocities and Seabird SBE37 CTDs moored at different heights above the seafloor to measure salinity and temperature. The mooring in the centre of the seamount also had a TRDI Workhorse Sentinel ADCP functioning at 300 kHz for current measurements. In total, 37 CTD casts were deployed across the expedition period to determine the water column properties. Data collected from moorings and CTDs were combined with real-time tidal and wind information to generate a high-resolution hydro-dynamic model that extends across model domain of 500 x 500 km. Outputs of the hydrodynamic model included current velocity, temperature and salinity time series at 49 different layers through the water column. Horizontal resolution of the model varied between 100 – 800 m across the seamount and vertical resolution was highest near the seafloor and at the ocean surface. Models runs were used to simulate the maximum near-seabed (at 1 m above) current velocity, derived at a resolution

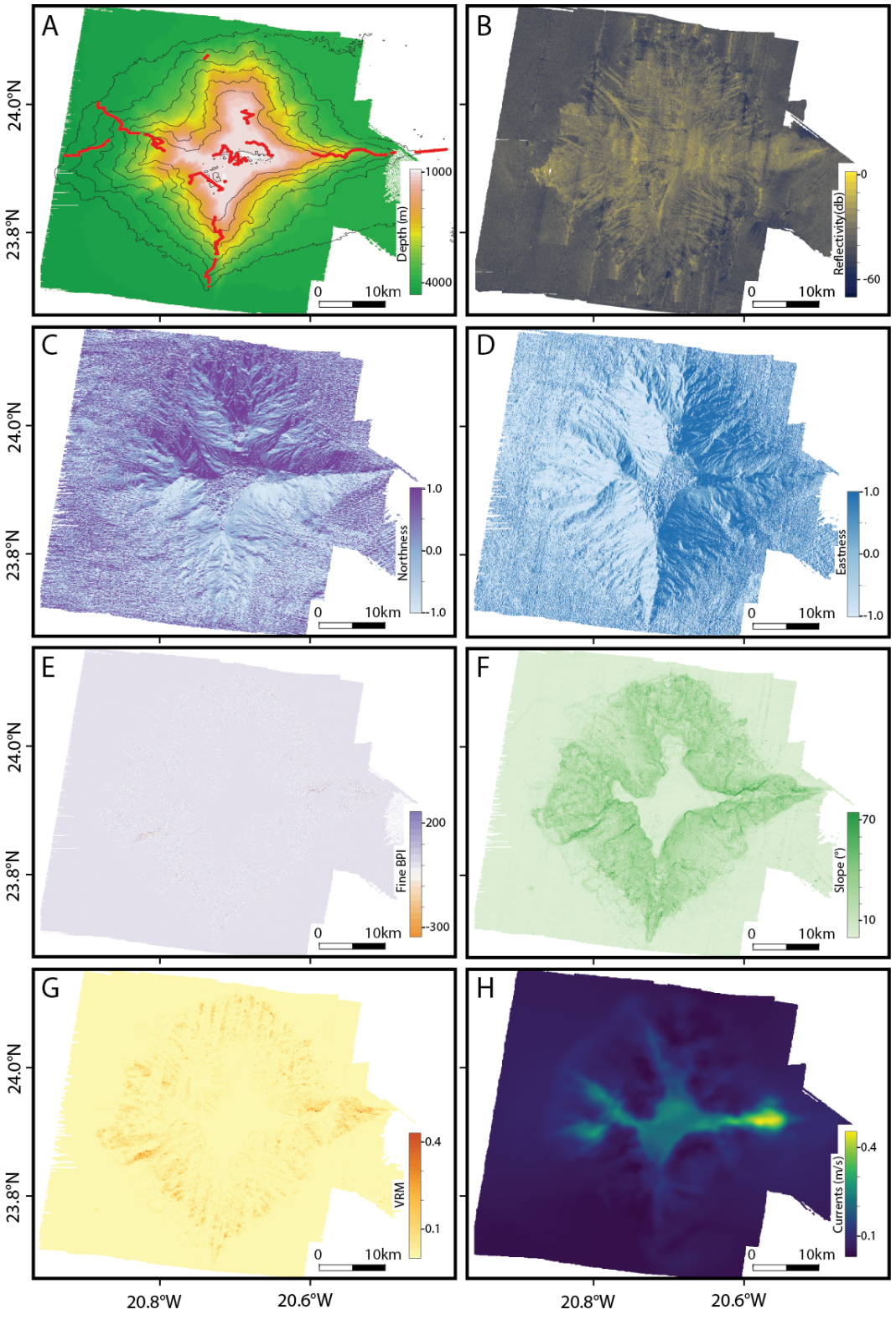

FIGURE 4.2: Compilation of environmental explanatory variable maps used in this study. A) Water depth, with 500 m contours and modelling data points extracted from ROV dives in red; B) Reflectivity, from backscatter data; C) Northness; D) Eastness; E) Fine-scale BPI; F) Slope; G) VRM, roughness; H) modelled maximum current velocity at 1 m above the seabed.

between 500 – 600 m that varied across Tropic Seamount. This layer was interpolated using ordinary kriging to match the 50 m cell resolution of the other environmental variables.

4.4.4 Mapping FeMn crusts at Tropic Seamount

Detailed mapping was carried out using ROV Isis on JC142, which was used to collect a range of biological and geological samples and observational data across 27 ROV dives. Observational data was collected using a mini Zeus HD video and SCORPIO camera. High-definition videos were collected across a range of seamount locations covering the summit and the four limbs, with surveys aiming to maintain a consistent altitude of 2 – 3 m above the seabed to keep a regular field of view. In total, over 300 hours of ROV footage were used to map outcrop morphology and crust environment. Outcrop mapping was undertaken to two scales to facilitate analysis and presentation. To generate coherent transect maps, changes in lithology across distances less than 10 m were mapped as the dominant lithology over that 10 m transect, to maintain reasonable data resolutions. To understand patterns in outcrop occurrence and environment, stills were extracted from high definition videos using Quicktime 7 Pro at a rate of one still per minute of survey time (approximately every 15 m). A total of 19654 stills were generated and after data cleaning, to remove duplicates and stills with incomplete survey data, 10300 stills were maintained for environmental observation and 18288 stills for presence and absence modelling. Data analysis of these stills was carried out using the open source software R (R Core Team, 2020), with detail of specific packages discussed in further detail in the relevant sections below.

To facilitate environment mapping, different categories were delineated according to outcrop texture and general facies and these categories corroborated with in-situ rock samples. The dominant environment was defined as those occupying most than 50% of the still frame. Six "type" environment categories were identified (Figure 4.3); sand plains (planar or rippled, Figure 4.3a); encrusted debris fields (Figure 4.3b and 4.3g); encrusted lobate fields (Figure 4.3c); nodular (Figure 4.3d) and micronodular fields (Figure 4.3h); crust pavements (Figure 4.3e); and encrusted carbonate platforms (Figure 4.3f). For the purposes of distribution modelling, nodular and micronodular fields were merged. "Sand plains" are regions with extensive sediment coverage, in most cases of unconsolidated sediments at the seabed surface. Observations of sediment push cores, gravity cores and ROV investigation show that these sand plains consist of pelagic silts and sands with largely uniform internal structures lacking in distinct sedimentary structures (Murton and scientific party, 2016).

Video transects also show discrete regions of current ripples and in some areas larger scale ripple-like forms made up of coarse sand and shell fragments. "Encrusted lobate fields" and "encrusted debris fields" are both environmental descriptors that are

classified according to their outcrop-scale texture that shows distinct differences from the typical pavement and nodular FeMn environments. The encrusted debris environments have been used to classify the highly variable and chaotic debris flows observed at Tropic Seamount. They can consist of various FeMn encrusted material, from corals to boulders, that appear to be broken and ex-situ with angular morphologies (Figure 4.3b) and a discontinuous in nature or chaotic regions with loose cover and encrusted mass flows (Figure 4.3g). Encrusted lobate fields display a more uniform, continuous outcrop texture with smooth rounded outcrop morphologies. "Nodular" and "micronodular" regions show FeMn encrustations with rounded morphology that can vary in axis length up to 10 cm. They are referred to in terms of morphology to remove reference to potential modes of growth that cannot be determined from video observation. "Pavement" regions show distinct, continuous regions of FeMn encrustation that are often considered as the typical facies of FeMn crusts. They are typically flat, uniform and spatially extensive and can give limited indication of the underlying substrate morphology. "Encrusted carbonate" facies show distinct morphologies at Tropic Seamount, of harder FeMn crust that protrudes over the carbonate substrate that has been preferentially eroded to give the cross-section appearance of a platform. The carbonate lithology of the substrate was corroborated using ROV samples.

4.5 Data Analysis

4.5.1 Distribution modelling of FeMn crusts

Prior to modelling of FeMn crust distribution, data exploration of the environmental explanatory variables showed non-linear relationships with the response variable, FeMn crust presence or absence, and none of the explanatory variables are normally distributed (Zuur et al., 2010). To maintain modelling assumptions of variable independence, an environmental variables selection process was carried out to determine the most appropriate input variables for model building and allow for improved result interpretation (Zuur et al., 2010). Collinearity was tested using pairs-wise plots and by inspecting Pearson's correlation values. Variables with Pearson's correlation values of >0.7 were removed from the model. The following seven environmental explanatory variables were retained after this process and used for model building; water depth, eastness, northness, fine BPI, slope, roughness and maximum current velocity. Modelling was also carried out with the above environmental variables with the addition of backscatter to investigate the role of backscatter on model predictive performance.

Ferromanganese crust distribution was modelled using three different algorithms that are commonly used for species distribution modelling in the biological sciences (e.g. Guisan and Zimmermann, 2000; Guisan and Thuiller, 2005; Cutler et al., 2007; Elith and Leathwick, 2009; Marmion et al., 2009) but have also been applied to terrain modelling

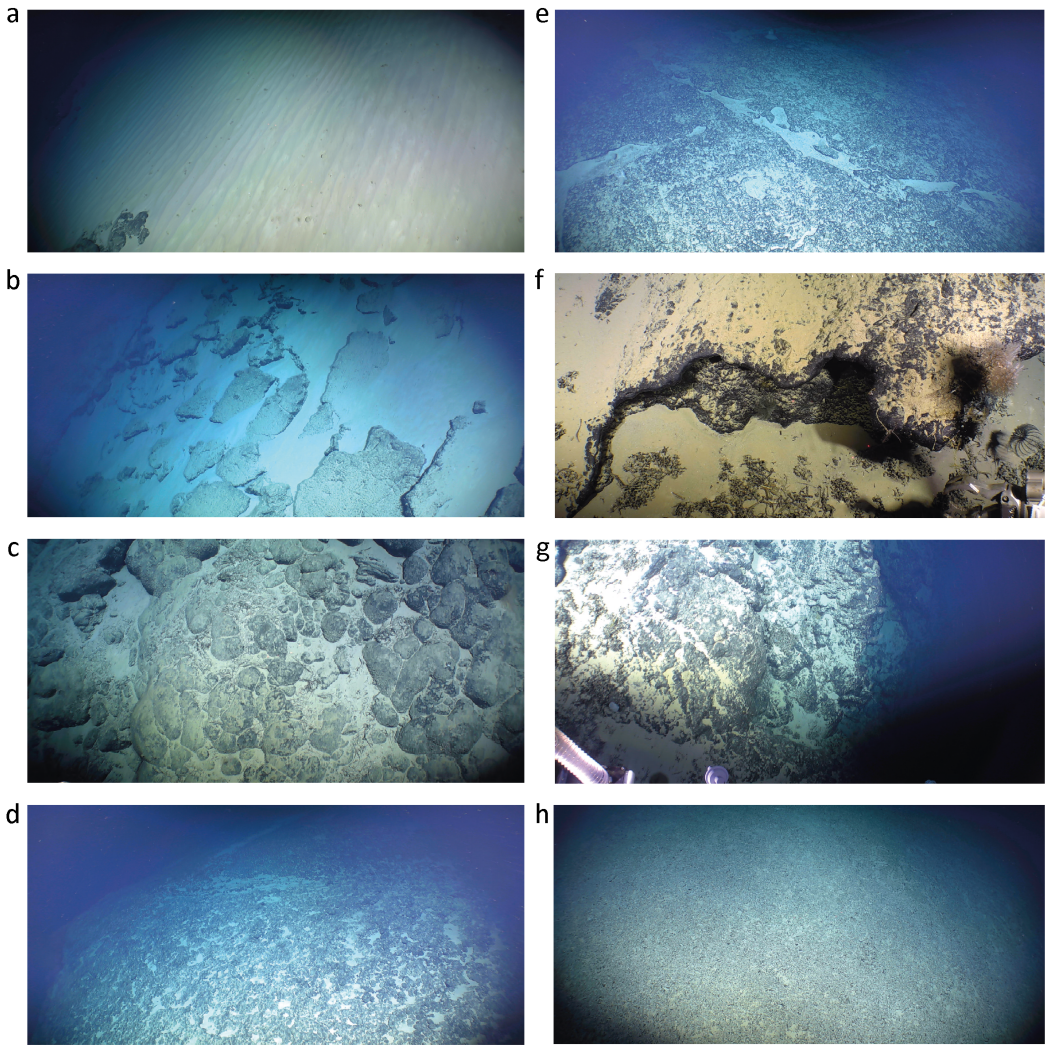

FIGURE 4.3: Type environments observed at Tropic Seamount; a) sand plains; b) encrusted debris fields, fragmented slabs; c) encrusted lobate fields; d) nodular fields; e) pavement; f) encrusted carbonate platforms; g) encrusted debris fields, fully encrusted mass flow; h) micronodular field.

(Erikstad et al., 2013; Li et al., 2016; Gazis et al., 2018); general additive models (GAMs), random forest (RF) and Maxent. This is the first application of these modelling techniques to investigate the distribution of FeMn crusts. Variable extraction, raster handling, statistical analyses and modelling was carried out using the open source software R (R Core Team, 2020), with packages "raster" (Hijmans, 2021), "sf" (Pebesma, 2018), "sp" (Bivand et al., 2013) and specific modelling packages described below. General Additive Models facilitate the modelling of non-linear relationships between response variables and explanatory variables, through the use of smoothers and link functions. The R package "mgcv" (Wood, 2017) was used to build a binomial GAM model using the logit link function for the binary response. Random forest modelling uses a classification algorithm that builds multiple decision trees from randomly selected subsets of data and predictor variables and then determines a consensus of decisions based on the

most common outcome (Breiman, 2001). Random forest methods do not make assumptions on response variable distributions, allow for interactions between the explanatory and response variables as well as non-linear relationships and are resistant to overfitting (when the number of predictors are larger than the number of observations) and as such have shown good predictive performance even with large, noisy datasets (Cutler et al., 2007). An RF model was applied using the "randomForest" package (Liaw and Wiener, 2002) and was run in classification mode with 500 trees, a node size of 5 and default settings for the number of randomly sampled variables at each split (for classification mode this is the square root of the number of variables). The final algorithm applied was Maxent, a machine learning method that estimates the distribution of a response variable by finding the probability distribution which shows the maximum entropy (i.e. that is most spread out) when constrained to the input conditions defined by the explanatory variables (Phillips and Dudík, 2008). Maxent was applied using the "maxnet" package (Phillips et al., 2017), that implements Maxent using the "glmnet" package (Friedman et al., 2010) for model fitting, on true presence and absence data.

Once models were refined, both RF and GAM models were run using the "biomod2" package to facilitate internal cross-validation and external validation processes (Thuiller et al., 2009). Finally, an ensemble model was built using the "biomod2" package to combine and summarise the observed variation in predictions and associated uncertainties, to give more robust predictions (Marmion et al., 2009). This ensemble model was built using the weighted average of the GAM and RF models as well as a committee averaging method (described in more detail in Section 4.5.2) to compare to the Maxent model output.

4.5.2 Model Evaluation

The performance of the individual models was assessed by using both internal and external validation processes. Evaluation of model performance was carried out against a random portion of 25% of the dataset, that was set aside for independent model validation prior to model building. The remaining 75% of the dataset was used to train, calibrate and cross-validate the model. The performance of the models during each of the 5 independent model runs was determined using iterative cross-validation on the training dataset, whereby the training data was randomly split at the start of each independent model run into a 70% training portion and evaluated against the remaining 30% portion. Performance of each of the individual models built was estimated using the following statistics: model Sensitivity, Specificity, the Area under the Curve (AUC) of the receiver operating characteristic (ROC), and the True Skill Statistic (TSS). The Sensitivity (True Positive Rate, TPR) is the proportion of correctly predicted presences and the Specificity (True Negative Rate, TNR) is the proportion of correctly predicted absences. These measures are independent of each other and of prevalence, which is

the proportion of the study sites that are presences. The AUC score gives a measure of how well the model built can discriminate presences and absences, using ROC curve plots of that describe the relationship between the Sensitivity and the Specificity of the model. For AUC, a value of 1 would indicate a model can perfectly distinguish presences from absences whereas a score of 0 would mean a model is predicting all presences incorrectly as absences. For thresholding purposes, an AUC score of >0.7 indicate that a model can adequately distinguish presences from absences, while an AUC of <0.5 indicates that model prediction is no better than random (Lobo et al., 2008). The TSS is another evaluation metric that relates the Sensitivity and Specificity of a model and is calculated as the sum of both minus 1 (Allouche et al., 2006).

4.6 Results

4.6.1 High-resolution mapping of FeMn crust distribution

Across the ROV survey observation tracks, 78% of the extracted stills indicated FeMn crust presence and type environments were highly variable over relatively short spatial scales (Figure 4.4). Crust growth was observed on all exposed surfaces and FeMn crust was also observed on the buried lower substrate surfaces of grab samples. Botryoidal textures exist on mm- to cm- scales, including in places where apparent individual nodules on the seabed are fused together to form a largely, irregular sheet-like surface in outcrop. Internally the crusts alternate from layered to homogenous, with planar and botryoidal layering. Pavement FeMn crust samples are characterised by relatively uniform growth, whereas crusts collected from the flanks associated with nodular, debris and lobate facies also show a more irregular growth texture. These samples appear to include conglomeratic sections, with internal clasts that display earlier FeMn crust growth included within younger crust matrices and as well as fragments of different lithologies (Figure 4.5). Widespread observation of multiple crust growth events and growth hiatuses support a complex growth history, particularly of flank samples (Yeo et al., 2018a).

The substrate lithologies at Tropic Seamount include carbonates, volcanics and phosphorites. Phosphatization occurs as total or partial alteration of a carbonate protolith or as discrete horizons within the crust layers. Within the substrates FeMn-impregnations can be extensive, forming dendrites and infilling pore spaces. The large variation in underlying substrate morphology can be masked in areas where crust growth is thick, particularly for the extensive debris-accumulation regions on the steep flanks of the seamount. In general, summit regions are dominated by carbonate and phosphorite substrates, whereas flank regions consist mainly of volcanics and phosphorites.

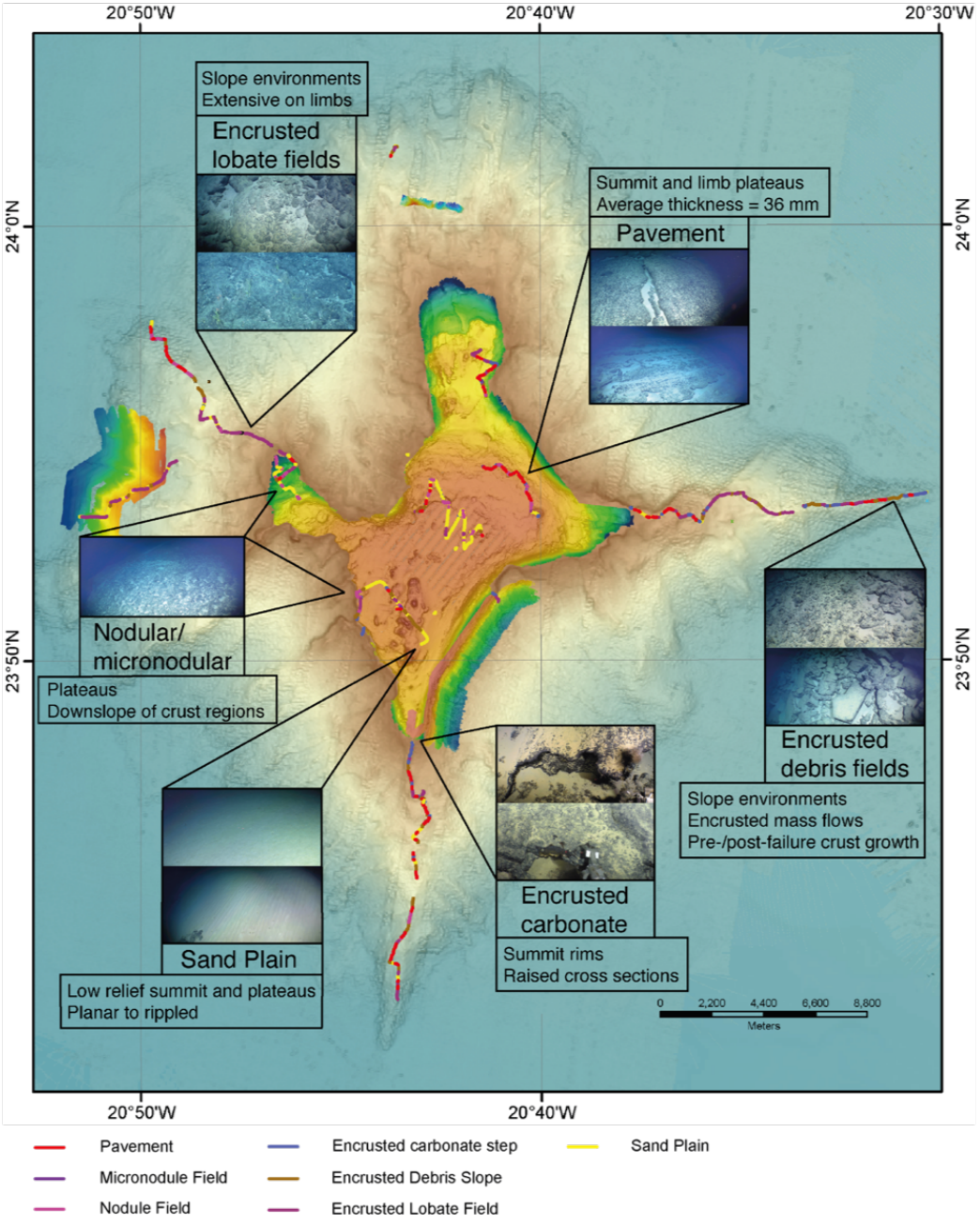

FIGURE 4.4: Distribution of Type environments from ROV observational data at Tropic Seamount.

FIGURE 4.5: Sample photographs to show the complex internal textures of FeMn crusts. a) Sample JC142_083_001 and b) JC142_083_007 show multiple FeMn growth events, as well as volcanic, phosphorite and crust fragment clasts within the FeMn crust matrix.

The distribution of different type environments can be compared with the physical environmental variables to give an indication of potential patterns with water depth, terrain derivatives and current velocities (Figure 4.6). For water depth, the distribution of sand plains, FeMn pavement, FeMn encrusted carbonate and nodular environments peak at shallow depths. All of these environments show clustering of occurrence around distinct depth horizons. For sand environments this is at depths approximately between 950 – 1050 m and then there are two distinct depth bands where sand plains are not observed, between 1500 – 2000 m and 2800 – 3300 m which largely coincide with debris dominated environments. Pavement regions show highest density of presence between 1000 – 1200 m and their peak presence corresponds with a peak in nodular environments and a slight decrease in sand plain occurrence. Pavements are also recorded at depths greater than 2500 m. Ferromanganese encrusted carbonates show a very similar depth distribution pattern to pavement environments but with a much more restricted range, with no occurrences recorded at depths below 2000 m. Nodular environments are focussed at 1100 m but with some patchy occurrences noted at depths between 2700 – 3600 m. In contrast, FeMn encrusted debris and lobate environment occurrence is relatively dispersed across water depths, with deeper peaks occurrences of 2800 m and 2200 m respectively.

Sand plains, pavement, carbonate and nodular environments also show similar occurrence patterns with slope, with these environments being observed most often at low slope angles. Sand plain occurrence peaks at the most shallow slope angles, at $<5°$, but also has intermittent occurrences recorded on more steep slopes. The greatest concentration of pavements, carbonate and nodular fields are observed at slopes of $<10°$ but peak at slope angles that are slightly steeper than the sediment peak. Encrusted carbonates show discrete occurrences at steeper slope angles, of approximately 50° and $>60°$, which may relate to distinct carbonate mounds and localised summit topography. Mirroring trends with water depth, debris and lobate environments are recorded at a wider range of slope angles but with debris fields showing a more limited range than lobate fields, at slope angles between 2°– 50° for debris and up to 55° for lobate. The general structural trends at Tropic Seamount likely drive the overall similarity in patterns of slope with water depth, with shallow depths corresponding to the majority of shallow slopes regions and steeper slope angles at depth on the seamount limbs.

These observations are supported by patterns in fine BPI. In general, sand plains, pavement and nodular environments show the largest clusters around 0, supporting highest presence in flatter regions. Nodular and sand environments profile are largely symmetrical around 0, implying that they show equal likelihood of being observed in both topography highs and lows. Pavement and encrusted carbonate environments both display asymmetric distribution patterns, with more observations at small positive fine BPI values indicating greater presence at relative topographic highs. Debris and lobate

fields again show more dispersed fine BPI values that support observations at a range of slopes and topographic variations.

Aspect shows relatively indistinct trends with environment type, with sand plain environments showing slightly higher density occurrence in southward facing locations compared to pavement, carbonate and nodular environments which have slightly more northwards facing characteristics. At the resolution used in this study, roughness and backscatter characteristics show high amounts of overlap across the different environments that makes correlating distinct trends difficult. A more detail study of the summit of Tropic Seamount, where AUV sidescan sonar surveys were conducted at a resolution of 0.5 m, showed distinct textural patterns in backscatter texture with environment type (Yeo et al., 2019).

Patterns in environment with maximum current velocities show three main groupings. Most debris environments coincide with the lowest current speed environments, between 0.10 – 0.22 m/s, with a mean of 0.12 m/s. Lobate fields are observed at the largest range, from 0.08 – 0.44 m/s, with a mean of 0.22 m/s. While sand plain environments are observed between 0.08 – 0.32 m/s, they are most prevalent at two distinct current velocities of 0.17 m/s and 0.21 m/s. Pavement and nodular environments show similar patterns with current velocity, with means of 0.22 m/s and no occurrences noted at velocities >0.26 m/s. Encrusted carbonates show the highest mean current velocity of 0.24 m/s.

4.7 Distribution modelling of FeMn crust occurrence

4.7.1 Model performance

All of the models run showed good performance across a range of statistical assessment measures (Table 4.1). The accuracy of the models was assessed using diagnostic plots and variance explained, which was highest for RF. For models run without backscatter, AUC (ROC) scores varied between 0.8 – 0.95 for the external evaluation dataset, indicating that all of the models performed well at discriminating between FeMn crust presence and absence (Lobo et al., 2008, indicated a score of >0.7 adequately discriminates presence from absence), with RF showing the best performance. Model sensitivity, which measures the proportion of accurately predicted presences, varied between 0.83 – 0.93, again with RF performing the best. Specificity values, a measure of the proportion of accurately predicted absences, ranged from 0.76 for GAM up to 0.94 for the ensemble model. For the TSS measure, which measures the difference between the true and false positive rates, scores varied between 0.65 – 0.83, with RF and the ensemble model both outperforming the GAM and Maxent models. Overall, the RF model

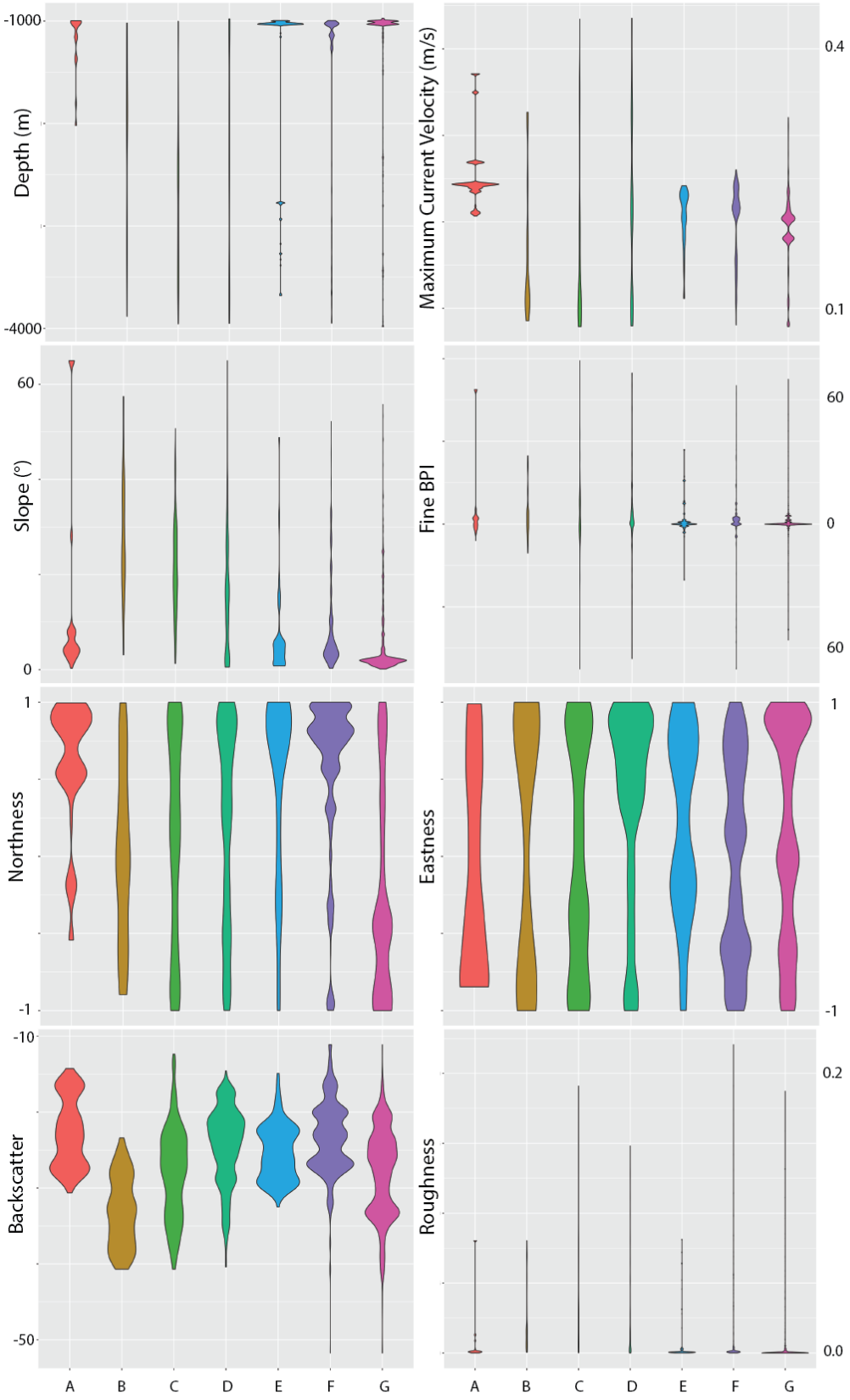

FIGURE 4.6: Violin plots to show the density distribution of FeMn presence for environmental explanatory variables in different type environments. Environments; A) Encrusted Carbonate; B) Cliff environments (included for comparison); C) Encrusted debris fields; D) Encrusted lobate fields; E) Nodular fields; F) Pavement; E) Sand plains.

Model	Variance explained	OOB Error Rate	Sensitivity	Specificity	AUC	TSS
Without backscatter:						
RF	72%	7%	0.93	0.91	0.95	0.83
GAM	37%		0.89	0.76	0.90	0.65
Maxent	37%		0.83	0.82	0.89	0.65
Ensemble (by CA)			0.86	0.94	0.80	0.80
Ensemble (by WM)			0.91	0.91	0.82	0.82
Including backscatter:						
RF	73%	7%	0.94	0.90	0.95	0.83
GAM	40%		0.88	0.81	0.91	0.69
Maxent	39%		0.87	0.82	0.91	0.70
Ensemble (by CA)			0.88	0.93	0.80	0.80
Ensemble (by WM)			0.93	0.89	0.83	0.83

TABLE 4.1: Modelling results for FeMn crust presence and absence, with evaluation scores to show comparative performance between models. Scores show performance assessed against the independent evaluation dataset. Ensemble model algorithms used: committee averaging (CA) and weighted mean of model performance (WM).

showed the best performance across all measures aside from specificity and this strong predictive accuracy is supported by its low Out of Bag (OOB) error rate of 7%.

The ensemble model was built to summarise the spatial variation in predictions and associated uncertainties, to build more robust predictive maps. A range of algorithms were originally applied for building the ensemble model. While a model that used the weighted mean of model performance measures showed slightly higher evaluation scores, the reduction in specificity suggests increased overprediction of presence. An ensemble model using committee averaging was chosen to aid interpretation of predictive output and to take a more pessimistic view of potential occurrence. This method converts probabilities from the RF and GAM models into binary presence or absence values given a specified ROC threshold. The committee averaging value then takes the average of these binary scores as a sum of the total number of models. This means that the ensemble model output represents both a prediction of presence or absence and a measure of uncertainty, where the values close to 1 or 0 indicating high model agreements on presence or absence respectively and values around 0.5 showing low model agreement.

When backscatter is included in the modelling process there is a relatively limited impact on performance measures. In general, there are small improvements in the variance explained and TSS scores for most models. The largest improvements in performance are observed for the GAM model, which shows small increases in specificity and AUC measures (5% and 1% respectively) and a larger improvement in TSS score, although this is coupled by a slight decrease in model sensitivity. This could suggest an

increase in overprediction of FeMn crust presence by the GAM model when backscatter is included. The performance of the Maxent model also shows small improvements in sensitivity and AUC. There appears to be limited impact on RF performance in all measures.

4.7.2 Variable Influence on Distribution Modelling

For modelling, the same environmental explanatory variables were used for model runs and contributed to the outcomes of the three algorithms (GAM, RF and Maxent). A separate model run was also conducted to include backscatter, to investigate the effect on model prediction and performance. The relative importance of these variables to presence-absence model predictions varied but all three ranked water depth as the most influential variable followed by the maximum current velocity. Roughness was also deemed important for RF but of low importance to GAM and Maxent modelling. Slope, northness, eastness, fine BPI and backscatter had some effect on the probability of FeMn crust presence in the models run but had lower influence on model outcomes. In particular, backscatter appeared to have a slightly higher influence on GAM predictions when compared to slope, aspect and fine BPI, but similar influence to these minor explanatory variables for RF and Maxent. This supports the slightly larger performance improvements for GAM when backscatter is included in modelling, as discussed in Section 4.7.1.

Maxent consistently predicted higher probability of occurrence than both GAM and RF models for all variables. Overall, the GAM, RF and Maxent models all showed similar responses in probability of FeMn occurrence to the main explanatory variables of water depth and maximum current velocity (Figure 4.7). For water depth, all models predicted a fall in presence probability in water depths shallower than 1500 m, with lowest probabilities corresponding to summit regions. The Maxent and GAM models also show a distinct drop in presence probability at water depths of 2500 m. For maximum current velocities, all models show the lowest probability of presence at current speeds of below 0.06 m/s. At higher current speeds, the models show slight divergence in prediction probabilities. For RF, the highest probability of presence is predicted across a relatively wide range of velocities, between 0.07 – 2.50 m/s. For GAM this occurs in 4 distinct bands around 0.07 m/s, 0.15 – 0.17 m/s, 0.21 – 0.25 m/s and then above 3.30 m/s. Maxent shows 3 bands of higher probability, at 0.07 – 0.10 m/s, 0.12 – 0.30 m/s and then above 3.30 m/s. Roughness was an important variable within the RF model, which showed a distinct drop in probability of occurrence at roughness values greater than 0.151. Roughness was of low importance for GAM and Maxent model predictions but GAM showed similar patterns to RF, with reduced probability at values $>$0.105 as well as between 0.05 – 0.055, while for Maxent little variation in probability was expected across all values. The Maxent models showed little variation in predicted

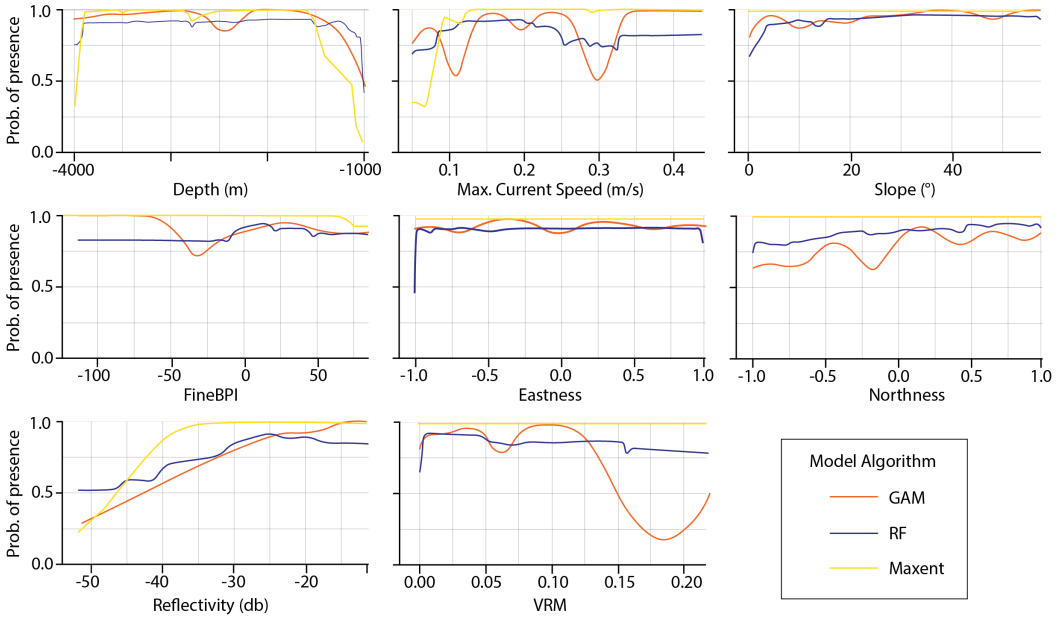

FIGURE 4.7: Response plots to show the probability of FeMn crust presence predicted for the environmental explanatory variables for the three models (GAM, RF, Maxent) run in this study. The response curves show the average of model runs and shows the effect of individual explanatory variables on presence probability once the effects of the other explanatory variables have been averaged out.

probability with slope and aspect and a reduction in probability at fine BPI values >50. The GAM and RF models showed slightly different trends to Maxent to these lower importance variables. In general, these models predicted higher probabilities of occurrence for more north-facing areas and with increasing slope. Both models show a distinct drop in probability in occurrence in regions with slopes of <5° and greatest probability between 30 – 40°. All models showed an increase in presence probability with increasing backscatter reflectivity. The Maxent model predicts the highest probability of occurrence across a wider range of reflectivity, whereas GAM and RF models show highest probabilities at more discrete reflectivity values. For GAM this is at the highest reflectivity and for RF this is at more intermediate values, with a small drop at the highest reflectivity.

4.7.3 Predicted FeMn distribution

Model predictions were applied across the full spatial extent of the environmental explanatory variable raster layers (Figure 4.8). As the model was trained using data from ROV dive surveys, focussed on the summit and along the spurs of Tropic Seamount, predictions between the limbs are less reliable because there may be slight variations in the environmental patterns that have not been adequately ground-truthed. Discussions of model predictions in these regions are included in this study but the higher uncertainties in these inter-limb flank regions is noted and a conservative approach to

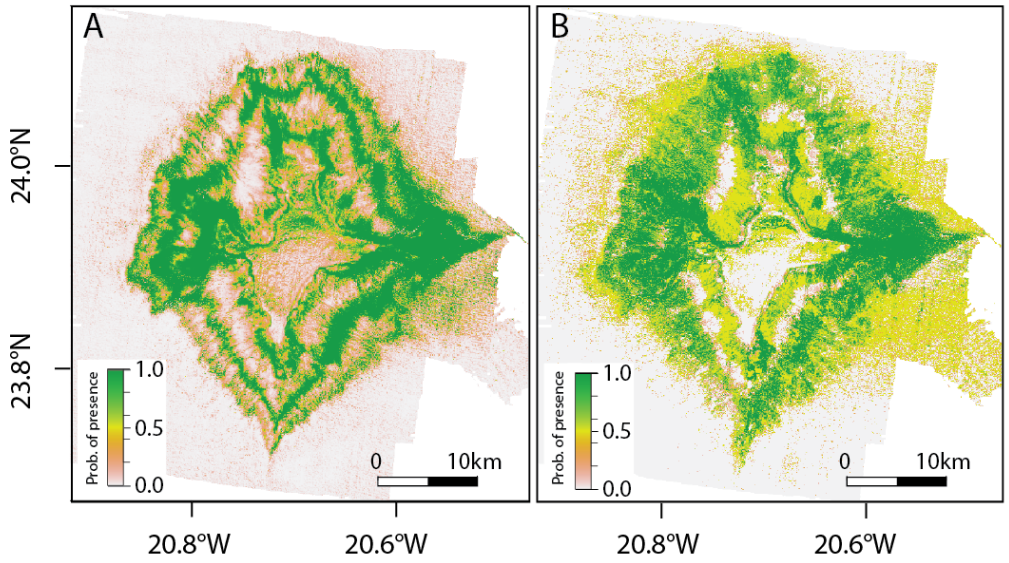

FIGURE 4.8: Predicted distribution of FeMn crusts at Tropic Seamount using; A) Maxent; B) An ensemble model of RF and GAM outputs built using committee averaging.

outcrop occurrence is taken. The inclusion of backscatter into model building had an overall limited impact on modelling outcomes in terms of predicted distribution and model performance. This is likely because seamount-scale variability in backscatter at the resolution of this study (resampled on a 50 m grid) may not adequately distinguish the textural patterns of different environments as effectively from other factors such as slope. Given that patterns in predicted distributions for model outcomes are essentially the same with and without backscatter, for the purposes of understanding the potential drivers of FeMn crust distribution with environmental variables the models run without backscatter are presented and assessed below.

The different model algorithms applied produced similar patterns in crust occurrence but with slight differences between the predicted likelihood of FeMn crust presence. All models predicted the highest likelihood of crust presence in an almost continuous band along the eastern limb of Tropic Seamount, as well as over significant areas on the western limb. Predicted crust presence patterns along the north and south limbs are less continuous, focussed in distinct bathymetric bands. On the summit of Tropic Seamount, all models predicted highest presence along the northern half of the rim, whereas the centre and southern regions are predicted to be largely absent of crusts. In the higher uncertainty inter-limb regions, all models show distinct bands where crust presence is less likely, although the RF models predict higher likelihoods in these regions that the GAM and Maxent models. An ensemble model was built using RF and GAM predictive outputs to summarise the variation in predictions and uncertainties between these algorithms. The resulting ensemble map shows very similar patterns in FeMn crust occurrence to the Maxent model but with more conservative probabilities and highlighting higher uncertainties within the inter-limb regions.

4.8 Discussion

4.8.1 Environmental drivers influencing FeMn distribution on seamounts

It has been stipulated that FeMn crust formation has four prerequisites (Hein and Koschinsky, 2014; Hein et al., 2013); a supply of Mn and Fe (Halbach and Puteanus, 1983); distinct redox conditions of the water column (Koschinsky and Halbach, 1995); exposed hard surfaces on which to form (Halbach and Puteanus, 1983); and a stable surface to allow for sustained accumulation (Hein et al., 1985). These can effectively be considered as two separate characteristics that can affect the distribution of FeMn crusts; those of the water column and those of the substrate.

4.8.2 The role of water column properties on FeMn crust distribution

For all models run in this study, water depth appears to be the most significant variable that determines whether FeMn crusts are present. Past studies have reported hydrogenetic crusts across a large range of water depths, between 400 – 7000 m, with the thickest proposed to form at depths between 800 – 2500 m (Hein et al., 2009a). Numerous studies have suggested that the interaction with an Oxygen Minimum Zone (OMZ) is an important factor that drives active hydrogenetic crust growth on seamounts, following a colloid-chemical model developed from the analysis of Pacific Ocean hydrogenetic crusts (e.g. Halbach and Puteanus, 1983, 1984; Koschinsky and Halbach, 1995; Hein et al., 1997; Glasby et al., 2010). The OMZ is thought to act as a reduced reservoir within the water column that supports the accumulation of dissolved metal species and is as a source of the key components of FeMn crust (Koschinsky and Halbach, 1995). Seafloor obstructions, such as seamounts, cause upwelling of oxygenated deep waters. The subsequent interaction and mixing of these water masses allows for the formation of colloid complexes and precipitation of FeMn crusts (Koschinsky and Halbach, 1995). Numerous studies in the Pacific Ocean (e.g. Klinkhammer and Bender, 1980; Landing and Bruland, 1980, 1997) and Indian Ocean (e.g. Saager et al., 1989; Morley et al., 1993) have showed a peak in dissolved Mn coinciding with an OMZ (Johnson et al., 1996). In the Atlantic Ocean, a distinct dissolved Mn-rich OMZ is not widely recorded (e.g. Statham et al., 1998; Wu et al., 2014).

At Tropic Seamount, the water column properties were studied across 37 CTD stations during the JC142 sampling campaign (Murton and scientific party, 2016). Dissolved oxygen content varied from 100 – 223 μmol/kg through the water column, with a core of minimum dissolved oxygen concentrations (100 – 110 μmol/kg) observed between 600 – 800 m water depths, approximately 200 m above Tropic's summit (Murton and scientific party, 2016). In contrast, dissolved oxygen concentrations in the Pacific and Indian ocean OMZs are generally as much lower, with large regions at $<$45 μmol/kg

and values down to <4.5 μmol/kg (e.g. Karstensen et al., 2008). While there is evidence of crust presence across a range of water depths, the models run in this study generally showed two depth bands where probability of crust presence at Tropic Seamount was highest, between 1500 – 2200 m and 2700 – 3300 m. The uniformity of relatively high dissolved oxygen concentrations observed in this study and of dissolved Fe and Mn through the water column for this region of the Atlantic (Wu et al., 2014; Hatta et al., 2015) do not correlate with the seamount-scale distribution patterns predicted from the models within this study. FeMn crust occurrence trends with depth at Tropic Seamount are likely driven by more localised factors than the inherent properties of the overlying water column, which may be more useful for regional, basin-scale studies of FeMn crust occurrence. Comparable observations of active crust growth irrespective of depth from high precision sampling at the Takuyo-Daigo seamount chain in the Pacific also highlight the importance of local, seamount-scale studies to improve our understanding of crust growth processes (Usui et al., 2017).

4.8.3 The role of local topography and currents

Aside from changes in water column properties, the characteristics of the seamount structure and substrate will also change from the summit to the base. The volcanic basement of Tropic Seamount formed at 119 Ma, with evidence of some late stage eruptions until approximately 60 Ma, after which it has remained inactive (Van Den Bogaard, 2013). While extinct seamounts such as Tropic may have maintained long periods of tectonic quiescence, there are still events such as flank collapse that can significantly alter the topography (e.g. Hühnerbach and Masson, 2004; Chaytor et al., 2007; Palomino et al., 2016). The Du et al. (2020) study in the Pacific Ocean found that slope angle had a key influence on depositional patterns on the Magellan Seamounts, with FeMn crusts only recorded on slopes between 4 – 20°. In comparison, FeMn presence at Tropic Seamount was observed across a wide range of slope angles from 4° to over 50°. The Hühnerbach and Masson (2004) study of Atlantic continental margin landslides noted that slope angles do not appear to influence the occurrence of landslides and attributed this to the influence of other key parameters not captured that can affect slope stability, such as the geotechnical characteristics of the substrate and surface sediments. In this study, slope appeared to be of relatively low importance for all the modelling algorithms. But trends in environment and FeMn crust facies with position at Tropic Seamount support a theory of varying stability of different substrate lithologies controlling FeMn crust distribution. This is discussed in more detail below.

There are two bathymetric bands that show the lowest predicted probabilities of FeMn crust presence at 950 – 1500 m and 2200 – 2700 m. When considered in the context of its overall morphology, we observe spatial trends in the different type environments around the star-shaped seamount structure. Between 950 – 1500 m water depths, the

dominant facies observed are sand plains at the summit centre and pavements and encrusted carbonate around the summit edge. The centre of the seamount summit is characterised by shallow bathymetry (between 950 – 1050 m), low slope angles, fine BPI scores around 0 and moderate to low maximum current velocities. These regions are dominated by homogenous and rippled mobile sand plains in the summit centre. The very low slope angles, of $<4°$, coincide with the highest probability of sediment occurrence and lowest FeMn crust occurrence. This observation of low FeMn crust coverage in regions of low slope angles has been noted at other seamount sites (e.g. Yamazaki and Sharma, 1998; Du et al., 2017). The accumulation of sediment ponds in these regions is likely driven by the interaction of local topographic features with patterns in current, as supported by the importance of maximum current velocity in the FeMn occurrence predictive modelling. Higher probability of crust presence was predicted at intermediate maximum current velocities of 0.15 – 0.17 m/s. Seamounts present environments of complex circulatory patterns as they interact with large scale basin flows (e.g. Royer, 1978; Roden, 1994; Howe et al., 2006) and numerous studies have modelled the spatial and temporal variability of currents around seamounts due to factors including tidal effects and the formation of Taylor column structures (e.g. Brechner Owens and Hogg, 1980; Mohn et al., 2009). The presence of seamounts is also known to affect the sedimentary processes of surrounding regions (e.g. Palomino et al., 2016). At Tropic Seamount, Cooper and Spearman (2017) showed that flows were dominated by anti-cyclonic rotating currents above the summit centre, generated by internal tides. The hydrodynamic model (Figure 4.2H) shows maximum current velocities on the eastern and western limbs and minimum current velocities in the northern and southern spurs and interlimb regions, as well as a weak Taylor cap (Cooper and Spearman, 2017). This pattern of rotating currents, when interacting with topographic features on the summit, can lead to low current velocity "shadow" regions. The predictive modelling shows a reduced probability of FeMn crust presence below 0.12 m/s, which corresponds to the summit centre, interlimb regions and areas around the base of Tropic Seamount. This means that below this threshold maximum current velocity, sediment deposition is likely maintained in these regions. This acts to either bury hard surfaces so that they are unavailable for FeMn precipitation or leads to the burial of previously exposed FeMn pavements and encrusted carbonates. This burial of FeMn crust outcrop means that this study likely represents a conservative prediction of actual FeMn occurrence and highlights the limitation of visual ground-truthing methods. While visual surveys are key to understanding interactions with species distribution, observational data alone cannot fully capture the full extent of FeMn crust coverage or spatial variations in thickness. The further development of geophysical survey techniques that can measure thickness variability on a range of scales will be key to mapping these features in-situ and improving tonnage estimates (e.g. Thornton et al., 2013; Nishida et al., 2015; Neettiyath et al., 2021).

Sparse nodular fields are observed within these central sand plain regions. Relative nodule density on the summit varies between 50% to over 90% but is dominated by 50% nodule coverage. Towards the edges of the summit, pavement and encrusted carbonate environments dominate. The crust pavement coverage varies from full coverage with little underlying substrate visible to patches with approximately 50% crust cover, with more continuous pavements observed at the summit rims. Encrusted carbonate steps are focused around the edges of the summit as well as in isolated mounds within the centre of the summit. The summit rim regions, particularly in the east and west of Tropic Seamount, experience high maximum current velocities as flow is concentrated up the flanks of seamount. This may correlate with the band of low crust presence probability between 1100 – 1500 m and at relatively high flow speeds of 0.25 – 0.34 m/s. In these summit edge regions, encrusted carbonate is exposed to enhanced erosion and is more susceptible to gravitational collapse. This eroded and slumped material may then accumulate further down the flanks where it stabilises and again provides a suitable surface for FeMn crust precipitation. Therefore, the 1000 – 1500 m band of low FeMn presence probability coincides with areas that inhibit crust formation due to rim erosion and sediment accumulation processes.

The transition to sloped environments leads to highly variable outcrops dominated by debris fields and cliffs. These include loose debris, such as coral debris with thin FeMn coatings, or encrusted debris in which underlying clastic rocks have been fused and covered in FeMn crust. Nodular and micronodular regions were observed on the western spur and on average showed higher relative nodule densities, between 75% to over 90%, than nodule fields on the summit. The dominance of both consolidated and loose encrusted debris shows a complex history of gravitational collapse pre- and post-FeMn crust formation. While mechanical testing of substrate was not conducted within this study, the transition on flanks between volcanics, phosphorites and clastic substrates will also be associated with changes in physical properties that will likely control the distribution of collapse events. From video observation, cliff environments display greater evidence of underlying substrate texture, including lava cooling joints, while intermittent shallow slopes show slumped slabs and lobate field interspersed with rippled sands. The observed slumped slabs and blocky debris fields indicate larger scale flank collapse events. This suggests that local scale variations in crust occurrence on the flanks may be driven by a combination of small scale slope failures, slumping of encrusted brecciated material and flank collapse processes that leads to lower model probabilities of crust presence in a water depth band between 2200 – 2700 m. This region likely represents the exposed scar from instability processes. The relative topographic low created in these regions may generate local current velocity minima that can encourage sediment deposition, compounding the development of an environment that does not support FeMn crust formation. While there is evidence at Tropic Seamount that these collapse events can create concentrated regions of thicker crusts, as fragments accumulate and are covered by later growth, this process also acts

to reduce the available surface over the million-year timescales that prospective FeMn crusts grow.

4.8.4 Implications for FeMn crust studies and resource assessments

Predictive modelling is limited by the availability and resolution of the input data that is used to train the model. Outcrop mapping from observational ROV surveys in this study have demonstrated high spatial FeMn crust heterogeneity and increasing data resolution of environmental explanatory variables, particularly of key variables like hydrodynamics, could improve model predictions further. Past studies have commonly used backscatter to determine variations in both FeMn nodule and crust distributions. This study supports the findings of Joo et al. (2020) that the resolution of shipboard backscatter surveys is not sufficient to capture the large variability in FeMn environment textures and abundance that can occur over small spatial scales and are best suited to regional studies. Also key to predictive outcrop studies is ensuring adequate ground-truthing of survey areas, to prevent projecting the models further than their capabilities. In this study, ROV surveys and mapping were limited to summit regions and along the spurs. The lack of sample sites in the inter-limb regions is the likely driver of higher model uncertainties observed in these areas (Figure 4.8) and expanding video surveys to these regions would incorporate a larger variety of seamount environments and could enable more accurate modelling and further improve understanding on distribution controls. The inclusion of other environmental layers, such as interpretations of underlying seamount structure and lithology, may also improve predictive capabilities of the models. Increasing the sampling size and expanding the variables collected and their resolution can be difficult for deep marine surveys, hence this study represents an assessment of what they key drivers that likely determine FeMn crust distribution on seamount structures, namely the availability, stability and longevity of exposed surfaces for FeMn crusts to precipitate onto. This understanding can therefore be applied to other seamount sites to help target survey regions for future FeMn crust studies.

The regions of highest predicted probability of FeMn crust presence, on the eastern and western spurs, would likely pose the largest challenges to exploitation from a technological perspective. Exploration of FeMn crusts remains in its infancy and the extent of engineering constraints on potential FeMn crust extraction are still largely unknown, but it is thought that deep water operations and highly variable terrains will be the most difficult conditions for FeMn recovery (e.g. Hein et al., 2009a, 2010; Petersen et al., 2016). Mine-site assessment modelling has noted that the most viable sites are likely to be those in water depths less than 2500 m and on flat-topped summit regions (Hein

et al., 2009a; Du et al., 2017; Yeo et al., 2019, 2018a). At Tropic Seamount, these constraints are likely to significantly limit the economically viable regions for FeMn exploitation.

Another key consideration for FeMn crust exploitation is the potential environmental impact. Seamounts are known to be sites of considerable biological importance, acting as hotspots for biodiversity and can host numerous vulnerable marine ecosystems (e.g. Clark et al., 2010; Schlacher et al., 2014; Watling and Auster, 2017; Victorero et al., 2018). Some areas of high predicted FeMn crust presence at Tropic Seamount also coincide with areas of high predicted sponge presence (Ramiro-Sánchez et al., 2019). Ramiro-Sánchez et al. (2019) used comparable species distribution modelling techniques to predict Poliopogon amadou sponge occurrences around Tropic Seamount. They found that water depth (likely corresponding to distinct water mass characteristics) and current speed were also the main variables affecting model predictions and a band of high presence probability is predicted between 2500 – 3000 m and associated with current velocities of $<$0.2 – 0.28 m/s (Ramiro-Sánchez et al., 2019). While some of these regions appear to overlap with areas of high predicted crust presence, there is limited overlap with crust distribution above 2500 m water depth. By conducting predictive modelling of FeMn crust distribution at the scale of the individual seamount and at comparable scales to biological surveys, these could be used in conjunction with species distribution models of vulnerable species to develop highly targeted environmental impact assessments.

4.9 Conclusions

This study presents the outcomes of the first high-resolution, seamount-scale FeMn crust mapping campaign conducted in the Atlantic basin. At Tropic Seamount, FeMn crust presence was observed on all exposed hard substrate survey, including encrusting coral debris. Predictive models built using a range of algorithms (RF, GAM and Maxent) consistently showed that regions of highest probability of crust presence related to the water depth and maximum current velocities. This study has found that water column properties have a limited role in determining the local-scale distribution of FeMn crusts on seamount structures and are best applied for basin-scale studies of predicted occurrence. At the scale of individual seamounts, local-scale topographic features have the greatest influence on FeMn crust distribution. Observations of FeMn crust are more likely to occur in regions with either stable substrate or sites of accumulated slumped material that also coincide with sufficiently high maximum current speeds combined with local topography that prevent the pooling of sediment. This supports that for similar seamount environments, the largest limitations on FeMn crust presence are the availability of exposed hard rock substrate to precipitate onto and the sustained exposure of that surface to allow for crust growth. Improved understanding of the history of

formation and underlying seamount structure as well as local current regimes can help to identify areas of FeMn coverage at other seamount sites. This work demonstrates the applicability of distribution models frequently used in environmental studies of species distribution to the study of FeMn crusts to improve understanding on distribution controls at the scale of individual seamounts. Ensemble modelling techniques performed particularly well, making accurate predictions of crust occurrence when assessed against independent testing data even in the absence of backscatter data. The application of these techniques could be used in future studies, for example to improve resource estimates. In particular, this method for modelling local variations in FeMn crust occurrence could be used in conjunction with species distribution models, for example of vulnerable species or species abundance, to strengthen resource management and more accurately assess potential impacts of exploitation.

Chapter 5

Accumulation and preservation processes at the seamount-scale: controls on FeMn crusts

This chapter investigates the variation in preservation and growth rates around Tropic Seamount and the relationship with FeMn crust composition, to further understanding of the controls on FeMn crust thickness at the scale of an individual seamount. The SEM analysis of upper FeMn crust surfaces was conducted with Dr Isobel Yeo and has been published in the paper (Yeo et al., 2019) on which I am listed as a co-author and to which I contributed to the data collection, but the data analysis, results and discussion presented in this chapter pertain entirely to my own work.

5.1 Abstract

The shift to low-carbon energy generation has led to changes in demand patterns for elements. Ferromanganese (FeMn) crusts are of economic interest as a potential resource due to their extreme enrichment in numerous elements that are vital for the manufacture of some of these technologies, such as Co and Te. While the concentrations of these elements in FeMn crusts is promising, there remains a need to better understand the variability in both the grade and tonnage of deposits at the sub-basin scale. This study presents the findings of an investigation into the variability of composition and thickness of FeMn crust at the scale of an individual seamount. Tropic Seamount in the NE Atlantic shows promising concentrations of key target elements, with average concentration of 0.5 wt% Co and 51 ppm Te, but significant variation in these concentrations. Textural variation in the upper surfaces of FeMn crusts from Tropic Seamount show distinct distribution patterns, with evidence of extensive surface erosion from

the seamount summit, at water depths of 1000 m, down to 2000 m. This is matched by trends in elemental distribution of key target elements, with the highest Co and Te concentrations observed in summit regions. Comparisons with growth textures and estimated growth rates from Co-chronometry suggest that both the incorporation of detrital material and the removal of FeMn crust growth horizons are factors that affect the accumulation of FeMn crusts and the subsequent composition through dilution processes. The relationship between erosive processes and modelled current velocities at Tropic Seamount is a complex one. It is proposed that a key driver of erosive potential is the sediment load of the current, which is affected by patterns in sediment distribution, microtopography and current speeds, as well as sediment flux over time.

5.2 Introduction

Hydrogenetic FeMn crusts are Fe- and Mn-rich precipitates that precipitate from seawater directly onto exposed hard rock substrates between 400 m and 7000 m water depths (Hein and Koschinsky, 2014). They are of particular interest for resource studies due to their extreme enrichment in numerous elements above mean continental crust concentrations and the surrounding seawater from which they form (Hein et al., 2000). This is due in part to their very slow rates of formation, between 1 – 5 mm/Myr, porosities and high specific surface areas (mean of 325 m^2g^{-1}) that support the accumulation of elements such as Co and Te which are important for the development of "green" energy technologies (Hein et al., 2000, 2010, 2013).

There are a number of processes thought to affect the chemical composition of FeMn crusts, including the characteristics of the surrounding seawater (e.g. Hodkinson and Cronan, 1991; Hein et al., 2016), and the variations in composition have been extensively described, in particular for Pacific Ocean crusts (e.g. Hein and Koschinsky, 2014). The composition of hydrogenetic FeMn crusts also reflects the amount of dilution from non-hydrogenetic phases, including siliciclastic and biogenic material and alteration processes like phosphatisation (e.g. Koschinsky et al., 1996; Glasby et al., 2007). Ferromanganese crusts at continental margins have been observed to have higher terrestrial inputs of detrital material and show higher proportions of Fe, Si, Al and Cr as well as high growth rates when compared to deep ocean basin crusts (e.g. Conrad et al., 2017). This can lead to lower observed enrichment in elements of economic interest, due to detrital dilution and reduction in the amount of time the hydrogenetic growth surface is exposed to the water column (e.g. Koschinsky et al., 1996; Conrad et al., 2017) The textural characteristics of FeMn crusts can give an indication of depositional history, with frequently complex growth textures, intercalations of clastic material and evidence of erosive horizons (e.g. Yeo et al., 2018a; Josso et al., 2020a).

Currently, both the local scale variation in composition and thickness of FeMn crusts remains poorly quantified, particularly for the Atlantic Ocean, but there may be factors such as microtopography that vary at this length-scale and play important roles in driving variations (Usui et al., 2017; Lusty et al., 2018). In recent years, the application of remote surveying techniques, including the use of remotely operated vehicles (ROVs) and automated underwater vehicles (AUVs), to FeMn crust surveys has begun to shed light on some of these processes, by facilitating systematic mapping and sampling campaigns (e.g. Usui et al., 2013; Yeo et al., 2019). Estimating crust thicknesses remain a challenge for resources modelling, with Usui et al. (2017) noting significant variation in FeMn crust thicknesses down to local scales. This focus of this study is Tropic Seamount, an isolated seamount in the NE Atlantic. Past studies of Tropic Seamount have found promising concentrations of economic elements (e.g. Koschinsky et al., 1996; Marino et al., 2017), despite the potentially significant effect of detrital dilution due to its position within the Saharan dust plume (e.g. Grousset and Biscaye, 2005; Josso et al., 2020b). This study aims to investigate the composition of FeMn crusts from the Atlantic Ocean and the potential controls on FeMn crust accumulation and preservation.

5.3 Materials and methods

5.3.1 Materials

The samples and data were collected during the research expedition JC142 in 2016 on board the RRS James Cook to Tropic Seamount (23° 53.77 N, 20° 46.06 W) in the NE Atlantic, 450 km from the West African coast (Figure 5.1A). Tropic Seamount is a flat-topped seamount (guyot) characterised by four limbs that extend from the summit at water depths of 1000 m down the flanks to the seamount base at 4100 m. The bathymetric data used in this study were collected using the ship's Kongsberg EM120 (12 kHz) multibeam echosounder and final grids and maps produced at a 50 m resolution (Murton and scientific party, 2016; Yeo et al., 2018b). A hydrographic model was also built by HR Wallingford for Tropic Seamount using physical data collected during JC142 (Figure 5.1B) (Murton and scientific party, 2016; Cooper and Spearman, 2017; Spearman et al., 2020; Murton et al., 2020). A range of oceanographic instrumentation was deployed on moorings and CTDs across the seamount and the data used to build a TELEMAC flow model of the current regime in the vicinity of Tropic Seamount (Murton and scientific party, 2016; Cooper and Spearman, 2017; Spearman et al., 2020; Murton et al., 2020). The data used in this study was built using model runs to simulate the maximum current velocity at 1 m above the seabed, at variable resolutions between 500 – 600 m that changed across the 500 km x 500 km model domain. This layer was then interpolated using ordinary kridging and resampled at a 50 m cell resolution to match

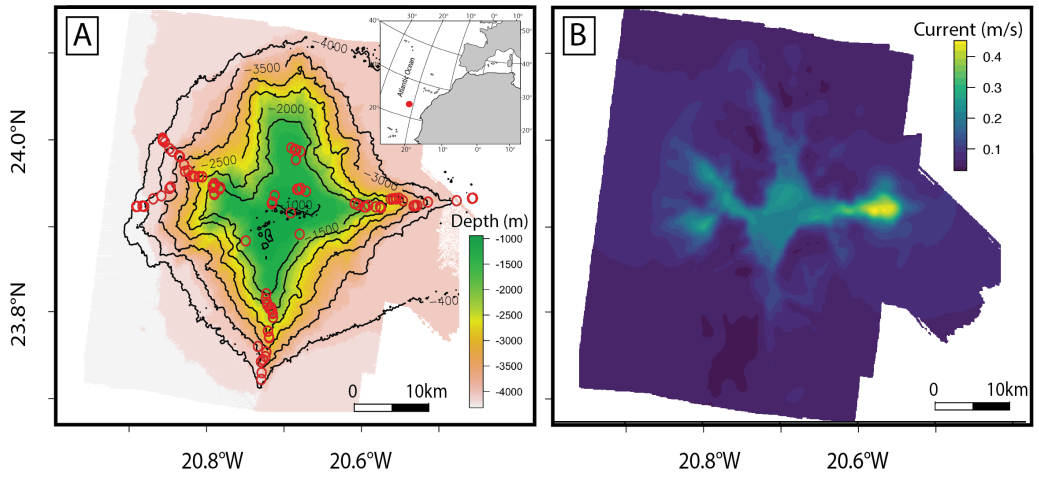

FIGURE 5.1: Maps to show (A) the bathymetry and location of samples analysed in this study (red circles) and an inset map to show the location of Tropic Seamount in the NE Atlantic and (B) a map showing the hydrographic model of near-bed maximum current velocities (after Cooper and Spearman, 2017; Spearman et al., 2020; Murton et al., 2020)

.

the bathymetry resolution using the "gstat" and "raster" packages in R (Pebesma, 2004; Hijmans, 2021).

The samples analysed in this study were collected by ROV Isis (National Oceanography Centre Southampton) using the manipulator arms from a range of water depths, spanning 997 – 3894 m (see Table 5.1 for full list of sample location details). Samples were orientated from ROV video footage of in-situ position on the seabed. A total of 106 well-spatially constrained FeMn crust samples were collected and analysed for FeMn crust thickness and surface texture and 101 samples were analysed for elemental composition. The FeMn crusts analysed were variable in substrate, including carbonates, volcanics and phosphorites as well as some FeMn crusts recovered without the original substrate. The thickness of FeMn crusts collected from Tropic Seamount were highly variable, ranging from mm-thin patinas up to 200 mm thick encrustations on FeMn pavements and slabs. In general, the upper surfaces exposed to the water column appeared to show the thickest growth when compared to lower surfaces. In order to understand the compositional variation of FeMn crusts with limited impact from the composition of the substrate and of phosphatisation observed in lower portions of Tropic Seamount FeMn crusts (Marino et al., 2017; Josso et al., 2020a), only the upper 10 mm of FeMn crust growth was analysed.

TABLE 5.1: Location and details of FeMn crust sampled by ROV

Sample Name	Latitude	Longitude	Water depth	FeMn crust thickness
	Decimal degrees		(m)	(mm)
JC142_009_010	23.852550	-20.742600	1025	20
JC142_020_017	23.882100	-20.695667	997	30

Sample Name	Latitude	Longitude	Water depth	FeMn crust thickness
	Decimal degrees		(m)	(mm)
JC142_039_003	23.889533	-20.564083	2713	30
JC142_039_005	23.889467	-20.566250	2662	50
JC142_039_007	23.889050	-20.568017	2606	20
JC142_039_012	23.894717	-20.579017	2499	90
JC142_039_015	23.897350	-20.582917	2480	40
JC142_039_017	23.896667	-20.585817	2377	25
JC142_039_019	23.897017	-20.586483	2430	50
JC142_039_020	23.896817	-20.588900	2307	30
JC142_039_021	23.896650	-20.589550	2267	20
JC142_039_024	23.896317	-20.591717	2215	20
JC142_047_007	23.891850	-20.715450	999	20
JC142_047_012	23.900483	-20.712433	1010	30
JC142_055_001	23.750083	-20.718467	2700	30
JC142_055_002	23.751150	-20.718667	2654	20
JC142_055_006	23.757050	-20.719617	2463	25
JC142_055_007	23.757050	-20.719617	2463	25
JC142_055_008	23.757233	-20.719800	2490	30
JC142_055_017	23.771683	-20.714467	2164	30
JC142_055_021	23.779483	-20.715583	2041	20
JC142_055_023	23.781983	-20.716233	1935	45
JC142_058_010	23.906933	-20.689117	1015	25
JC142_058_012	23.907000	-20.688283	1016	30
JC142_058_014	23.906633	-20.687483	1014	40
JC142_058_022	23.907917	-20.685150	1024	30
JC142_058_030	23.904850	-20.679767	1022	60
JC142_061_014	23.947100	-20.685517	1183	30
JC142_061_018	23.949167	-20.691300	1100	90
JC142_061_021	23.950833	-20.694967	1059	40
JC142_078_001	23.961367	-20.828917	3894	25
JC142_078_005	23.960283	-20.828933	3845	35
JC142_078_009	23.957017	-20.826533	3694	60
JC142_078_016	23.947200	-20.818917	3325	35
JC142_078_019	23.942683	-20.812050	3101	100
JC142_078_020	23.941450	-20.810783	3024	20
JC142_078_023	23.932967	-20.806567	2822	90
JC142_078_028	23.926167	-20.805617	2675	20
JC142_078_030	23.926750	-20.802283	2600	30
JC142_078_035	23.921183	-20.799217	2400	20
JC142_080_001	23.911067	-20.776867	1238	40

Sample Name	Latitude	Longitude	Water depth	FeMn crust thickness
	Decimal degrees		(m)	(mm)
JC142_080_002	23.909150	-20.776800	1278	30
JC142_080_012	23.901733	-20.775217	1213	55
JC142_080_013	23.901733	-20.775217	1213	50
JC142_083_001	23.889050	-20.856500	3777	90
JC142_083_002	23.889117	-20.855567	3734	25
JC142_083_006	23.889533	-20.850000	3530	80
JC142_083_006	23.889533	-20.850000	3530	80
JC142_083_007	23.889133	-20.848133	3512	170
JC142_083_010	23.897117	-20.838833	3424	30
JC142_083_015	23.900300	-20.830267	3340	50
JC142_083_021	23.908117	-20.821867	3103	20
JC142_083_022	23.909800	-20.820533	2999	25
JC142_091_001	23.897133	-20.506167	3872	60
JC142_091_003	23.897057	-20.506797	3868	60
JC142_091_004	23.897001	-20.507112	3861	20
JC142_091_012	23.894517	-20.523133	3595	80
JC142_091_031	23.893167	-20.553017	2997	40
JC142_094_005	23.887183	-20.601833	1834	60
JC142_094_006	23.888250	-20.602817	1804	70
JC142_094_015	23.888217	-20.607267	1637	30
JC142_094_019	23.889967	-20.615083	1616	35
JC142_094_020	23.888150	-20.617683	1580	40
JC142_094_021	23.888250	-20.619000	1548	45
JC142_094_024	23.890300	-20.625467	1433	30
JC142_094_031	23.891783	-20.628767	1340	40
JC142_094_034	23.891917	-20.629267	1319	30
JC142_100_015	23.859550	-20.686583	1173	40
JC142_107_001	23.920900	-20.796950	2330	70
JC142_107_002	23.920867	-20.795517	2292	10
JC142_107_003	23.920567	-20.790983	1969	50
JC142_107_005	23.920350	-20.787750	1803	50
JC142_107_013	23.913417	-20.775217	1452	60
JC142_107_015	23.911350	-20.774417	1435	40
JC142_107_019	23.909067	-20.768917	1236	70
JC142_107_020	23.907150	-20.769983	1216	90
JC142_107_032	23.903067	-20.775433	1222	40
JC142_109_005	23.706200	-20.726800	3832	4
JC142_109_007	23.713250	-20.726367	3665	10
JC142_109_014	23.726933	-20.725083	3276	30

Sample Name	Latitude	Longitude	Water depth	FeMn crust thickness
	Decimal degrees		(m)	(mm)
JC142_109_017	23.730250	-20.722367	3186	35
JC142_109_018	23.735133	-20.721450	3084	35
JC142_109_020	23.741042	-20.730117	2947	40
JC142_113_002	23.775867	-20.714767	2067	35
JC142_113_004	23.776983	-20.715117	2058	30
JC142_113_006	23.781217	-20.718150	1956	20
JC142_113_009	23.784800	-20.720333	1780	20
JC142_113_012	23.787750	-20.720683	1686	25
JC142_113_013	23.791533	-20.721883	1624	25
JC142_113_016	23.796733	-20.721283	1437	25

5.3.2 Inductively-coupled plasma mass spectroscopy

Samples were prepared for compositional analysis by cutting blocks of the upper 10 mm of 101 FeMn crusts which were then air dried. FeMn crusts were agate-milled to produce homogenous powders. For acid digestion, 250 mg of sample powder was predigested using 3 mL 5 % HNO_3 + 2 mL concentrated HCl + 1 mL concentrated HNO_3. This solution was evaporated at 80 °C for 14 hours and then allowed to cool. An acid digestion mixture of 0.5 mL concentrated $HClO_4$ + 1.5 mL concentrated HF and 3.5 mL concentrated HNO_3 was then added and evaporated using a heating scheme of increasing temperatures from 80 °C to 160 °C over an 18-hour period. When dry, the samples were cooled to 50 °C and 2.5 mL of 1:1 HNO_3:HCl mixture was added and heated for 30 minutes. After cooling to 30 °C, 10 mL MQ water + 2.5 mL H_2O_2 was added and heated at 30 °C for 15 minutes. The solution was then diluted to a final acid concentration of 5% with 10 mL of MQ water for analysis. Compositional analysis was conducted using an Agilent 8900 Triple Quadrupole Inductively Couple Plasma Mass Spectrometer (ICP-QQQ) at the British Geological Survey, alongside three certified reference materials (J-Mn1, Nod-A1 and Nod-P1). Precisions were better than 5% (relative standard deviation, RSD) for P, S, K, Ca, Ti, V, Cr, Co, Ni, Cu, Zn, Ge, Se, Rb, Zr, Nb, Ag, Cd, In, Sn, Sb, Te, Cs, Ba, the REEs, Hf, Ta, W, Tl, Pb, Th and U. Precisions of $\leq$10% RSD were measured for Li, Be, Na, Mg, Al, Mn, Fe, As, Y, Sr, and Mo (see Appendix A.1).

5.3.3 Scanning electron microscopy

Scanning electron microscopy (SEM) analyses was carried out on both upper surface FeMn crust material and on polished sample sections. To investigate trends in the preservation of FeMn crust surfaces, a Hitachi TM-1000 SEM (British Ocean Sediment

Core Research Facility, NOCS) was used to image the upper sample surface at 250 X and 800 X magnifications to facilitate classification. No sample preparation is required for this technique. For high-resolution SEM imaging and sample characterisation, carbon-coated polished section of sample JC142_078_019, located at 3101 m water depths on the W-spur of Tropic Seamount, was analysed using a LEO1450 Variable Pressure SEM and an Oxford Instruments X-Act 10 mm^2 area semi-quantitative energy dispersive X-ray (EDS) detector with Silicon Drift detector (SDD) using Aztec Energy software at the University of Southampton. Microstructures were investigated using a backscattered electron detector for compositional analysis and a secondary electron detector for topographic imagery. Analyses were conducted at a resolution of 512 X 384 pixels with an accelerating voltage of 20 kV and dwell time of 305 μs per pixel with 11% overlap and a working probe distance of 19 mm. Element mapping focussed on the distribution of key elements of interest, including Fe and Mn, as well as Al and Ca for indicators of siliciclastic and bioclastic detrital input.

5.4 Results

5.4.1 Geochemical characterisation of Tropic ferromanganese crusts

5.4.1.1 Major and trace element concentrations

Table 5.2 and Table 5.3 shows the major and trace element composition of 101 of the FeMn crusts analysed (the composition of the REY is available in Appendix B.1 and the full chemical composition is available in Appendix B.3). Samples showed high concentrations of Fe, which varied between 9.2 – 32.7 wt% but had an average of 23.0 wt%. Manganese also showed high but slightly lower concentrations relative to Fe, as has been observed for Atlantic Ocean FeMn crusts in past studies (e.g. Koschinsky et al., 1995; Marino et al., 2017), between 9.1 – 23.7 wt% and with an average value of 16.7 wt%. The Fe/Mn ratios vary between 0.94 – 1.97, with an average of 1.40, reflecting hydrogenetic precipitation. This hydrogenetic mode of formation is supported by the REY patterns and trace element compositions, as shown in Figure 5.3.

TABLE 5.2: Major element composition of Tropic FeMn crusts

Sample Name	Na	Mg	Al	K	Ca	Ti	Mn	Fe
	wt%	wt%	wt%	wt%	wt%	wt%	wt%	wt%
JC142_009_010	1.00	1.24	1.14	0.32	2.39	0.54	16.55	20.19
JC142_020_017	1.24	1.31	0.92	0.26	2.20	0.60	17.30	17.99
JC142_039_003	1.21	1.17	1.75	0.38	2.23	0.58	14.85	19.10
JC142_039_005	1.18	1.09	1.29	0.29	2.39	0.55	16.04	18.68
JC142_039_007	1.09	1.23	1.82	0.33	3.08	0.87	13.72	17.24

Sample Name	Na	Mg	Al	K	Ca	Ti	Mn	Fe
	wt%	wt%	wt%	wt%	wt%	wt%	wt%	wt%
JC142_039_012	0.97	1.23	1.38	0.38	1.82	0.52	14.72	17.69
JC142_039_015	1.03	1.08	1.24	0.27	1.84	0.61	14.84	18.97
JC142_039_017	1.21	1.42	1.82	0.32	2.29	0.95	17.08	21.48
JC142_039_019	1.16	1.19	1.33	0.31	1.96	0.71	15.32	21.53
JC142_039_020	1.03	1.19	1.41	0.25	1.96	0.71	14.64	17.84
JC142_039_021	1.11	1.31	1.80	0.33	2.26	0.77	14.75	18.06
JC142_039_024	1.16	1.79	2.45	0.47	5.59	0.64	14.40	18.16
JC142_047_007	1.14	1.56	1.48	0.43	1.90	0.43	17.90	19.52
JC142_047_012	0.91	2.58	2.45	0.47	1.85	0.32	19.79	22.01
JC142_055_001	1.07	1.80	2.57	0.46	3.35	0.91	15.56	22.22
JC142_055_002	0.88	1.12	1.23	0.29	2.13	0.79	13.45	19.97
JC142_055_006	0.92	1.15	1.16	0.29	2.58	0.89	16.12	22.19
JC142_055_007	0.85	1.05	1.32	0.30	2.18	0.75	12.12	19.16
JC142_055_008	1.25	1.58	2.55	0.47	2.39	0.97	18.33	27.43
JC142_055_017	1.61	1.68	1.55	0.38	2.88	1.26	22.14	28.77
JC142_055_021	1.35	1.64	1.76	0.40	2.72	0.92	20.85	27.96
JC142_055_023	1.24	1.56	1.32	0.33	2.67	1.21	21.54	29.36
JC142_058_010	1.08	1.41	1.02	0.33	2.39	0.59	19.98	22.40
JC142_058_012	1.02	1.51	1.18	0.40	6.59	0.55	18.65	22.28
JC142_058_014	1.15	1.51	1.20	0.40	2.25	0.54	18.74	21.79
JC142_058_022	1.12	1.42	1.02	0.32	2.49	0.61	21.26	22.24
JC142_058_030	1.46	1.83	1.07	0.37	7.69	0.81	21.74	24.41
JC142_061_014	1.18	1.44	0.93	0.37	3.08	0.63	18.74	27.07
JC142_061_018	1.15	1.40	1.04	0.34	2.41	0.68	20.33	24.71
JC142_061_021	1.32	1.63	1.53	0.39	3.78	0.50	20.85	23.43
JC142_078_001	1.32	1.55	2.27	0.43	2.17	0.88	19.48	32.70
JC142_078_005	1.26	1.60	2.78	0.67	1.42	0.57	14.73	20.04
JC142_078_009	0.84	1.04	1.35	0.31	1.90	0.79	15.73	22.34
JC142_078_016	1.21	1.53	2.27	0.49	2.21	0.88	19.10	26.29
JC142_078_019	0.98	1.12	1.62	0.34	1.78	0.68	14.76	23.27
JC142_078_020	1.34	1.52	2.04	0.50	6.18	1.39	21.61	27.72
JC142_078_023	1.06	1.18	1.53	0.41	1.99	0.84	15.80	22.90
JC142_078_028	1.13	1.48	2.29	0.50	2.61	1.10	18.23	23.01
JC142_078_030	1.08	1.24	1.48	0.36	2.59	1.07	15.83	25.15
JC142_078_035	1.19	1.52	1.66	0.43	2.24	0.70	21.41	27.74
JC142_080_001	1.20	1.58	1.08	0.36	2.81	1.01	22.21	27.24
JC142_080_002	1.23	1.63	1.23	0.35	4.10	0.93	21.34	29.17
JC142_080_012	1.42	1.73	1.43	0.43	2.60	0.85	23.70	25.81
JC142_080_013	1.04	1.50	1.23	0.40	2.07	0.67	20.28	21.09

Sample Name	Na	Mg	Al	K	Ca	Ti	Mn	Fe
	wt%	wt%	wt%	wt%	wt%	wt%	wt%	wt%
JC142_083_001	1.06	1.34	2.07	0.47	1.79	0.94	16.31	19.29
JC142_083_002	0.92	1.15	2.18	0.50	1.55	0.84	13.67	19.39
JC142_083_006	1.11	1.53	2.11	0.46	2.95	1.04	21.73	29.43
JC142_083_006	1.11	1.53	2.11	0.46	2.95	1.04	21.73	29.43
JC142_083_007	1.57	1.67	2.36	0.58	3.23	0.99	20.56	30.85
JC142_083_010	0.88	1.21	1.64	0.48	1.54	0.52	15.42	20.41
JC142_083_015	1.08	1.58	2.04	0.48	3.35	0.93	17.28	23.68
JC142_083_021	0.98	1.04	1.76	0.51	9.54	0.69	11.16	18.92
JC142_083_022	1.03	1.24	2.31	0.58	4.48	1.04	13.14	22.36
JC142_091_001	0.95	1.13	1.71	0.39	1.72	0.59	14.43	24.05
JC142_091_003	1.08	1.32	2.23	0.47	1.85	0.90	17.51	27.11
JC142_091_004	1.01	1.29	1.95	0.39	1.85	0.62	14.30	21.14
JC142_091_012	0.89	1.07	1.43	0.29	2.02	0.61	14.94	24.04
JC142_091_031	0.91	1.12	1.39	0.31	2.20	0.75	14.44	21.66
JC142_094_005	1.30	1.24	0.80	0.32	2.56	0.44	19.15	26.86
JC142_094_006	1.25	1.30	0.83	0.31	2.44	0.61	18.04	30.02
JC142_094_015	1.21	1.25	1.06	0.32	2.88	0.54	21.30	27.64
JC142_094_019	1.15	1.39	1.25	0.31	2.33	0.68	18.63	27.57
JC142_094_020	1.10	0.73	0.49	0.23	10.73	0.40	13.85	15.83
JC142_094_021	1.01	1.24	0.82	0.35	13.11	0.36	16.63	15.64
JC142_094_024	1.11	0.71	0.59	0.29	18.85	0.28	9.12	9.33
JC142_094_031	1.20	1.42	1.19	0.30	2.42	0.67	16.84	26.52
JC142_094_034	1.10	0.77	0.50	0.26	21.01	0.38	10.61	12.24
JC142_100_015	1.04	1.22	0.85	0.29	2.42	0.56	17.99	26.71
JC142_107_001	0.90	1.31	1.61	0.37	2.76	1.03	14.96	25.47
JC142_107_002	1.00	1.38	1.67	0.37	2.21	0.98	16.23	26.80
JC142_107_003	1.46	1.81	2.12	0.40	2.56	0.92	16.22	27.02
JC142_107_005	1.21	1.36	1.07	0.31	2.61	0.76	18.77	27.30
JC142_107_013	1.09	1.66	1.72	0.39	3.16	0.66	16.68	26.11
JC142_107_015	1.07	1.36	0.84	0.27	2.62	0.69	18.58	28.78
JC142_107_019	1.00	2.19	1.55	0.56	6.51	0.42	17.37	17.34
JC142_107_020	1.17	2.08	1.89	0.46	2.14	0.59	19.93	24.15
JC142_107_032	1.05	1.58	1.43	0.46	2.26	0.54	18.98	27.13
JC142_109_005	0.99	1.13	1.84	0.36	1.63	0.55	12.97	22.54
JC142_109_007	1.29	1.52	2.92	0.61	1.80	0.79	13.33	26.28
JC142_109_014	1.18	1.66	2.89	0.66	2.56	0.66	14.28	23.29
JC142_109_017	1.22	1.35	2.23	0.47	1.71	0.49	15.44	24.92
JC142_109_018	1.18	1.39	1.95	0.38	2.98	0.87	15.69	27.26
JC142_109_020	1.26	1.60	2.41	0.53	1.81	0.56	15.95	23.16

Sample Name	Na	Mg	Al	K	Ca	Ti	Mn	Fe
	wt%	wt%	wt%	wt%	wt%	wt%	wt%	wt%
JC142_113_002	1.17	1.38	1.49	0.37	2.43	0.81	16.19	29.73
JC142_113_004	1.16	1.42	1.39	0.34	2.55	0.90	17.12	29.82
JC142_113_006	0.98	1.34	1.27	0.31	2.42	0.82	14.15	22.28
JC142_113_009	0.92	1.16	1.10	0.25	2.85	0.65	13.80	23.36
JC142_113_012	1.23	1.38	1.17	0.29	2.51	0.75	17.76	28.53
JC142_113_013	1.31	1.58	2.42	0.63	2.38	0.99	11.60	20.02
JC142_113_016	1.05	1.36	0.91	0.26	2.68	0.72	18.60	28.63

TABLE 5.3: Key minor element composition of Tropic FeMn crusts

Sample Name	Li	Co	Ni	Cu	Zn	Mo	Te
	ppm	ppm	ppm	ppm	ppm	ppm	ppm
JC142_009_010	10.2	6369	2777	453	499	648	58.6
JC142_020_017	7.7	7482	2913	345	464	481	75.9
JC142_039_003	11.3	5208	3010	829	599	486	40.5
JC142_039_005	6.2	5008	2903	717	570	582	38.3
JC142_039_007	7.3	4920	2554	624	470	359	44.6
JC142_039_012	11	4541	3697	698	588	485	51.2
JC142_039_015	6.5	4769	2610	508	559	478	41.9
JC142_039_017	7.7	6588	2857	445	553	460	61.2
JC142_039_019	6.5	5840	2663	496	578	527	55.4
JC142_039_020	7.2	5145	2700	429	490	435	46.4
JC142_039_021	12.3	5201	2795	506	503	412	46.3
JC142_039_024	34.8	4507	4888	1183	683	382	39.5
JC142_047_007	38.4	6674	4732	696	707	583	52.5
JC142_047_012	53	6710	6137	1366	934	505	42.6
JC142_055_001	42.6	5364	4218	1312	710	347	46.8
JC142_055_002	9.3	3959	2096	576	571	413	36.9
JC142_055_006	5.4	5318	2294	469	578	492	42.1
JC142_055_007	7	4021	1928	567	507	383	36.2
JC142_055_008	17.5	5191	2963	927	814	528	50.5
JC142_055_017	5.9	8415	3005	460	771	706	72.6
JC142_055_021	13.2	6032	3267	847	837	694	57
JC142_055_023	4.7	8174	2643	482	833	662	77.9
JC142_058_010	6.4	7038	2686	298	543	600	63.9
JC142_058_012	19.9	6767	2470	479	618	578	62.1
JC142_058_014	17.3	7286	3429	506	677	578	61.1
JC142_058_022	17.7	8153	2786	531	613	760	71.3
JC142_058_030	11.1	10734	3527	514	628	653	90.7

Sample Name	Li	Co	Ni	Cu	Zn	Mo	Te
	ppm	ppm	ppm	ppm	ppm	ppm	ppm
JC142_061_014	4.2	6805	2720	359	680	777	73.3
JC142_061_018	7.7	7545	2674	366	626	714	72.5
JC142_061_021	23.1	5907	3777	699	860	688	51.6
JC142_078_001	14.5	4139	2564	1270	734	653	38.4
JC142_078_005	38.9	2584	4826	2218	739	399	22.2
JC142_078_009	6.3	4031	2182	483	519	530	33.2
JC142_078_016	31.8	4418	4199	1319	750	550	35.4
JC142_078_019	10.7	4333	2979	1164	697	530	40.6
JC142_078_020	12.4	8062	3197	888	732	589	61.1
JC142_078_023	14	4641	3173	645	558	535	45.3
JC142_078_028	14.9	5977	3114	518	625	540	47
JC142_078_030	6.5	6173	2470	702	573	509	54
JC142_078_035	24	7726	5196	1583	1070	710	56.4
JC142_080_001	20.7	9659	3495	567	652	585	84.6
JC142_080_002	4	9135	3125	493	675	721	88.7
JC142_080_012	27	9867	4946	771	777	689	82.9
JC142_080_013	33	7673	4709	737	730	563	69.3
JC142_083_001	23.6	5197	3798	1344	566	401	38.3
JC142_083_002	18.9	4131	2406	859	468	373	35.3
JC142_083_006	15.6	5700	3599	897	742	681	43.1
JC142_083_006	15.6	5700	3599	897	742	681	43.1
JC142_083_007	26.5	5427	4329	1591	799	659	47.1
JC142_083_010	22.9	3015	4987	1856	782	516	27.4
JC142_083_015	44.3	4312	4376	1088	713	433	32.3
JC142_083_021	10.9	2829	1687	410	421	350	20.3
JC142_083_022	16.2	4172	2372	783	502	380	36.9
JC142_091_001	16	2575	2347	836	546	494	20.9
JC142_091_003	14.9	5079	2955	1069	615	552	41.8
JC142_091_004	15.6	3165	2619	847	511	441	22.8
JC142_091_012	8.8	3293	2292	522	521	502	28.5
JC142_091_031	8.1	4464	2450	591	471	469	38.2
JC142_094_005	2.9	5992	3574	774	833	892	56.4
JC142_094_006	3.4	6985	2917	357	768	804	57
JC142_094_015	7.2	5247	3453	932	1059	872	77.1
JC142_094_019	12.5	7171	3234	615	744	634	63.6
JC142_094_020	2	2556	2046	438	634	460	57.9
JC142_094_021	11.2	3243	6629	662	1004	445	50.3
JC142_094_024	4.3	1920	2251	272	305	267	44.4
JC142_094_031	9.9	7226	2903	570	603	581	76.1

Sample Name	Li	Co	Ni	Cu	Zn	Mo	Te
	ppm	ppm	ppm	ppm	ppm	ppm	ppm
JC142_094_034	3.1	2516	2448	293	435	312	57.4
JC142_100_015	2.6	7272	2286	291	478	710	62.7
JC142_107_001	6.8	6786	2527	619	567	442	60.8
JC142_107_002	7.4	6788	2928	628	604	508	61.9
JC142_107_003	38.5	8546	4383	1051	786	397	90.5
JC142_107_005	3.7	6788	3215	453	585	686	57
JC142_107_013	22.5	5891	3545	544	656	534	51.9
JC142_107_015	1.6	6902	2487	192	563	694	66.3
JC142_107_019	61.4	6016	6028	937	738	405	43.3
JC142_107_020	60.7	7418	6674	1153	850	575	61.8
JC142_107_032	27.5	6380	4418	581	788	620	54.6
JC142_109_005	11.7	2682	2201	896	486	425	22.8
JC142_109_007	24.2	3065	1810	1562	527	408	28.7
JC142_109_014	35.4	3608	4362	2100	659	348	30.6
JC142_109_017	26.2	2895	4357	1916	797	531	27.9
JC142_109_018	12.3	4554	2804	644	593	489	38.5
JC142_109_020	41.5	3591	5149	1976	768	505	34.3
JC142_113_002	6.4	5283	2475	419	614	520	46.4
JC142_113_004	5.9	5893	2680	340	611	592	52.3
JC142_113_006	17.7	6197	3224	528	550	426	55.2
JC142_113_009	4	4563	2380	406	524	508	43.1
JC142_113_012	4.2	5803	2759	256	614	633	54.8
JC142_113_013	21.7	3225	3392	871	604	366	47
JC142_113_016	2.8	6682	2706	212	533	684	66.2

The concentrations of key critical elements of interest are high, with Co concentrations between 0.19 – 1.07 wt% (average of 0.54 wt%) and Te concentrations between 20.3 – 90.7 ppm (average of 51.1 ppm). Both Co and Te show strong correlations with water depth, with R^2 values of 64% and 77% respectively. The highest concentrations of both Co and Te are observed in the summit regions, with decreasing concentrations with increasing water depth (Figure 5.2). In general, FeMn crusts are observed to have low Al/Nd ratios compared to continental crustal rocks and detrital sediments, as they preferentially incorporate Nd and other trace metals over Al (Hein et al., 2000). Average Al/Nd ratios of 59 of Tropic FeMn crusts closely match those measured in FeMn crust averages for the Pacific Ocean basin of 65 (Hein et al., 2000) but also extend up to 180, suggesting an important role for variable detrital inputs in FeMn crust around Tropic Seamount.

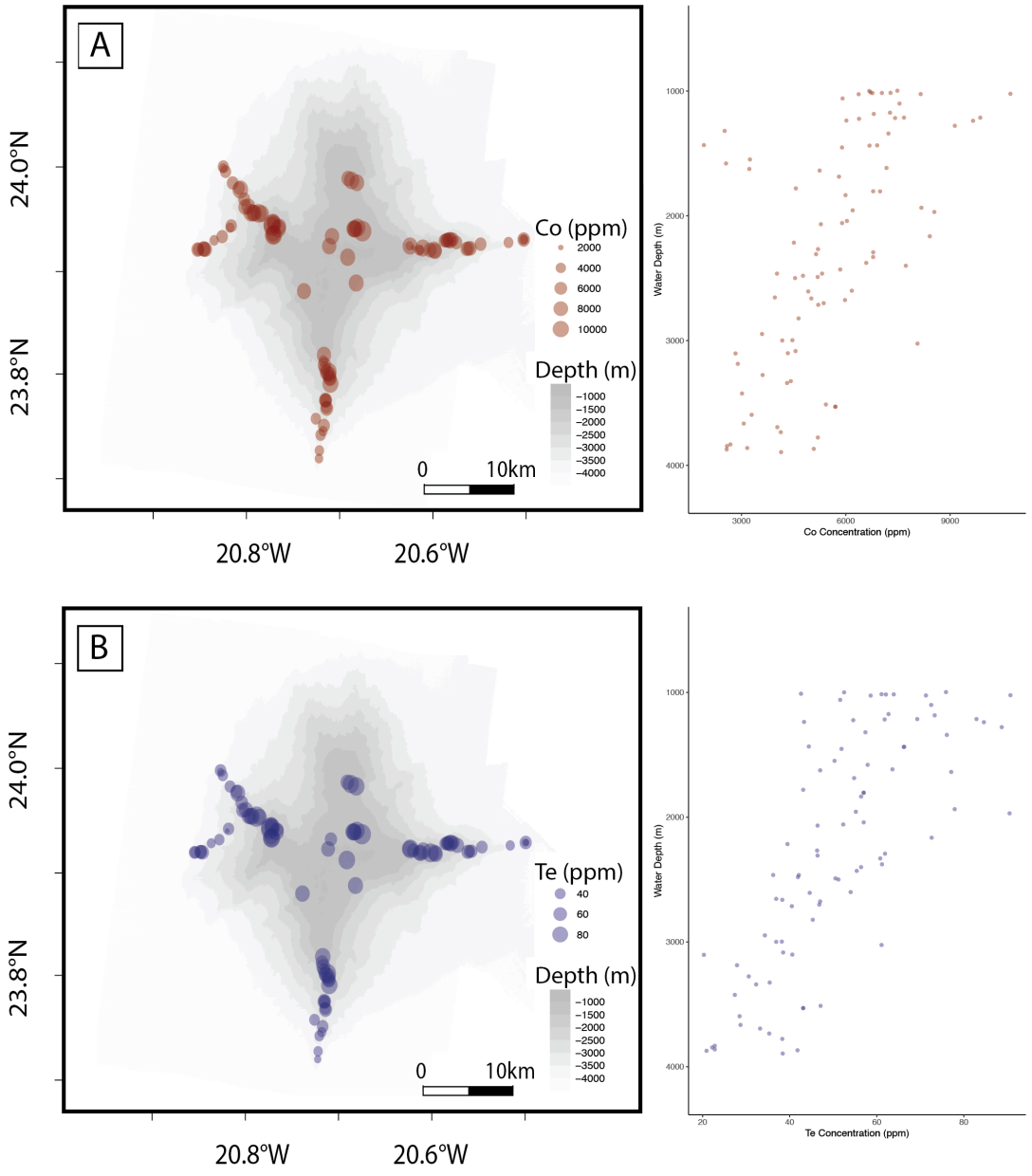

FIGURE 5.2: Maps of elemental concentration variations for (A) Co and (B) Te, with point sized scaled relative to concentration, shown alongside concentration variation with depth. For both elements, the highest concentrations are observed for summit samples. R^2 values for concentration with depth: Co = 64% and Te = 77%.

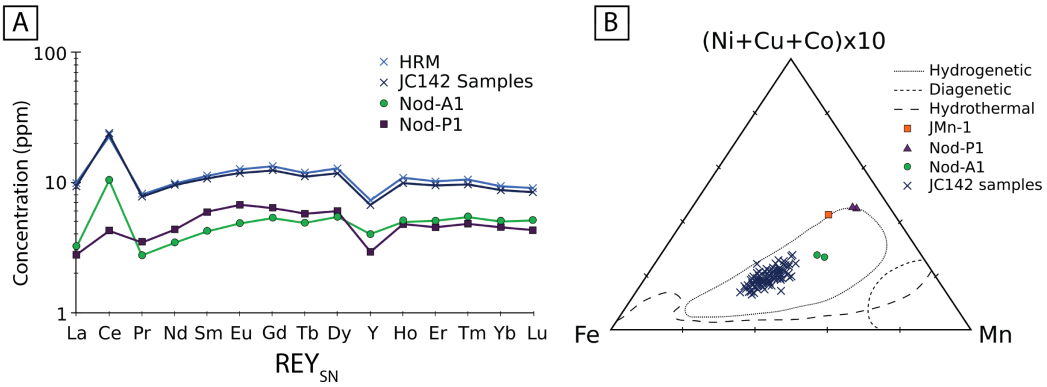

FIGURE 5.3: Diagnostic plots indicating hydrogenetic mode of FeMn crust formation. (A) Shale-normalised (PAAS; McLennan, 2001; Condie, 1993) REY plots for FeMn crusts from Tropic Seamount (JC142) in comparison to Nod-A1 and Nod-P1 profiles, as well as the house reference material (HRM) which was a Tropic Seamount crust run with repeat analyses alongside other samples. (B) Discrimination diagram based on the content of the major (Fe and Mn) and trace (Ni, Cu and Co) concentrations in FeMn crusts, showing Tropic Seamount crusts plotting within the hydrogenetic field (after Hein et al., 2009b).

5.4.2 Growth Rate estimations

To investigate the potential variability in growth rates around Tropic Seamount, Co-chronometry methods were used. The accurate age dating of FeMn crusts is analytically challenging due to their slow rates of precipitation, between 1 – 5 mm per million years (e.g. Hein et al., 2009b; Hein and Koschinsky, 2014), that leads to condensed stratigraphic sections that limit sampling resolutions for conventional dating techniques. Absolute dating techniques are also limited up to 10 Myrs for Be-isotope methods (Claude et al., 2005) which means that for ages older than this, age estimates must be made using extrapolation or comparative stratigraphic methods. Josso et al. (2019) recently demonstrated the strength in using cross-validation between multiple techniques to build reliable composite age models for FeMn crusts but this methodology remains analytically complex. One method widely used to estimate crust growth rates is Co-chronometry, due to its ease of application (Ling et al., 1997; Abouchami et al., 1999; Frank et al., 1999). This method assumes a constant Co supply to oceans and has been developed by Puteanus and Halbach (1988)and Manheim and Lanebostwick (1988) to estimate crust accumulation rates from empirical relationships between growth rates determined using absolute dating methods. Hiatuses in FeMn precipitation or erosive periods cannot be accounted for using these methodologies and so provides a minimum accumulation rate. Two empirical relationships were developed:

$$\text{Growth Rate} = \frac{1.28}{([\text{Co}] - 0.24)} \tag{5.1}$$

$$\text{Growth Rate} = 0.68 \times \left(\frac{50 \times \text{Co}}{\text{Fe} + \text{Mn}} \right)^{1.67} \tag{5.2}$$

The method developed by Puteanus and Halbach (1988), Equation 5.1, assumes pure hydrogenetic growth and doesn't include detrital inputs whereas the model of Manheim and Lanebostwick (1988), Equation 6.2 has accounted for a range of accumulation contributions and therefore is more widely applied. Both models were applied to FeMn crust data in this study (see Appendix B.2). The Puteanus and Halbach (1988) model estimated growth rates between 1.54 – 110.34 mm/Myr, with an average of 9.6 mm/Myr for samples with over 0.24 wt% Co. When only Co concentrations greater than 0.3 wt% were considered, the maximum estimated growth rate was 45.39 mm/Myr and the average was 5.84 mm/Myr. Estimated growth rates using the Manheim and Lanebostwick (1988) model vary between 0.52 – 4.23 mm/Myr, with an average of 1.52 mm/Myr. Given Al/Nd indications of detrital inputs of FeMn crusts in this study and the limitations on minimum Co concentrations for applying the Puteanus and Halbach (1988), growth rates determine using the Manheim and Lanebostwick (1988) equation were used for comparisons of growth rates with other variables in the following discussions. More accurate growth rate values determined using composite modelling techniques by Josso et al. (2019) showed average growth rates of 4 mm/Myr for a drillcore sample from Tropic Seamount's summit, who also highlighted the caveats with using empirical methods for growth rate estimation which are considered within the discussion.

5.5 SEM Energy Dispersive X-ray Spectroscopy (SEM-EDS)

Back-scattered electron imagery and element mapping for key major elements was conducted by SEM-EDS for sample JC142_078_019 to understand the inter-elemental relationships between key constituent elements (Figure 5.4). Backscatter images show distinctive layered growth patterns that vary up through the section, with distinct changes denoted by different "zones" in Figure 5.4. Within Zone 1 in the lower layers there are regular, well-laminated layers that form a massive texture. These layers are Fe- and Mn-rich, with Mn dominating the massive structures and higher Fe concentrations in between indistinct columnar structures. Overlying this in Zone 2 is a layer of chaotic material with increased concentrations of Si and Ca as well as distinct bioclastic structures that supports the presence of entrained bioclastic and detrital material. Into Zone 3, this growth is followed by alternations between regular sub-millimetre columnar growth and laminated layering that show high Mn concentrations within the column core and higher Fe concentration between the columns. Higher Si concentrations are also observed in these inter-column regions. This gradually transitions into Zone 4, which displays larger more regular FeMn crust columns up through the section that is topped by an apparent erosive horizon, above which a layer of relatively irregular

columnar growth caps the sample in Zone 5. The upper, chaotic portion of growth at the top of the sample in Zone 5 also shows horizons with anomalously high Mn concentrations that are interpreted to correspond to localised diagenetic redistribution. Overall, Fe and Mn are observed to anticorrelate, which matches observations from numerous FeMn crust studies, with Fe concentrations higher in between columns and Mn dominating in massive layers and columnar growth sections. Higher Ca and Si are observed interstitially to columnar and massive growth, corresponding to regions with more chaotic textures and lower Mn concentrations, from the accumulation of detrital grains. While both Fe and Mn are associated with FeMn crust growth layers, Fe is also observed within some detrital material.

5.6 Surface erosion mapping at Tropic Seamount

Textural mapping of the upper FeMn crust surface was carried out for 106 samples across the summit and limbs of Tropic Seamount. Figure 5.5 shows the classification of surface textures used to categorise FeMn crust. Samples that were observed to maintain primary growth textures, such as distinct preserved botryoidal growth that is characteristic of FeMn crusts, were defined as having preserved recent growth surfaces (Figures 5.5A and 5.5B). Samples that showed no evidence of primary growth textures, with flat and smooth upper surfaces, were classified as eroded with no recent FeMn crust growth preserved (Figures 5.5D and 5.5E). Of the 106 samples images, 45 had preserved recent growth surfaces and 61 were eroded. Some samples were also observed to have biogenic structures, present as concentric foraminiferal clasts incorporated in their upper surfaces (Figures 5.5C and 5.5F). Josso et al. (2019) and Yeo et al. (2018a) also observed bioclastic material in Tropic Seamount FeMn crusts, dominantly foraminifera but also including fish bone fragments.

Figure 5.6 shows the distribution across Tropic Seamount of FeMn crusts observed to have predominantly eroded upper surfaces and where the crusts have preserved growth textures. Three main trends in the distribution of different surface textures were observed. Firstly, all analysed samples from the summit, at water depths above 1200 m, show abraded upper surfaces. Secondly, a larger proportion of samples collected from the upper regions of Tropic Seamount showed evidence of abrasion, with 74% of samples between 1200 – 2000 m having an eroded upper surface, rising to a total of 84% of samples with eroded surfaces for all samples collected at water depths shallower than 2000 m. With increasing water depth, a greater proportion of surfaces show preserved growth textures, with only 40% of samples showing eroded surfaces between 2000 – 4000 m water depths. Thirdly, there appears to be a general pattern in the distribution of eroded samples between limb locations on the star-shaped Tropic Seamount. Overall the largest proportion of eroded surfaces are observed for samples on the eastern limb of Tropic Seamount, across the widest range of water depths.

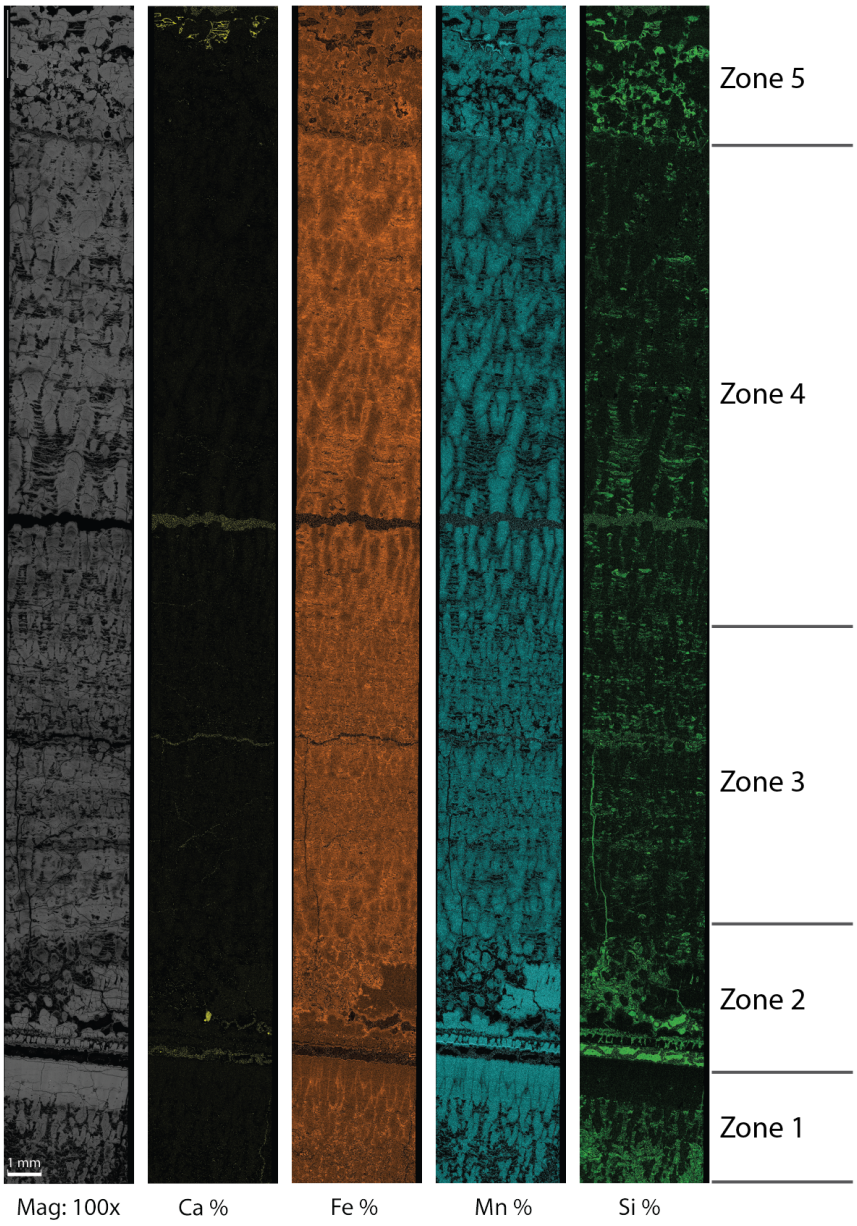

FIGURE 5.4: SEM-EDS imagery of JC142_078_019 to show the characteristic FeMn crust textures observed at Tropic Seamount and the distributions of Ca, Fe, Mn and Si, with brighter colours equally higher concentrations. Anomalously high values in void spaces associated with sample preparation (distinguished by shape and texture) have been omitted from the analysis. Variational "Zones" have been labelled to denote areas of distinct characteristics, as described in Section 5.5

.

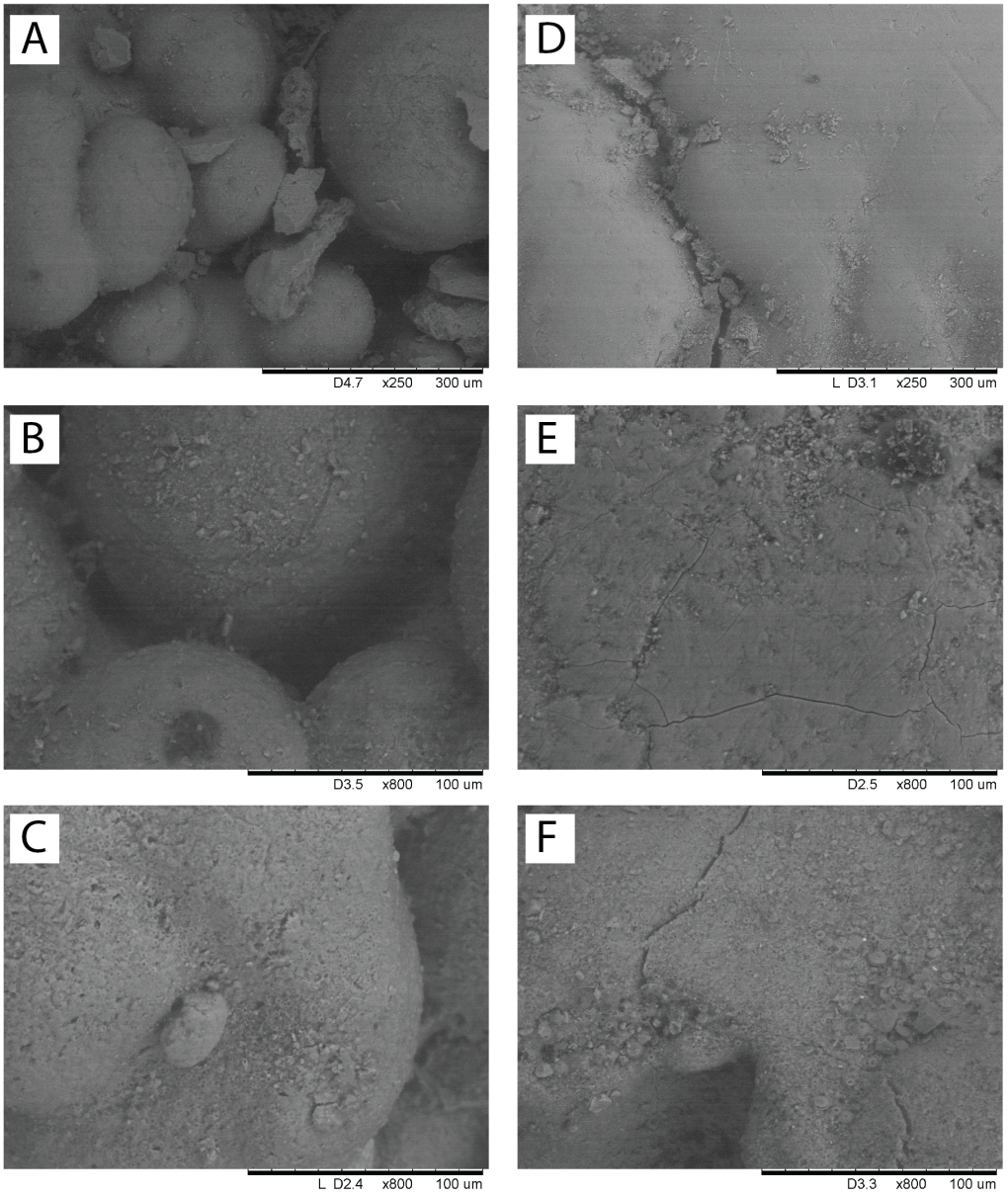

FIGURE 5.5: SEM images of the upper surfaces of FeMn crust surfaces. Representative samples are shown to demonstrate the classification of surface texture used to classify samples in this study: (A), (B) and (C) show preserved recent botryoidal growth surfaces and (D) and (E) show eroded surfaces where primary growth textures have been removed. Images (C) and (F) also show evidence of biogenic material on FeMn crust surfaces.

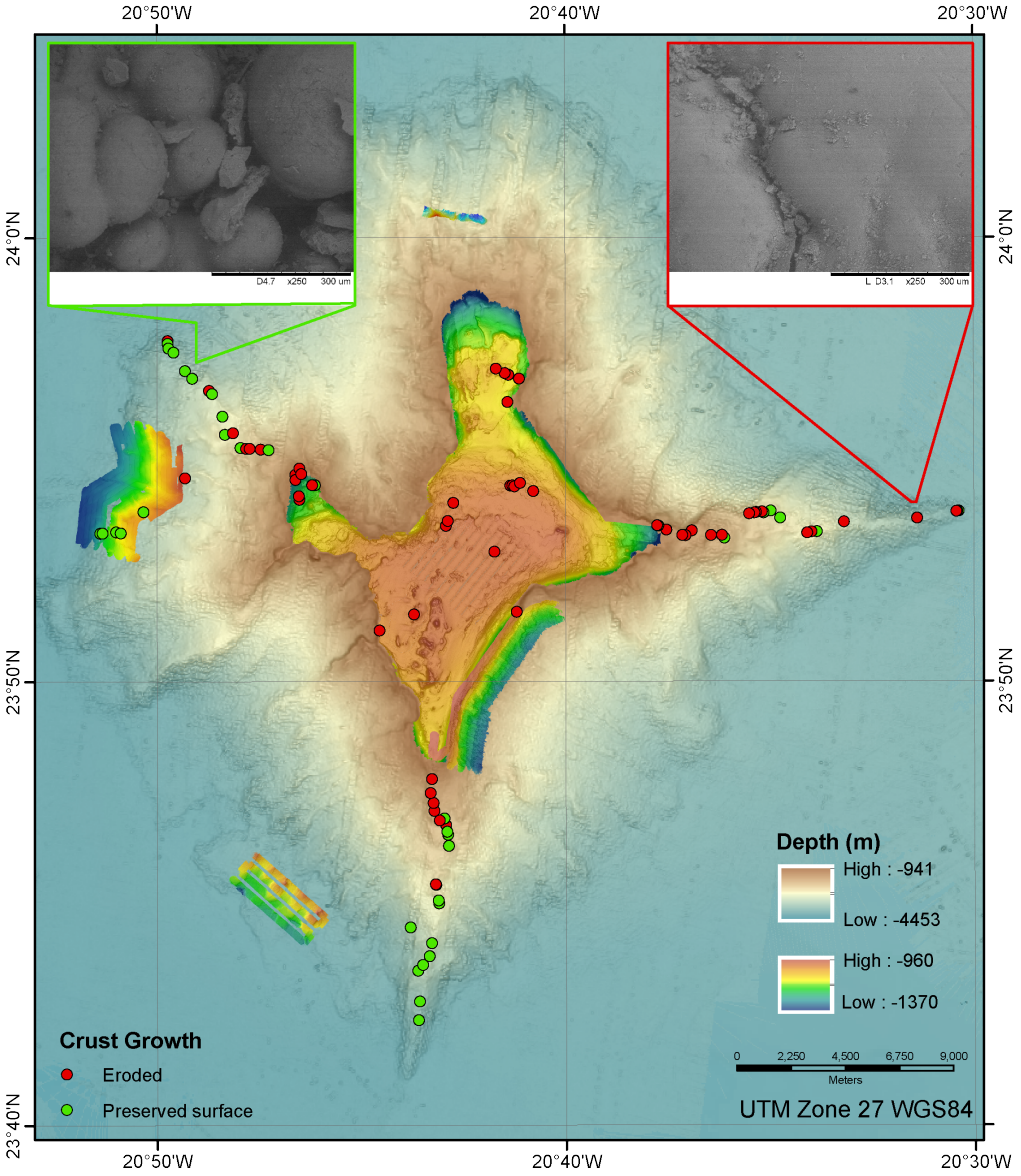

FIGURE 5.6: Distribution of FeMn crust preserved recent growth surfaces determined from SEM analysis. Eroded surfaces are shown in red and preserved surfaces in green, with inset SEM images to show representative textures for each of the sub-types.

5.7 Discussion

5.7.1 Resource potential of FeMn crusts

The concentration of key elements of interest within recent FeMn crust growth from Tropic Seamount were compared with average compositions of FeMn crusts from the Atlantic Ocean, the Indian Ocean and a region widely studied due to the high target element enrichments in the Pacific Ocean known as the Prime Crust Zone (Hein et al., 2013; Hein and Koschinsky, 2014). In general, major and minor bulk compositions of Tropic Seamount closely fit average Atlantic Ocean FeMn crust compositions, with

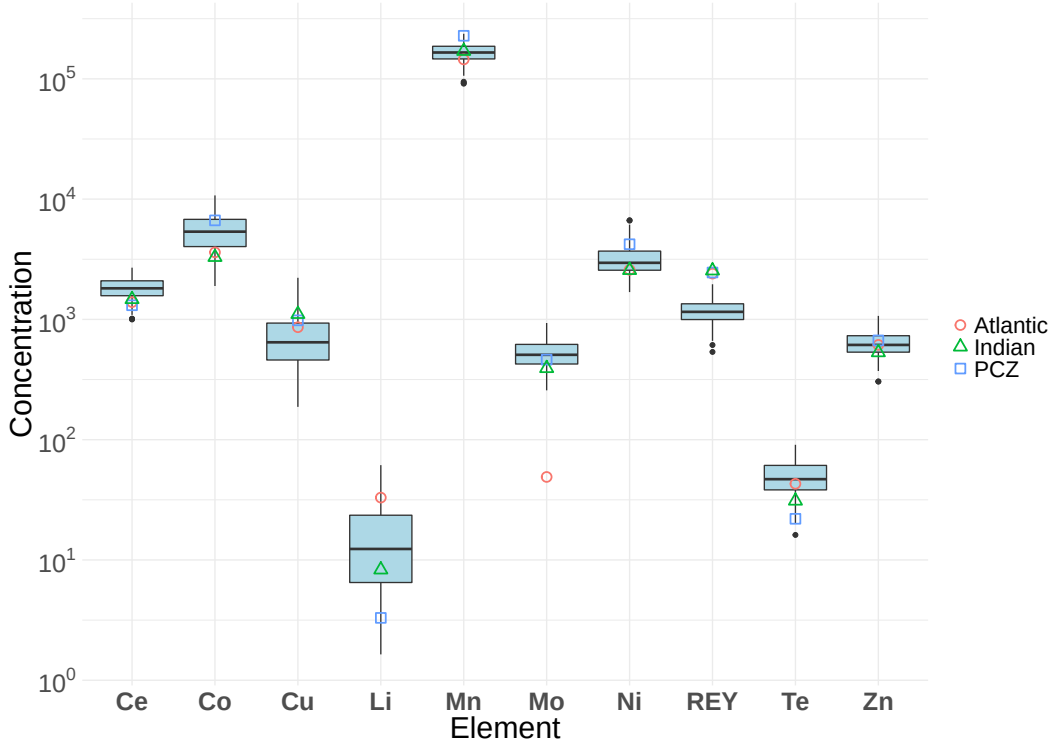

FIGURE 5.7: Comparison of the average concentrations (in ppm) of key elements between the Tropic Seamount FeMn crusts analysed in this study and other regions including the Atlantic Ocean (red circles), Indian Ocean (green triangles) and the Prime Crust Zone in the Pacific Ocean. Summary statistics for Tropic Seamount FeMn crusts are shown by the blue box and whisker plots: the bold bar shows median (n=101) concentrations, the upper and lower box limits denote the 75% and 25% quantile respectively and then whiskers extends to 1.5x of the inter-quartile range. Average values for Atlantic, PCZ and Indian ocean crusts are from Hein et al. (2013).

17 wt% Mn and 22.5 wt% Fe (Figure 5.7). The Mn/Fe ratios and trace element patterns of FeMn crusts at Tropic Seamount indicated hydrogenetic crust growth. Hydrogenetic formation is associated with the extreme enrichment of a range of elements, such as Co, Te, REY and Cu, that are of interest for use in a range of modern technologies, including solar photovoltaic cells and electric vehicle batteries (Hein et al., 2010, 2013).

This extreme enrichment has been attributed to the very slow formation rates of hydrogenetic FeMn crust alongside high surface areas and porosity (Hein et al., 2000; Bau et al., 2014). This allows for sustained periods of scavenging of trace metals from the surrounding seawater and is further enhanced for elements such as Co due to the effects of surface oxidation (e.g. Burns, 1976; Peacock and Moon, 2012). At Tropic Seamount, the average concentrations of critical metals and E-Tech elements, measured as 0.5 wt% Co and 48 ppm Te in this study, are higher than the Atlantic values and match or exceed average concentrations of Co, Te, Ce, Mo, Zn Cu and REY in the Pacific Ocean, (Hein et al., 2013). The extreme enrichment of Te is proposed to be due to the coprecipitation of Te(IV) with Fe-oxyhydroxide phases (Kashiwabara et al., 2014). While Tropic Seamount crusts show promising average compositions, Atlantic FeMn

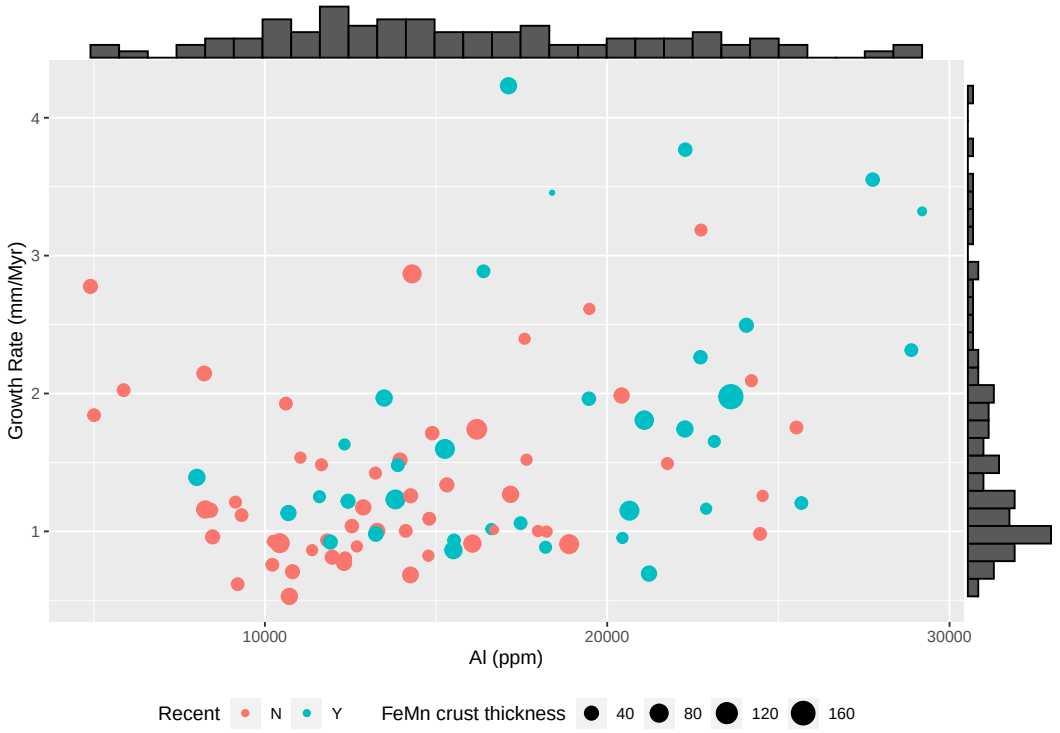

FIGURE 5.8: Relationship between growth rate and Al concentration in FeMn crusts, used here as a proxy for detrital input (R^2 = 37%, $p<0.05$). The colour denotes the preservation state of the recent surface (blue is preserved, red is not preserved) while the points are scaled in size relative to the measured FeMn crust thickness. The outer bar charts show the relative density distribution.

crusts generally show lower Mn/Fe ratios than Pacific crusts, as observed at Tropic Seamount, which shows an average Mn/Fe ratio of 0.74. This has largely been attributed to higher detrital inputs for Atlantic crusts due to the proximity to sources of aeolian and riverine material (e.g. Koschinsky et al., 1996; Hein et al., 2016).

High inputs of detrital material increase the dilution effect of the main target elements and can reduce the overall grade of FeMn deposits (Hein et al., 2016; Yeo et al., 2018a). This was observed from the anticorrelation between regions of high Mn and Fe concentrations and Si- and Ca- rich detrital material from SEM-EDS analysis (Figure 5.4). The influx of detrital material may also affect FeMn crust growth rates due to the effect that it imparts on texture, with detritus-rich horizons corresponding to regions of more chaotic textures and increased porosity (Figure 5.4, e.g. Hein et al., 1992; Yeo et al., 2018a). To investigate the controls on FeMn crust growth rates, estimates from Co-chronometry were compared to textural, environmental and hydrographic characteristics. While Co-chronometry is limited due to the inability to account for erosive horizons or growth hiatuses, it can allow for the growth rate estimation of a large number of samples due to its reliance on trace element concentration. For the purposes of this study, this means that relationships with spatial variables at a range of water depths and environments can be investigated alongside other indicators. In order to

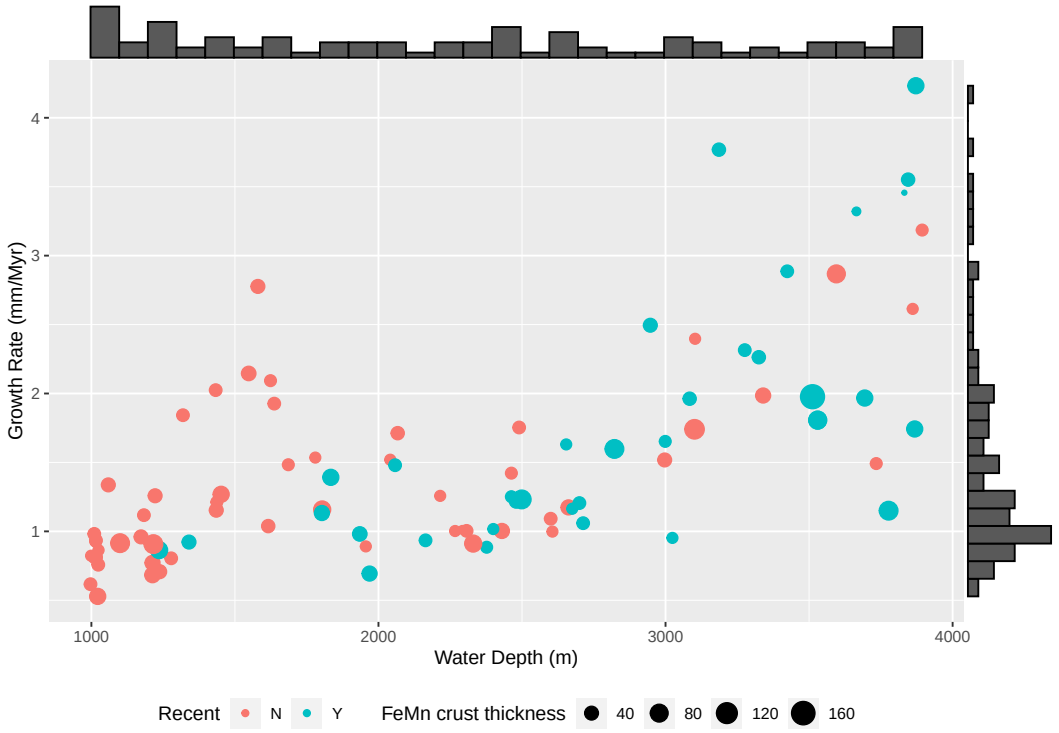

FIGURE 5.9: Relationship between water depth and estimated growth rate of FeMn crusts (R^2 = 65%, $p<0.05$). The colour denotes the preservation state of the recent surface (blue is preserved, red is not preserved) while the points are scaled in size relative to the measured FeMn crust thickness. The outer bar charts show the relative density distribution.

understand the potential relationship between growth rate and detrital phases, Al has been used as an indicator of potential detrital inputs (Figure 5.8) as it is associated with alumino-siliciclastic detrital phase for FeMn crusts in the Atlantic Ocean (e.g. Marino et al., 2017). A weak positive relationship between Al concentrations and growth rates supports the theory of increased detrital inputs leading to elevated FeMn crust growth rates at Tropic Seamount.

In order to understand the variability of growth rates with environment, Figure 5.9 demonstrates the positive relationship between water depth and estimated growth rate, with growth rates increasing with water depth and the slowest growing crusts located at the summit of Tropic Seamount. These slow growing FeMn crusts also correspond to samples that show eroded upper surfaces. When the relationship between growth rate and modelled maximum current velocities at the sample locations is considered, the relationship between the two variables appears more nuanced (Figure 5.10). While there doesn't appear to be a direct linear relationship, the fastest growing crusts, with growth rates above 3 mm/Myr, occur at low maximum current speeds of <0.11 m/s.

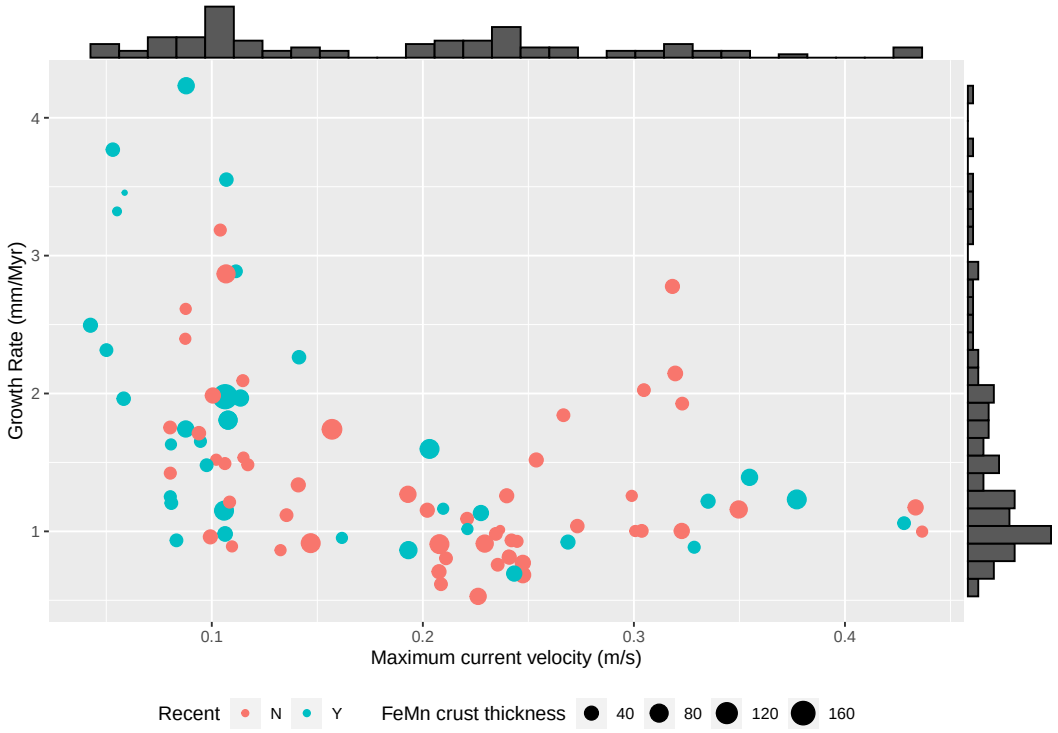

FIGURE 5.10: Relationship between growth rate and maximum current velocities of FeMn crusts (R^2 = -44%, $p<0.05$). The colour denotes the preservation state of the recent surface (blue is preserved, red is not preserved) while the points are scaled in size relative to the measured FeMn crust thickness. The outer bar charts show the relative density distribution.

The relationships between growth rate, detrital fluxes, water depth and maximum current velocities supports the following mechanism of control on growth rates. As increased detrital fluxes are associated with higher growth rates, the flux of detrital material to crusts is dependent on the deposition of sediment for sufficient periods that it can be incorporated into FeMn crusts. The micro-topographies of botryoidal surface textures of FeMn crusts have been suggested by Yeo et al. (2018a) to support the trapping of interstitial detrital material observed in Tropic FeMn crusts. Furthermore, the movement of sediment grains requires a threshold motion and in deep waters the boundary layer where frictional forces are active can exist in a narrow band near the seabed (Soulsby, 1983). This could suggest that at the low current speeds observed in some areas of Tropic Seamount, more detrital material may be incorporated into FeMn crust growth and potentially lead to the high growth rates observed for some of these samples. In contrast, from observations between lower growth rates and eroded surfaces at water depths above 2000 m, this could suggest that in some regions the deposition of detrital material is hindered, to the point at which FeMn material is removed.

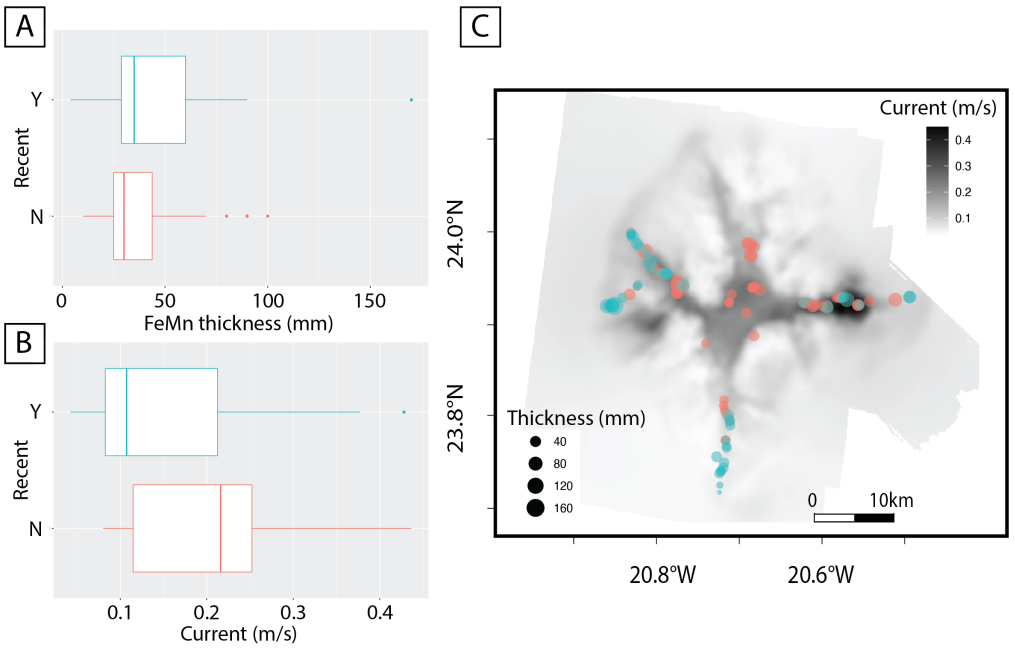

FIGURE 5.11: Relationships between preservation of recent growth surfaces with (A) FeMn crust thickness (B) Maximum current velocities and (C) with position on Tropic Seamount. The boxplots of (A) and (B) show preserved recent surfaces in blue and eroded in red, with box plots with the median marked as a solid line and extending to the 25% and 75% quantiles.

5.7.2 Controls on FeMn crust preservation

The thickness of FeMn crust reflects the balance between accumulation, of hydrogenetic growth at Tropic Seamount, and removal processes such as erosion. Mapping FeMn crust surface erosion at Tropic Seamount showed trends in the distribution of erosional surfaces with location around the seamount structure. Overall, FeMn crusts analysed from water depths shallower than 2000 m dominantly showed erosive surfaces, including all samples from the summit region. Erosion of the seabed requires the abrasive action of sediment grains that are entrained and carried by moving water masses (e.g. Kamphuis, 1990; Thompson and Amos, 2004). When the erosive state of FeMn crust surfaces is compared to the maximum current velocities extracted from the corresponding sample location, samples with preserved recent growth surfaces experience median current speeds of 0.15 m/s and a range between 0.04 – 0.43 m/s. Samples with eroded upper surfaces show higher median flow speeds of 0.21 m/s and a range between 0.08 – 0.44 m/s. Overall, recent preserved surfaces experience lower current speeds but there is significant overlap in the range (Figure 5.11) that suggests that there is complexity in the relationship between erosive state and current speeds at Tropic Seamount that is not fully captured by a direct comparison. This matches observations of limited direct relationship between FeMn growth rates and maximum current velocities (Figure 5.10).

Thompson and Amos (2004) found that during flume experiments, erosion rates increased as sand transport increased. The overlap between preservation state of FeMn crust surfaces and maximum current velocities is likely due to the number of other variables that will add complexity to modelling shear stresses at the seabed other than flow velocity. This could include variations in the mechanical resistance of the FeMn crusts. The SEM-EDS imagery of FeMn crusts showed significant textural variation through growth horizons, from dendritic growth and massive laminations to chaotic, detrital-rich horizons. It is likely that these textural differences will be associated with corresponding variations in mechanical properties that will affect resistance to abrasion. Furthermore, given the relationship between suspended material and erosional strength (e.g. Thompson and Amos, 2004), the availability of local sources of bedload will likely affect patterns of erosion. In turn, the local scale topography likely affects the distribution patterns of sediment (e.g. Palomino et al., 2016) and generate complex local-scale current interactions that may also affect erosion patterns. The majority of eroded samples were observed at or near the summit of Tropic Seamount, where detailed outcrop mapping from ROV imagery and sidescan sonar data showed significant regions of sand plains (Yeo et al., 2019) that could provide a local sediment source for abrasion. While current speeds alone appear to be a weak metric to determine erosion extent, the similarities in observed thickness between eroded and preserved surfaces (Figure 5.11) could imply that active erosional processes may not be fully capturing the role of erosive patterns through time. Josso et al. (2020a) noted high variability of growth rates in a FeMn crust from Tropic Seamount's summit region that varied from 1 – 24 mm/Ma, with growth rate varying through different periods of FeMn crust formation. It is likely that over the extended periods of FeMn crust formation, there have been variations in hydrography such as the opening and closure of oceanographic gateways and glaciations (e.g. Josso et al., 2020a, 2021). While that may mean that direct relationships derived from recent observations are complex, it should be noted that the scale of these changes may be associated with more coherent changes across Tropic Seamount rather than the local scale variation observed in this study. Changes in factors such as sediment flux, seamount water depth as it subsided from shallow water environments through time (e.g. Palomino et al., 2016; Josso et al., 2020b) and seamount morphology have likely all played an integral role in determining the erosive patterns, and in turn FeMn crust thickness, at Tropic Seamount during the history of FeMn crust deposition.

5.8 Conclusions

Ferromanganese crusts from Tropic Seamount are characterised by hydrogenetic growth, with significant enrichments, with average Co concentrations of 0.5 wt% and Te concentrations of 48 ppm. While elemental concentrations are promising from a resource perspective, there was significant variability in the thickness of FeMn crust collected across

the seamount structure. Estimations of growth rate from Co-chronometry showed average growth rates of between 1.52 to 5.84 mm/Myr. Observations from SEM-EDS and relationships between growth rates and geochemical detrital proxies were compared with environmental factors including water depth and current velocities and show that detrital inputs play an important role in crust accumulation but can also lead to the dilution of elements of economic interest. The preservation state of the upper surface of FeMn crusts may be an important indicator of regions that have been swept free of detrital material. While this is associated with removal of material, the overall effect of minimising dilution of hydrogenetic phases by detritus and maintaining an exposed surface may promote dominantly hydrogenetic growth and therefore have a positive effect on resource grades. At Tropic Seamount, the most prospective regions are observed at the seamount summit, corresponding to areas that are likely to be the most technically feasible to exploit.

Chapter 6

Seamount-scale controls on FeMn crust composition, NE Atlantic

For elemental analyses the methodology described in this section describes reagent ratios only, due to the different sample weights and digestion schemes used between laboratories. For further information on the exact reagent volumes used please refer to Section 3.3.1. Lead LA ICP-MS analyses were conducted by Dr Horstwood and Dr Josso at Environmental Science Centre, British Geological Survey following successful application to NERC Isotope Geosciences Facilities Steering Committee for a collaborative study (IP-1860-118).

6.1 Abstract

This study provides the first detailed investigation into the systematic variation in FeMn crust composition at the local scale of an individual seamount in the Atlantic Ocean. Element concentrations of 121 upper and lower surface scrapes (<1 mm) from a range of depths and local environments and 26 drill core subsamples were analysed and quantitative statistical methods used to understand the key drivers of compositional variance in FeMn crusts. Compositional variance was correlated against a range of environmental parameters, including water depth, dissolved oxygen concentration in seawater, slope angle and maximum current velocities, to assess the potential role of both oceanographic and topographic parameters on FeMn crust chemistry.

For all samples, the variations in the composition of the main constituents of FeMn crusts (Fe oxyhydroxides and Mn oxides) exerted the strongest controls on chemistry, with the Fe oxyhydroxide phase dominating the variance signatures. Upper and lower FeMn crust surfaces showed differences in the factors driving compositional differences, particularly in REY behaviours, with lower surface mineralogy likely influenced

by burial and increased susceptibility to replacement by CFA phases. When compared to oceanographic parameters, Fe concentrations of upper surface scrapes, as well as Co and Te, were observed to decrease with increasing water depth and dissolved oxygen, with highest concentrations observed at Tropic Seamount's summit at 1000 m.

The increase in Mn/Fe with increasing water depth is the opposite to observations made in the Pacific Ocean. This has been attributed to patterns in the dissolved metal contents of the overlying water column which are influenced by inputs from Saharan dust and biogenic remineralisation at depth. At the local summit scale, topographic parameters such as slope and maximum current velocities show negative correlations with detrital phases such as Al. The correlation of Fe oxyhydroxide phases and Mn oxides with some topographic factors likely represent the role of topography on controlling local patterns of detrital accumulation, which in turn can lead to different levels of dilution of hydrogenetic phases.

6.2 Introduction

Ferromanganese (FeMn) crusts have been observed in all ocean basins, commonly encrusting seamount, ridge and plateau substrates in water depths between 400 to 7000 m (Hein and Koschinsky, 2014; Lusty et al., 2018). Ferromanganese crusts show significant enrichment in a range of trace elements, with accumulation attributed to sorption and coprecipitation processes (Koschinsky and Halbach, 1995; Koschinsky et al., 2003; Hein and Koschinsky, 2014). Three main genetic endmembers, with characteristic chemical compositions, are commonly used to classify FeMn crusts; hydrogenetic growth, from the precipitation of Mn and Fe oxyhydroxide colloids from seawater; hydrothermal growth, that precipitates from hydrothermal fluids; and diagenetic growth, precipitated from interstitial pore fluids (e.g. Bau et al., 2014). A simple chemical colloid model is widely used to described the first-order mode of formation and metal enrichment for hydrogenetic FeMn crusts (Koschinsky and Halbach, 1995). In seawater, positive ions are sorbed onto negatively charged dissolved Mn oxides and negative and neutral ions onto weakly positively charged Fe oxyhydroxides. Precipitation of these colloid complexes can be triggered by changes in oxidation state. The Oxygen Minimum Zone (OMZ) is thought to play an important role in FeMn crust formation, by providing a reduced reservoir that supports the accumulation of dissolved Mn and Fe colloid species (Koschinsky and Halbach, 1995). Subsequent oxidation of these species, such as through mixing with oxygenated bottom-waters due to upwelling at seafloor obstructions, can trigger the precipitation of FeMn crusts (Koschinsky and Halbach, 1995).

Other processes, such as surface oxidation, can lead to the significant enrichment of elements such as Co, Te, Ce and Tl over time (e.g. Koschinsky and Halbach, 1995; Koschinsky and Hein, 2003). Hydrothermal FeMn crusts can form in a wide range of settings, from hydrothermal vent plume fall-out to more diffuse hydrothermal circulation (e.g. German et al., 2002; Hein et al., 2008), where reduced hydrothermal fluids precipitate upon mixing with colder, oxygenated seawater and sorb dissolved trace metals. They precipitate rapidly, with growth rates of up to 10^5 mm/Myr, in comparison to hydrogenetic crusts that grow 1 – 5 mm per million years (Hein et al., 2008, 2010; Hein and Koschinsky, 2014). Diagenetic FeMn crusts precipitate due to the oxidation of reduced pore fluids, from the decay of accumulated organic matter, within the sediment column. The diagenesis can be oxic or sub-oxic, depending on the concentration of dissolved oxygen within the surrounding sediment (Hein and Koschinsky, 2014; Wegorzewski and Kuhn, 2014). This mode of formation is commonly associated with FeMn nodules.

Ferromanganese crusts vary significantly in their composition across a range of scales, both spatially and temporally. This is because FeMn crusts composition reflects the environment and mode of formation. The variation in composition of FeMn crusts through time has been suggested to be affected by changes in a range of factors affected by the geological setting, from changing seawater conditions during growth to varying fluxes of hydrogenetic, diagenetic, hydrothermal, detrital and biogenic material (e.g. Hein et al., 1992). To better understand the role of formation history and environment for the FeMn crusts in this study, the geochemistry of the rare earth elements and yttrium (REY) has been investigated alongside major and trace element chemistry. Seawater has very low concentrations of REY, between 10^{-13} to 10^{-10} mol/kg, which has been attributed to the limited REY inputs into the oceans and short residence times (Elderfield, 1982; Zhang and Nozaki, 1996). The REY in FeMn crusts are significantly enriched over seawater concentrations on the order of 10^8 and generally show similar geochemical behaviour between them except for Ce and Y (Hein and Koschinsky, 2014). The distinct characteristics of REY composition can provide indicators of the mode of FeMn crust formation. The patterns of trivalent REY in FeMn crusts is driven by the exchange equilibrium between the dissolved REY complexes in seawater (mostly in the form of carbonate complexes) and the surface REY complexes on FeMn crusts (Bau et al., 1996; Bau, 1999). Positive Ce anomalies are observed for slow-growing hydrogenetic FeMn crusts due to partial surface oxidation over long time periods of Ce after Ce(III) surface complexation (Bau and Koschinsky, 2009). In contrast, hydrothermal crusts display negative Ce anomalies that reflect rapid precipitation and preservation of seawater Ce-characteristics (e.g. Kuhn et al., 1998; Bau et al., 2014). Yttrium anomalies are described by comparing Y with its geochemical twin, Ho, due to their similar ionic charges, radii, electrochemical behaviours and seawater concentrations but divergent behaviours in FeMn crusts (e.g. Bau et al., 1996). This is attributed to differences in the relative stabilities of the surface complexes that form (Bau et al., 1996).

Pacific Ocean FeMn crusts have been studied extensively, particularly from a region called the Prime Crust Zone in the NW Pacific where crusts are suggested to have the greatest economic potential (Hein et al., 2009b). Ferromanganese crust occurrence have been observed throughout the Atlantic, Indian and Arctic ocean basins (e.g. Baturin et al., 2014; Koschinsky and Halbach, 1995; Muinos et al., 2013; Marino et al., 2017; Rajani et al., 2005; Banakar et al., 1997; Hein et al., 2016) but fewer studies have been conducted to date as these basins are proposed to have lower overall economic potential, as they have fewer seamounts and ridges and greater detrital inputs than the Pacific Ocean (e.g. Hein et al., 2013; Hein and Koschinsky, 2014).

There have also been limited studies of the compositional variation of FeMn crusts at the spatial scale of an individual seamount or ridge, with systematic sampling limited by the historic use of dredging (Glasby et al., 2000). The use of remotely operated underwater vehicles (ROVs) facilitate high-resolution and well spatially constrained sampling campaigns but so far investigations of compositional variations of FeMn crusts at this scale has been limited to one seamount in the Pacific Ocean and one in the Atlantic Ocean (Usui et al., 2017; Yeo et al., 2018a). The characterisation of FeMn crusts at the local to outcrop scale is vital to improving understanding of the controls on FeMn crust formation and composition (Hein et al., 2000; Glasby et al., 2007).

In order to better understand the role of spatial environmental controls on FeMn crust formation, FeMn crust samples that formed at the same time periods should be compared to avoid the impact of temporal variability in growth environment. Accurate age modelling of FeMn crusts remains analytically challenging, as their slow growth rates limits the resolution of subsampling by conventional micro-drilling and absolute dating methods using Be-isotopes are limited up to 10 Myr (Claude et al., 2005). For samples older than this, techniques applied for age estimates include extrapolation methods or comparative stratigraphic methods, such as cobalt-chronology, magnetostratigraphy, Os-isotopes as well as biostratigraphy (Manheim and Lanebostwick, 1988; Puteanus and Halbach, 1988; Joshima and Usui, 1998; Oda et al., 2011; Cowen et al., 1993; Noguchi et al., 2017).

Josso et al. (2019) showed the strength in using composite modelling techniques that combine multiple independent age proxies with absolute dating methods to construct robust age models for FeMn crusts. Having a fully characterised age model for FeMn crusts from a target site provides the potential to build a reference age model that allows a relative chronostratigraphy to be built for other FeMn crusts, using more rapid and less intensive data collection techniques. In particular, Josso et al. (2020a,b) showed the strength of using age-correlated Pb isotope laser ablation multicollector inductively coupled plasma mass spectrometry (LA MC ICP-MS) to rapidly produce datasets at high spatial resolutions that allow for the precise correlation of multiple FeMn crusts using chronostratigraphic techniques. To minimise the potential effects of changing environmental conditions over time, this study investigates the composition of growth

horizons that formed at the same time. This includes the uppermost recent FeMn crust growth surfaces as well as target contemporaneous horizons identified using Pb-isotope chronostratigraphy. This study investigates the key environmental drivers of compositional variance in FeMn crusts using statistical analyses to examine variance at a detailed, seamount-scale spatial resolution that has not yet been described in the Atlantic Ocean.

6.3 Materials and methods

6.3.1 Geological Setting and Data Collection

The study area is located in the NE Atlantic Ocean within the Saharan Seamount chain, 450 km from the coast of West Africa and to the south of the Canary Island Seamount Province (Figure 6.1). Tropic Seamount is a flat-topped, star-shaped guyot covering a surface area of 1530 km^2 that sits on Late Cretaceous oceanic crust, with a current summit depth of 1000 m and a base at 4000 m water depths (Figure 6.2; Van Den Bogaard, 2013; Marino et al., 2017). The seamount structure comprises of volcanic substrates, with volcanism extending from 119 Ma to 114 Ma with potential later eruptions until 60 Ma, as well as carbonates dated to 84 ± 4 Ma and episodes of phosphatisation (Van Den Bogaard, 2013; Josso et al., 2019). Modern circulation in this region is dominated by the North Atlantic Central Water (NACW) at intermediate depths, overlying South Atlantic Central water (SACW) at 700m and Antarctic Intermediate Water (AAIW) at 1000m (Muinos et al., 2008; Marino et al., 2017). Deep waters that flow from south to north are the Eastern North Atlantic Deep Water (ENADW) below 1500 m and Antarctic Bottom Waters (AABW) at 4000 m (Muinos et al., 2008; Marino et al., 2017). There is evidence of FeMn crust growth at Tropic Seamount from 77 – 73 Ma onwards (Josso et al., 2019). Data and samples used within this study were collected during research expedition JC142 from 29th October to 8th December 2016 on board the RRS James Cook as part of the MarineE-tech project (UK's Natural Environmental Research Council SoS Minerals research program). Samples were collected to high spatial accuracy using a remotely operated vehicle, the ROV ISIS 6500, operated by the National Oceanography Centre Southampton (NOCS), UK. Grab samples were collected using the ROV Isis manipulator arms and drill-core samples were collected using an ROV-mounted rock drill designed to recover cores up to 280 mm in length and 50 mm in diameter (Murton and scientific party, 2016). Full details of samples analysed in this study are available in Appendix C.1 and Appendix C.2.

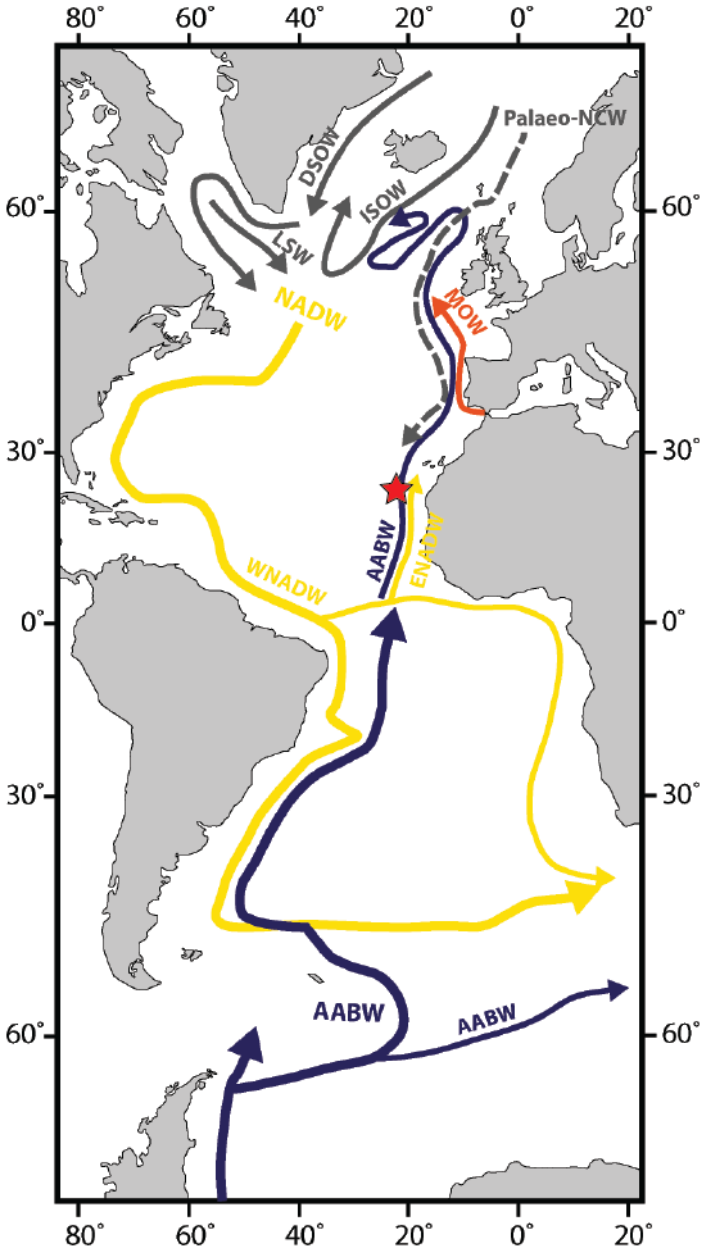

FIGURE 6.1: Schematic showing simplified modern oceanographic circulation in the Atlantic Ocean of the main intermediate and deep water masses: Denmark Strait Overflow Water – DSOW; Iceland Scotland Overflow Water – ISOW; Labrador Sea Water – LSW; North Atlantic Deep Water – NADW; Antarctic Bottom Water – AABW; Mediterranean Overflow Waters – MOW; Northern Component Waters – NCW. Based on Muinos et al (2008) and Marino et al. (2017).

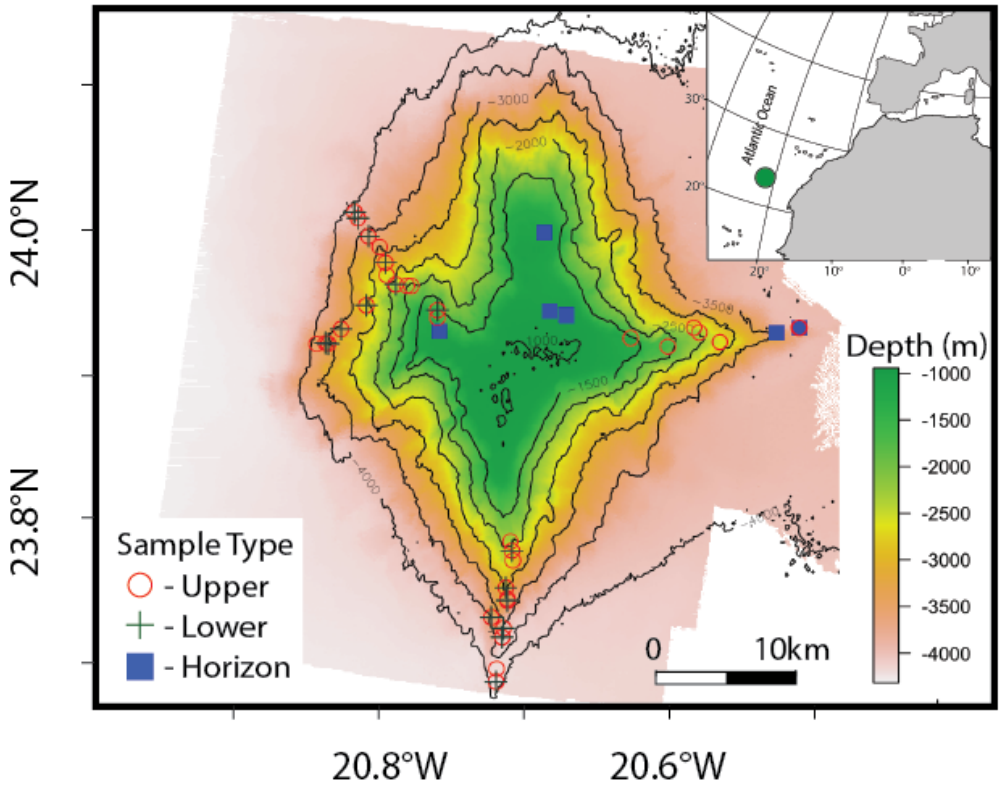

FIGURE 6.2: Main figure shows a bathymetric map of Tropic Seamount and samples analysed in this study, with data collected during research expedition JC142, and an inset showing the location of Tropic Seamount (Murton and scientific party, 2016). Bathymetry from EM120 ship-based sonar data gridded at 50 m, with contours at 500 m water depth intervals. ROV samples analysed in this study include upper (red circles) and lower (green crosses) surface scrape samples and detailed horizon samples (blue squares).

6.3.2 Surface Scrape Materials

Ferromanganese crust surface scrapes (n = 121) were subsampled from 100 FeMn crusts collected using the ROV Isis manipulator arms across a range of water depths (994 – 3894 m) and seamount environments (Figure 6.2). Both the uppermost (exposed to the overlying water column) and lowermost surfaces (facing the sediment surface) were sampled for FeMn crusts where the in-situ orientation could be clearly determined from seafloor imagery. The surface texture of samples was noted according to whether the most recent growth surface was preserved. A ceramic blade was used to remove 1 g of material from the outer 1 mm of the FeMn crust surface. This material was oven dried at 60 °C for 24 hours and homogenized using an agate pestle and mortar prior to elemental analysis. While the precise age of this surface scrape material has not been determined, Josso et al. (2019) recorded distinct Pliocene growth in the upper portions of a dated core sample from Tropic Seamount, with evidence of FeMn crust deposition after an erosional episode at 2.5 ± 1.9 Ma. Given the very slow growth

rates of FeMn crusts, it is assumed that the maximum possible age of the recent growth surfaces sampled is 2.5 ± 1.9 Ma as the dated erosional horizon as this was observed >1 mm from the uppermost surface of the dated core (Josso et al., 2019). Average growth rates at Tropic Seamount were estimated to be between 1 – 24 mm/Myr and an average of 3 - 4 mm/Myr (Koschinsky et al., 1996; Josso et al., 2019). Therefore, due to sampling resolution, the age of formation for the surface scrape samples likely ranges from recent to 1 Mya or up to 2.5 ± 1.9 Ma if faster growth rates are assumed. Manual subsampling methods of FeMn crusts is limited to age resolutions of 500 kyr – 1 Myr and therefore discussions of trends are made in the context of the averaged effect of any changes during this time period, including changes in palaeoceanography and detrital flux input. This study aims to minimise the effect of changing conditions over time by limiting subsampling to a narrow potential age range so that the locational controls can be compared and so the role of paleoceanographic changes on FeMn crust composition are beyond the scope of this study.

6.3.3 Targeting growth horizons for elemental analysis

Six drill-cores and two ROV grab samples were selected for subsampling to investigate the variability in contemporaneous horizon chemistry around Tropic Seamount (Figure 6.2). The drill-core samples were collected across different regions of the seamount summit, at water depths between 1012 – 1028 m, and two grab samples were collected from the seamount flanks at 3595 m and 3872 m. To identify horizons for subsampling, Pb LA MC ICP-MS was used to identify target horizons, as detailed below.

Josso et al. (2019) built a detailed age model for a Tropic Seamount FeMn crust drill-core (JC142_085_004) that has been used alongside Pb LA MC ICP-MS profiles as the reference for relative chronostratigraphic modelling in this study. The age model used cross-validated U-Pb LA MC ICP-MS and absolute dating of the carbonate substrate alongside Co-chronometry and Os isotope age proxies to calibrate a Bayesian statistical model of Markov Chain Monte Carlo (MCMC) that related depth through the FeMn crust drill-core sample with age, spanning the last 75 ± 2 Ma (Josso et al., 2019). Lead LA MC ICP-MS isotopic data, validated with solution Pb isotope data, for dated sample JC142_085_004 (Josso et al., 2019, 2020a) was used in this study for referencing. Excursions in Pb LA MC ICP-MS isotopic ratios for Tropic FeMn crust samples were correlated to this reference profile to give relative formation ages and to target contemporaneous growth horizons for geochemical analysis. Lead LA MC ICP-MS analyses were carried out at the Environmental Science Centre, British Geological Survey following Bauer and Horstwood (2018) and Josso et al. (2020a). Sample analyses were conducted using Elemental Scientific Lasers NWR193UC LA system with TV2 two volume ablation cell coupled to a ThermoScientific Neptune Plus MC ICP-MS. Sample sections were analysed using a rectangular 15x150 µm ablation spot at 10 µm/s above

the sample surface, on a continuous time-resolved basis. Lead isotope ratios were measured every 0.265 s and normalised using standard sample bracketing against NodA-1, Nod-P1, JMn-1 and an in-house reference material, with further processing using Iolite (v3.65) data reduction software (Paton et al., 2011) (the full analytical results are available in Appendix C.6). Five target horizons were identified and chosen as key target horizons due to their distinguishable excursions that could be traced across more than one of the eight drill-core samples (Figure 6.3). Multiple distinct target horizons were identified from the Pb LA MC ICP-MS profiles for each sample, but due to differences in FeMn crust growth rates some samples had compressed sections. As physical sub-sampling is limited by the diameter of the micro-drill (0.6 mm), for samples with compressed sections the most distinct horizons were selected. A total of 26 horizons were subsampled using a 500 μm micro-drill to extract 5 – 10 mg of material.

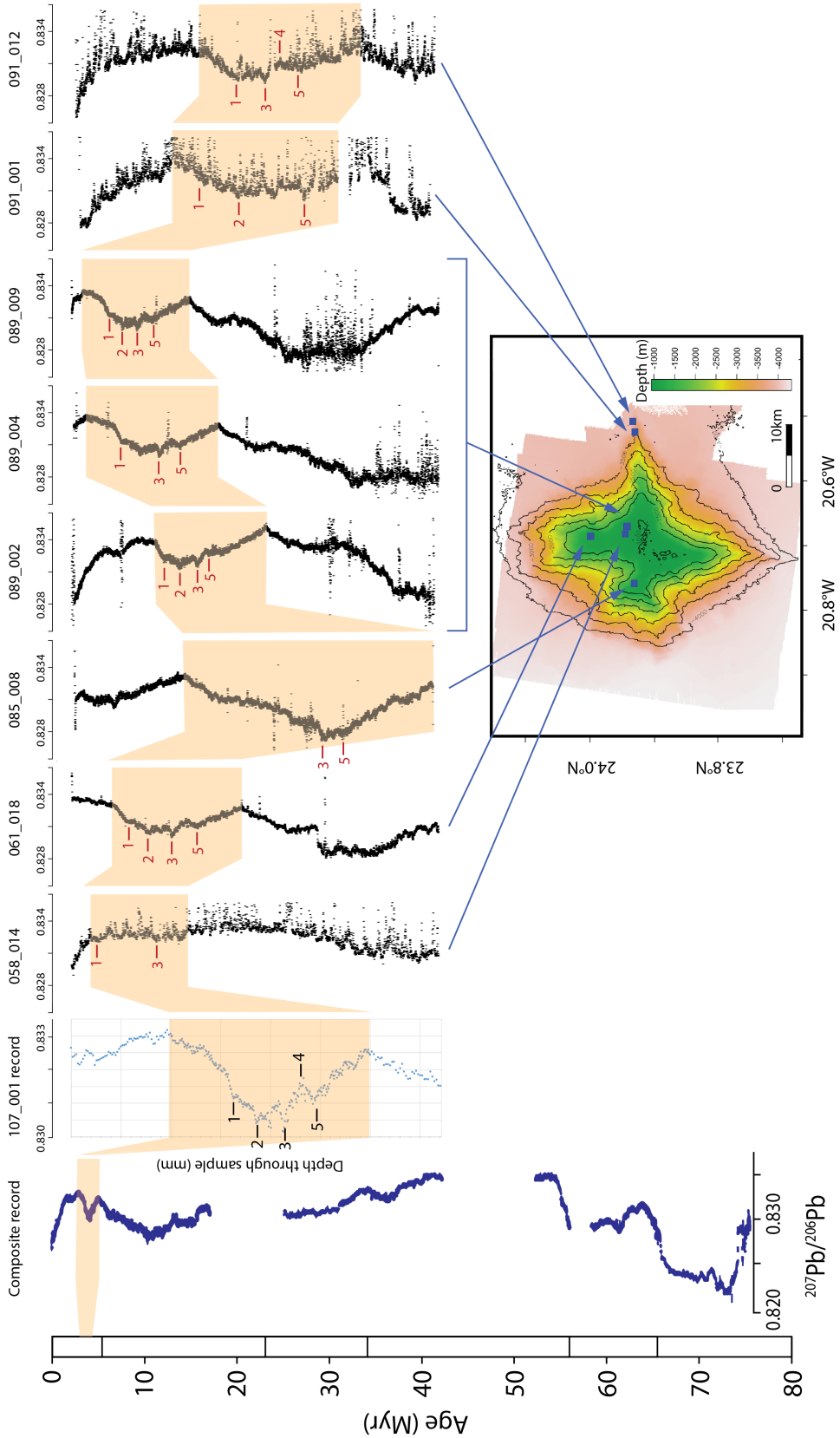

FIGURE 6.3: Correlated Pb LA MC ICP-MS profiles used to select target horizon subsamples. The composite Pb LA MC ICP-MS stratigraphy and 107_001 reference record used for relative stratigraphic correlation were determined by Josso et al. (2019, 2020a). The location of each sample is noted on the inset map and target horizons that were analysed in this study, identified by correlating distinct $^{207}Pb/^{206}Pb$ excursions, are labelled 1 to 5 in red.

6.3.4 Elemental analysis

Surface scrape analyses were carried out at the British Geological Survey Keyworth. De-ionized, 18 MΩ-grade water from a Millipore system (MQ water) was used for rinsing and dilution. All acids were distilled in quartz or Teflon sub-boiling distillation systems and all Savillex Teflon was acid cleaned. Sample powders were pre-digested using a 3:2:1 ratio of 5% nitric (HNO_3), hydrochloric (HCl) and HNO_3. This solution was evaporated at 80 °C for 14 hours and then allowed to cool. An acid digestion mixture of 1:3:7 of perchloric ($HClO_4$), hydrofluoric (HF) and HNO_3 acids was then added and evaporated using a heating scheme of increasing temperatures from 80 °C to 160 °C over an 18-hour period. When dry, the samples were cooled to 50 °C and 1:1 HNO_3:HCl mixture was added and heated for 30 minutes. After cooling to 30 °C a 4:1 mixture of MQ water and hydrogen peroxide (H_2O_2) was added and heated at 30 °C for 15 minutes. Finally, the mixture was diluted to a final acid concentration of 5% with MQ water.

Measurements were conducted using a Agilent 8900 Triple Quadrupole Inductively Couple Plasma Mass Spectrometer (ICP-QQQ), which facilitates Te measurement due to improved sensitivities and lower detection limits. The data reduction process corrects for the machine run blank values, interferences (if not removed by different gas modes then through the analysis of single element solutions e.g. LREE oxides on HREE), reagent blanks, dilution and digestion blanks to give solid sample concentrations. Reagent blank values from both runs were used to determine machine detection limits, as the 3SD values for 8 blank measurements. Three different internal standard solutions, selected for different elemental contents, were run at regular intervals to monitor instrumental drift and sample duplicates were run every 15 samples. Accuracy against two FeMn nodule reference materials; NOD-A1 and NOD-P1 (Flanagan and Gottfried, 1980). Replicate measurements of standards were run alongside an in-house reference material (HRM, sample JC142_112_003) which is currently being developed to facilitate crust studies. After correction for instrumental drift, blank values and dilution weights, the replicate measurements of internal standard solutions gave precisions of $\leq$5% relative standard deviation (RSD) for P, S, K, Ca, Ti, V, Cr, Co, Ni, Cu, Zn, Ge, Se, Rb, Zr, Nb, Ag, Cd, In, Sn, Sb, Te, Cs, Ba, the REEs, Hf, Ta, W, Tl, Pb, Th and U. Precisions of $\leq$10% RSD were measured for Li, Be, Na, Mg, Al, Mn, Fe, As, Y, Sr, and Mo. Measured values for the three reference materials shows good correlation with reported values for most of the measured elements, except for Ge, Se, Ag, In, Sn and Tb which are therefore excluded from the data analysis.

Trace elemental analysis of subsampled FeMn crust horizons for comparative chemostratigraphy was conducted at the University of Southampton (NOCS). Samples powders were pre-digested in aqua regia for 12 hours before evaporating to dry at 80 °C. Once cooled, a 1:3 mixture of HNO_3 and HF were added before samples were heated at

130 °C for 12 hours and then evaporated to dry using a scheme of temperatures increasing from 130 °C to 180 °C. Once cooled, 6 M HCl was added and samples fluxed at 130 °C for 12 hours, then dried. Once dry, 6 M HCl was again added, fluxed at 130 °C for 12 hours and then samples were cooled and made up to a 3 M HCl solution with MQ water. For ICP-MS analyses, samples were dried and made up to a running solution of 3% HNO_3 with an internal spike of 20 ppm Be and 5 ppm Re and In. Elemental concentrations were determined using a Thermo Scientific X-Series III ICP-MS, with runs calibrated against six certified rock standard reference materials. Internal standard solutions (Be, Re and In) were run at regular intervals (every 10 samples) to monitor instrumental drift and sample duplicates were run every 15 samples and reagent blanks were used to determine detection limits. Accuracy was assessed against multiple analyses of NodA-1 and NodP-1 reference materials. Internal sample precision was $\leq$5% RSD for Ca, To, V, Mn, Fe, Co, Ni, Zn, Sr, Y, Ba, La, Ce, Pr, Nd, W, Pb. T, U, Cu, Zr, Nb, Mo and REE. Precisions of $\leq$10% RSD were measured for Sn and the REE and $>$10% for Li, Sc, Cr, Rb, Cs. Measured values showed lower correlations with reported values for NodA-1 and NodP-1. This is likely due to the much smaller sample weights analysed for subsampled horizons and these reference materials (5 – 10 mg) and reported heterogeneities in reference materials potentially related to poor homogenisation processes (e.g. Josso et al., 2021). Hence, elemental concentrations for horizon data in this study are limited to discussions of relative changes between horizon subsamples and not for absolute comparison to other samples or crust studies.

6.3.5 Statistical Correlation and Factor Analysis of FeMn crust Composition

To facilitate data interrogation, surface scrape analyses were subset into different groups to investigate correlation and factor analyses. Samples with preserved recent growth surfaces were targeted (n = 56), as they are likely to most accurately reflect FeMn crust growth in environmental conditions comparable to current conditions, and are used to understand seamount-scale processes driving compositional variance in FeMn crusts. These recent growth samples were also subset into upper (n = 37) and lower (n = 19) surfaces to investigate the variance between exposed and buried FeMn crust composition. In order to investigate the drivers of compositional variability without depth-driver effects, statistical analyses were also conducted for horizon drill-core samples collected from the seamount summit (n = 19) that occur within a narrow depth band (1012 – 1028 m).

To assess statistically significant variance in FeMn crust composition, in terms of elemental correlations and variations with environmental factors, correlation matrices and factor analyses were generated in R using the “caret”, “corrplot”, “Hmisc”, “factoextra”, and “psych” packages (Kuhn, 2020; Wei et al., 2017; Kassambara and Mundt,

2020; Revelle, 2020). Pearson correlation coefficient matrices were generated from normalised (centred and scaled) geochemical data and environmental data. All correlations discussed in this study are statistically significant with a confidence level of 95% or greater. Q-mode factor analyses of trace element data were conducted on normalised data to give equal weighting to different magnitudes of scale. Factors were derived from Varimax-rotated orthogonal principal factors (Kaiser, 1958), with the appropriate number of factors to retain determined from scree plots of eigenvalues.

6.3.6 Environmental variables

Bathymetric data used within this study was collected across the whole seamount using the shipboard Konsberg EM120 (12kHz) multibeam echosounder system. Data was processed using Caris Hips and Sips and QPS Fledermaus (Murton and scientific party, 2016; Yeo et al., 2018b), with a 50 m grid spacing. This bathymetric data was used to investigate trends in surface scrape composition given the coverage of this dataset across the whole seamount. High-resolution bathymetry was collected at summit regions using a Konsberg EM2040 multibeam echosounder (200 kHz) mounted on the autonomous underwater vehicle (AUV) AutoSub600, operated by NOCS, UK. This data was processed and navigation corrected using MB-System, with a final grid resolutions of 5 m (Murton and scientific party, 2016; Yeo et al., 2018b). Given the limited extent of this high-resolution bathymetry, this was used to investigate trends in the targeted drill-core horizon samples from the summit. Secondary terrain derivatives were generated from bathymetric data using Benthic Terrain Modeller tool (Walbridge et al., 2018) in ArcGIS 10.7.1. These included Aspect (eastness and northness), Bathymetric Position Index (BPI, fine and broad scale), slope and terrain ruggedness. These were used to provide quantitative seafloor descriptor variables to assess potential relationships between primary and secondary bathymetric effects and FeMn crust composition. A current model describing the maximum near-seabed (1 m above) current velocities for Tropic Seamount (Cooper and Spearman, 2017; Spearman et al., 2020; Murton et al., 2020) was resampled to a 50 m cell resolution and used to investigate trends with local current regimes. The values for all of the above variables were extracted from raster maps at the sample locations in R using the "sf" and "raster" packages (Pebesma, 2018; Hijmans, 2021). Sample water depths were determined from ROV Isis reported depths and were used to estimate dissolved oxygen values, by interpolation to the nearest 5 m value from a CTD profile of the full water column (Murton and scientific party, 2016).

6.4 Results

6.4.1 Chemical composition of FeMn surfaces

The FeMn crust surface scrape samples (n = 121) are Fe- and Mn- rich, composed of 10.6 – 29.1 wt% Fe and 7.1 – 25.7 wt% Mn and are characterised by high Mn/Fe ratios ranging from 0.59 – 1.63. All samples show high concentrations of elements of economic interest, including Co (2655 – 10730 ppm), Cu (144 – 2498 ppm), Zn (356 – 1208 ppm), Te (15.5 – 94.6 ppm) and REY (1879 – 4168 ppm). Full details of the chemical composition of the surface scrape samples are available in Appendix C.3. All samples display positive Ce anomalies varying between 1.2 – 5.1, with an average of value of 2.7. High variability across a large range of major and trace elements was observed across all surface scrape samples (Table 6.1). Of the major elements, P and Ca display the greatest variance, with RSD of 137% and 79% respectively. The main constituent elements of Fe and Mn also show significant variability, with RSDs of 16% and 17%.

TABLE 6.1: Statistics for all FeMn crust surface scrape samples

	Minimum	Maximum	Range	Mean	SD (%)	RSD (%)
wt%						
Fe	10.6	29.1	18.5	21.1	3.4	16
Mn	7.1	25.7	18.6	17.4	2.9	17
Al	0.6	3.4	2.8	1.5	0.5	35
Mg	1.0	2.8	1.7	1.5	0.4	24
Ca	1.7	19.2	17.5	4.4	3.5	79
Na	0.6	1.5	0.9	1.1	0.2	14
K	0.2	0.7	0.5	0.3	0.1	25
Ti	0.3	1.4	1.1	0.8	0.2	25
P	0.3	6.4	6.1	0.7	1.0	137
(ppm)						
Ag	0.00	0.16	0.17	0.03	0.03	111
Ba	590	3883	3293	1204	443	37
Be	3.78	16.23	12.45	9.01	2.60	29
Bi	7.1	50.2	43.1	18.5	6.5	35
Cd	2.07	14.01	11.95	4.45	2.44	55
Co	2655	10730	8075	5736	1482	26
Cr	4.1	49.2	45.1	18.9	9.4	50
Cs	0.04	1.72	1.68	0.30	0.23	76
Cu	144	2498	2354	593	457	77
Ga	0.00	20.24	25.49	2.00	3.86	193
Hf	0.03	20.19	20.16	2.61	4.34	166
Li	1	181	180	26	32	125

	Minimum	Maximum	Range	Mean	SD (%)	RSD (%)
Mo	124	697	574	354	89	25
Nb	16.5	264.2	247.7	46.7	37.6	81
Ni	1106	10676	9570	3336	1856	56
Pb	803	2932	2129	1737	583	34
Pt	0.057	0.980	0.923	0.199	0.128	65
Rb	2.5	23.5	21.0	6.9	3.3	47
S	1992	4912	2920	3186	551	17
Sb	12.8	173.6	160.8	35.0	20.3	58
Se	0.22	4.25	4.03	0.99	0.42	42
Sn	3.00	10.98	7.98	4.83	1.28	27
Sr	919	1923	1004	1434	217	15
Ta	0.00	5.23	5.29	0.49	1.01	206
Te	15.5	94.6	79.1	44.6	19.7	44
Th	28.3	130.3	102.0	66.9	19.0	28
Tl	26.8	261.7	234.8	99.0	40.7	41
U	7.25	18.49	11.23	13.54	2.39	18
V	563	1632	1069	1089	248	23
W	23.6	153.6	130.0	62.6	21.0	33
Zn	356	1208	853	618	162	26
Zr	0.5	1191.1	1190.6	129.2	221.8	172
La	154	1015	860	334	111	33
Ce	798	2596	1798	1655	321	19
Pr	34.2	167.8	133.7	74.9	22.3	30
Nd	144	728	584	310	95	31
Sm	31.1	131.7	100.7	65.2	18.6	28
Eu	7.56	33.05	25.48	15.28	4.31	28
Gd	35.6	169.6	134.0	68.0	20.0	29
Tb	5.22	23.98	18.76	9.79	2.77	28
Dy	29.6	162.6	133.0	57.7	17.0	30
Y	103	1296	1193	217	120	55
Ho	5.73	35.52	29.79	10.88	3.43	32
Er	15.6	106.6	91.0	30.0	10.0	33
Tm	2.17	14.55	12.38	4.15	1.34	32
Yb	13.5	90.4	76.9	25.6	8.2	32
Lu	2.07	14.26	12.19	3.85	1.27	33

The major element composition between upper and lower FeMn crust surface scrapes were largely comparable, with <0.3 wt% difference in mean concentrations for Al, Mg,

Ca, Na, K, Ti and P. On average, upper surfaces had higher mean Fe (+1.6 wt%) and lower mean Mn (-1.5 wt%). There was greater difference for trace metal concentrations between upper and lower surfaces, in particular for key metals of economic interest such as Co, Cu and Ni. While numerous trace elements showed differences in mean concentrations between upper and lower surfaces, these were all within the standard deviations measured for both surfaces.

When only recent growth surfaces are considered, the RSD of P and Ca reduce significantly (Tables 6.2 and 6.3). This suggests that the variation of these elements is strongly controlled by active depositional processes that display commonality across the sample sites and that the higher variance across the full sample suite is likely driven by sampling of different age horizons. While variance generally reduces across the other major and traces elements, significant variation is still observed including for Fe (up to 13% RSD) and Mn (up to 15% RSD). This variation is less likely to be attributed to changes in composition with time, given the recent nature of the sampled surfaces, and likely relates to environmental factors affecting composition.

TABLE 6.2: Statistics for all recent upper surface scrape samples (n=37)

	Minimum	Maximum	Range	Mean	SD (%)	RSD (%)
wt%						
Fe	16.8	27.8	11.0	21.5	2.6	12
Mn	12.4	21.9	9.5	17.3	2.4	14
Al	0.8	2.4	1.6	1.4	0.4	28
Mg	1.1	2.2	1.0	1.4	0.2	17
Ca	2.2	10.1	7.9	3.7	1.5	40
Na	0.9	1.5	0.6	1.2	0.1	12
K	0.3	0.5	0.3	0.4	0.1	19
Ti	0.5	1.4	0.9	0.8	0.2	21
P	0.4	0.7	0.4	0.5	0.1	18
(ppm)						
Ag	0.00	0.09	0.10	0.03	0.03	108
Ba	786	2722	1936	1128	449	40
Be	4.62	15.50	10.88	8.36	2.37	28
Bi	10.8	28.9	18.1	16.2	3.8	24
Cd	2.34	9.29	6.95	3.58	1.55	43
Co	2655	8664	6009	5510	1347	24
Cr	6.1	35.0	28.9	17.3	7.4	43
Cs	0.11	1.02	0.91	0.36	0.19	53
Cu	164	2285	2121	614	505	82
Ga	0.00	7.15	11.51	1.34	2.81	211
Hf	0.06	10.80	10.74	1.60	2.64	165
Li	1	90	89	17	21	122
Mo	239	697	458	352	89	25
Nb	17.6	98.9	81.3	36.1	18.0	50
Ni	1379	9018	7639	2993	1735	58
Pb	1033	2374	1341	1530	390	26
Pt	0.07	0.41	0.34	0.15	0.08	52
Rb	3.7	16	12.3	7.74	2.68	35
S	2265	3985	1720	3014	411	14
Sb	14.2	98.3	84.1	28.9	17.3	60
Se	0.23	1.66	1.43	1.06	0.31	29
Sn	3.00	7.44	4.44	4.31	1.03	24
Sr	1032	1863	831	1419	194	14
Ta	0	2.88	2.93	0.29	0.59	204
Te	15.8	68.0	52.2	35.2	13.3	38
Th	53.4	126.0	72.6	73.0	13.6	19
Tl	38.2	169.0	130.8	90.2	35.9	40

	Minimum	Maximum	Range	Mean	SD (%)	RSD (%)
U	9.92	17.8	7.88	13.31	2.03	15
V	623	1477	854	1069	214	20
W	36.1	154.0	117.9	59.7	22.8	38
Zn	428	967	539	584	145	25
Zr	4.1	622.0	617.9	82.7	143.9	174
La	187	501	314	337	81	24
Ce	1401	2587	1186	1719	240	14
Pr	43.9	114.0	70.1	78.0	18.3	23
Nd	176	481	305	322	77	24
Sm	37.2	99.3	62.1	68.0	15.8	23
Eu	9.06	23.00	13.94	15.78	3.53	22
Gd	39.1	101.0	61.9	69.4	15.8	23
Tb	5.64	14.50	8.86	9.94	2.25	23
Dy	32.4	83.3	50.9	57.3	12.9	22
Y	110	280	170	199	43	22
Ho	6.09	15.00	8.91	10.57	2.31	22
Er	16.3	40.5	24.2	28.7	6.2	22
Tm	2.32	5.43	3.11	3.93	0.83	21
Yb	14.7	33.1	18.4	24.1	4.8	20
Lu	2.35	4.91	2.56	3.58	0.68	19

TABLE 6.3: Statistics for all recent lower surface scrape samples (n=19)

	Minimum	Maximum	Range	Mean	SD (%)	RSD (%)
wt%						
Fe	14.0	23.5	9.5	19.9	2.6	13
Mn	15.6	25.7	10.1	18.9	2.8	15
Al	0.9	3.4	2.5	1.7	0.6	33
Mg	1.3	2.5	1.2	1.6	0.3	19
Ca	1.9	7.4	5.5	3.7	1.4	37
Na	1.0	1.5	0.4	1.2	0.1	10
K	0.2	0.7	0.4	0.4	0.1	26
Ti	0.6	1.4	0.8	0.9	0.2	23
P	0.3	0.6	0.3	0.5	0.1	17
(ppm)						
Ag	0.00	0.06	0.07	0.03	0.02	59
Ba	836	1588	752	1105	213	19
Be	5.60	11.50	5.90	7.98	1.58	20
Bi	7.1	19.8	12.7	14.4	3.6	25
Cd	2.70	14.00	11.30	5.25	2.80	53
Co	3626	10730	7104	5965	1780	30
Cr	4.1	20.3	16.3	12.7	5.6	44
Cs	0.08	0.80	0.72	0.32	0.18	57
Cu	183	2498	2315	887	655	74
Ga	0.00	13.80	19.05	2.42	3.96	163
Hf	0.06	11.70	11.64	2.67	4.30	161
Li	5	181	176	38	43	115
Mo	205	418	213	311	55	18
Nb	17.7	116.0	98.3	47.1	30.4	65
Ni	1659	10676	9017	4422	2690	61
Pb	926	2254	1328	1402	357	25
Pt	0.08	0.31	0.23	0.17	0.06	37
Rb	3.51	14.9	11.39	7.79	2.97	38
S	2193	3451	1258	2926	396	14
Sb	16.1	42.5	26.4	27.9	7.1	25
Se	0.22	4.25	4.03	1.19	0.79	67
Sn	3.05	7.17	4.12	4.50	1.00	22
Sr	925	1720	795	1342	242	18
Ta	0	3.04	3.1	0.48	0.88	181
Te	19.3	66.0	46.7	34.7	14.5	42
Th	47.2	130.0	82.8	72.9	20.3	28
Tl	64.6	262.0	197.4	123.3	47.1	38

	Minimum	Maximum	Range	Mean	SD (%)	RSD (%)
U	8.11	16.6	8.49	13.01	2.25	17
V	564	1232	668	943	198	21
W	31.6	79.0	47.4	51.6	12.5	24
Zn	485	1123	638	660	191	29
Zr	2.0	589.0	587.0	117.5	187.4	160
La	154	447	293	293	90	31
Ce	1269	2596	1327	1722	310	18
Pr	36.6	100.0	63.4	67.8	20.5	30
Nd	149	419	270	281	86	31
Sm	34.4	87.3	52.9	59.7	16.8	28
Eu	7.96	20.40	12.44	14.01	3.96	28
Gd	35.7	89.7	54.0	61.7	17.2	28
Tb	5.22	12.90	7.68	8.91	2.40	27
Dy	29.6	76.1	46.5	51.7	13.7	27
Yttrium	103	251	148	180	45	25
Ho	5.73	13.80	8.07	9.61	2.44	25
Er	15.6	38.5	22.9	26.3	6.6	25
Tm	2.17	5.47	3.30	3.66	0.90	25
Yb	13.5	33.5	20.0	22.7	5.4	24
Lu	2.07	5.08	3.01	3.42	0.77	22

6.4.2 Chemical composition of targeted FeMn crust horizon layers

Across the 26 subsampled horizons, overall compositions were comparable to surface scrape samples, with 14.4 – 21.7 wt% Fe and 10.8 – 17.8 wt% Mn (Table 6.4, full geochemical results available in Appendix C.4). Of the major elements analysed for the target horizons, Ca and Ti concentrations were generally lower, at 0.5 – 5.5 wt% and 0.3 – 0.6 wt% respectively. Significant variation was observed across all of the subsamples, with RSD of 9% for Fe, 13% for Mn, 75% for Ca and 12% for Ti. Summit samples show higher concentrations of Mn, Ca, Ti, Co, Ni, Mo, V, Cr, Sr, Zr, Nb, Zn, Ba, P, U, Ce, Lu, Hf and Y when compare to deep samples and lower concentrations of Fe, Cu, Zn, Li, Sc, Rb, Cs, Ta, W, Th, La, Pr, Nd, Sm, Eu, Gd, Tb, Dy, Ho, Er, Tm and Yb (Table 6.5 and 6.6). Significant variation in composition between summit samples, collected from a relatively narrow range of water depths (1014 – 1127 m), is also observed, suggesting that there are factors other than those that vary with water depth that are contributing to controls on FeMn crust geochemistry. The variability in composition between

horizons of different ages is comparable in size to that observed when comparing contemporaneous horizon composition and supports an environmental control on FeMn crust composition.

TABLE 6.4: Statistics for all horizon FeMn crust samples (n=26)

	Minimum	Maximum	Range	Mean	SD (%)	RSD (%)
wt%						
Fe	14.4	21.7	7.4	18.8	1.7	9
Mn	10.8	17.8	7.0	14.3	1.8	13
Ca	0.5	5.5	4.9	1.7	1.3	75
Ti	0.3	0.5	0.2	0.4	0.1	12
(ppm)						
Ba	895	1506	611	1161	170	15
Co	1523	6703	5180	4314	1496	35
Cr	11.24	42.55	31.31	25.29	8.07	32
Cs	0.07	0.45	0.38	0.20	0.11	54
Cu	162	709	547	311	158	51
Hf	6.27	9.27	3.00	7.47	1	10
Li	2	39	37	7	8	125
Mo	330	548	218	439	63	14
Nb	46.34	82.85	36.51	65.19	10.37	16
Ni	1301	3288	1987	1811	416	23
Pb	887	2676	1789	1775	508	29
Rb	1.58	9.18	7.60	4.60	2	46
Sc	7.83	15.36	7.53	11.29	1.71	15
Sm	29.57	78.59	49.02	55.75	12.34	22
Sn	0.06	1.57	1.52	0.46	0.39	85
Sr	824	1621	797	1226	213	17
Ta	1.34	2.66	1.32	1.78	0.32	18
Th	19.93	71.73	51.80	40.74	13	33
U	7.80	13.59	5.79	11.11	1.79	16
V	658.05	1117.83	459.78	877.54	129.63	15
W	126.67	379.03	252.36	191.03	55.20	29
Zn	10.74	292.70	281.96	150.10	82	55
Zr	294.83	444.96	150.13	377.90	36	10
La	177	396	218	289	48	17
Ce	1280	2107	827	1683	207	12
Pr	37.10	92.45	55.35	67.59	14.13	21
Nd	148	367	219	271	56	21
Sm	29.57	78.59	49.02	55.75	12.34	22

	Minimum	Maximum	Range	Mean	SD (%)	RSD (%)
Eu	6.95	18.26	11.31	13.19	2.85	22
Gd	31.03	75.51	44.48	55.82	10.73	19
Tb	4.83	11.76	6.93	8.66	1.65	19
Dy	27.96	62.93	34.97	48.50	8.00	16
Yttrium	104.43	196.26	91.82	166.17	22	13
Ho	5.78	11.63	5.85	9.44	1.34	14
Er	16.32	31.06	14.74	25.58	3.26	13
Tm	2.34	4.35	2.01	3.69	0.45	12
Yb	15.15	26.31	11.16	22.52	2.49	11
Lu	2.34	3.89	1.55	3.30	0.34	10

TABLE 6.5: Statistics for summit horizon FeMn crust samples (n=19)

	Minimum	Maximum	Range	Mean	SD (%)	RSD (%)
wt%						
Fe	14.4	21.5	7.1	18.6	1.8	10
Mn	11.8	17.8	6.0	15.0	1.5	10
Ca	0.8	5.5	4.6	2.0	1.4	67
Ti	0.3	0.5	0.2	0.5	0.1	11
(ppm)						
Ba	895	1506	611	1193	180	15
Co	1523	2643	1119	2116	411	19
Cr	12.14	42.55	30.40	27.18	7.50	28
Cs	0.07	0.31	0.24	0.15	0.06	42
Cu	162	508	347	245	89	37
Hf	6.27	8.87	2.60	7.53	1	9
Li	2	39	37	5	9	163
Mo	330	548	218	454	64	14
Nb	50.75	82.85	32.10	68.12	8.59	13
Ni	1413	3288	1875	1915	426	22
Pb	1488	2676	1187	2031	312	15
Rb	1.58	8.35	6.77	3.74	2	43
Sc	7.83	12.30	4.46	10.48	1.07	10
Sm	29.57	74.08	44.52	51.28	10.52	21
Sn	0.06	1.57	1.52	0.51	0.44	86
Sr	992	1621	630	1326	147	11
Ta	1.34	2.66	1.32	1.75	0.28	16
Th	19.93	71.73	51.80	35.56	12	32
U	9.66	13.59	3.93	11.92	1.32	11
V	664.14	1117.83	453.69	923.26	117.29	13

	Minimum	Maximum	Range	Mean	SD (%)	RSD (%)
W	130.78	264.37	133.59	186.34	41.75	22
Zn	10.74	270.25	259.50	130.35	73	56
Zr	294.83	444.96	150.13	382.71	39	10
La	177	396	218	287	51	18
Ce	1384	2107	723	1742	194	11
Pr	37.10	92.45	55.35	63.40	13.18	21
Nd	148	367	219	255	52	20
Sm	29.57	74.08	44.52	51.28	10.52	21
Eu	6.95	17.15	10.20	12.16	2.44	20
Gd	31.03	70.06	39.03	52.23	9.35	18
Tb	4.83	10.78	5.95	8.07	1.41	17
Dy	27.96	58.98	31.02	46.07	7.35	16
Yttrium	104.43	196.26	91.82	167.90	21.39	13
Ho	8.38	11.63	3.25	10.08	1.20	12
Er	21.75	29.68	7.93	26.14	2.94	11
Tm	3.16	4.31	1.15	3.76	0.40	11
Yb	19.70	25.79	6.09	22.92	2.11	9
Lu	2.81	3.63	0.82	3.26	0.29	9

TABLE 6.6: Statistics for deep horizon FeMn crust samples (n=7)

	Minimum	Maximum	Range	Mean	SD (%)	RSD (%)
wt%						
Fe	17.8	21.7	4.0	19.5	1.3	7
Mn	10.8	13.7	2.9	12.3	0.9	8
Ca	0.5	1.1	0.6	0.8	0.2	22
Ti	0.4	0.5	0.1	0.4	0.1	12
(ppm)						
Ba	920	1178	258	1076	111	10
Co	1523	2643	1119	2116	411	19
Cr	11.24	35.07	23.83	20.16	7.79	39
Cs	0.25	0.45	0.20	0.34	0.08	23
Cu	336	709	373	491	167	34
Hf	6.70	9.27	2.57	7.29	0.90	12
Li	5	25	19	10	7	66
Mo	331	431	100	397	36	9
Nb	46.34	79.62	33.28	57.24	11.21	20
Ni	1301	1865	564	1529	220	14
Pb	887	1198	311	1081	120	11

	Minimum	Maximum	Range	Mean	SD (%)	RSD (%)
Rb	5.72	9.18	3.46	6.94	1.53	22
Sc	12.18	15.36	3.18	13.49	1.03	8
Sm	57.00	78.59	21.59	67.90	8.20	12
Sn	0.13	0.66	0.52	0.34	0.20	60
Sr	824	1055	231	955	85	9
Ta	1.41	2.54	1.13	1.85	0.42	23
Th	49.11	59.47	10.36	54.80	4.38	8
U	7.80	9.58	1.78	8.90	0.62	7
V	658.05	848.16	190.10	753.44	64.53	9
W	126.67	379.03	252.36	203.77	84.89	42
Zn	53	293	240	204	86	42
Zr	346.84	423.27	76.43	364.85	27.56	8
La	235	347	111	294	44	15
Ce	1280	1756	476	1523	158	10
Pr	66.12	91.65	25.53	78.97	10.20	13
Nd	262	363	101	314	42	13
Sm	57.00	78.59	21.59	67.90	8.20	12
Eu	13.50	18.26	4.76	16.01	1.85	12
Gd	54.73	75.51	20.78	65.53	8.15	12
Tb	8.69	11.76	3.07	10.25	1.14	11
Dy	46.84	62.93	16.09	55.09	5.92	11
Yttrium	128.39	191.24	62.85	161.47	25.27	16
Ho	8.38	11.63	3.25	10.08	1.20	12
Er	21.75	29.68	7.93	26.14	2.94	11
Tm	3.16	4.31	1.15	3.76	0.40	11
Yb	19.70	25.79	6.09	22.92	2.11	9
Lu	2.81	3.63	0.82	3.26	0.29	9

6.4.3 Elemental Correlations with Environmental Variables

Due to the variation of the structure of Tropic Seamount and the intersection with the surrounding water masses, there is a complex interaction between some of the environmental variables that means they may co-vary. Tables 6.7 and 6.8 summarise the statistically significant correlation patterns between environments and elements for recent surface scrape samples (the full correlation matrix is available in Appendix C.5). Values for water depth and dissolved oxygen content for surface scrape sites are strongly correlated (R^2 = 96%) and so the main driver in elemental correlation can be difficult to

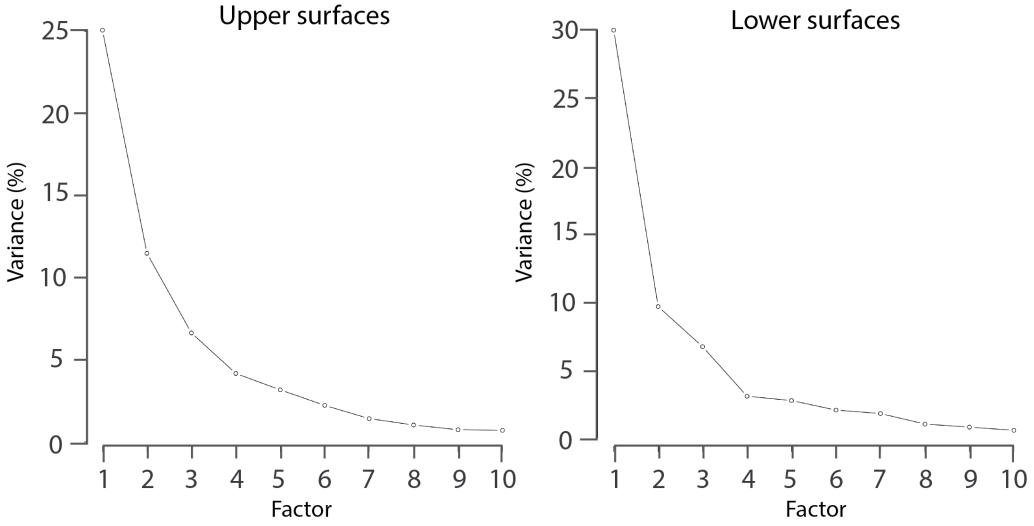

FIGURE 6.4: Scree plots to show the variance explained (%) by each factor, for factor analyses of the upper and lower FeMn crust surface scrape samples.

determine but they are included in the analysis to investigate any elements that may display different correlative patterns between the two factors. Due to the interaction of the seamount morphology, outcrop texture and currents, weak negative correlations are also observed between maximum current velocity and water depth (R^2 = -38%) and dissolved oxygen concentration (R^2 = -35%). Water depth also shows a weak positive correlation with roughness (R^2 = 35%). Broad and fine BPI showed no significant correlations with surface scrape element concentrations so were not included in this discussion. Similarly, northness only showed a weak negative correlation with Rb (R^2 = -28%) and is not considered here. Roughness and maximum current velocities both showed weak correlations with depth, fine BPI and broad BPI and currents also show correlations with dissolved oxygen concentrations. These interactions are considered when discussing the drivers factors behind elemental correlations with environment.

6.4.4 Surface Scrape Factor analyses

In order to better understand the processes controlling the chemical composition of FeMn crust composition, factor analyses were limited to the recent surface scrape samples. The recent surface scrape samples (n = 56) were subset into upper (n = 37) and lower (n = 19) surfaces for the factor analysis to determine if the controls on crust composition would vary with FeMn crust orientation. Scree plots were used to determine the appropriate number of factors to include for the separate analyses, with the cut off made at the point of inflection in the variance explained (Figure 6.4). For the upper samples, 4 factors explained 78% of the total variance and were retained. For the lower samples, 3 factors explained 76% of the variance and were retained.

TABLE 6.7: Summary of statistically significant ($p<0.05$) correlation outputs for recent surface scrape samples (n = 56) for elements and key environmental variables (bold). Abbreviations: Dissolved oxygen (dO), positive (+ve), negative (-ve).

Water depth		**Dissolved oxygen concentration**		**Eastness**	
Positive	**Negative**	**Positive**	**Negative**	**Positive**	**Negative**
dO	Pb	K	Pb	Fe	Li
K	Sr	Cs	Sr	Ce	Al
Al	Te	Rb	Sn	LREE	K
Cs	As	Al	Te	REE	
Rb	Sn	Se	As	Nd	
Mn/Fe	V	Mn/Fe	V	REY	
Cu	Co/Mn	Cu	Co/Mn	Mo	
Na	Bi	Na	Bi	Eu	
Se	P	Ge	Ba	V	
LREE/HREE	S	LREE/HREE	Be	Pr	
Roughness	Fe	Mn	S	Sm	
Ni	Be		Fe	Tb	
Li	Co/Ni		P	As	
Ge	Ba		Co/Ni		
Mn	Ce Anomaly		Sb		
	Cr		Co		
	Sb		**Currents**		
	U		U		
	Currents		Cr		
	Co		Ce Anomaly		
	La		W		
	W		La		
	Y		Zn		
	Er		Y		
	Ho		**Broad BPI**		
	Dy				
	Gd				
	HREE				
	Tb				
	Tm				
	Lu				

6.4.5 Upper Surface Scrape Factor analyses

Table 6.9 shows the results of the factor analysis for the upper surface scrape samples. Factor 1 explained 47% of the variance in upper sample compositions and is the main controlling factor for the REY, with strong positive loadings recorded for REY (not including Ce which shows a weaker loading), U, Sr, Th as well as S, As, Bi, V, Fe and Pb. It also shows strong negative loadings for Al, K, Cu, Li and Rb and Pt. A positive correlation of REY and Fe has been observed in numerous studies (e.g. Muinos et al., 2013; Hein et al., 2016; Marino et al., 2017) and this phase was similarly attributed to Fe oxyhydroxide phases in FeMn crusts. While REY associations with phosphatised

TABLE 6.8: Summary of statistically significant ($p<0.05$) correlation outputs for recent surface scrape samples (n = 56) for elements and key environmental variables (bold). Abbreviations: Dissolved oxygen (dO), positive (+ve), negative (-ve).

Slope		**Roughness**		**Currents**	
Positive	**Negative**	**Positive**	**Negative**	**Positive**	**Negative**
HREE	LREE/HREE	**FineBPI**	Co/Mn	W	**BroadBPI**
Ho	Li	**Depth**	Te	**Northness**	LREE/HREE
Dy	Cu	**BroadBPI**	Pb	Mo	Li
Tm	Al	K	Bi	S	**FineBPI**
Er	Ni		Sr	Bi	Cu
Yb				Sr	Cs
Lu				Pb	**dO**
Gd				Te	**Depth**
Eu				As	K
Tb				Sb	Rb
Y				U	Al
Nd				La	
Pr				V	
Sm				In	
La				Yb	
Ce Anomaly				Ce Anomaly	
REY				Be	
Co/Ni				Tm	
REE				Lu	
U				Er	
LREE				Co/Ni	
				Ho	
				Y	
				HREE	
				Ta	
				Fe	
				Dy	
				Gd	
				Nd	
				Tb	
				Eu	
				Sn	
				Pr	
				P	
				Sm	

phases have also been observed in other studies (e.g. Koschinsky et al., 1997; Koschinsky and Halbach, 1995; Wen et al., 1997; Mohwinkel et al., 2014), the association with Fe oxyhydroxide phases in these samples is supported by the anticorrelation in elements commonly attributed to phases that dilute FeMn oxides, such as detrital sediments or carbonate-fluorapatite (CFA). A range of Fe oxides have been reported in FeMn crusts but for hydrogenetic crusts are usually dominated by feroxyhyte, ferrihydrite and goethite-type phases (Hein et al., 2000; Hein and Koschinsky, 2014). Marino et al. (2017) observed that goethite was the dominant Fe oxide phase in CISP FeMn crusts. Goethite-type phases are also reported to support the significant enrichment of REY in numerous types of Fe-rich deposits (e.g. Koeppenkastrop and De Carlo, 1992; Kalatha et al., 2017; Li et al., 2020). Hence, as the most significant Fe oxyhydroxide phase in FeMn crusts from this region is likely responsible for the largest amount of composition variance and the REY association, Factor 1 is attributed to a goethite-type Fe oxyhydroxide phase.

Factor 2 for the upper surface scrape samples explains 24% of the variance and shows strong positive loadings for Ba, Sb, W, Pb, Te, Bi, V, Be, Pt, Sn, Cr, Fe, Mo, S, As, Zn, P and Se as well as for Tl, Lu and Co. Strong negative loadings are observed for Rb, K, Cs and Al as well as Ca, Se and Ti. The simple chemical colloid model described by Koschinsky and Halbach (1995) supports the observation of positive loading of elements that exist as negatively charged ions and neutral complexes in seawater, such as Te, V, Mo and As, that are subsequently sorbed onto the surface of positively charged Fe oxyhydroxides. This factor also shows strong negative correlations to elements commonly associated with detrital phases (e.g. K, Al, Ti) and CFAs. Iron is commonly observed as a loading across multiple factors due to its role in numerous phases associated with FeMn crusts, including hydrogenetic Fe oxyhydroxides, intergrown Fe- and Mn oxyhydroxides, detrital and biogenic phases, which can add complexity to factor analysis studies (e.g. Halbach and Puteanus, 1983; Hein et al., 2000; Verlaan and Cronan, 2021). This factor also shows significant loadings for elements associated with biogenic phases, such as Ba, Bi, V and Zn (e.g. Wen et al., 1997; Koschinsky and Hein, 2003; De Carlo et al., 1987). This factor is therefore attributed to a different hydrogenetic Fe oxyhydroxide phase to Factor 1 that may also be influenced by biogenic phases.

Factor 3 explains 20% of the variance for the upper samples and shows strong positive loadings for Ni, Mn, Mg, Co, Na, Cd, Tl, Li, Zn, Cu and Ti and negative loadings for Se, Ca and Cr. Following the simple chemical colloid model and observations of elemental correlations from numerous other studies (e.g. Wen et al., 1997; Koschinsky and Halbach, 1995; Verlaan and Cronan, 2021), this factor is attributed to an Mn oxide phase that anticorrelates with both dilution phases such as carbonates and CFAs as well as Fe oxides.

Factor 4 explains 9% of the variability and shows positive loadings for the high field-strength elements (Zr, Nb, Hf and Ta) and negative loadings for elements commonly

attributed to Mn oxide phases such as Co. The HFSE content of FeMn crusts has been attributed to both Fe oxides as well as detrital aluminosilicates (Bau et al., 1996; Koschinsky and Hein, 2003; Schmidt et al., 2014). In this study, the average Zr/Hf ratios measured (mean of 53) are comparable to the average of Zr/Hf = 69 for continental crust (Hans Wedepohl, 1995) and significantly lower than modern deep water values of 95 – 110 for the N Atlantic (Schmidt et al., 2014). Hence, Factor 4 is attributed to detrital phases. Due to the proximity to land masses, FeMn crusts in the Atlantic Ocean show greater influence from atmospheric dust and fluvial inputs and commonly display higher Fe concentrations than Pacific Ocean crusts (Koschinsky et al., 1996). Tropic Seamount lies within the dispersal zone of the Saharan dust plume from the nearby western African craton and past studies have also observed the influence of detrital inputs on FeMn crust composition in this region (Marino et al., 2017; Yeo et al., 2018a; Josso et al., 2020b, 2021).

TABLE 6.9: Factor analysis for recent upper surface scrape samples (n=56). Factor loading values for individual elements are shown in descending order, from strong positive loading to strong negative loadings. Elements in bold are loaded factors, with coloured values highlighting the statistically significant elements: R^2>0.45 in green and R^2<-0.45 in orange. Summary statistics: EV (eigenvalue), PTV (proportion of total variance), CVE (cumulative variance explained).

Factor 1		Factor 2		Factor 3		Factor 4	
Tb	**0.978**	**Ba**	**0.897**	**Ni**	**0.845**	**Zr**	**0.974**
Gd	**0.977**	**Sb**	**0.846**	**Mn**	**0.83**	**Hf**	**0.964**
Eu	**0.976**	**W**	**0.837**	**Mg**	**0.811**	**Ta**	**0.964**
Dy	**0.972**	**Pb**	**0.804**	**Co**	**0.792**	**Nb**	**0.873**
Sm	**0.971**	**Te**	**0.777**	**Na**	**0.786**	**Ag**	**0.427**
Pr	**0.966**	**Bi**	**0.77**	**Cd**	**0.751**	**P**	**0.276**
Nd	**0.966**	**V**	**0.724**	**Tl**	**0.734**	**Fe**	**0.201**
Ho	**0.966**	**Be**	**0.718**	**Li**	**0.656**	**V**	**0.191**
La	**0.952**	**Pt**	**0.704**	**Zn**	**0.633**	**As**	**0.174**
Er	**0.952**	**Sn**	**0.694**	**Cu**	**0.625**	**U**	**0.169**
Tm	**0.947**	**Cr**	**0.655**	**Ti**	**0.598**	**Ga**	**0.157**
Yb	**0.942**	**Fe**	**0.65**	**Al**	**0.424**	**S**	**0.156**
Lu	**0.922**	**Mo**	**0.626**	**Ga**	**0.404**	**Mo**	**0.108**
Y	**0.891**	**S**	**0.625**	**Pt**	**0.372**	**Mn**	**0.103**
U	**0.87**	**As**	**0.625**	**Sn**	**0.363**	Na	0.09
REY	**0.862**	**Zn**	**0.578**	**Th**	**0.328**	Pr	0.08
Sr	**0.749**	**P**	**0.527**	**REY**	**0.292**	Nd	0.08
Th	**0.718**	**Sr**	**0.492**	**Te**	**0.248**	Sm	0.08
S	**0.592**	**Tl**	**0.324**	**Sb**	**0.231**	Eu	0.08
As	**0.563**	**Lu**	**0.296**	**Nb**	**0.209**	Gd	0.08
Bi	**0.56**	**Co**	**0.27**	**S**	**0.207**	Tb	0.08
V	**0.495**	**Y**	**0.266**	**K**	**0.18**	Dy	0.08

Factor 1		Factor 2		Factor 3		Factor 4	
Fe	**0.461**	**Yb**	**0.246**	**Ba**	**0.179**	Y	0.07
Pb	**0.456**	**Tm**	**0.241**	**Mo**	**0.146**	Pb	0.07
P	**0.382**	**Er**	**0.229**	W	0.08	La	0.07
Ce	**0.354**	**U**	**0.209**	Hf	0.05	Mg	0.06
In	**0.346**	**La**	**0.182**	Be	0.04	Cu	0.06
Ti	**0.342**	**Mg**	**0.175**	Pb	0.04	Sr	0.06
Be	**0.335**	**Ho**	**0.164**	Bi	0.02	Ho	0.06
Se	**0.318**	**Ga**	**0.148**	Zr	-0.01	Er	0.05
Mo	**0.301**	**Dy**	**0.129**	Ta	-0.01	Be	0.04
Co	**0.286**	REY	0.09	U	-0.02	Zn	0.04
Te	**0.267**	Tb	0.08	Lu	-0.04	Tm	0.04
Ag	**0.238**	Mn	0.07	La	-0.08	Yb	0.04
Ge	**0.216**	Nd	0.07	Ce	-0.08	Pt	0.03
Sn	**0.214**	Zr	0.06	Pr	-0.08	Lu	0.03
Ta	**0.162**	Nb	0.06	Nd	-0.08	W	0.02
W	**0.119**	Gd	0.06	Yb	-0.1	Se	0.01
Zr	0.09	Hf	0.05	**Tm**	**-0.104**	Cd	0.01
Nb	0.08	Ta	0.03	**Dy**	**-0.127**	In	0
Mn	0.07	Pr	0.03	**Sm**	**-0.128**	Ba	0
Hf	0.02	Eu	0.03	**Ho**	**-0.13**	Li	-0.01
Ca	-0.02	Ni	0.01	**Eu**	**-0.131**	Ni	-0.01
Na	-0.03	Cd	0.01	**Er**	**-0.134**	Bi	-0.02
Tl	**-0.19**	Sm	0	**Tb**	**-0.137**	Tl	-0.03
Sb	**-0.224**	Ag	-0.01	**Gd**	**-0.148**	REY	-0.03
Cr	**-0.253**	Ce	-0.01	**Sr**	**-0.176**	Th	-0.04
Ba	**-0.318**	In	-0.02	**Y**	**-0.217**	Al	-0.06
Mg	**-0.368**	Na	-0.07	**In**	**-0.228**	Sn	-0.06
Ga	**-0.38**	Li	-0.09	**Ge**	**-0.231**	Sb	-0.06
Zn	**-0.411**	Ge	-0.1	**Rb**	**-0.249**	K	-0.08
Cd	**-0.422**	**Cu**	**-0.143**	**Fe**	**-0.276**	Cs	-0.08
Cs	**-0.47**	**Th**	**-0.199**	**Cs**	**-0.302**	Rb	-0.09
Ni	**-0.496**	**Ti**	**-0.333**	**V**	**-0.326**	**Ti**	**-0.112**
Rb	**-0.515**	**Se**	**-0.349**	**P**	**-0.351**	**Cr**	**-0.112**
Pt	**-0.525**	**Ca**	**-0.37**	**Ag**	**-0.391**	**Te**	**-0.116**
K	**-0.615**	**Al**	**-0.463**	**As**	**-0.432**	**Ge**	**-0.125**
Cu	**-0.654**	**Cs**	**-0.492**	**Cr**	**-0.45**	**Ca**	**-0.129**
Li	**-0.655**	**K**	**-0.497**	**Ca**	**-0.489**	**Ce**	**-0.138**
Al	**-0.669**	**Rb**	**-0.518**	**Se**	**-0.604**	**Co**	**-0.212**
EV	21.75		11.11		9.45		4.30
PTV (%)	36		19		16		7

	Factor 1	Factor 2	Factor 3	Factor 4
CVE (%)	36	55	70	78

6.4.6 Lower Surface Scrape Factor analyses

Table 6.10 summarises the outcomes of factor analyses for the lower surface scrape samples. For the lower surfaces, fewer factors were deemed to play a significant role on the compositional variability of samples, showing differing controls on composition between upper and lower FeMn crust surfaces. Factor 1 describes 40% of the variance and shows strong positive loadings for the REY (including Ce), Sr, Ti, U, Bi, Co, Se, P and Fe and strong negative loadings for Nb, Mn, Ni, Hf, Ta, Cd, Zr, Na, Ti, K, Cu, Al and Li. The strong positive loadings for REY and Fe and negative loading for Mn and elements associated with detrital phases supports the role of an Fe oxyhydroxide phase for this factor. The similar loading across all the REY, including Ce, suggests slightly different behaviours to those observed for Factor 1 of the upper samples.

Factor 2 describes 21% of the variance and shows strong positive loadings for V, As, Fe, S, P, Cr, Pb, Be, Sr, Bi and U and strong negative loadings for HFSE, Mn, Ni, Cd, Zr, Na, Tl, K, Cu, Al and Li. This phase is attributed to an Fe oxyhydroxide phase that anticorrelates with Mn oxides and detrital phases.

Factor 3 contributes 16% of the variance and has positive loadings for Sb, Te, W, Ba, Pt, Sn, Co, Pb, Mo and Tl as well as moderate for Mn while strong negative loadings are shown for Cs, Rb, Ca and K. This factor is attributed to a hydrogenetic Mn oxide phase that anticorrelates with carbonate and CFA phases.

TABLE 6.10: Factor analysis for recent lower surface scrape samples (n=19). Factor loading values for individual elements are shown in descending order, from strong positive loading to strong negative loadings. Elements in bold are loaded factors, with coloured values highlighting the statistically significant elements: >0.45 in green and <-0.45 in orange. Summary statistics: EV (eigenvalue), PTV (proportion of total variance), CVE (cumulative variance explained).

Factor 1		Factor 2		Factor 3	
Sm	**0.953**	**V**	**0.866**	**Sb**	**0.889**
Gd	**0.952**	**As**	**0.86**	**Te**	**0.868**
Pr	**0.951**	**Fe**	**0.805**	**W**	**0.816**
Eu	**0.951**	**S**	**0.748**	**Ba**	**0.725**
Tb	**0.951**	**P**	**0.733**	**Pt**	**0.678**
Dy	**0.949**	**Cr**	**0.679**	**Sn**	**0.676**
Ho	**0.949**	**Pb**	**0.64**	**Co**	**0.673**
Nd	**0.948**	**Be**	**0.624**	**Pb**	**0.661**
La	**0.944**	**Sr**	**0.573**	**Mo**	**0.601**

Factor 1		Factor 2		Factor 3	
REY	**0.94**	**Bi**	**0.526**	**Tl**	**0.596**
Er	**0.935**	**U**	**0.51**	**Bi**	**0.439**
Tm	**0.935**	**Ag**	**0.366**	**In**	**0.438**
Yttrium	**0.927**	**In**	**0.329**	**Be**	**0.426**
Yb	**0.927**	**Ca**	**0.289**	**Ti**	**0.425**
Lu	**0.914**	**La**	**0.268**	**Mn**	**0.393**
Th	**0.84**	**Mo**	**0.243**	**Mg**	**0.388**
Ce	**0.795**	**Pr**	**0.239**	**Li**	**0.373**
Sr	**0.741**	**Nd**	**0.235**	**Ce**	**0.367**
Ti	**0.706**	**Eu**	**0.234**	**Th**	**0.351**
U	**0.706**	**Yttrium**	**0.229**	**Zn**	**0.347**
Bi	**0.626**	**Gd**	**0.227**	**U**	**0.321**
Co	**0.595**	**Tb**	**0.227**	**Cd**	**0.275**
Se	**0.57**	**Sm**	**0.222**	**REY**	**0.263**
P	**0.493**	**Dy**	**0.204**	**V**	**0.258**
Fe	**0.464**	**Ho**	**0.195**	**Ag**	**0.222**
S	**0.431**	**Er**	**0.193**	**Yb**	**0.209**
As	**0.398**	**Te**	**0.149**	**Tm**	**0.207**
Ca	**0.355**	**Tm**	**0.136**	**Ni**	**0.195**
Te	**0.349**	**W**	**0.117**	**Er**	**0.192**
Pb	**0.32**	**Yb**	**0.115**	**As**	**0.173**
Sn	**0.311**	**Th**	**0.113**	**Lu**	**0.173**
V	**0.279**	Sn	0.06	**S**	**0.169**
In	**0.261**	Lu	0.04	**Ho**	**0.163**
W	**0.253**	REY	0.02	**Se**	**0.158**
Mo	**0.22**	Se	-0.08	**La**	**0.147**
Ag	**0.121**	**Ba**	**-0.162**	**Dy**	**0.145**
Ta	**0.116**	**Cs**	**-0.168**	**Nb**	**0.12**
Zr	0.07	**Co**	**-0.169**	**Tb**	**0.119**
Nb	0	**Ce**	**-0.192**	**Nd**	**0.107**
Hf	-0.01	**Ge**	**-0.206**	**Ga**	**0.105**
Be	-0.02	**Pt**	**-0.217**	**Gd**	**0.104**
Sb	-0.07	**Rb**	**-0.288**	Pr	0.1
Ge	**-0.178**	**Sb**	**-0.334**	Sm	0.1
Cr	**-0.272**	**Ti**	**-0.347**	Sr	0.09
Cs	**-0.295**	**Mg**	**-0.372**	Eu	0.09
Na	**-0.333**	**Ga**	**-0.412**	Yttrium	0.08
Mn	**-0.339**	**Zn**	**-0.428**	Ta	0.08
Tl	**-0.341**	**Li**	**-0.452**	Cu	0.07
Rb	**-0.394**	**Al**	**-0.507**	Fe	0.06

Factor 1		Factor 2		Factor 3	
K	**-0.513**	**Cu**	**-0.587**	Zr	0.01
Al	**-0.556**	**K**	**-0.59**	Hf	-0.02
Pt	**-0.56**	**Tl**	**-0.591**	P	-0.09
Ba	**-0.568**	**Na**	**-0.606**	**Ge**	**-0.116**
Ga	**-0.588**	**Zr**	**-0.607**	**Al**	**-0.258**
Cd	**-0.646**	**Cd**	**-0.611**	**Na**	**-0.311**
Ni	**-0.649**	**Ta**	**-0.648**	**Cr**	**-0.398**
Li	**-0.677**	**Hf**	**-0.654**	**K**	**-0.451**
Zn	**-0.748**	**Ni**	**-0.671**	**Ca**	**-0.46**
Cu	**-0.75**	**Mn**	**-0.683**	**Rb**	**-0.682**
Mg	**-0.773**	**Nb**	**-0.706**	**Cs**	**-0.722**
EV	24.063		12.288		9.399
PTV (%)	40		21		16
CVE (%)	40		61		76

6.4.7 Horizon Factor analyses

Table 6.11 shows the results of factor analyses for target horizon samples from Tropic Seamount's summit (n = 19). To facilitate statistical analysis, all summit samples were included. It has been assumed in this study that local environmental conditions have experienced limited changes to current conditions at the resolution at which these horizons have been sampled (between 3 – 5 Mya) and for most elements, the RSD between contemporaneous horizons exceeds that between horizons within each sample. Three significant factors were retained following assessment of scree plots and eigenvalues and they explained 80% of the total sample variance. Factor 1 explains 43% of the observed variance and showed strong positive loadings for the REY, Sc, Fe, Sr, Ce, Mo, V, U and Hf and strong negative loadings for Li, Cu and Ni. Due to the high loadings of Fe and elements commonly associated with negatively charged metal complexes in seawater, such as Mo and V (Koschinsky and Halbach, 1995), this factor is attributed to an Fe oxyhydroxide phase.

Factor 2 explains 19% of the variance and shows strong positive loadings for Ba, U, Mn, Zr, V, Zn, Mo, Pb, Fe and Sr and strong negative loadings for Ca, Cs and Sn. This factor is attributed to an Mn oxide phase that likely also shows biogenic influence due to the strong loadings for elements such as Ba, V, Zn and Fe (Wen et al., 1997; Van Der Weijden and Kruissink, 1977; Koschinsky and Hein, 2003).

Factor 3 explains 18% of the variance is has strong positive loading values for Co, Ta, Th, Pb, Nb, Pr, Sm, W, Nd, La, Mn, Eu and Hf and strong negative loadings for Zn and

Cr. This factor is interpreted to represent an Mn oxide phase, due to strong positive loadings for Mn and elements commonly scavenged by Mn oxides during hydrogenetic crust growth, such as Co, Pb and the LREE (Koschinsky and Halbach, 1995). Cobalt in FeMn crusts is usually exclusively observed with the Mn oxide phase Hein et al. (1992).

TABLE 6.11: Factor analysis for target horizon samples from Tropic Seamount's summit (n=19). Factor loading values for individual elements are shown in descending order, from strong positive loading to strong negative loadings. Elements in bold are loaded factors, with coloured values highlighting the statistically significant elements: >0.45 in green and <-0.45 in orange. Summary statistics: EV (eigenvalue), PTV (proportion of total variance), CVE (cumulative variance explained).

Factor 1		Factor 2		Factor 3	
Y	**0.939**	**Ba**	**0.865**	**Co**	**0.848**
Tm	**0.937**	**U**	**0.824**	**Ta**	**0.817**
Er	**0.934**	**Mn**	**0.744**	**Th**	**0.772**
Ho	**0.922**	**Zr**	**0.734**	**Pb**	**0.686**
Yb	**0.917**	**V**	**0.721**	**Nb**	**0.543**
Lu	**0.912**	**Zn**	**0.709**	**Pr**	**0.541**
Dy	**0.903**	**Mo**	**0.686**	**Sm**	**0.518**
Gd	**0.875**	**Pb**	**0.572**	**W**	**0.516**
Tb	**0.874**	**Fe**	**0.564**	**Nd**	**0.515**
Eu	**0.843**	**Sr**	**0.465**	**La**	**0.501**
La	**0.826**	**Ce**	**0.43**	**Mn**	**0.486**
Sm	**0.826**	**Ni**	**0.366**	**Eu**	**0.478**
Nd	**0.823**	**Cu**	**0.33**	**Hf**	**0.472**
Pr	**0.808**	**Lu**	**0.328**	**Tb**	**0.43**
Sc	**0.793**	**Yb**	**0.323**	**Ti**	**0.416**
Fe	**0.786**	**Ti**	**0.312**	**Gd**	**0.415**
Sr	**0.767**	**Ta**	**0.283**	**Sr**	**0.41**
Ce	**0.735**	**W**	**0.279**	**Dy**	**0.362**
Mo	**0.629**	**Tm**	**0.253**	**Zr**	**0.328**
V	**0.599**	**La**	**0.243**	**Ho**	**0.304**
U	**0.499**	**Ho**	**0.224**	**Er**	**0.258**
Hf	**0.481**	**Er**	**0.222**	**Yb**	**0.204**
Th	**0.439**	**Dy**	**0.211**	**Tm**	**0.199**
W	**0.439**	**Gd**	**0.204**	**U**	**0.185**
Pb	**0.369**	**Tb**	**0.197**	**Fe**	**0.169**
Mn	**0.363**	**Hf**	**0.185**	**Li**	**0.161**
Cr	**0.285**	**Eu**	**0.176**	**Ce**	**0.153**
Ti	**0.277**	**Pr**	**0.168**	**Lu**	**0.138**
Ba	**0.267**	**Nd**	**0.165**	Mo	0.09
Zr	**0.257**	**Co**	**0.163**	Ba	0.04
Ca	**0.256**	**Sm**	**0.147**	Ni	-0.01

Factor 1		Factor 2		Factor 3	
Co	**0.164**	Li	0.04	Sn	-0.06
Ta	**0.134**	Sc	-0.01	Cu	-0.07
Sn	**0.129**	Th	-0.04	Y	-0.07
Nb	0.03	Y	-0.06	V	-0.1
Rb	-0.09	Nb	-0.08	**Ca**	**-0.185**
Cs	**-0.155**	**Cr**	**-0.115**	**Sc**	**-0.237**
Zn	**-0.267**	**Rb**	**-0.359**	**Cs**	**-0.319**
Ni	**-0.744**	**Sn**	**-0.606**	**Rb**	**-0.413**
Cu	**-0.798**	**Cs**	**-0.617**	**Zn**	**-0.496**
Li	**-0.841**	**Ca**	**-0.772**	**Cr**	**-0.689**
EV	17.59		7.78		7.21
PTV (%)	43		19		18
CVE (%)	43		62		80

6.5 Discussion

6.5.1 Formation controls on FeMn crust composition

The enrichment of numerous elements, including Co, Mo, Te, Pt and the REY, in FeMn crusts relative to Earth's continental crust abundances and seawater concentrations have been extensively reported (e.g. Hein et al., 2000, 2010, 2013; Hein and Koschinsky, 2014). These enrichments are driven by very slow rates of formation, between 1 – 10 mm/Myr, as well as high specific surface areas (325 m^2g^{-1}) (Hein et al., 2000).

Numerous methods have been applied to classify the genetic type of FeMn crusts (Bau et al., 1996, 2014; Josso et al., 2017). Cerium anomalies measure the decoupling of Ce from the other REY due to surface oxidation enrichment processes and have been calculated as Ce_{SN}/Ce^*_{SN} (where SN indicates shale normalised values relative to Post-Archean Australian Shale PAAS concentrations from McLennan, 2001; Condie, 1993). The Ce^*_{SN} value is calculated as:

$$Ce^*_{SN} = 0.5La_{SN} + 0.5Pr_{SN} \tag{6.1}$$

The surface scrape samples analysed in this study display generally high concentrations of HFSE, strong positive Ce anomalies and significant enrichments in Co that support a dominantly hydrogenetic mode of formation (Figure 6.5). Both upper and lower surfaces show comparable Ce anomalies and Y/Ho ratios as well as REY distribution patterns (Figure 6.5 and Figure 6.6). The REY distribution profiles show distinct

positive Ce anomalies and negative Y anomalies (Y_{SN}/Ho_{SN} <1) that are characteristic of hydrogenetic FeMn crusts (Bau et al., 2014). Two upper surface samples show evidence of positive Y anomalies (Figure 6.6). Enrichments in Y, alongside the REE, Ni, Zn and Cu, have been observed during phosphatisation of FeMn crusts (e.g. Bau et al., 1996; Koschinsky et al., 1997). This observation in two of the surface samples, collected at a water depth of 1236 m, could suggest some localised element redistribution.

While Mn/Fe ratios for all samples show overall hydrogenetic characteristics of Mn/Fe <1 (mean = 0.91, n=121), 7 lower surface samples have slightly higher Mn/Fe ratios up to 1.7 and a higher mean (1.0, n=19) when compared to the upper surfaces (0.8, n=37). The uppermost crust surfaces are exposed to the overlying water column and their formation is likely to be dominated by hydrogenetic precipitation whereas the lower surfaces may also be influenced by pore fluids, depending on the depth of burial and the oxygen penetration depth into the sediments, that generate a trend towards more diagenetic signatures (Figure 6.5). These localised differences in oxygen environment can also drive differences in mineralogy which in turn can control the composition of FeMn crusts.

For both the upper and lower FeMn crust surface scrapes analysed in this study, an Fe oxyhydroxide phase is interpreted as the most significant driver of compositional variance in the samples (Factor 1). But each of these factors showed slight differences between upper and lower surface scrapes in the suite of elements associated with the Fe oxyhydroxide phase. In particular, the upper surface scrape samples showed positive loadings for the REY but not Ce, whereas the lower surface scrape samples showed positive loadings for all REY including Ce. The distinct behaviour of Ce from the REY in hydrogenetic FeMn crusts has been widely reported (e.g. Hein et al., 1997; Bau, 1999; Bau and Koschinsky, 2009; Bau et al., 2014). The divergent behaviour of Ce is driven by the surface oxidation of soluble Ce(III) to insoluble Ce(IV) after sorption onto FeMn crusts that prevents further exchange with surrounding seawater (e.g. Bau and Koschinsky, 2009; Bau et al., 2014). A relative enrichment in Ce when compared to other REY indicates accumulation during slow FeMn crust growth and hence positive Ce anomalies are observed in hydrogenetic crusts (e.g. Bau, 1999; Bau et al., 2014). While lower surface scrape samples show comparable Ce anomaly values to upper samples, the difference in REY factor loading supports differing controls on Fe oxyhydroxide formation and composition between upper and lower surfaces. More coherent behaviour between the REY and Ce could suggest either slightly elevated growth rates that would limit the relative enrichment of Ce above the other REY, a relative depletion of Ce in the fluids the lower crust surfaces precipitate from or differences in Ce behaviour due to different dominant Fe oxyhydroxide phases.

Higher growth rates have been observed for diagenetic nodules, due to more rapid mobilisation and subsequent re-precipitation of Mn within porewaters (Reyss et al., 1982). Cobalt chronometry was developed to estimate the accumulation rate of FeMn crusts

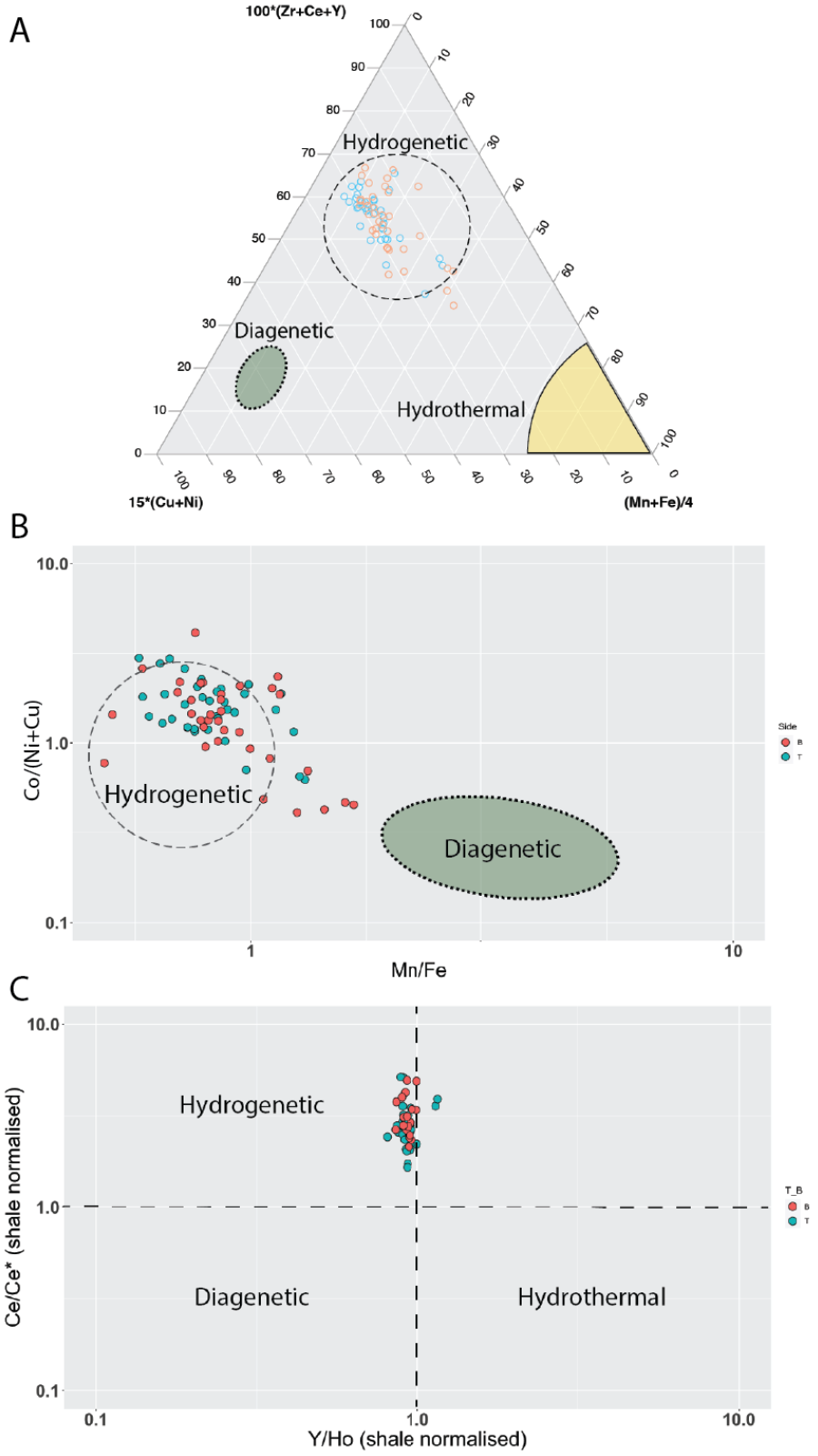

FIGURE 6.5: Discriminatory diagrams used to determine genetic types of FeMn deposits. In each of the plots, the field associated with each genetic type is labelled where they are expected to plot; hydrogenetic, diagenetic and hydrothermal FeMn deposits. Upper surfaces are plotted in blue and lower in pink throughout. (A) shows a ternary plot with surface scrapes and (B) on Co/(Ni+Cu) vs Mn/Fe (after Josso et al., 2017) and (C) on shale normalised (PAAS; McLennan, 2001; Condie, 1993) values of Ce anomaly vs Y/Ho (after Bau et al., 2014). All surface scrapes plot with the hydrogenetic fields.

to extrapolate beyond the limits of more accurate methods such as thorium-230 dating and $^{10}Be/^{9}Be$ chronology (Puteanus and Halbach, 1988; Manheim and Lanebostwick, 1988). These models assume a constant Co supply to oceans and a direct relationship between Co concentration and dilution driven by varying growth rates and detrital inputs. While the values therefore give a minimum possible age, as they cannot account for growth hiatuses and erosion, the following equation can be applied to investigate potential differences in growth rates between upper and lower crust surfaces (Puteanus and Halbach, 1988; Manheim and Lanebostwick, 1988):

$$\text{Growth Rate} = 0.68 \times \left(\frac{50 \times \text{Co}}{\text{Fe} + \text{Mn}}\right)^{1.67} \tag{6.2}$$

When this equation is applied to the surface scrape samples, we see that upper sample growth rates vary from 0.58 – 3.25 mm/Myr with a mean of 1.38 mm/Myr and lower surfaces show slower overall growth rates, between 0.45 – 2.02 mm/Myr with a mean of 1.20 mm/Myr. No significant correlation is observed between the Co chronometry growth rate values and calculated Ce anomaly and therefore growth rate is unlikely to be the greatest driver of compositional difference between upper and lower crust surfaces in these samples. While mean Ce concentrations between upper and lower surfaces are almost identical (1720 ppm and 1722 ppm respectively), upper surfaces generally show higher concentrations of REY with a mean of 1227 ppm compared to 1083 ppm for lower surfaces. This does not support the theory of a relative depletion of Ce compared to the other REY. This could suggest that the differences in REY behaviour are more likely driven by differences in the dominant Fe oxyhydroxide mineralogy of upper and lower surfaces.

Another example of differing controls on compositional variance between upper and lower surface scrape samples is observed between the Mn oxide phases. Factor 3 for the lower samples is attributed to the hydrogenetic Mn oxide phase and controlled a significant proportion of the variance (16%). This factor showed a strong negative loading for carbonate and CFA associations, unlike the Mn oxide factor (Factor 3) for the upper surface scrape samples. This higher anticorrelation in lower samples with Cs, Rb, Ca and K suggests that lower surfaces are more susceptible to replacement of FeMn crust with carbonates or CFA phases. Similar replacement mechanisms have been observed during widespread phosphatisation events during the expansion of oxygen-minimum zones (Hein et al., 1993; Koschinsky et al., 1997). The localised replacement observed here could be driven by sustained exchanged with pore fluids from the surrounding sediment.

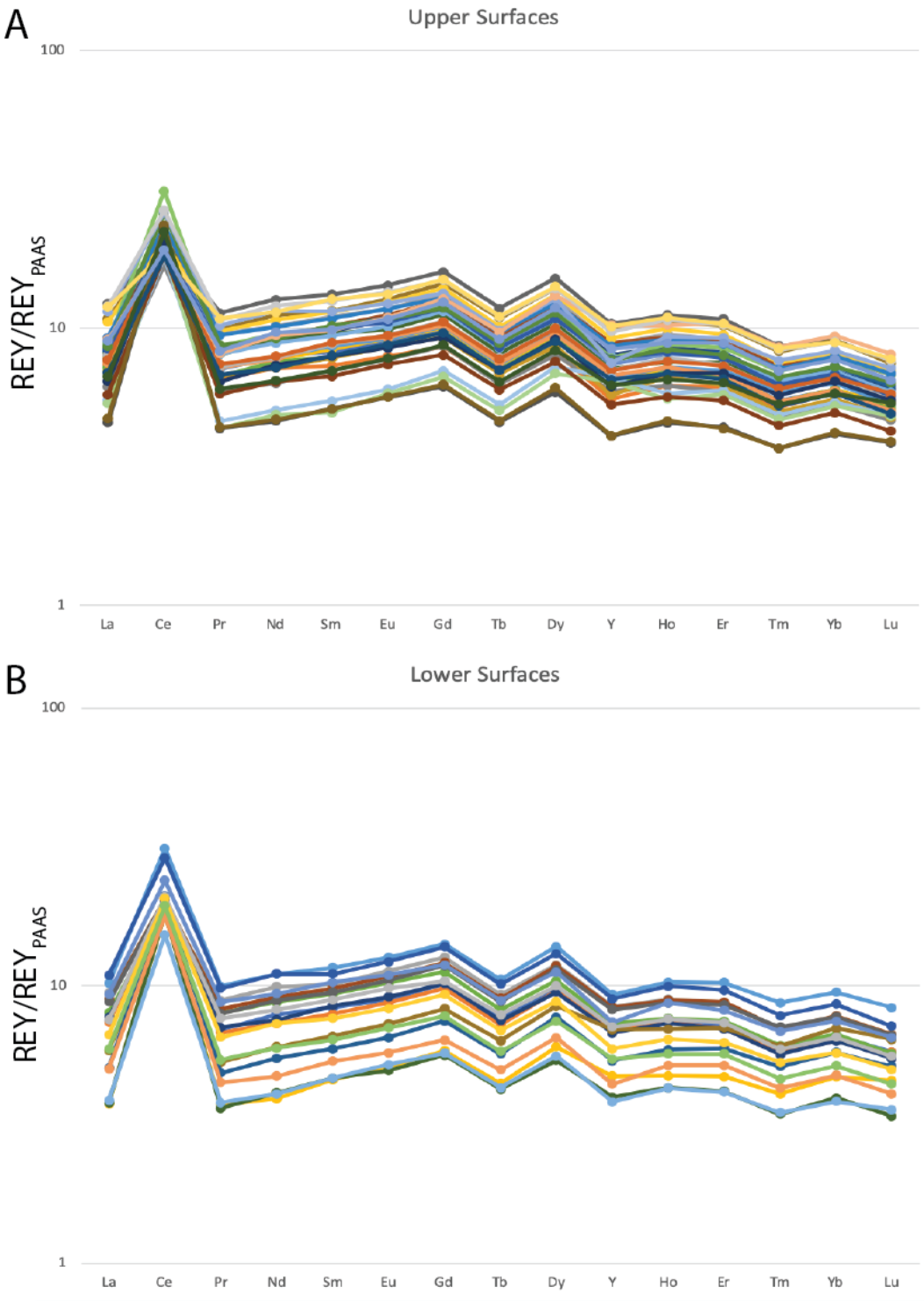

FIGURE 6.6: Distribution patterns of REY, normalised to shales for A) upper and B) lower FeMn crust surface scrape samples (PAAS; McLennan, 2001; Condie, 1993).

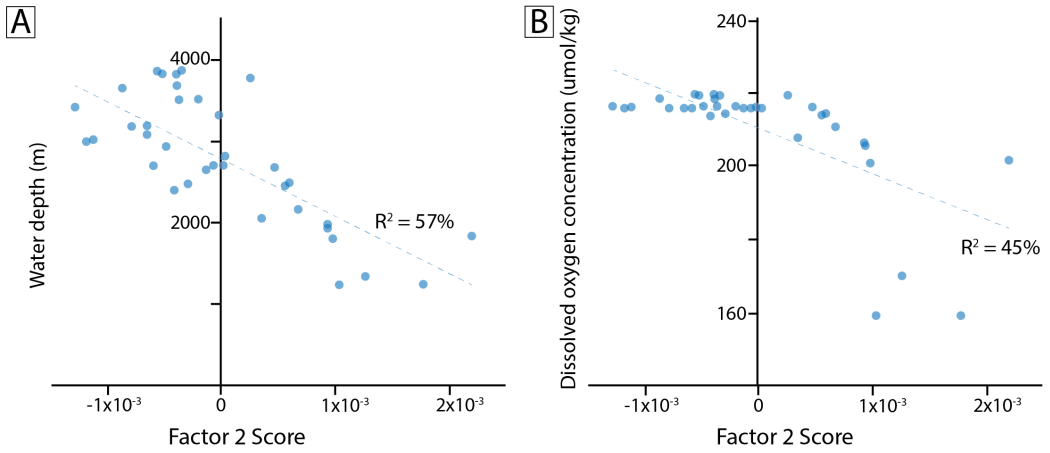

FIGURE 6.7: Factor score correlations with environmental variables for upper surface scrape samples. Significant correlations were observed for Factor 2 (an Fe oxyhydroxide phase) with A) water depth and B) dissolve oxygen concentrations.

6.5.2 Water-Depth Related Controls on FeMn Crust Composition

To investigate the potential locational variations and drivers of compositional variation in FeMn crusts, the factor analysis scores for individual upper surface scrape samples for each of the factors was plotted against the environmental variable values for those samples. Figure 6.7 shows the significant correlations between factor score values and environmental variables for upper surface scrape samples. The strongest correlations were observed between Factor 2 (an Fe oxyhydroxide phase with biogenic influence) and water depth (R^2 = 57%; Figure 6.7A) and dissolved oxygen concentrations (R^2 = 45%; Figure 6.7B), with Factor 2 decreasing with increasing water depth and dissolved oxygen. Both water depth and dissolved oxygen concentrations are strongly intercorrelated (R^2 = 96%) but Factor 2 shows slightly lower correlations with dissolved oxygen. This suggests that there is potentially another depth-controlled variable aside from dissolved oxygen concentration that is also affecting the distribution of this Fe oxyhydroxide phase.

Elemental trends with water depth have been widely reported for FeMn crusts and has been attributed to variations in dissolved oxygen concentrations of the water column (e.g. De Carlo et al., 1987; Hodkinson and Cronan, 1991; Mizell et al., 2020). The interaction with an OMZ is thought to play a key role in hydrogenetic FeMn crust formation (e.g. Koschinsky and Halbach, 1995). Surface primary productivity driven by nutrient upwelling generates sinking organic matter that sinks and consumes oxygen as it decays, producing an OMZ. This band of low oxygen acts as a reservoir for dissolve Mn^{2+} species and other dissolved ions. At Tropic Seamount the current minimum in oxygen concentration sits at 800 m water depth, approximately 200 m above the seamount summit where FeMn crust growth was observed but the OMZ can indirectly influence

FeMn crust growth through advection and diffusion processes (Klinkhammer and Bender, 1980; Halbach and Puteanus, 1984). Seafloor protrusions such as seamounts allow for upwelling and turbulent mixing of more oxygenated bottom waters, allowing Mn^{2+} to be oxidized and form oxide- and hydroxide- colloids. The mixed colloid species form due to the interaction of opposing surface charges between a central Mn- or Fe- core and other oxide and hydroxide elements (e.g. Koschinsky and Halbach, 1995). Trace metals can then be scavenged from the water column and adsorbed onto colloid surfaces of opposite charge. Metal cations such as Co^{2+} and Ni^{2+} (manganophiles) form colloid complexes with MnO_2^- colloids and anions such as MoO_4^{2-} are associated with Fe-oxyhydroxide colloid complexes. These associations are supported by investigations into the crystal structure and bonding environments of different metal ions using spectroscopic analyses, such as X-ray absorption spectroscopy (e.g. Manceau et al., 1992; Kashiwabara et al., 2013; Takahashi et al., 2000). In deeper waters, it has been proposed that trends with depth for FeMn crusts on Pacific Ocean seamounts are more dependent on Fe inputs from carbonate dissolution (Halbach and Puteanus, 1984). The solubility of carbonate increases with increasing pressure, whereas silica and biogenic silica sediments are less susceptible to changing pressure and so their accumulation patterns with depth are largely controlled by physical transport process (Heath, 1974). Mizell et al. (2020) observed weak correlations between depth-controlled elements and estimated carbonate ion concentrations for Pacific Ocean FeMn crusts that supports this theory. It has been proposed that biogenic carbonate dissolution can release colloidal Fe, while increased carbonate ion concentrations lead to increased pH that can increase the oxidation rate of Fe(II) in seawater (Halbach and Puteanus, 1984). This would lead to an overall increase in Fe supply and precipitation with depth. At Tropic Seamount, the opposite trend is observed, with the concentration of Fe in FeMn crusts decreasing with increasing water depth (Table 6.7). This follows patterns of dissolved Fe (dFe) concentrations through the modern water column in the NE Atlantic, where dFe is observed to peak between 500 – 1000 m water depths and then decrease at depth (Fitzsimmons et al., 2013; Buck et al., 2015). This coincides with the depth of the OMZ at Tropic Seamount and provides an enhanced source of Fe for FeMn crust precipitation. This suggests that the Fe:Mn ratio of the surrounding waters exerts a fundamental control on dominant mineralogy of FeMn crusts. Isotopic studies conducted by Conway and John (2014) suggested that a significant proportion of dissolved iron in the North Atlantic was sourced from Saharan dust deposition, alongside smaller inputs from lateral mixing of dFe from African continental margin sediments. Fitzsimmons et al. (2013) attributed this peak in dFe with the OMZ due to enhanced fertilisation of surface waters with aeolian dust and subsequent remineralisation at intermediate depths of Fe-rich biogenic material. The association of upper surface Fe oxyhydroxides with biogenic phase signatures observed in this study supports the influence of remineralisation of Fe-rich organics on the composition of Fe-phases at Tropic Seamount.

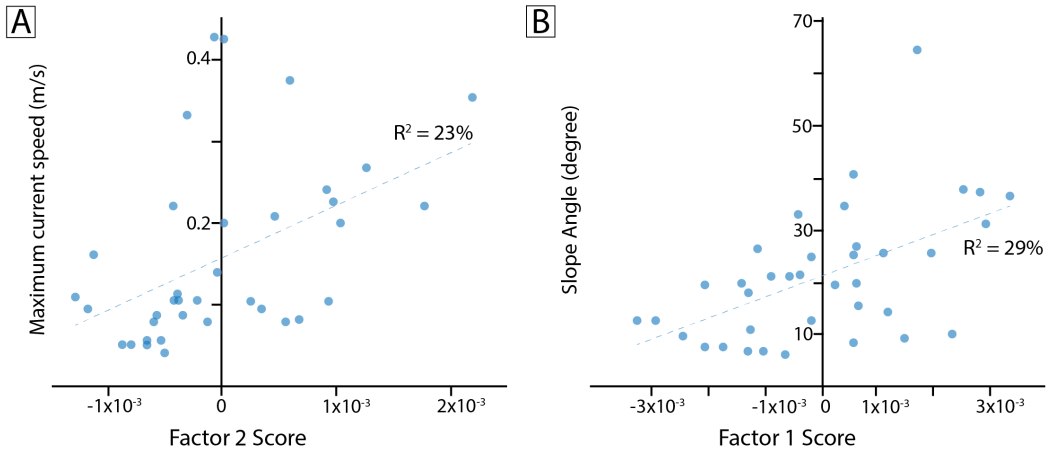

FIGURE 6.8: Factor score correlations between upper surface scrape for A) Factor 2 (Fe oxyhydroxide) and maximum current velocity and B) Factor 1 (goethite-type Fe oxyhydroxide) and slope angle.

A weak positive correlation is also observed with maximum current velocities (R^2 = 23%; Figure 6.8A). Maximum current velocities show a weak negative correlation with water depth (R^2 = 22%) which could suggest that both the dissolved oxygen content and variable current speeds may play a role in the variability in Factor 2. The role of currents on FeMn crust texture and composition has been debated. Hein et al. (1992, 2000) suggested that lower energy environments and current speeds supported the formation of uniform, laminar FeMn crust growth with minimal detrital content whereas higher energy environments initiated the formation of botryoidal and columnar type textures due to the deposition of detrital material carried by these currents into topographic lows. Josso et al. (2020b) proposed the opposite scenario, whereby higher currents prevent the deposition of detrital material and leads to laminar growth textures. Yeo et al. (2018a) also noted that the dominant detrital grains within Tropic Seamount FeMn crust horizons associated with chaotic textures were intact foraminifera that were likely deposited in low energy environments. The positive correlation between maximum current velocities and Factor 2, which is interpreted as a hydrogenetic Fe-oxyhydroxide, supports the theory that higher energy current environments play a role in affecting the relative proportions of hydrogenetic Fe- and Mn- phase growth relative to detrital input, which in turn affects FeMn crust composition.

A weak positive correlation between Factor 1 (a goethite-type Fe oxyhydroxide phase) and the slope angle of the substrate (R^2 = 29%; Figure 6.8B), but no other significant correlations are observed with the environmental variables assessed in this study and it is likely that there are other drivers of variability that are not captured by the secondary bathymetric derivatives. Variations in the slope angle in seamount environments could control a range of factors that might affect FeMn crust composition. The slope angle can determine trends in sediment deposition around the seamount structure (Palomino et al., 2016). Slope angle may also be related to the stability of the

seamount structure, depending on the mechanical and structural properties of the underlying substrate (Hühnerbach and Masson, 2004). A stable, sediment-free substrate is stipulated to be a prerequisite for FeMn crust formation, as it provides a hard surface onto which FeMn crust can slowly accumulate (Halbach and Manheim, 1982; Hein et al., 1985). These slow accumulation rates also support significant enrichment of numerous elements, such as Co and Ce, as increased exposure times allow for the slow redox kinetics of surface oxidation processes. As all samples analysed in this study were the most recent growth surfaces, it is unlikely that there will be significant differences between samples in formation age that would be a sufficient driver of the variance in composition observed. Therefore slope-driven trends in sediment deposition patterns are more likely to contribute to variations in local trends in FeMn crust composition, for example through the accumulation of detrital or biogenic debris material.

6.5.3 Local Environmental Controls on FeMn Crust Composition

Water depth and dissolved oxygen concentrations have been observed to play important roles in the composition of FeMn crusts. While these factors can account for some of the variance we have observed across the seamount structure in this study, analysis of FeMn crust horizons also show comparable levels of variance (Table 6.5 and Table 6.6) even for summit samples at similar water depths and dissolved oxygen concentrations. Factor analyses of summit samples found three key phases that are driving 80% of the observed compositional variance which have been interpreted as an Fe oxyhydroxide phase with variability dominated by REY concentrations, an Mn oxide phase that shows biogenic influence and an Mn oxide phase that shows distinct hydrogenetic signatures (e.g. Co association). The individual sample scores for each factor were compared to the environmental variable values at those sites as well as geochemical indicators to investigate potential controls on the phase associations.

Scores for Factor 1, interpreted as an Fe oxyhydroxide phase that explains 43% of the compositional variance, did not show distinct correlations with any of the environmental factor used in this study but showed a strong negative correlation with Ce anomaly values (R^2 = 72%, Figure 6.9). Similarly, Factor 3 a hydrogenetic Mn oxide that explains 19% of the variance, also showed strong negative correlations with Ce anomalies (R^2 = 61%; Figure 6.10). Sequential leaching studies and spectroscopic studies have shown that Ce is associated with Mn oxide phases in FeMn crusts (e.g. Koschinsky et al., 1995; Takahashi et al., 2000) but Bau and Koschinsky (2009) observed comparable Ce anomalies for both Fe- and Mn- phases. The relationship between Ce anomaly and both Factors 1 and 3 supports an association with both Fe oxyhydroxides and Mn oxides in these samples. As previously discussed, Ce behaviour is redox-sensitive and positive Ce anomalies are distinctive of hydrogenous FeMn crusts (e.g. Kuhn et al., 1998; Bau and Koschinsky, 2009; Bau et al., 2014). This suggests that the primary source of

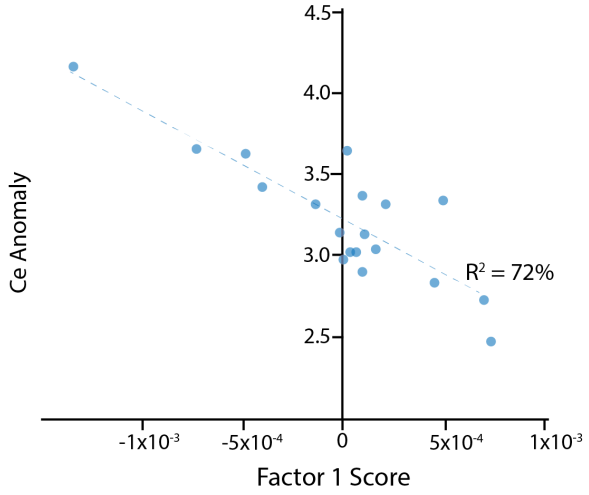

FIGURE 6.9: Factor score correlations for summit horizon samples between Factor 1 (an Fe oxyhydroxide) and Ce anomalies.

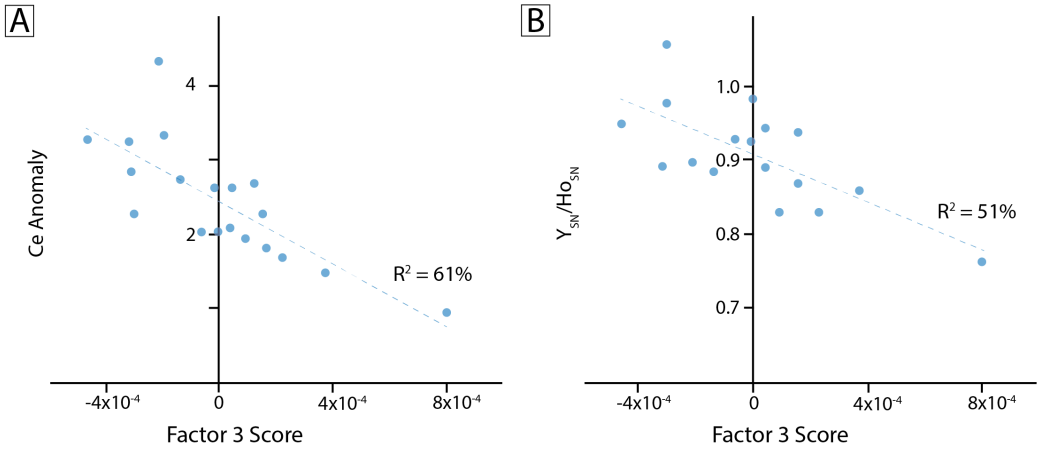

FIGURE 6.10: Factor score correlations for Factor 3 (a hydrogenetic Mn oxide) and A) Ce anomaly and B) Y_{SN}/Ho_{SN}.

compositional variance in FeMn crusts at the local scale could be differences in redox, potentially due to the effects on bonding environment and phase association.

Factor 3 scores also showed a negative correlation with Y_{SN}/Ho_{SN} ratios ($R^2 = 51\%$; Figure 6.10B). Unlike Factor 3, Factor 1 scores did not show any correlation with Y_{SN}/Ho_{SN} ratio, suggesting different mechanisms of REY incorporation between Fe oxyhydroxides and Mn oxides. Slight differences in Y behaviour have been reported between Fe oxyhydroxides and Mn oxides, with Fe oxyhydroxides showing slightly larger Y anomalies (Bau et al., 2014). While a change in Ce anomaly can be an indicator of changing redox environment due to surface oxidation processes (Bau and Koschinsky, 2009), in general hydrogenetic FeMn crusts usually show coherent REY distribution patterns as they represent a relatively simple exchange equilibrium between seawater REY(III) complexes and Fe and Mn phase REY(III) surface complexes (Bau et al., 1996).

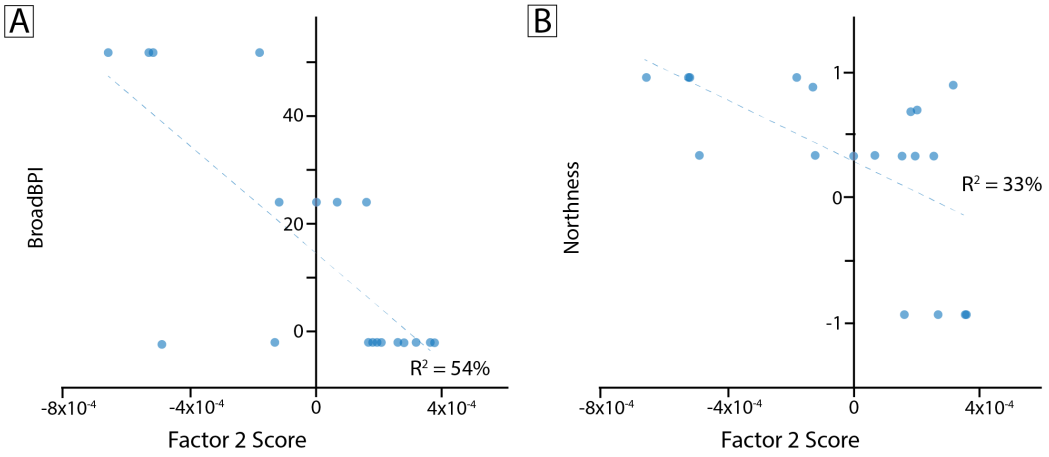

FIGURE 6.11: Factor correlation scores for summit horizon samples between Factor 2 (an Mn Oxide with biogenic influence) and A) Broad BPI and B) Northness.

Hydrogenetic crusts show distinctively low Y anomalies ($Y_{SN}/Ho_{SN} < 1$) due to the preferential scavenging of Ho onto metal oxyhydroxide surfaces when compared to Y, as Y surface complexes have lower stabilities (Bau et al., 1996), whereas hydrothermal deposits have positive Y anomalies (Bau et al., 2014). The differences in correlations between Fe oxyhydroxides and Mn oxides with REY observed in this study support differential Y – Ho scavenging processes between these phases.

The second phase that has been interpreted to account for 19% of the variance in composition in the FeMn crusts studied is an Mn oxide phase that is associated with biogenic input. In particular, this factor showed the highest loading for Ba, which is dominantly associated with Mn oxides in FeMn crusts, most likely as sorbed Ba^{2+} (Koschinsky and Hein, 2003). In marine environments, FeMn oxyhydroxides act as a Ba sink with concentrations between 1000 – 2000 ppm (Dymond et al., 1992) and have been associated with Mn oxides, although it has been noted that in leaching experiments of phosphatised crusts that Ba was likely also associated with apatite (Koschinsky and Halbach, 1995).

Barium content in FeMn crusts is thought to reflect variations in the biological activity of the overlying water column, but may also relate to the provenance and sedimentation rate of opal and alumino-silicate phases and residual particulate barite (e.g. Dymond et al., 1992; Gonneea and Paytan, 2006). Hydrothermal fluids also have elevated concentrations of Ba but there are no other geochemical indicators within the samples analysed in this study of hydrothermal FeMn crust formation. Factor 2 also shows strong negative loadings for Ca which supports a Ba-enrichment of Mn oxide phases that anticorrelate with Ca due to dilution by carbonates, rather than being driven by carbonate-associated Ba. Dymond et al. (1992) noted that Ba concentrations at depth may be affected by diagenesis, due to redox mobilisation in sediments and FeMn crusts under suboxic conditions. When compared with environmental variables, this factor

showed moderate negative correlations with both BPI (R^2 = 54%) and northness measures (33%) (Figure 6.11). This shows high correlations of biogenically-influenced Mn oxide phases with regions corresponding to topographic lows in relation to their surroundings (low BPI values) and also a potential role for aspect. This relationship may relate to either spatial patterns in bioproductivity above Tropic seamount, that change the flux of biogenic material to different regions, or to local biogenic sedimentation patterns driven by deposition in relatively low energy areas of the summit, such as substrate depressions.

While this factor does not show significant correlations with current speed (R^2 = 11%), at the local scale of the summit surface the interaction of currents with local topography can lead to small scale variations in surface sediment distribution. Seamount structures are widely proposed to be areas of elevated productivity, as they can drive the upwelling of nutrient-rich deep waters to surface regions (Dower et al., 1992; Genin and Boehlert, 1985; Genin, 2004), although it is noted that this is likely limited to seamounts with summits near the ocean surface (e.g. Genin, 2004). Tropic Seamount is an isolated seamount and it has been proposed that it does not affect surface ocean waters (Giljan et al., 2020). The short temporal scales of variability in primary productivity will not be recorded by FeMn crusts due to their slow rates of formation. Furthermore, the scale of variation in surface productivity and the translation of that variability to waters 2000 m below is unlikely to match the scale of compositional variance observed in FeMn crusts and it is proposed that near-bed transport processes play a more important role. At Tropic Seamount, current modelling showed weak anti-cyclonic rotating circulation patterns around the seamount summit with a potential weak Taylor cap close to the seabed (Cooper and Spearman, 2017). Palomino et al. (2016) noted that sedimentary distribution patterns on Tropic Seamount's summit are characterised by mixed sediment accumulation, with filled depressions causing relatively homogenous summit morphologies, an observation supported by high-resolution outcrop mapping by (Yeo et al., 2019). The rotating nature of these flows close to the seabed could mean that detrital material, such as barite, could be concentrated in depressions at the summit and subsequently influence the composition of proximal FeMn crusts. Therefore, it is proposed that local scale depositional patterns of detrital biogenic phases, driven by topography and its interactions with current regimes, is the more likely driver of Mn oxide variability on seamount summit environments.

6.6 Conclusions

The surface scrape chemistry of 121 FeMn crust samples from Tropic Seamount was investigated to understand the controls on FeMn crust composition at the scale of individual seamounts. While the overall composition showed consistent hydrogenetic

growth across the seamount, with dominantly distinct positive Ce anomalies and negative Y anomalies, significant variance in major and trace element concentrations were observed. Q-mode factor analyses were conducted on a range of sample subsets to improve understanding of local scale controls on composition. Comparisons of upper and lower recent growth surfaces show that while Fe oxyhydroxides exert the greatest control on composition, the local formation conditions lead to differences in elemental associations and behaviours. In particular, the associations between the REY and Ce differ between upper and lower surfaces, with lower surfaces displaying greater susceptibility to replacement of Mn oxides by CFA phases. The observation of compositional variability with water depth at Tropic Seamount was observed for numerous elements and included water depth controls that extended beyond dissolved oxygen concentration. In particular, the increase in Mn/Fe of surface scrapes with increasing water depth is stipulated to be driven primarily by changes in the proportions between the main mineralogical constituents of FeMn crusts, with greater Fe oxyhydroxides at summit regions and Mn oxides dominating at depth. This divergence in behaviour from Pacific Ocean studies is due to the proximity of Tropic Seamount to continental dust and margin sediment sources. In this region of the NE Atlantic, it is proposed that dissolved metal concentration availability exert the greatest control on these proportions, with enhanced dissolved Fe in summit regions and decreasing with depth. At the local scale, variation in FeMn crust composition was observed between samples collected from a narrow range of water depths, from Tropic Seamount's summit. The key drivers of variance appear to be related to local redox environment, which may be exerting controls on mineral phases and species bonding behaviours. Composition of both Fe oxyhydroxides and Mn oxides are also observed to vary with different physical environmental variables, such as slope angle, current velocities and local topographic environment. This is likely due to the controls that topographic features impart on the distribution patterns of detrital phases (particularly biogenic) through sediment accumulation and the related dilution of hydrogenetic phases.

Chapter 7

Conclusions and further work

There is an extensive history of exploration of FeMn crust deposits in the world's ocean basins since 1970s. Rejuvenated interest in FeMn crusts over the past two decades as a potential source of some the elements that are critical to the expansion of renewable energy technologies, as well as the improvement in exploration methods has contributed to the increased interest in potential exploitation of these resources. While the spatial variability of FeMn crust characteristics have been widely reported at the scale of the ocean basin, there remains a need to quantify and understand the variability of FeMn crusts at the scale of individual seamounts. This is particularly necessary for the Atlantic Ocean seamounts, which remain understudied in comparison to Pacific seamounts. Improving understanding at this spatial resolution is necessary to allow for accurate resource assessments at the scale of the potential mine-site and also to understand the potential impacts of these activities on the surrounding environment and to develop robust environmental impact assessments.

In order to provide new insights into the variability of FeMn crusts at the scale of an individual seamount, I have undertaken detailed observational, textural and geochemical investigations and investigated the potential controls on FeMn crust formation, distribution and preservation for Tropic Seamount in the NE Atlantic. The principal outcomes of this work are provided below, and is followed by a discussion on potential further areas of research.

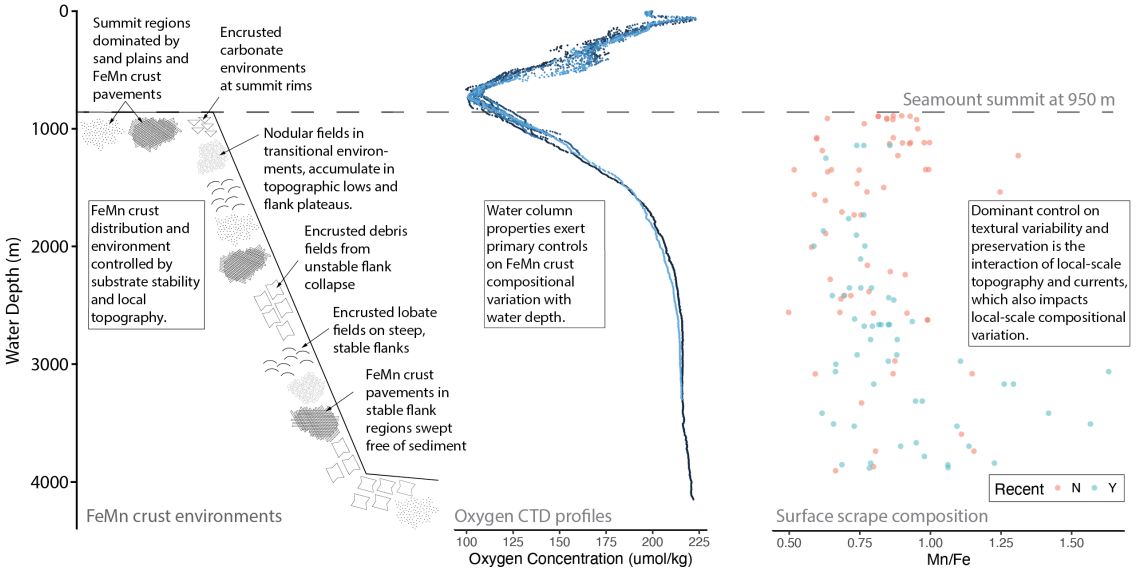

FIGURE 7.1: Schematic diagram to summarise the key findings of this study into the controls on FeMn crust occurrence, preservation and composition at Tropic Seamount.

7.1 Conclusions of the study

7.1.1 Controls on seamount-scale ferromanganese crust distribution: Tropic Seamount, NE Atlantic

The detailed distribution of FeMn crust and the controls on occurrence at sub-basin scales is required to develop appropriate economic and environmental impact assessments, but requires further quantification. To improve understanding of the variation of FeMn crust distribution, I have conducted detailed FeMn crust outcrop mapping at Tropic Seamount using observational data collected from ROV (Chapter 4). Variations in observed FeMn crust "type" environment have been used to develop an understanding of key trends in outcrop variability (Figure 7.1). This observational data has also been used to build a seamount-scale FeMn crust distribution model that provides statistically robust predicted presence and absence probabilities. This work predicted that FeMn crust presence was highest around the outer summit regions and along seamount flanks. The main controls on occurrence variability are proposed to depend on both the substrate characteristics and interactions of local topography and current regimes which exert fundamental controls on the amount and distribution of exposed hard surface and the period of exposure. This work was also the first of its kind to apply distribution models commonly used in species distribution modelling to model the distribution of FeMn crusts. The high predictive accuracy of the models built within this study demonstrate the strength of using these techniques to improve understandings of FeMn crust occurrence.

7.1.2 Seamount-scale FeMn crust accumulation and preservation and the effects on composition

The variability of FeMn crust thickness and composition has been widely reported in past studies but characterisation of this variation at high-spatial resolutions across an individual seamount have been limited to one seamount in the Pacific Ocean. Furthermore, understandings of thickness variation remain one of the most significant sources of uncertainty in deposit modelling. At Tropic Seamount, FeMn crusts accumulate through hydrogenetic growth (Chapter 5 and Chapter 6). Average Co concentrations of 0.5 wt% measured at Tropic Seamount were observed to be higher than reported Atlantic and Indian Ocean averages and average Te concentrations of 51 ppm exceed those reported averages for Atlantic, Indian and Pacific Ocean basins (Chapter 5). While average trace element concentration are promising, significant spatial variation was observed. In order to elucidate the potential trends and controls on FeMn crust accumulation and composition, variations in preservation and growth rates around Tropic Seamount were investigated. Textural observations and elemental trends support the significant role of detrital inputs on potential resource grade, with increased detrital inputs leading to increase dilution of target elements. Patterns in erosive surfaces demonstrate the important role that near-bed shear stresses play in maintaining an exposed surface that encourages the slow accumulation of hydrogenetic growth and associated enrichment in trace elements such as Co, with the most prospective concentrations observed at summit regions at Tropic Seamount, and also minimises the effect of detrital dilution. Detrital inputs can also lead to higher estimated FeMn crust growth rates and presents a complex challenge for determining resource potential. The flux of detrital material to FeMn crusts is controlled by a range of factors, including source availability and the interaction of near-bed currents with local topography (Figure 7.1).

7.1.3 Seamount-scale controls on ferromanganese crust composition in the NE Atlantic

Ferromanganese crusts vary significantly in their composition across a range of scales, both spatially and temporally, as composition reflects the environment and mode of formation. The spatial controls on FeMn crust variability at the scale of an individual seamount have been hindered by the lack of availability of data collected systematically at high spatial scales. This is further complicated by the slow growth rates of FeMn crusts that limits physical sampling techniques. This means that bulk compositional analysis of FeMn crusts averages the compositional changes over long time periods that may have experienced significant changes in oceanography and can mask the potential role of location environmental factors. To address this, I targeted contemporaneous FeMn growth horizons, including surface scrape materials, and analysed samples from a range of locations and environments from Tropic Seamount (Chapter

6). Factor analyses showed that at Tropic Seamount, the primary driver of compositional variability is the composition of Fe-oxyhydroxide phases and subsequent ratio of Fe-oxyhydroxides and Mn-oxides. The controls on the composition of phases varied between upper and lower recent growth surfaces, as observed from differences in the behaviour and associations of the REY. This is likely due to the influence of burial on local redox and well as the role for interstitial fluids on lower surfaces. Samples also showed systematic trends with both water depth and dissolved oxygen concentrations that differ from those reported for Pacific Ocean FeMn crusts (Figure 7.1). This study found that for Tropic Seamount FeMn crusts, Mn/Fe increased with increasing water depth. This is likely due to the importance of proximal continental dust sources that coincide with biogenic remineralisation at depth and could be a key consideration for FeMn crusts in this region. At comparable water depths, analysis of composition from summit regions showed relationships between local microtopography and detrital phases. This demonstrates the importance of understanding local scale topography and the role this can play on detrital flux to FeMn crusts as this is a significant factor in the local scale variability of crust composition.

7.2 Areas for further research

7.2.1 Further work on FeMn occurrence controls

Chapter 4 showed the strength in using statistical distribution modelling for understanding the local scale variation in FeMn crusts across a single seamount in the NE Atlantic. While this can be a powerful technique to predict outcrop distribution and has been shown to be highly accurate for this sample site, the applicability of the model at other sample sites is unknown as the dataset is trained on environments observed at Tropic Seamount. I suggest future research to firstly assess the predictive strength of this model at other sample sites. This would require similarly detailed studies at other sites, but further research could be conducted to understand the accuracy limits of models built with less detailed datasets. This could be tested using Tropic Seamount data, by comparing model performance with increasingly restricted input data. Once the limits of model performance by input data are quantified, similar studies could be made at other sample sites, with both similar morphologies as well as different encrusted structures to better understand which of the environmental variable might dominate predictive strengths under these conditions. At the moment, high spatial resolution studies at other sites are limited due to the time intensive nature of such surveys. For future research I suggest that the automation of environment categorisation combined with the distribution modelling techniques displayed here could be a powerful technique for predicting FeMn crust distribution.

7.2.2 Variability of FeMn crust accumulation and preservation

As shown in Chapter 5, the estimated growth rates of FeMn crusts at Tropic seamount vary with location but relationships between estimated growth rates and accumulated FeMn crust thickness remain complex. Growth rate estimates in this study were calculated using Co-chronology from the composition of recent growth horizons (the uppermost 10 mm). While this provides a tool to compare with modern hydrographic regimes, there is also evidence of variations in growth rates over time and for future work a more quantitative assessment of growth rates would allow for further interrogation of the controls on crust growth. To maintain the high spatial resolutions required to better understand the controls location around the seamount imparts on growth rate, a potential approach could be to use comparable methods to those used in Chapter 6 for developing an extensive Pb LA ICP-MS correlative stratigraphy for some of the samples analysed in Chapter 5. This could also be combined with correlating textural and geochemical mapping, such as trace element LA ICP-MS profiles and SEM-EDS maps, as well as mineralogical characterisation through the full FeMn crust growth profile. This would provide an opportunity to further validate and fully quantify the correlation between FeMn crust accumulation and preservation, and facilitate an investigation into the role of erosive periods through time.

7.2.3 Variability of FeMn crust composition

In Chapter 6, I used factor analyses of chemical composition and elemental correlation matrices to identify key phases that affect the compositional variability of FeMn crusts at Tropic Seamount. To validate the findings in this chapter, for further work I would undertake more detailed methodologies to determine the mineralogy of FeMn crust samples. While X-Ray Diffractive could be used to provide further information on mineralogy, the high proportion of amorphous Fe-Mn-oxyhydroxides within FeMn crusts limits the ability to discriminate between the specific polymorphs and phases. For future work to quantify the mineralogy of Tropic Seamount's FeMn crusts, I would conduct electron microprobe analyser (EMPA) studies. I could also undertake sequential leaching processes for FeMn crust material, to separate the different phases prior to elemental analysis and shed more light on the elemental associations observed in this study.

7.2.4 Improving FeMn crust resource models at the seamount-scale

Each of the investigations within this study were conducted with the intention to investigate some of the process-driven controls on FeMn crust variability to improve theoretical understanding to better inform genetic models. In turn, the techniques applied within this study would also lend themselves to the development of a detailed empirical model of FeMn crust resources at Tropic Seamount. For future work, these techniques can be combined to build a detailed resource assessment of FeMn crusts at Tropic Seamount. This would require appropriate choice of modelling resolutions, informed by a detailed understanding of the scale of controlling processes on variance, and an accompanying investigation of the associated uncertainties. This would be particularly powerful if conducted after the suggestions of further work detailed for distributional, thickness and compositional detailed above as it could facilitate the application of this deposit model to other potential sites.

Appendix A

Supplementary material to the geochemical analyses

A.1 Data validation for ICP-QQQ analyses of FeMn crusts

TABLE A.1: Data Validation for ICP-QQQ values for 10 mm FeMn crust samples

	Nod-A1 (n=2)			Nod-P1 (n=2)			HRM (n=4)			
Element	Mean	External	Accuracy	Mean	Precision	External	Mean	Precision	Accuracy	Internal
mg/kg	mg/kg	%RSD	%RE	mg/kg	%RSD	%RE	mg/kg	%SD	%RE	%RSD
7 Li	81.4	9	7	148.4	2	5	5.5	0.73	13	7
9 Be	6.2	3	11	2.4	28	52	11.9	1.27	11	6
23 Na	8057.5	10	6	17896.6	2	9	10594.0	366.55	3	6
24 Mg	29194.1	8	2	20409.3	6	3	11237.5	501.12	4	6
27 Al	20184.9	5	1	23155.7	2	9	12720.3	551.93	4	6
31 P	5405.2	12	11	2049.5	13	2	5656.2	727.43	13	4
32 S	3123.8	13	7	800.9	15	20	3042.7	413.57	14	4
39 K	4820.6	6	3	10345.3	6	3	3459.9	298.92	9	4
42 Ca	116003.4	7	5	23327.6	4	6	21233.6	1767.56	8	5
47 Ti	2864.8	12	10	2635.2	11	12	7306.5	915.36	13	2
51 V	646.4	5	16	506.9	5	2	1172.5	109.18	9	3
52 Cr	21.6	1	32	16.4	0	1	25.6	2.56	10	4
55 Mn	181803.1	11	2	284717.3	7	2	144588.0	20057.45	14	3
56 Fe	115495.1	3	6	63778.0	1	10	242009.6	15407.61	6	6
59 Co	3231.8	8	4	2307.9	4	1	4860.4	539.32	11	4
60 Ni	6728.4	3	6	14676.6	5	10	2264.3	188.84	8	3
63 Cu	1135.8	6	3	11632.3	4	1	498.7	51.32	10	4
66 Zn	576.9	10	2	1540.1	7	4	545.9	77.85	14	3
71 Ga	7.5	0	19	28.9	2	3	8.2	0.62	8	-
72 Ge	0.0	16	94	0.1	27	91	0.1	0.01	21	4

	Nod-A1 (n=2)			Nod-P1 (n=2)			HRM (n=4)			
Element	Mean	External	Accuracy	Mean	Precision	External	Mean	Precision	Accuracy	Internal
mg/kg	mg/kg	%RSD	%RE	mg/kg	%RSD	%RE	mg/kg	%SD	%RE	%RSD
75 As	287.7	14	7	80.5	10	7	466.7	50.65	11	7
78 Se	0.1	9	96	0.5	2	78	0.7	0.03	4	3
85 Rb	10.4	14	2	25.1	18	10	7.3	1.14	16	3
88 Sr	1635.2	7	7	673.4	5	1	1518.6	135.17	9	6
89 Y	111.9	9	4	81.7	5	13	203.1	25.09	12	3
90 Zr	294.6	11	12	244.9	6	14	539.7	47.57	9	3
93 Nb	45.2	10	5	20.0	7	5	93.5	13.15	14	2
95 Mo	399.7	9	11	678.6	4	11	479.2	57.65	12	5
107 Ag	0.0	32	81	0.1	15	69	0.0	0.01	26	2
111 Cd	8.1	11	9	24.5	5	11	2.5	0.34	14	5
115 In	0.1	33		0.1	15		0.1	0.01	11	2
118 Sn	3.6	10	21	2.6	6	39	5.9	0.81	14	2
121 Sb	37.2	10	10	54.3	7	3	60.7	9.02	15	2
125 Te	35.0	9	13	5.0	4	3	44.6	5.67	13	3
133 Cs	0.6	14	5	1.7	11	10	0.3	0.05	16	3
137 Ba	1386.6	13	17	2507.7	5	2	1202.4	114.34	10	3
139 La	119.6	20	1	105.3	9	3	367.8	33.19	9	5
140 Ce	815.6	11	12	338.3	4	7	1784.7	157.60	9	3
141 Pr	24.6	13	1	30.8	7	4	71.0	6.50	9	3
146 Nd	109.4	14	16	138.2	8	4	311.5	30.63	10	3
147 Sm	23.7	14	12	33.1	8	5	62.4	5.76	9	2
153 Eu	5.3	15	6	7.3	8	6	13.7	1.39	10	2

Element	Nod-A1 (n=2)			Nod-P1 (n=2)			HRM (n=4)			
	Mean	External	Accuracy	Mean	Precision	External	Mean	Precision	Accuracy	Internal
mg/kg	mg/kg	%RSD	%RE	mg/kg	%RSD	%RE	mg/kg	%SD	%RE	%RSD
157 Gd	24.9	12	4	29.6	7	5	62.7	5.27	8	2
159 Tb	3.7	13	86	4.4	7	86	9.1	0.81	9	3
163 Dy	24.0	12	5	26.2	7	4	56.3	5.45	10	2
165 Ho	4.9	13	3	4.8	7	6	10.8	1.01	9	3
166 Er	14.7	11	24	13.1	6	4	29.6	2.86	10	2
169 Tm	2.2	11	3	1.9	7	2	4.2	0.39	9	2
172 Yb	14.0	9	1	12.7	5	3	26.4	2.33	9	2
175 Lu	2.2	14	2	1.8	6	3	3.9	0.34	9	3
178 Hf	6.3	10	23	3.8	7	6	11.8	1.01	9	1
181 Ta	0.7	9	4	0.3	10	11	2.4	0.20	8	3
182 W	83.7	8	4	56.7	5	1	105.0	8.33	8	1
205 Tl	124.2	12	9	217.8	10	22	73.1	10.21	14	4
208 Pb	861.1	11	2	468.9	9	7	1762.1	176.20	10	3
209 Bi	10.3	12	1	5.1	8	12	15.6	1.58	10	-
232 Th	22.3	11	8	14.9	7	9	46.2	4.51	10	3
238 U	6.9	9	2	4.0	8	3	12.3	2.17	18	5

A.2 Data validation for ICP-QQQ analyses of surface scrape FeMn crusts

TABLE A.2: Data Validation for ICP-QQQ values for surface scrape FeMn crust samples

	Nod-A1 (n=2)			Nod-P1 (n=2)			HRM (n=4)		
Element mg/kg	Mean mg/kg	External %RSD	Accuracy %RE	Mean mg/kg	Precision %RSD	External %RE	Mean mg/kg	Precision %SD	Accuracy %RE
7 Li	74	7	2	135	4	4	3.9	1.82	47
9 Be	5	5	10	2	47	69	10.8	1.94	18
23 Na	7480	6	1	15378	2	6	9482.5	304.75	3
24 Mg	26185	7	9	18123	5	9	10679.7	581.77	5
27 Al	18387	4	10	21214	2	17	11459.4	511.58	4
31 P	4727	12	22	1803	3	10	4188.7	130.25	3
32 S	2783	10	17	716	11	28	2453.6	50.38	2
39 K	4423	8	11	9455	3	5	3132.6	118.72	4
42 Ca	104707	5	5	20333	2	8	18973.8	1836.09	10
47 Ti	2648	6	17	2461	2	18	6730.7	138.46	2
51 V	584	8	24	462	5	7	959.0	34.84	4
52 Cr	21	3	33	15	2	12	21.5	1.10	5
55 Mn	167134	5	10	270520	1	7	130046.8	1923.83	1
56 Fe	107126	7	2	57782	2	0	214032.2	5241.94	2
59 Co	3033	8	2	2086	4	9	4354.5	163.82	4
60 Ni	6033	8	5	13684	4	2	1865.0	59.42	3
63 Cu	990	7	10	10734	3	7	414.4	14.86	4
66 Zn	538	6	9	1460	2	9	502.6	12.56	2

	Nod-A1 (n=2)			Nod-P1 (n=2)			HRM (n=4)		
Element	Mean	External	Accuracy	Mean	Precision	External	Mean	Precision	Accuracy
mg/kg	mg/kg	%RSD	%RE	mg/kg	%RSD	%RE	mg/kg	%SD	%RE
71 Ga	4	50	38	25	20	12	1.7	2.22	134
72 Ge	0	52	97	0	51	95	0.0	0.02	100
75 As	259	5	16	75	1	13	394.3	15.30	4
78 Se	0	138	97	1	24	76	0.7	0.22	34
85 Rb	10	6	1	24	5	14	6.9	0.21	3
88 Sr	1350	5	23	584	2	14	1182.1	21.12	2
89 Y	109	6	6	81	2	13	196.8	5.99	3
90 Zr	17	135	95	171	39	40	94.1	146.91	156
93 Nb	26	10	39	18	0	12	37.8	24.09	64
95 Mo	344	7	23	588	3	23	397.4	11.62	3
107 Ag	0	289	102	0	74	70	0.0	0.01	-194
111 Cd	7	7	1	22	5	1	2.1	0.06	3
115 In	0	31	-	0	78	-	0.1	0.03	39
118 Sn	3	10	10	3	2	59	5.0	0.22	4
121 Sb	33	7	3	51	1	4	52.1	1.80	3
125 Te	36	0	15	5	13	13	40.1	3.02	8
133 Cs	1	10	2	2	2	13	0.2	0.03	14
137 Ba	1397	6	16	2457	3	4	1264.4	32.07	3
139 La	107	8	10	100	5	7	319.3	10.38	3
140 Ce	717	7	2	302	3	5	1675.4	77.02	5
141 Pr	23	8	7	30	3	7	68.4	2.71	4
146 Nd	98	8	4	129	5	3	282.1	7.76	3

	Nod-A1 (n=2)			Nod-P1 (n=2)			HRM (n=4)		
Element	Mean	External	Accuracy	Mean	Precision	External	Mean	Precision	Accuracy
mg/kg	mg/kg	%RSD	%RE	mg/kg	%RSD	%RE	mg/kg	%SD	%RE
147 Sm	21	5	1	31	3	3	58.2	1.52	3
153 Eu	5	8	3	7	3	4	13.6	0.44	3
157 Gd	24	10	6	30	5	5	61.3	1.59	3
159 Tb	4	7	86	4	5	86	8.9	0.26	3
163 Dy	23	9	0	26	7	6	53.5	2.52	5
165 Ho	5	6	9	5	3	9	10.3	0.40	4
166 Er	14	8	18	13	5	6	28.4	1.00	3
169 Tm	2	5	3	2	6	6	4.0	0.15	4
172 Yb	13	8	6	12	5	7	24.8	0.83	3
175 Lu	2	9	5	2	6	6	3.8	0.16	4
178 Hf	0	22	98	2	43	42	2.1	3.31	158
181 Ta	0	166	103	0	116	75	0.4	0.75	174
182 W	78	8	10	54	4	6	95.8	4.96	5
195 Pt	1	9	2	0	9	2	0.2	0.02	10
205 Tl	111	7	3	196	4	10	70.3	2.70	4
208 Pb	775	9	8	421	5	16	1595.4	72.84	5
209 Bi	10	5	4	5	1	13	14.9	0.38	3
232 Th	21	6	12	14	3	12	43.5	1.85	4
238 U	7	9	2	4	7	5	11.0	0.43	4

A.3 Data validation for ICP-MS analyses of horizon FeMn crusts

TABLE A.3: Data Validation for ICP-MS values for horizon FeMn crust samples

Element	Nod-A1 (n=2)			Nod-P1 (n=2)		
mg/kg	Mean	%RSD	%RE	Mean	%RSD	%RE
7Li	77.8	49	2	78.4	67	44
44Ca	51385.6	82	54	51654.0	78	54
45Sc	8.9	10	30	8.6	9	30
47Ti	2305.9	4	31	2328.5	3	31
51V	434.6	15	44	442.2	11	44
52Cr	1.0	1496	97	2.0	742	97
55Mn	224039.0	29	13	221332.8	29	27
56Fe	75023.0	35	39	76064.4	33	39
59Co	2385.7	20	23	2413.2	17	23
60Ni	8733.2	41	37	9021.7	43	33
65Cu	5538.4	95	403	5787.9	96	50
66Zn	392.2	383	167	-311.6	566	167
85Rb	14.6	52	43	14.7	56	44
86Sr	919.5	45	47	955.3	46	47
89Y	95.7	15	18	96.7	14	18
90Zr	249.8	6	26	254.0	4	26
93Nb	31.0	43	28	31.2	41	28
95Mo	450.4	30	1	452.8	31	40
118Sn	1.3	372	143	2.3	226	143
133Cs	1.1	66	82	1.1	58	40
137Ba	1778.7	31	7	1810.2	32	46
139La	100.2	3	15	101.9	2	15

Element	Nod-A1 (n=2)			Nod-P1 (n=2)		
mg/kg	Mean	%RSD	%RE	Mean	%RSD	%RE
140Ce	496.0	48	32	495.9	46	32
141Pr	25.8	16	4	26.4	16	19
146Nd	106.6	16	13	108.2	17	9
147Sm	24.7	19	18	25.4	23	14
153Eu	6.1	21	23	6.1	22	18
157Gd	25.3	13	3	25.6	15	3
159Tb	3.9	13	1	4.1	12	1
163Dy	22.8	8	0	23.0	9	14
165Ho	4.5	4	10	4.5	3	10
166Er	12.8	5	10	12.7	3	6
169Tm	2.0	6	8	1.9	6	8
172Yb	12.4	5	10	12.5	2	10
175Lu	2.0	7	11	1.9	8	11
178Hf	4.4	22	27	4.6	25	27
181Ta	0.5	27	31	0.9	64	31
182W	67.1	22	23	68.3	21	23
208Pb	615.8	36	27	618.8	34	27
232Th	17.8	23	26	18.0	21	26
238U	5.2	32	25	5.3	32	25

A.4 Rare earth element composition of Post-Archean Australian Shale

TABLE A.4: PAAS values from McLennan (2001); Condie (1993)

Element	Concentration (ppm)
La	41
Ce	83
Pr	10.1
Nd	38
Sm	7.5
Eu	1.61
Gd	6.35
Tb	1.23
Dy	5.5
Ho	1.34
Er	3.75
Tm	0.63
Yb	3.53
Lu	0.61
Y	27

Appendix B

Supplementary material to Chapter 5

B.1 Rare Earth Element and Y concentrations

TABLE B.1: Rare Earth Element and Y concentrations in FeMn crusts from Tropic Seamount

Sample Name	La	Ce	Pr	Nd	Sm	Eu	Gd	Tb	Dy	Ho	Er	Tm	Yb	Lu	Y	REY
	ppm	ppm	ppm	ppm	ppm	ppm	ppm	ppm	ppm	ppm	ppm	ppm	ppm	ppm	ppm	ppm
JC142_009_010	335	1810	69.7	303	59.6	12.8	56.4	8.09	49.8	9.50	25.3	3.72	22.1	3.34	158	2926
JC142_020_017	360	1745	72.0	309	61.5	13.0	58.1	8.48	51.8	9.95	28.2	3.97	25.1	3.62	180	2930
JC142_039_003	262	1380	55.6	232	47.0	9.8	40.7	5.91	34.4	6.20	17.7	2.44	16.4	2.30	102	2214
JC142_039_005	305	1336	68.1	288	56.8	12.0	49.7	7.17	41.3	7.52	21.2	2.88	19.3	2.67	122	2340
JC142_039_007	338	1454	69.4	302	62.3	13.3	60.5	8.76	52.8	9.92	27.4	3.89	24.8	3.61	178	2609
JC142_039_012	235	1298	45.6	193	38.0	8.2	34.8	5.10	30.3	5.64	15.7	2.26	14.5	2.13	101	2029
JC142_039_015	307	1406	65.8	278	55.2	12.0	51.1	7.38	43.6	7.89	22.2	3.02	19.9	2.75	130	2412
JC142_039_017	416	1878	85.9	369	74.0	16.2	72.3	10.50	62.8	11.80	34.0	4.45	29.7	4.04	217	3286
JC142_039_019	363	1787	77.7	331	65.9	14.1	60.6	8.71	51.7	9.48	26.5	3.66	23.5	3.27	158	2984
JC142_039_020	331	1400	66.7	291	57.8	12.5	56.9	8.19	49.8	9.39	25.9	3.63	22.8	3.33	165	2504
JC142_039_021	300	1448	58.9	257	50.4	11.1	50.1	7.27	44.9	8.57	24.4	3.40	22.0	3.21	156	2445
JC142_039_024	234	1091	46.4	204	41.1	9.0	40.7	5.79	36.0	7.11	20.9	2.91	19.5	2.91	192	1953
JC142_047_007	238	1648	46.9	200	39.7	8.5	37.5	5.52	34.4	6.71	19.3	2.78	17.7	2.62	119	2427
JC142_047_012	160	1014	31.5	136	27.1	5.9	26.7	3.97	24.9	4.89	14.1	2.02	13.4	1.99	84.4	1551
JC142_055_001	284	1632	58.9	254	52.4	11.3	52.6	7.66	46.9	8.92	25.7	3.64	23.8	3.52	170	2635
JC142_055_002	340	1510	65.8	289	58.4	13.0	60.2	8.75	54.0	10.40	28.3	3.99	25.0	3.81	188	2659
JC142_055_006	412	1941	84.8	369	74.4	16.2	72.5	10.50	64.0	12.00	32.6	4.53	28.0	4.25	205	3331
JC142_055_007	308	1664	63.1	272	55.3	12.1	54.0	8.01	49.1	9.41	25.8	3.67	23.2	3.52	168	2719
JC142_055_008	374	2107	74.7	327	66.5	15.0	68.4	10.20	63.8	12.60	35.5	5.16	33.2	5.18	251	3449
JC142_055_017	588	2522	129.0	510	102.0	22.4	100.2	14.60	88.0	16.50	44.3	6.16	37.7	5.58	295	4481
JC142_055_021	433	2151	83.5	370	74.5	16.6	77.7	11.50	72.9	14.40	40.7	5.82	37.2	5.78	296	3691
JC142_055_023	565	2474	119.0	485	97.6	21.4	96.5	14.10	86.2	16.30	43.7	6.10	37.5	5.50	301	4369
JC142_058_010	386	2119	78.5	336	65.9	14.6	62.8	9.31	57.2	10.90	30.5	4.35	26.8	4.03	196	3402
JC142_058_012	315	1789	60.7	262	51.4	11.3	48.6	7.19	44.3	8.53	23.6	3.37	20.7	3.13	160	2809
JC142_058_014	319	2024	60.1	261	51.2	11.3	48.6	7.25	44.4	8.71	24.3	3.50	21.8	3.35	138	3027

Sample Name	La	Ce	Pr	Nd	Sm	Eu	Gd	Tb	Dy	Ho	Er	Tm	Yb	Lu	Y	REY
	ppm	ppm	ppm	ppm	ppm	ppm	ppm	ppm	ppm	ppm	ppm	ppm	ppm	ppm	ppm	ppm
JC142_058_022	365	2062	73.7	315	63.2	13.6	56.8	8.35	50.4	9.52	25.6	3.68	22.5	3.32	145	3218
JC142_058_030	409	2436	83.8	361	72.2	15.5	67.2	9.93	61.2	11.90	33.8	4.75	29.2	4.40	249	3849
JC142_061_014	412	2410	79.4	342	69.2	15.2	65.2	9.70	60.6	11.70	32.6	4.70	28.9	4.39	210	3756
JC142_061_018	412	2298	81.2	350	69.0	15.0	64.2	9.57	58.1	11.00	30.1	4.25	25.9	3.88	165	3597
JC142_061_021	292	2139	56.8	247	49.0	10.8	47.1	7.02	43.6	8.54	24.3	3.45	21.8	3.39	170	3124
JC142_078_001	501	2692	134.0	508	108.0	23.3	94.7	14.30	81.8	14.30	37.8	5.23	32.4	4.66	215	4466
JC142_078_005	190	1490	43.9	183	40.2	8.4	34.3	5.17	30.5	5.49	14.9	2.16	13.7	2.09	89.8	2154
JC142_078_009	417	1913	92.1	404	84.2	18.5	80.9	11.80	71.7	13.20	35.3	4.90	30.0	4.35	225	3406
JC142_078_016	385	2076	83.7	361	74.6	16.4	71.0	10.60	63.9	11.80	32.1	4.59	28.8	4.26	201	3425
JC142_078_019	307	1916	58.6	249	51.0	11.1	47.6	7.09	42.6	8.04	22.2	3.24	20.4	3.09	139	2886
JC142_078_020	534	2500	112.0	463	94.9	20.7	93.4	13.60	83.1	15.50	42.4	6.02	37.4	5.57	292	4314
JC142_078_023	382	1659	78.9	340	67.1	14.7	61.4	8.97	53.6	9.83	26.5	3.74	23.0	3.36	152	2884
JC142_078_028	413	1848	84.6	365	72.3	16.3	68.8	10.20	61.7	11.70	32.1	4.53	28.4	4.11	207	3228
JC142_078_030	439	2125	89.3	385	78.8	17.0	75.5	10.90	66.4	12.30	33.5	4.73	29.1	4.31	212	3583
JC142_078_035	303	2094	59.2	251	50.1	10.7	44.3	6.62	39.2	7.24	20.0	2.91	18.5	2.80	130	3040
JC142_080_001	484	2501	93.5	407	81.4	17.4	75.2	11.20	69.0	13.00	35.7	5.03	31.2	4.57	211	4040
JC142_080_002	493	2670	93.0	406	79.9	17.7	77.2	11.50	71.8	13.90	39.1	5.57	34.5	5.16	266	4284
JC142_080_012	404	2325	78.3	336	66.2	14.5	62.1	9.29	56.7	10.90	30.6	4.35	27.1	4.07	189	3618
JC142_080_013	313	1798	61.5	264	52.8	11.4	49.0	7.27	43.9	8.32	22.9	3.30	20.2	3.00	144	2803
JC142_083_001	316	1596	64.7	285	59.5	13.1	58.7	8.76	52.8	10.00	27.5	3.95	24.9	3.75	192	2717
JC142_083_002	307	1604	66.5	283	59.5	13.0	55.3	8.21	48.9	9.09	25.0	3.58	22.5	3.37	170	2679
JC142_083_006	478	2278	116.0	460	97.4	21.1	93.0	13.70	82.5	15.20	41.1	5.80	35.9	5.29	282	4025
JC142_083_006	478	2278	116.0	460	97.4	21.1	93.0	13.70	82.5	15.20	41.1	5.80	35.9	5.29	282	4025
JC142_083_007	423	2333	91.1	391	82.7	17.8	76.9	11.60	69.4	12.70	34.5	4.91	30.6	4.51	208	3792
JC142_083_010	205	1502	41.2	176	35.4	7.8	32.8	4.93	29.3	5.34	14.3	2.07	13.2	1.93	93.4	2165
JC142_083_015	345	1685	70.4	312	65.6	14.2	64.2	9.48	57.7	11.00	30.0	4.25	26.6	4.00	198	2897

Sample Name	La	Ce	Pr	Nd	Sm	Eu	Gd	Tb	Dy	Ho	Er	Tm	Yb	Lu	Y	REY
	ppm	ppm	ppm	ppm	ppm	ppm	ppm	ppm	ppm	ppm	ppm	ppm	ppm	ppm	ppm	ppm
JC142_083_021	311	1314	62.3	276	56.4	12.4	56.0	8.12	49.3	9.17	24.9	3.48	21.5	3.18	163	2371
JC142_083_022	376	1761	72.7	315	64.1	14.0	60.9	8.94	54.3	10.30	28.7	4.05	25.7	3.89	182	2982
JC142_091_001	349	1751	81.9	352	74.8	16.4	69.1	10.40	61.0	10.90	29.2	4.12	25.4	3.66	166	3005
JC142_091_003	426	2480	97.7	410	88.5	18.9	76.2	11.50	66.7	11.90	31.5	4.40	27.7	4.09	192	3947
JC142_091_004	297	1400	65.7	286	60.7	13.0	60.3	8.65	51.9	9.83	27.3	3.88	24.8	3.68	191	2504
JC142_091_012	362	1576	80.4	352	73.1	15.9	73.4	10.60	64.6	11.90	33.2	4.54	28.9	3.99	214	2905
JC142_091_031	354	1582	79.3	343	69.2	14.9	66.4	9.58	56.8	10.30	28.5	3.93	24.9	3.46	180	2826
JC142_094_005	430	1997	87.9	377	74.2	15.9	67.8	9.73	57.6	10.40	29.0	3.96	26.1	3.53	164	3354
JC142_094_006	430	2027	88.7	391	78.2	16.9	72.7	10.50	63.2	11.60	32.0	4.37	27.6	3.77	181	3439
JC142_094_015	283	2461	55.7	218	42.5	8.5	33.1	4.98	28.3	4.99	14.3	2.04	14.1	2.02	86.2	3259
JC142_094_019	394	2169	80.6	345	67.8	14.8	63.6	9.17	54.6	9.97	27.5	3.83	24.5	3.42	152	3420
JC142_094_020	426	2116	54.6	239	41.9	9.5	49.4	7.00	48.1	10.70	32.5	4.75	30.8	4.89	353	3428
JC142_094_021	299	1727	36.4	158	27.2	6.1	31.4	4.41	30.2	6.78	21.3	3.00	20.2	3.11	221	2595
JC142_094_024	269	999	40.7	184	34.7	8.0	40.6	5.75	39.3	8.78	26.6	3.90	25.2	4.00	315	2005
JC142_094_031	386	2173	76.5	332	66.0	14.2	64.0	9.24	56.7	10.90	30.6	4.29	27.5	3.96	199	3454
JC142_094_034	225	1627	36.4	158	30.5	6.8	32.2	4.66	30.2	6.40	19.4	2.80	18.9	2.80	197	2398
JC142_100_015	400	2283	82.2	357	71.0	15.3	66.7	9.67	58.1	10.90	30.3	4.21	26.0	3.67	171	3589
JC142_107_001	394	2078	78.1	343	69.0	15.0	68.2	9.84	59.7	11.30	32.1	4.39	28.6	3.97	200	3395
JC142_107_002	390	2089	79.3	345	68.5	15.1	68.9	10.00	61.5	11.60	32.9	4.57	29.7	4.18	204	3414
JC142_107_003	345	2074	62.9	273	53.9	11.6	52.5	7.60	46.6	9.00	26.0	3.68	24.8	3.61	172	3166
JC142_107_005	497	2015	106.0	448	88.0	19.0	84.4	12.00	71.0	13.10	37.5	5.02	33.1	4.51	233	3667
JC142_107_013	325	1853	64.4	283	56.8	12.5	57.9	8.47	53.3	10.40	30.0	4.23	27.6	3.91	193	2984
JC142_107_015	444	2207	88.5	386	77.5	16.8	76.7	11.09	68.8	13.30	38.8	5.17	33.6	4.55	242	3714
JC142_107_019	186	1172	36.1	157	31.6	6.9	31.8	4.57	28.7	5.84	17.1	2.42	15.7	2.32	157	1855
JC142_107_020	233	1813	45.1	191	37.9	8.1	36.2	5.28	32.5	6.17	17.9	2.51	16.4	2.33	100	2547
JC142_107_032	322	1985	63.3	275	54.9	11.8	52.8	7.70	46.9	8.92	25.1	3.55	22.4	3.20	140	3023

Sample Name	La	Ce	Pr	Nd	Sm	Eu	Gd	Tb	Dy	Ho	Er	Tm	Yb	Lu	Y	REY
	ppm	ppm	ppm	ppm	ppm	ppm	ppm	ppm	ppm	ppm	ppm	ppm	ppm	ppm	ppm	ppm
JC142_109_005	303	1574	69.8	300	63.7	13.7	60.6	8.86	52.0	9.43	25.5	3.56	22.6	3.20	155	2665
JC142_109_007	257	1889	61.5	252	53.5	11.6	46.9	7.13	40.0	6.73	17.7	2.53	16.2	2.24	85.2	2749
JC142_109_014	222	1594	48.1	206	43.4	9.3	40.4	5.98	35.0	6.28	17.2	2.48	16.0	2.37	105	2354
JC142_109_017	222	1639	47.7	199	41.6	8.9	37.1	5.47	32.0	5.72	16.0	2.26	15.0	2.12	97.1	2371
JC142_109_018	398	1924	80.1	355	72.9	15.9	73.9	10.70	66.5	12.40	34.2	4.85	30.6	4.42	218	3301
JC142_109_020	211	1524	38.6	164	33.6	7.2	32.8	4.76	29.2	5.57	16.0	2.25	15.0	2.18	101	2187
JC142_113_002	393	1961	75.2	333	67.4	14.9	71.1	10.20	64.3	12.60	36.2	4.93	32.6	4.59	243	3324
JC142_113_004	447	2107	86.2	381	76.2	16.6	79.0	11.30	70.3	13.50	37.5	5.24	33.1	4.72	242	3611
JC142_113_006	357	1683	69.4	299	59.9	13.0	60.1	8.65	52.7	10.10	27.8	3.84	24.3	3.44	188	2860
JC142_113_009	352	1539	65.4	285	57.1	12.5	59.2	8.57	53.2	10.30	29.3	4.12	26.6	3.88	198	2704
JC142_113_012	430	1896	83.3	368	73.3	16.1	76.3	11.10	68.6	13.30	38.7	5.21	34.1	4.74	258	3377
JC142_113_013	235	1522	43.7	191	38.7	8.6	40.3	5.71	35.1	6.74	18.0	2.68	16.3	2.51	132	2298
JC142_113_016	451	2176	85.9	377	74.4	16.1	74.8	10.90	67.3	12.90	36.3	5.02	32.3	4.54	226	3650

B.2 Key environmental information

TABLE B.2: Key environmental information for FeMn crusts from Tropic Seamount, with growth rates: (Ref 1 Manheim and Lanebostwick, 1988), (Ref 2 Puteanus and Halbach, 1988)

Sample Name	Latitude	Longitude	Water depth	Recent	FeMn	Max. current	Mn	Fe	Co	Al	Growth Rate		Fe/Mn
	Decimal degrees		(m)	surface	thickness (mm)	velocity m/s	wt%	wt%	wt% (Ref 1)	wt% (Ref 2)	mm/Myr		
JC142_009_010	23.852550	-20.742600	1025	N	20	0.13	16.55	20.19	0.64	1.14	0.86	3.22	1.22
JC142_020_017	23.882100	-20.695667	997	N	30	0.21	17.30	17.99	0.75	0.92	0.62	2.52	1.04
JC142_039_003	23.889533	-20.564083	2713	Y	30	0.43	14.85	19.10	0.52	1.75	1.06	4.56	1.29
JC142_039_005	23.889467	-20.566250	2662	N	50	0.43	16.04	18.68	0.50	1.29	1.17	4.91	1.17
JC142_039_007	23.889050	-20.568017	2606	N	20	0.44	13.72	17.24	0.49	1.82	1.00	5.08	1.26
JC142_039_012	23.894717	-20.579017	2499	Y	90	0.38	14.72	17.69	0.45	1.38	1.23	5.98	1.20
JC142_039_015	23.897350	-20.582917	2480	Y	40	0.34	14.84	18.97	0.48	1.24	1.22	5.40	1.28
JC142_039_017	23.896667	-20.585817	2377	Y	25	0.33	17.08	21.48	0.66	1.82	0.88	3.06	1.26
JC142_039_019	23.897017	-20.586483	2430	N	50	0.32	15.32	21.53	0.58	1.33	1.00	3.72	1.40
JC142_039_020	23.896817	-20.588900	2307	N	30	0.30	14.64	17.84	0.51	1.41	1.00	4.66	1.22
JC142_039_021	23.896650	-20.589550	2267	N	20	0.30	14.75	18.06	0.52	1.80	1.00	4.57	1.22
JC142_039_024	23.896317	-20.591717	2215	N	20	0.30	14.40	18.16	0.45	2.45	1.26	6.07	1.26
JC142_039_5base	23.889467	-20.566250	2662	N	50	0.43	-	-	-	-	-	-	-
JC142_047_007	23.891850	-20.715450	999	N	20	0.24	17.90	19.52	0.67	1.48	0.82	2.99	1.09
JC142_047_008	23.891850	-20.715450	999	N	30	0.24	-	-	-	-	-	-	-
JC142_047_009	23.893650	-20.714700	1011	N	20	0.24	-	-	-	-	-	-	-
JC142_047_012	23.900483	-20.712433	1010	N	30	0.23	19.79	22.01	0.67	2.45	0.98	2.97	1.11
JC142_055_001	23.750083	-20.718467	2700	Y	30	0.08	15.56	22.22	0.54	2.57	1.21	4.32	1.43
JC142_055_002	23.751150	-20.718667	2654	Y	20	0.08	13.45	19.97	0.40	1.23	1.63	8.21	1.48
JC142_055_006	23.757050	-20.719617	2463	Y	25	0.08	16.12	22.19	0.53	1.16	1.25	4.39	1.38
JC142_055_007	23.757050	-20.719617	2463	N	25	0.08	12.12	19.16	0.40	1.32	1.42	7.90	1.58

Sample Name	Latitude	Longitude	Water depth	Recent	FeMn	Max. current	Mn	Fe	Co	Al	Growth Rate		Fe/Mn
	Decimal degrees		(m)	surface	thickness (mm)	velocity m/s	wt%	wt%	wt% (Ref 1)	wt% (Ref 2)	mm/Myr		
JC142_055_008	23.757233	-20.719800	2490	N	30	0.08	18.33	27.43	0.52	2.55	1.75	4.59	1.50
JC142_055_017	23.771683	-20.714467	2164	Y	30	0.08	22.14	28.77	0.84	1.55	0.93	2.13	1.30
JC142_055_021	23.779483	-20.715583	2041	N	20	0.10	20.85	27.96	0.60	1.76	1.52	3.52	1.34
JC142_055_023	23.781983	-20.716233	1935	Y	45	0.11	21.54	29.36	0.82	1.32	0.98	2.22	1.36
JC142_058_010	23.906933	-20.689117	1015	N	25	0.24	19.98	22.40	0.70	1.02	0.93	2.76	1.12
JC142_058_012	23.907000	-20.688283	1016	N	30	0.24	18.65	22.28	0.68	1.18	0.93	2.93	1.19
JC142_058_014	23.906633	-20.687483	1014	N	40	0.24	18.74	21.79	0.73	1.20	0.81	2.62	1.16
JC142_058_022	23.907917	-20.685150	1024	N	30	0.24	21.26	22.24	0.82	1.02	0.76	2.22	1.05
JC142_058_030	23.904850	-20.679767	1022	N	60	0.23	21.74	24.41	1.07	1.07	0.53	1.54	1.12
JC142_061_004	23.938333	-20.690267	1134	N	50	0.16	-	-	-	-	-	-	-
JC142_061_006	23.938333	-20.690267	1134	N	80	0.16	-	-	-	-	-	-	-
JC142_061_014	23.947100	-20.685517	1183	N	30	0.14	18.74	27.07	0.68	0.93	1.12	2.91	1.44
JC142_061_016	23.948533	-20.689833	1122	N	25	0.15	-	-	-	-	-	-	-
JC142_061_018	23.949167	-20.691300	1100	N	90	0.15	20.33	24.71	0.75	1.04	0.91	2.49	1.22
JC142_061_021	23.950833	-20.694967	1059	N	40	0.14	20.85	23.43	0.59	1.53	1.34	3.65	1.12
JC142_078_001	23.961367	-20.828917	3894	N	25	0.10	19.48	32.70	0.41	2.27	3.19	7.36	1.68
JC142_078_005	23.960283	-20.828933	3845	Y	35	0.11	14.73	20.04	0.26	2.78	3.55	69.57	1.36
JC142_078_007	23.958583	-20.828583	3772	Y	25	0.11	-	-	-	-	-	-	-
JC142_078_009	23.957017	-20.826533	3694	Y	60	0.11	15.73	22.34	0.40	1.35	1.97	7.85	1.42
JC142_078_015	23.950100	-20.821867	3476	Y	50	0.13	-	-	-	-	-	-	-
JC142_078_016	23.947200	-20.818917	3325	Y	35	0.14	19.10	26.29	0.44	2.27	2.26	6.34	1.38
JC142_078_019	23.942683	-20.812050	3101	N	100	0.16	14.76	23.27	0.43	1.62	1.74	6.62	1.58
JC142_078_020	23.941450	-20.810783	3024	Y	20	0.16	21.61	27.72	0.81	2.04	0.95	2.26	1.28
JC142_078_023	23.932967	-20.806567	2822	Y	90	0.20	15.80	22.90	0.46	1.53	1.60	5.71	1.45
JC142_078_028	23.926167	-20.805617	2675	Y	20	0.21	18.23	23.01	0.60	2.29	1.16	3.58	1.26

Sample Name	Latitude	Longitude	Water depth	Recent	FeMn	Max. current	Mn	Fe	Co	Al	Growth Rate		Fe/Mn
	Decimal degrees		(m)	surface	thickness (mm)	velocity m/s	wt%	wt%	wt% (Ref 1)	wt% (Ref 2)	mm/Myr		
JC142_078_030	23.926750	-20.802283	2600	N	30	0.22	15.83	25.15	0.62	1.48	1.09	3.39	1.59
JC142_078_035	23.921183	-20.799217	2400	Y	20	0.22	21.41	27.74	0.77	1.66	1.02	2.40	1.30
JC142_078_7base	23.958583	-20.828583	3772	Y	25	0.11	-	-	-	-	-	-	-
JC142_080_001	23.911067	-20.776867	1238	N	40	0.21	22.21	27.24	0.97	1.08	0.71	1.76	1.23
JC142_080_002	23.909150	-20.776800	1278	N	30	0.21	21.34	29.17	0.91	1.23	0.80	1.90	1.37
JC142_080_012	23.901733	-20.775217	1213	N	55	0.25	23.70	25.81	0.99	1.43	0.68	1.71	1.09
JC142_080_013	23.901733	-20.775217	1213	N	50	0.25	20.28	21.09	0.77	1.23	0.77	2.43	1.04
JC142_083_001	23.889050	-20.856500	3777	Y	90	0.11	16.31	19.29	0.52	2.07	1.15	4.58	1.18
JC142_083_002	23.889117	-20.855567	3734	N	25	0.11	13.67	19.39	0.41	2.18	1.49	7.39	1.42
JC142_083_006	23.889533	-20.850000	3530	Y	80	0.11	21.73	29.43	0.57	2.11	1.81	3.88	1.35
JC142_083_006	23.889533	-20.850000	3530	Y	80	0.11	21.73	29.43	0.57	2.11	1.81	3.88	1.35
JC142_083_007	23.889133	-20.848133	3512	Y	170	0.11	20.56	30.85	0.54	2.36	1.98	4.23	1.50
JC142_083_010	23.897117	-20.838833	3424	Y	30	0.11	15.42	20.41	0.30	1.64	2.89	20.81	1.32
JC142_083_015	23.900300	-20.830267	3340	N	50	0.10	17.28	23.68	0.43	2.04	1.99	6.69	1.37
JC142_083_021	23.908117	-20.821867	3103	N	20	0.09	11.16	18.92	0.28	1.76	2.40	29.84	1.70
JC142_083_022	23.909800	-20.820533	2999	Y	25	0.09	13.14	22.36	0.42	2.31	1.65	7.22	1.70
JC142_083_21base	23.908117	-20.821867	3103	Y	20	0.09	-	-	-	-	-	-	-
JC142_083_2base	23.889117	-20.855567	3734	Y	25	0.11	-	-	-	-	-	-	-
JC142_091_001	23.897133	-20.506167	3872	Y	60	0.09	14.43	24.05	0.26	1.71	4.23	73.14	1.67
JC142_091_003	23.897057	-20.506797	3868	Y	60	0.09	17.51	27.11	0.51	2.23	1.74	4.78	1.55
JC142_091_004	23.897001	-20.507112	3861	N	20	0.09	14.30	21.14	0.32	1.95	2.61	16.73	1.48
JC142_091_012	23.894517	-20.523133	3595	N	80	0.11	14.94	24.04	0.33	1.43	2.87	14.33	1.61
JC142_091_031	23.893167	-20.553017	2997	N	40	0.25	14.44	21.66	0.45	1.39	1.52	6.20	1.50
JC142_094_005	23.887183	-20.601833	1834	Y	60	0.35	19.15	26.86	0.60	0.80	1.39	3.56	1.40
JC142_094_006	23.888250	-20.602817	1804	N	70	0.35	18.04	30.02	0.70	0.83	1.16	2.79	1.66

Sample Name	Latitude	Longitude	Water depth	Recent	FeMn	Max. current	Mn	Fe	Co	Al	Growth Rate		Fe/Mn
	Decimal degrees		(m)	surface	thickness (mm)	velocity m/s	wt%	wt%	wt% (Ref 1)	wt% (Ref 2)	mm/Myr		
JC142_094_015	23.888217	-20.607267	1637	N	30	0.32	21.30	27.64	0.52	1.06	1.93	4.50	1.30
JC142_094_019	23.889967	-20.615083	1616	N	35	0.27	18.63	27.57	0.72	1.25	1.04	2.68	1.48
JC142_094_020	23.888150	-20.617683	1580	N	40	0.32	13.85	15.83	0.26	0.49	2.78	82.05	1.14
JC142_094_021	23.888250	-20.619000	1548	N	45	0.32	16.63	15.64	0.32	0.82	2.15	15.18	0.94
JC142_094_024	23.890300	-20.625467	1433	N	30	0.30	9.12	9.33	0.19	0.59	2.02	-	1.02
JC142_094_031	23.891783	-20.628767	1340	Y	40	0.27	16.84	26.52	0.72	1.19	0.92	2.65	1.57
JC142_094_034	23.891917	-20.629267	1319	N	30	0.27	10.61	12.24	0.25	0.50	1.84	110.34	1.15
JC142_100_015	23.859550	-20.686583	1173	N	40	0.10	17.99	26.71	0.73	0.85	0.96	2.63	1.49
JC142_107_001	23.920900	-20.796950	2330	N	70	0.23	14.96	25.47	0.68	1.61	0.91	2.92	1.70
JC142_107_002	23.920867	-20.795517	2292	N	10	0.24	16.23	26.80	0.68	1.67	1.01	2.92	1.65
JC142_107_003	23.920567	-20.790983	1969	Y	50	0.24	16.22	27.02	0.85	2.12	0.69	2.08	1.67
JC142_107_005	23.920350	-20.787750	1803	Y	50	0.23	18.77	27.30	0.68	1.07	1.13	2.92	1.45
JC142_107_013	23.913417	-20.775217	1452	N	60	0.19	16.68	26.11	0.59	1.72	1.27	3.67	1.56
JC142_107_015	23.911350	-20.774417	1435	N	40	0.20	18.58	28.78	0.69	0.84	1.15	2.84	1.55
JC142_107_019	23.909067	-20.768917	1236	Y	70	0.19	17.37	17.34	0.60	1.55	0.86	3.54	1.00
JC142_107_020	23.907150	-20.769983	1216	N	90	0.21	19.93	24.15	0.74	1.89	0.91	2.55	1.21
JC142_107_032	23.903067	-20.775433	1222	N	40	0.24	18.98	27.13	0.64	1.43	1.26	3.22	1.43
JC142_107_3base	23.920567	-20.790983	1969	N	50	0.24	-	-	-	-	-	-	-
JC142_107_5base	23.920350	-20.787750	1803	Y	50	0.23	-	-	-	-	-	-	-
JC142_109_005	23.706200	-20.726800	3832	Y	4	0.06	12.97	22.54	0.27	1.84	3.46	45.39	1.74
JC142_109_007	23.713250	-20.726367	3665	Y	10	0.06	13.33	26.28	0.31	2.92	3.32	19.25	1.97
JC142_109_014	23.726933	-20.725083	3276	Y	30	0.05	14.28	23.29	0.36	2.89	2.31	10.60	1.63
JC142_109_017	23.730250	-20.722367	3186	Y	35	0.05	15.44	24.92	0.29	2.23	3.77	25.86	1.61
JC142_109_018	23.735133	-20.721450	3084	Y	35	0.06	15.69	27.26	0.46	1.95	1.96	5.94	1.74
JC142_109_020	23.741042	-20.730117	2947	Y	40	0.04	15.95	23.16	0.36	2.41	2.50	10.75	1.45

Sample Name	Latitude	Longitude	Water depth	Recent	FeMn	Max. current	Mn	Fe	Co	Al	Growth Rate		Fe/Mn
	Decimal degrees		(m)	surface	thickness (mm)	velocity m/s	wt%	wt%	wt% (Ref 1)	wt% (Ref 2)	mm/Myr		
JC142_109_13base	23.724783	-20.727067	3347	Y	30	0.05	-	-	-	-	-	-	-
JC142_109_14base	23.726933	-20.725083	3276	Y	30	0.05	-	-	-	-	-	-	-
JC142_113_002	23.775867	-20.714767	2067	N	35	0.09	16.19	29.73	0.53	1.49	1.71	4.44	1.84
JC142_113_004	23.776983	-20.715117	2058	Y	30	0.10	17.12	29.82	0.59	1.39	1.48	3.66	1.74
JC142_113_006	23.781217	-20.718150	1956	N	20	0.11	14.15	22.28	0.62	1.27	0.89	3.37	1.57
JC142_113_009	23.784800	-20.720333	1780	N	20	0.11	13.80	23.36	0.46	1.10	1.54	5.92	1.69
JC142_113_012	23.787750	-20.720683	1686	N	25	0.12	17.76	28.53	0.58	1.17	1.48	3.76	1.61
JC142_113_013	23.791533	-20.721883	1624	N	25	0.11	11.60	20.02	0.32	2.42	2.09	15.52	1.73
JC142_113_016	23.796733	-20.721283	1437	N	25	0.11	18.60	28.63	0.67	0.91	1.21	2.99	1.54
JC142_113_2base	23.775867	-20.714767	2067	Y	35	0.09	-	-	-	-	-	-	-

B.3 Full geochemical results

All the full geochemical results are available in the DIGITAL MATERIAL 1

Appendix C

Supplementary material to Chapter 6

C.1 Surface scrape sample information

TABLE C.1: Surface scrape locations, preservation state and sample surface details

Sample name	Water depth (m)	Latitude	Longitude	Recent crust growth?	Upper or Lower
JC142_039_003T_2	2713	23.8895333	-20.564083	Y	Upper
JC142_039_003T	2713	23.8895333	-20.564083	Y	Upper
JC142_039_012	2499	23.8947167	-20.579017	Y	Upper
JC142_039_015	2480	23.89735	-20.582917	Y	Upper
JC142_055_001T	2700	23.7500833	-20.718467	Y	Upper
JC142_055_001T_2	2700	23.7500833	-20.718467	Y	Upper
JC142_055_002	2654	23.75115	-20.718667	Y	Upper
JC142_055_006	2463	23.75705	-20.719617	Y	Upper
JC142_055_017	2164	23.7716833	-20.714467	Y	Upper
JC142_055_023	1935	23.7819833	-20.716233	Y	Upper
JC142_078_005T	3845	23.9602833	-20.828933	Y	Upper
JC142_078_009T	3694	23.9570167	-20.826533	Y	Upper
JC142_078_016T	3325	23.9472	-20.818917	Y	Upper
JC142_078_020	3024	23.94145	-20.810783	Y	Upper
JC142_078_023T	2822	23.9329667	-20.806567	Y	Upper
JC142_078_028	2675	23.9261667	-20.805617	Y	Upper
JC142_078_035T	2400	23.9211833	-20.799217	Y	Upper
JC142_083_001	3777	23.88905	-20.8565	Y	Upper
JC142_083_006T	3530	23.8895333	-20.85	Y	Upper
JC142_083_007T	3512	23.8891333	-20.848133	Y	Upper
JC142_083_010T	3424	23.8971167	-20.838833	Y	Upper
JC142_083_022T	2999	23.9098	-20.820533	Y	Upper
JC142_091_001	3872	23.8971333	-20.506167	Y	Upper

Sample name	Water depth (m)	Latitude	Longitude	Recent crust growth?	Upper or Lower
JC142_091_003	3868	23.8970567	-20.506797	Y	Upper
JC142_094_005	1834	23.8871833	-20.601833	Y	Upper
JC142_094_031	1340	23.8917833	-20.628767	Y	Upper
JC142_107_003	1969	23.9205667	-20.790983	Y	Upper
JC142_107_005	1803	23.92035	-20.78775	Y	Upper
JC142_107_019T_2	1236	23.9030667	-20.768917	Y	Upper
JC142_107_019T	1236	23.90715	-20.768917	Y	Upper
JC142_109_005T	3832	23.7062	-20.7268	Y	Upper
JC142_109_007	3665	23.71325	-20.726367	Y	Upper
JC142_109_017T	3186	23.73025	-20.722367	Y	Upper
JC142_109_017T_2	3186	23.73025	-20.722367	Y	Upper
JC142_109_018T	3084	23.7351333	-20.72145	Y	Upper
JC142_109_020T	2947	23.7410417	-20.730117	Y	Upper
JC142_113_004T	2058	23.7769833	-20.715117	Y	Upper
JC142_055_001B	2700	23.7500833	-20.718467	Y	Lower
JC142_055_001B_2	2700	23.7500833	-20.718467	Y	Lower
JC142_055_006B	2463	23.75705	-20.719617	Y	Lower
JC142_078_005B	3845	23.9602833	-20.828933	Y	Lower
JC142_078_009B	3694	23.9570167	-20.826533	Y	Lower
JC142_078_016B	3325	23.9472	-20.818917	Y	Lower
JC142_078_023B	2822	23.9329667	-20.806567	Y	Lower
JC142_078_035B_2	2400	23.9211833	-20.799217	Y	Lower
JC142_078_035B	2400	23.9211833	-20.799217	Y	Lower
JC142_083_006B	3530	23.8895333	-20.85	Y	Lower
JC142_083_007B	3512	23.8891333	-20.848133	Y	Lower
JC142_083_010B	3424	23.8971167	-20.838833	Y	Lower
JC142_083_022B	2999	23.9098	-20.820533	Y	Lower
JC142_107_019B	1236	23.90715	-20.768917	Y	Lower
JC142_109_005B	3832	23.7062	-20.7268	Y	Lower
JC142_109_017B	3186	23.73025	-20.722367	Y	Lower
JC142_109_018B	3084	23.7351333	-20.72145	Y	Lower
JC142_109_020B	2947	23.7410417	-20.730117	Y	Lower
JC142_113_004B	2058	23.7769833	-20.715117	Y	Lower
JC142_009_005	994	23.85862	-20.72855	N	-
JC142_009_010	1025	23.85255	-20.74260	N	-
JC142_020_017	997	23.8821	-20.695667	N	-
JC142_039_005B	994	23.8586167	-20.72855	N	-
JC142_039_005T	2662	23.8894667	-20.56625	N	-
JC142_039_005T_2	2662	23.8894667	-20.56625	N	-
JC142_039_007	2606	23.88905	-20.568017	N	-
JC142_039_017R	997	23.8821	-20.695667	N	-
JC142_039_019	2430	23.8970167	-20.586483	N	-
JC142_039_021	2267	23.89665	-20.58955	N	-
JC142_039_024	2215	23.8963167	-20.591717	N	-
JC142_047_007B	2606	23.88905	-20.568017	N	-

Sample name	Water depth (m)	Latitude	Longitude	Recent crust growth?	Upper or Lower
JC142_047_007T	999	23.89185	-20.71545	N	-
JC142_055_007	2463	23.75705	-20.719617	N	-
JC142_055_007R	2463	23.75705	-20.719617	N	-
JC142_055_008	249	23.7572333	-20.7198	N	-
JC142_058_010	1015	23.9069333	-20.689117	N	-
JC142_058_014	1014	23.9066333	-20.687483	N	-
JC142_058_022B	1024	23.9079167	-20.68515	N	-
JC142_058_030	1022	23.90485	-20.679767	N	-
JC142_061_014B	1183	23.9471	-20.685517	N	-
JC142_061_018	1100	23.9491667	-20.6913	N	-
JC142_061_021	1059	23.9508333	-20.694967	N	-
JC142_078_001	3894	23.9613667	-20.828917	N	-
JC142_078_019B	3101	23.9426833	-20.81205	N	-
JC142_078_019T	3101	23.9426833	-20.81205	N	-
JC142_078_030B	2600	23.92675	-20.802283	N	-
JC142_078_030T	2600	23.92675	-20.802283	N	-
JC142_080_002	1278	23.90915	-20.7768	N	-
JC142_080_012B	1213	23.9017333	-20.775217	N	-
JC142_080_012T	1213	23.9017333	-20.775217	N	-
JC142_080_013	1213	23.9017333	-20.775217	N	-
JC142_083_002B	3734	23.8891167	-20.855567	N	-
JC142_083_002T	3734	23.8891167	-20.855567	N	-
JC142_083_015	3340	23.9003	-20.830267	N	-
JC142_083_021	3103	23.8945167	-20.821867	N	-
JC142_091_004	3861	23.897001	-20.507112	N	-
JC142_091_012	3595	23.8945167	-20.523133	N	-
JC142_091_031	2997	23.8931667	-20.553017	N	-
JC142_094_006B	1804	23.88825	-20.602817	N	-
JC142_094_006T	1804	23.88825	-20.602817	N	-
JC142_094_015	1637	23.8882167	-20.607267	N	-
JC142_094_019B	1616	23.8899667	-20.615083	N	-
JC142_094_019T	1616	23.8899667	-20.615083	N	-
JC142_094_020	1580	23.88815	-20.617683	N	-
JC142_094_021	1548	23.88825	-20.619	N	-
JC142_094_024_2	1433	23.8903	-20.625467	N	-
JC142_094_024	1433	23.8903	-20.625467	N	-
JC142_094_034B	1319	23.8919167	-20.629267	N	-
JC142_094_034T	1319	23.8919167	-20.629267	N	-
JC142_100_015B	1173	23.85955	-20.686583	N	-
JC142_100_015T	1173	23.85955	-20.686583	N	-
JC142_107_001	233	23.9209	-20.79695	N	-
JC142_107_002	2292	23.9208667	-20.795517	N	-
JC142_107_013	1452	23.9134167	-20.775217	N	-
JC142_107_015B	1435	23.91135	-20.774417	N	-
JC142_107_015T	1435	23.91135	-20.774417	N	-

Sample name	Water depth (m)	Latitude	Longitude	Recent crust growth?	Upper or Lower
JC142_107_020	1216	23.90715	-20.769983	N	-
JC142_107_032B	1222	23.9030667	-20.775433	N	-
JC142_107_032T	1222	23.9030667	-20.775433	N	-
JC142_113_002	2067	23.7758667	-20.714767	N	-
JC142_113_006	1956	23.7812167	-20.71815	N	-
JC142_113_009	1780	23.7848	-20.720333	N	-
JC142_113_012	1686	23.78775	-20.720683	N	-
JC142_113_016	1437	23.7967333	-20.721283	N	-

C.2 Horizon sample information

TABLE C.2: Horizon locations

Name	Water depth (m)	Latitude	Longitude	ROV Tool	Horizon depth (mm)
058_014_H1	1014	23.906633	-20.687483	Drill	21.4
058_014_H3	1014	23.906633	-20.687483	Drill	18.2
061_018_H1	1100	23.949167	-20.6913	Drill	22.8
061_018_H2	1100	23.949167	-20.6913	Drill	21.2
061_018_H3	1100	23.949167	-20.6913	Drill	19.6
061_018_H5	1100	23.949167	-20.6913	Drill	17.6
085_008_H3	1127	23.8958	-20.767367	Drill	42.5
085_008_H5	1127	23.8958	-20.767367	Drill	40
089_002_H1	1025	23.9039318	-20.675344	Drill	40.5
089_002_H2	1025	23.9039318	-20.675344	Drill	38
089_002_H3	1025	23.9039318	-20.675344	Drill	35.5
089_002_H5	1025	23.9039318	-20.675344	Drill	33.5
089_004_H1	1026	23.9042687	-20.675494	Drill	35.5
089_004_H3	1026	23.9042687	-20.675494	Drill	35
089_004_H5	1026	23.9042687	-20.675494	Drill	30.5
089_009_H1	1028	23.9045364	-20.67563	Drill	55.5
089_009_H2	1028	23.9045364	-20.67563	Drill	52.5
089_009_H3	1028	23.9045364	-20.67563	Drill	50.5
089_009_H5	1028	23.9045364	-20.67563	Drill	48
091_001_H1	3872	23.897133	-20.506167	Grab	16.5
091_001_H2	3872	23.897133	-20.506167	Grab	13.5
091_001_H5	3872	23.897133	-20.506167	Grab	11
091_012_H1	3595	23.894517	-20.523133	Grab	20.6
091_012_H3	3595	23.894517	-20.523133	Grab	17.6
091_012_H4	3595	23.894517	-20.523133	Grab	14
091_012_H5	3595	23.894517	-20.523133	Grab	13.8

C.3 Full geochemical results for surface scrape material

All the full geochemical results for surface scrape materials analysed are available in the DIGITAL MATERIAL 2

C.4 Full geochemical results for horizon material

All the full geochemical results for horizon materials analysed are available in the DIGITAL MATERIAL 3

C.5 Correlation matrix for surface scrape material

The full correlation matrix generated from upper surface sample scrape material are available in the DIGITAL MATERIAL 4

C.6 Compiled Pb LA ICP-MS datasets

The full Pb LA ICP-MS results for samples used to identify sample horizons for analysis are available in the DIGITAL MATERIAL 5 (a zip. file contained separate sheets for each sample).

References

W. Abouchami, S. L. Goldstein, S. J. G. Gazer, A. Eisenhauer, and A. Mangini. Secular changes of lead and neodymium in central Pacific seawater recorded by a Fe– Mn crust. *Geochimica et Cosmochimica Acta*, 61(18):3957–3974, 1997.

W. Abouchami, S. J. G. Galer, and A. Koschinsky. Pb and Nd isotopes in NE Atlantic Fe-Mn crusts: Proxies for trace metal paleosources and paleocean circulation. *Geochimica Et Cosmochimica Acta*, 63(10):1489–1505, 1999.

O. Allouche, A. Tsoar, and R. Kadmon. Assessing the accuracy of species distribution models: Prevalence, kappa and the true skill statistic (TSS). *Journal of Applied Ecology*, 43(6):1223–1232, 2006.

A. C. Aplin and D. S. Cronan. Ferromanganese Oxide Deposits from the Central Pacific-Ocean .1. Encrustations from the Line-Islands Archipelago. *Geochimica Et Cosmochimica Acta*, 49(2): 427–436, 1985.

D. E. Archer and K. Johnson. A Model of the iron cycle in the ocean. *Global Biogeochemical Cycles*, 14(1):269–279, 2000.

A. L. Atkins, S. Shaw, and C. L. Peacock. Release of Ni from birnessite during transformation of birnessite to todorokite: Implications for Ni cycling in marine sediments. *Geochimica Et Cosmochimica Acta*, 189:158–183, 2016.

F. Aumento, D. E. Lawrence, and A. G. Plant. *The Ferro-Manganese Pavement on San Pablo Seamount*, volume 68. Department of Energy, Mines and Resources, 1968.

V. K. Banakar and D. V. Borole. Depth Profiles of Th-230(Excess), transition-metals and mineralogy of ferromanganese crusts of the Central Indian Basin and implications for palaeoceanographic influence on crust genesis. *Chemical Geology*, 94(1):33–44, 1991.

V. K. Banakar, J. N. Pattan, and A. V. Mudholkar. Palaeoceanographic conditions during the formation of a ferromanganese crust from the Afanasiy-Nikitin seamount, North Central Indian Ocean: Geochemical evidence. *Marine Geology*, 136(3-4):299–315, 1997.

V. K. Banakar, J. R. Hein, R. P. Rajan, and A. R. Chodankar. Platinum group elements and gold in ferromanganese crusts from Afanasiy-Nikitin seamount, equatorial Indian Ocean: Sources and fractionation. *Journal of Earth System Science*, 116(1):3–13, 2007.

E. D. Barton, J. Arístegui, P. Tett, and E. Navarro-Pérez. Variability in the Canary Islands area of filament-eddy exchanges. *Progress in Oceanography*, 62(2-4):71–94, 2004.

G. N. Baturin, V. T. Dubinchuk, G. I. Ivanov, and A. I. Siraev. A specific type of Fe-Mn mineralization on the Arctic seafloor. *Doklady Earth Sciences*, 458(2):1191–1196, 2014.

M. Bau. Rare-earth element mobility during hydrothermal and metamorphic fluid rock interaction and the significance of the oxidation-state of Europium. *Chemical Geology*, 93(3-4): 219–230, 1991.

M. Bau. Scavenging of dissolved yttrium and rare earths by precipitating iron oxyhydroxide: Experimental evidence for Ce oxidation, Y-Ho fractionation, and lanthanide tetrad effect. *Geochimica et Cosmochimica Acta*, 63(1):67–77, 1999.

M. Bau and A. Koschinsky. Oxidative scavenging of cerium on hydrous Fe oxide: Evidence from the distribution of rare earth elements and yttrium between Fe oxides and Mn oxides in hydrogenetic ferromanganese crusts. *Geochemical Journal*, 43(1):37–47, 2009.

M. Bau, A. Koschinsky, P. Dulski, and J. R. Hein. Comparison of the partitioning behaviours of yttrium, rare earth elements, and titanium between hydrogenetic marine ferromanganese crusts and seawater. *Geochimica Et Cosmochimica Acta*, 60(10):1709–1725, 1996.

M. Bau, K. Schmidt, A. Koschinsky, J. Hein, T. Kuhn, and A. Usui. Discriminating between different genetic types of marine ferro-manganese crusts and nodules based on rare earth elements and yttrium. *Chemical Geology*, 381:1–9, 2014.

A. M. Bauer and M. S. A. Horstwood. Small-volume Lu-Hf and U-Pb isotope determination of complex zircons by solution and laser ablation MC-ICP-MS. *Chemical Geology*, 476:85–99, 2018.

G. Bayon, C. R. German, K. W. Burton, R. W. Nesbitt, and N. Rogers. Sedimentary Fe–Mn oxyhydroxides as paleoceanographic archives and the role of aeolian flux in regulating oceanic dissolved REE. *Earth and Planetary Science Letters*, 224(3-4):477–492, 2004.

M. Benites, J. R. Hein, K. Mizell, T. Blackburn, and L. Jovane. Genesis and evolution of ferromanganese crusts from the summit of Rio Grande Rise, Southwest Atlantic Ocean. *Minerals*, 10(4), 2020.

E. D. Berezhnaya, A. V. Dubinin, M. N. Rimskaya-Korsakova, and T. H. Safin. Accumulation of Platinum Group Elements in hydrogenous fe-mn crust and nodules from the Southern Atlantic Ocean. *Minerals*, 8(7), 2018.

R. S. Bivand, E. Pebesma, and V. Gómez-Rubio. Further Methods for Handling Spatial Data. In *Applied Spatial Data Analysis with R*, Use R!, pages 127–150. Springer, New York, NY, 2013.

N. Blum, P. Halbach, and U. Münch. Geochemistry and mineralogy of alkali basalts from Tropic Seamount, Central Atlantic Ocean. *Marine geology*, 136(1-2):1–19, 1996.

B. R. Bolton, R. Both, N. F. Exon, T. F. Hamilton, J. Ostwald, and J. D. Smith. Geochemistry and Mineralogy of Seafloor Hydrothermal and Hydrogenetic Mn Oxide Deposits from the Manus Basin and Bismarck Archipelago Region of the Southwest Pacific-Ocean. *Marine Geology*, 85 (1):65–87, 1988.

E. Bonatti. Classification and genesis of submarine iron-manganese deposits. *Ferromanganese deposits on the ocean floor*, 1972.

W. Brechner Owens and N. G. Hogg. Oceanic observations of stratified Taylor columns near a bump. *Deep Sea Research Part A. Oceanographic Research Papers*, 27(12):1029–1045, 1980.

L. Breiman. Random Forests. *Machine Learning*, 45(1):5–32, 2001.

K. N. Buck, B. Sohst, and P. N. Sedwick. The organic complexation of dissolved iron along the U.S. GEOTRACES (GA03) North Atlantic Section. *Deep Sea Research Part II: Topical Studies in Oceanography*, 116:152–165, 2015.

R. G. Burns. Uptake of Cobalt into Ferromanganese Nodules, Soils, and Synthetic Manganese(IV) Oxides. *Geochimica Et Cosmochimica Acta*, 40(1):95–102, 1976.

K. W Burton, H.-F. Ling, and R. K. O'Nions. Closure of the Central American Isthmus and its effect on deep-water formation in the North Atlantic. *Nature*, 386(6623):382–385, 1997.

G. Calas. Mineral Resources and Sustainable Development. *Elements*, 13(5):301–306, 2017.

S. B. Castor and J. B. Hedrick. Rare Earth Elements. Society for Mining, Metallurgy, and Exploration: Industrial Minerals Volume, pages 769–792, 2006.

J. D. Chaytor, R. A. Keller, R. A. Duncan, and R. P. Dziak. Seamount morphology in the Bowie and Cobb hot spot trails, Gulf of Alaska. *Geochemistry, Geophysics, Geosystems*, 8(9), 2007.

I. Chiapello, G. Bergametti, L. Gomes, B. Chatenet, F. Dulac, J. Pimenta, and E. S. Suares. An Additional Low Layer Transport of Sahelian and Saharan Dust over the North-Eastern Tropical Atlantic. *Geophysical Research Letters*, 22(23):3191–3194, 1995.

M. R. Clark, A. A. Rowden, T. Schlacher, A. Williams, Mireille Consalvey, K. I. Stocks, A. D. Rogers, T. D. O'Hara, M. White, T. M. Shank, and J. M. Hall-Spencer. The Ecology of Seamounts: Structure, Function, and Human Impacts. *Annual Review of Marine Science*, 2 (1):253–278, 2010.

C. Claude, G. Suhr, A. W. Hofmann, and A. Koschinsky. U-Th chronology and paleoceanographic record in a Fe-Mn crust from the NE Atlantic over the last 700 ka. *Geochimica Et Cosmochimica Acta*, 69(20):4845–4854, 2005.

C. Claude-Ivanaj, A. W. Hofmann, I. Vlastelic, and A. Koschinsky. Recording changes in ENADW composition over the last 340 ka using high-precision lead isotopes in a Fe-Mn crust. *Earth and Planetary Science Letters*, 188(1-2):73–89, 2001.

K. C. Condie. Chemical composition and evolution of the upper continental crust: Contrasting results from surface samples and shales. *Chemical Geology*, 104(1):1–37, 1993.

T. Conrad, J. R. Hein, A. Paytan, and D. A. Clague. Formation of Fe-Mn crusts within a continental margin environment. *Ore Geology Reviews*, 87:25–40, 2017.

T. M. Conway and S. G. John. Quantification of dissolved iron sources to the North Atlantic Ocean. *Nature*, 511(7508):212–215, 2014.

A. J. Cooper and J. Spearman. Validation of a TELEMAC-3D model of a seamount. In *TELEMAC-MASCARET User Conference*, 2017.

J. B. Corliss, J. Dymond, L. I. Gordon, J. M. Edmond, R. P. V. Herzen, R. D. Ballard, K. Green, D. Williams, A. Bainbridge, K. Crane, and T. H. Vanandel. Submarine Thermal Springs on the Galapagos Rift. *Science*, 203(4385):1073–1083, 1979.

J. P. Cowen, E. H. DeCarlo, and D. L. McGee. Calcareous nannofossil biostratigraphic dating of a ferromanganese crust from Schumann Seamount. *Marine Geology*, 115(3):289–306, 1993.

R. D. Cutler, T. C. Edwards, K. H. Beard, D. Cutler, K. T. Hess, J. Gibson, and J. J. Lawler. Random Forests for Classification in Ecology. *Ecology*, 88(11):2783–2792, 2007.

E. H. De Carlo, G. M. McMurthy, and K. H. Kim. Geochemistry of ferromanganese crusts from the Hawaiian Archipelago—I. Northern survey areas. *Deep Sea Research Part A. Oceanographic Research Papers*, 34(3):441–467, 1987.

H. J. W. Debaar, M. P. Bacon, P. G. Brewer, and K. W. Bruland. Rare-Earth Elements in the Pacific and Atlantic Oceans. *Geochimica Et Cosmochimica Acta*, 49(9):1943–1959, 1985.

J. Dower, H. Freeland, and K. Juniper. A strong biological response to oceanic flow past Cobb Seamount. *Deep Sea Research Part A. Oceanographic Research Papers*, 39(7):1139–1145, 1992.

D. Du, X. Ren, S. Yan, X. Shi, Y. Liu, and G. He. An integrated method for the quantitative evaluation of mineral resources of cobalt-rich crusts on seamounts. *Ore Geology Reviews*, 84: 174–184, 2017.

D. Du, S. Yan, G. Yang, F. Shi, Z. Zhu, Q. Song, F. Yang, Y. Cui, and X. Shi. Depositional patterns constrained by slope topography changes on seamounts. *Scientific Reports*, 10(1):20534, 2020.

A. V. Dubinin, M. N. Rimskaya-Korsakova, E. D. Berezhnaya, T. Y. Uspenskaya, and O. M. Dara. Ferromanganese Crusts in the South Atlantic Ocean: Compositional Evolution and Specific Features of Ore Formation. *Geochemistry International*, 56(11):1093–1108, 2018.

R. A. Duce and N. W. Tindale. Atmospheric Transport of Iron and Its Deposition in the Ocean. *Limnology and Oceanography*, 36(8):1715–1726, 1991.

J. Dymond, E. Suess, and M. Lyle. Barium in Deep-Sea Sediment: A Geochemical Proxy for Paleoproductivity. *Paleoceanography*, 7(2):163–181, 1992.

J. D. Eckhardt, G. P. Glasby, H. Puchelt, and Z. Berner. Hydrothermal manganese crusts from Enarete and Palinuro Seamounts in the Tyrrhenian Sea. *Marine Georesources & Geotechnology*, 15(2):175–208, 1997.

H. Elderfield. Compositional Variations in Manganese Oxide Component of Marine Sediments. *Nature-Physical Science*, 237(76):110, 1972.

H. Elderfield. Marine Geochemistry of the Rare-Earth Elements. *Journal of the Geological Society*, 139:660–660, 1982.

J. Elith and J. R. Leathwick. Species Distribution Models: Ecological Explanation and Prediction Across Space and Time. *Annual Review of Ecology, Evolution, and Systematics*, 40(1):677–697, 2009.

V. A. Elrod, W. M. Berelson, K. H. Coale, and K. S. Johnson. The flux of iron from continental shelf sediments: A missing source for global budgets. *Geophysical Research Letters*, 31(12), 2004.

L. Erikstad, V. Bakkestuen, T. Bekkby, and R. Halvorsen. Impact of Scale and Quality of Digital Terrain Models on Predictability of Seabed Terrain Types. *Marine Geodesy*, 36(1):2–21, 2013.

European Commission. Critical raw materials for the EU: Report of the Ad-Hoc Working Group on defining critical raw materials. Technical Report, 2010.

European Commission. Study on the review of the list of Critical Raw Materials: Criticality Assessments. Technical report, European Commission, 2017.

J. N. Fitzsimmons, R. Zhang, and E. A. Boyle. Dissolved iron in the tropical North Atlantic Ocean. *Marine Chemistry*, 154:87–99, 2013.

F. J. Flanagan and D. Gottfried. USGS rock standards. III: Manganese-nodule reference samples USGS NOD-A-1 and USGS NOD-P-1. Technical Report, 1980.

G. L. Foster and D. Vance. In-situ Nd isotopic analysis of geological materials by laser ablation MC-ICP-MS. *Journal of Analytical Atomic Spectrometry*, 21(3):288–296, 2006.

M. Frank. Radiogenic isotopes: Tracers of past ocean circulation and erosional input. *Reviews of geophysics*, 40(1):8755–1209, 2002.

M. Frank, R. K. O'Nions, J. R. Hein, and V. K. Banakar. 60 Myr records of major elements and Pb-Nd isotopes from hydrogenous ferromanganese crusts: Reconstruction of seawater paleochemistry. *Geochimica Et Cosmochimica Acta*, 63(11-12):1689–1708, 1999.

M. Frank, N. Whiteley, S. Kasten, J. R. Hein, and R. K. O'Nions. North Atlantic deep water export to the Southern Ocean over the past 14 Myr: Evidence from Nd and Pb isotopes in ferromanganese crusts. *Paleoceanography*, 17(2), 2002.

J. Friedman, T. Hastie, and R. Tibshirani. Regularization Paths for Generalized Linear Models via Coordinate Descent. *Journal of statistical software*, 33(1):1–22, 2010.

A. Ganachaud. Error budget of inverse box models: The North Atlantic. *Journal of Atmospheric and Oceanic Technology*, 20(11):1641–1655, 2003.

I.-Z. Gazis, T. Schoening, E. Alevizos, and J. Greinert. Quantitative mapping and predictive modeling of Mn nodules' distribution from hydroacoustic and optical AUV data linked by random forests machine learning. *Biogeosciences*, 15(23):7347–7377, 2018.

A. Genin. Bio-physical coupling in the formation of zooplankton and fish aggregations over abrupt topographies. *Journal of Marine Systems*, 50(1):3–20, 2004.

A. Genin and G. W. Boehlert. Dynamics of temperature and chlorophyll structures above a seamount: An oceanic experiment. *Journal of Marine Research*, 43(4):907–924, 1985.

C. R. German, S. Colley, M. R. Palmer, A. Khripounoff, and G. P. Klinkhammer. Hydrothermal plume-particle fluxes at 13°N on the East Pacific Rise. *Deep Sea Research Part I: Oceanographic Research Papers*, 49(11):1921–1940, 2002.

G. Giljan, N. A. Kamennaya, A. Otto, D. Becher, A. Ellrott, V. Meyer, B. J. Murton, B. M. Fuchs, R. I. Amann, and M. V. Zubkov. Bacterioplankton reveal years-long retention of Atlantic deep-ocean water by the Tropic Seamount. *Scientific Reports*, 10(1):4715, 2020.

G. P. Glasby, K. Iizasa, M. Yuasa, and A. Usui. Submarine hydrothermal mineralization on the Izu-Bonin Arc, south of Japan: An overview. *Marine Georesources & Geotechnology*, 18(2): 141–176, 2000.

G. P. Glasby, X. W. Ren, X. F. Shi, and I. A. Pulyaeva. Co-rich Mn crusts from the Magellan Seamount cluster: The long journey through time. *Geo-Marine Letters*, 27(5):315–323, 2007.

G. P. Glasby, B. Mountain, T. C. Vineesh, V. Banakar, R. Rajani, and X. W. Ren. Role of Hydrology in the Formation of Co-Rich Mn Crusts from the Equatorial N Pacific, Equatorial S Indian Ocean and the NE Atlantic Ocean. *Resource Geology*, 60(2):165–177, 2010.

D. A Goddard, G Thompson, E. J. W Jones, and H Okada. The chemistry and mineralogy of ferromanganese encrustations on rocks from the Sierra Leone Rise, equatorial Mid-Atlantic Ridge and New England Seamount Chain. *Marine Geology*, 77(1):87–98, 1987.

M. E. Gonneea and A. Paytan. Phase associations of barium in marine sediments. *Marine Chemistry*, 100(1):124–135, 2006.

K. T. Goto, T. Nozaki, T. Toyofuku, A. H. Augustin, G. Shimoda, Q. Chang, J. I. Kimura, K. Kameo, H. Kitazato, and K. Suzuki. Paleoceanographic conditions on the Sao Paulo Ridge, SW Atlantic Ocean, for the past 30 million years inferred from Os and Pb isotopes of a hydrogenous ferromanganese crust. *Deep-Sea Research Part II-Topical Studies in Oceanography*, 146:82–92, 2017.

T. E Graedel, G. Gunn, and L. T. Espinoza. Metal resources, use and criticality. In G. Gunn, editor, *Critical Metals Handbook*, pages 1–19. John Wiley & Sons, 2014.

L. Z. Granina. Vertical Profiles of Concentrations of Iron and Manganese in the Silt Solutions (Lake Baikal). *Geokhimiya*, (10):1493–1500, 1991.

F. E. Grousset and P. E. Biscaye. Tracing dust sources and transport patterns using Sr, Nd and Pb isotopes. *Chemical Geology*, 222(3):149–167, 2005.

A. Guisan and W. Thuiller. Predicting species distribution: Offering more than simple habitat models. *Ecology Letters*, 8(9):993–1009, 2005.

A. Guisan and N. E. Zimmermann. Predictive habitat distribution models in ecology. *Ecological Modelling*, 135(2):147–186, 2000.

P. Halbach. Processes controlling the heavy metal distribution in Pacific ferromanganese nodules and crusts. *Geologische Rundschau*, 75(1):235–247, 1986.

P. Halbach and F. Manheim. Co-rich ferromanganese deposits in the marginal seamount regions of the Central Pacific Basin: Results of the MIDPAC 81 Survey. 1982.

P. Halbach and D. Puteanus. Occurrence and Formation of Co-Rich Ferromanganese Precipitates in Central Seamount Regions of the Pacific-Ocean. *Fortschritte Der Mineralogie*, 61(1): 76–78, 1983.

P. Halbach and D. Puteanus. The Influence of the Carbonate Dissolution Rate on the Growth and Composition of Co-Rich Ferromanganese Crusts from Central Pacific Seamount Areas. *Earth and Planetary Science Letters*, 68(1):73–87, 1984.

P. Halbach, R. Giovanoli, and D. Vonborstel. Geochemical Processes Controlling the Relationship between Co, Mn, and Fe in Early Diagenetic Deep-Sea Nodules. *Earth and Planetary Science Letters*, 60(2):226–236, 1982.

P. Halbach, M. Segl, D. Puteanus, and A. Mangini. Co-Fluxes and Growth-Rates in Ferromanganese Deposits from Central Pacific Seamount Areas. *Nature*, 304(5928):716–719, 1983.

P. Halbach, C. Kriete, B. Prause, and D. Puteanus. Mechanisms to Explain the Platinum Concentration in Ferromanganese Seamount Crusts. *Chemical Geology*, 76(1-2):95–106, 1989.

K. Hans Wedepohl. The composition of the continental crust. *Geochimica et Cosmochimica Acta*, 59(7):1217–1232, 1995.

M. Hatta, C. I. Measures, J. Wu, S. Roshan, J. N. Fitzsimmons, P. Sedwick, and P. Morton. An overview of dissolved Fe and Mn distributions during the 2010–2011 U.S. GEOTRACES north Atlantic cruises: GEOTRACES GA03. *Deep Sea Research Part II: Topical Studies in Oceanography*, 116:117–129, 2015.

R. G. Heath. Dissolved Silica and Deep-Sea Sediments. 1974.

D. Heggie, G. Klinkhammer, and D. Cullen. Manganese and Copper Fluxes from Continental-Margin Sediments. *Geochimica Et Cosmochimica Acta*, 51(5):1059–1070, 1987.

J. R. Hein and A. Koschinsky. Deep-ocean ferromanganese crusts and nodules. In *Treatise on Geochemistry*, pages 273–291. Elsevier, 2014.

J. R. Hein, F. T. Manheim, W. C. Schwab, and A. S. Davis. Ferromanganese Crusts from Necker Ridge, Horizon Guyot and S.P. Lee Guyot: Geological Considerations. *Marine Geology*, 69 (1-2):25–54, 1985.

J. R. Hein, F. T. Manheim, W. C. Schwab, and D. A. Clague. Cobalt-Rich Ferromanganese Crusts from Central Pacific. *AAPG Bulletin-American Association of Petroleum Geologists*, 70(7):925–925, 1986.

J. R. Hein, W. C. Schwab, and A. S. Davis. Cobalt-Rich and Platinum-Rich Ferromanganese Crusts and Associated Substrate Rocks from the Marshall-Islands. *Marine Geology*, 78(3-4): 255–283, 1988.

J. R. Hein, W. A. Bohrson, M. S. Schulz, M. Noble, and D. A. Clague. Variations in the Fine-Scale Composition of a Central Pacific Ferromanganese Crust: Paleoceanographic Implications. *Paleoceanography*, 7(1):63–77, 1992.

J. R. Hein, H. W. Yeh, S. H. Gunn, W. V. Sliter, L. M. Benninger, and C. H. Wang. Two Major Cenozoic Episodes of Phosphogenesis Recorded in Equatorial Pacific Seamount Deposits. *Paleoceanography*, 8(2):293–311, 1993.

J. R. Hein, A. Koschinsky, P. Halbach, F. T. Manheim, M. Bau, J.-K. Kang, and N. Lubick. Iron and manganese oxide mineralization in the Pacific. *Geological Society, London, Special Publications*, 119(1):123–138, 1997.

J. R. Hein, A. Koschinsky, M. Bau, F. T. Manheim, J.-K. Kang, and L. Roberts. Cobalt-rich ferromanganese crusts in the Pacific. *Handbook of marine mineral deposits*, 18:239–273, 2000.

J. R. Hein, A. Koschinsky, and A. N. Halliday. Global occurrence of tellurium-rich ferromanganese crusts and a model for the enrichment of tellurium. *Geochimica Et Cosmochimica Acta*, 67(6):1117–1127, 2003.

J. R. Hein, M. S. Schulz, R. E. Dunham, R. J. Stern, and S. H. Bloomer. Diffuse flow hydrothermal manganese mineralization along the active Mariana and southern Izu-Bonin arc system, western Pacific. *Journal of Geophysical Research: Solid Earth*, 113(B8), 2008.

J. R. Hein, T. A. Conrad, and R. E. Dunham. Seamount Characteristics and Mine-Site Model Applied to Exploration- and Mining-Lease-Block Selection for Cobalt-Rich Ferromanganese Crusts. *Marine Georesources & Geotechnology*, 27(2):160–176, 2009a.

J. R. Hein, A. Koschinsky, J. R. Bargar, and T. A. Conrad. Geochemistry of marine ferromanganese crusts. *Abstracts of Papers of the American Chemical Society*, 237, 2009b.

J. R. Hein, T. A. Conrad, and H. Staudigel. Seamount mineral deposits: A source of rare metals for high-technology industries. *Oceanography*, 23(1):184–189, 2010.

J. R. Hein, K. Mizell, A. Koschinsky, and T. A. Conrad. Deep-ocean mineral deposits as a source of critical metals for high-and green-technology applications: Comparison with land-based resources. *Ore Geology Reviews*, 51:1–14, 2013.

J. R. Hein, T. Conrad, K. Mizell, V. K. Banakar, F. A. Frey, and W. W. Sager. Controls on ferromanganese crust composition and reconnaissance resource potential, Ninetyeast Ridge, Indian Ocean. *Deep-Sea Research Part I-Oceanographic Research Papers*, 110:1–19, 2016.

J. R. Hein, N. Konstantinova, M. Mikesell, K. Mizell, J. N. Fitzsimmons, P. J. Lam, L. T. Jensen, Y. Xiang, A. Gartman, G. Cherkashov, D. R. Hutchinson, and C. P. Till. Arctic Deep Water Ferromanganese-Oxide Deposits Reflect the Unique Characteristics of the Arctic Ocean. *Geochemistry Geophysics Geosystems*, 18(11):3771–3800, 2017.

J. D. Hem. Redox Processes at Surfaces of Manganese Oxide and Their Effects on Aqueous Metal-Ions. *Chemical Geology*, 21(3-4):199–218, 1978.

A. Hernandez-Guerra, J. L. Pelegri, E. Fraile-Nuez, V. Benitez-Barrios, M. Emelianov, M. D. Perez-Hernandez, and P. Velez-Belchi. Meridional Overturning Transports at 7.5N and 24.5N in the Atlantic Ocean during 1992-93 and 2010-11. *Progress in Oceanography*, 128:98–114, 2014.

R. J. Hijmans. Raster: Geographic Data Analysis and Modeling. R package version 3.4-10. Technical report, 2021.

R. A. Hodkinson and D. S. Cronan. Regional and Depth Variability in the Composition of Cobalt-Rich Ferromanganese Crusts from the Sopac Area and Adjacent Parts of the Central Equatorial Pacific. *Marine Geology*, 98(2-4):437–447, 1991.

J. A. Howe, M. S. Stoker, D. G. Masson, C. J. Pudsey, P. Morris, R. D. Larter, and J. Bulat. Seabed morphology and the bottom-current pathways around Rosemary Bank seamount, northern Rockall Trough, North Atlantic. *Marine and Petroleum Geology*, 23(2):165–181, 2006.

V. Hühnerbach and D. G. Masson. Landslides in the North Atlantic and its adjacent seas: An analysis of their morphology, setting and behaviour. *Marine Geology*, 213(1):343–362, 2004.

K. Hyeong, J. Kim, C. M. Yoo, J. W. Moon, and I. Seo. Cenozoic history of phosphogenesis recorded in the ferromanganese crusts of central and western Pacific seamounts: Implications for deepwater circulation and phosphorus budgets. *Palaeogeography Palaeoclimatology Palaeoecology*, 392:293–301, 2013.

A. Jaeckel, K. M. Gjerde, and J. A. Ardron. Conserving the common heritage of humankind Options for the deep-seabed mining regime. *Marine Policy*, 78:150–157, 2017.

K. S. Johnson, K. H. Coale, W. M. Berelson, and R. M. Gordon. On the formation of the manganese maximum in the oxygen minimum. *Geochimica Et Cosmochimica Acta*, 60(8):1291–1299, 1996.

K. S. Johnson, R. M. Gordon, and K. H. Coale. What controls dissolved iron concentrations in the world ocean? *Marine Chemistry*, 57(3-4):137–161, 1997.

J. Joo, S.-S. Kim, J. W. Choi, S.-J. Pak, Y. Ko, S.-K. Son, J.-W. Moon, and J. Kim. Seabed Mapping Using Shipboard Multibeam Acoustic Data for Assessing the Spatial Distribution of Ferromanganese Crusts on Seamounts in the Western Pacific. *Minerals*, 10(2):155, 2020.

M. Joshima and A. Usui. Magnetostratigraphy of hydrogenetic manganese crusts from Northwestern Pacific seamounts. *Marine Geology*, 146(1-4):53–62, 1998.

P. Josso, E. Pelleter, O. Pourret, Y. Fouquet, J. Etoubleau, S. Cheron, and C. Bollinger. A new discrimination scheme for oceanic ferromanganese deposits using high field strength and rare earth elements. *Ore Geology Reviews*, 87:3–15, 2017.

P. Josso, I. Parkinson, M. S. A. Horstwood, P. Lusty, S. Chenery, and B. .J Murton. Improving confidence in ferromanganese crust age models: A composite geochemical approach. *Chemical Geology*, 513:108–119, 2019.

P. Josso, M.S.A. Horstwood, I.L. Millar, V. Pashley, P.A.J. Lusty, and B. J. Murton. Development of a Correlated Fe-Mn Crust Stratigraphy Using Pb and Nd Isotopes and Its Application to Paleoceanographic Reconstruction in the Atlantic. *Paleoceanography and Paleoclimatology*, 35 (10), 2020a.

P. Josso, J. Rushton, P. Lusty, A. Matthews, A. Chenery, D. Holwell, S. J. Kemp, and B. J. Murton. Late Cretaceous and Cenozoic paleoceanography from north-east Atlantic ferromanganese crust microstratigraphy. *Marine Geology*, 422:106122, 2020b.

P. Josso, T. van Peer, M. S. A. Horstwood, P. Lusty, and B. J. Murton. Geochemical evidence of Milankovitch cycles in Atlantic Ocean ferromanganese crusts. *Earth and Planetary Science Letters*, 553, 2021.

L. Jovane, J. R. Hein, I. A. Yeo, M. Benites, N. M. Bergo, P. V. F. Correa, D. M. Couto, A. D. Guimaraes, S. A. Howarth, H. R. Miguel, K. L. Mizell, D. S. Moura, F. L. V. Neto, M. Pompeu, I. M. M. Rodrigues, F. R. Santana, P. F. Serrao, T. E. Silva, P. M. Tura, C. L. Viscarra, M. G. Chuqui, V. H. Pellizari, C. N. Signori, I. C. A. Da Silveira, P. Y. G. Sumida, B. J. Murton, and F. P. Brandini. Multidisciplinary Scientific Cruise to the Rio Grande Rise. *Frontiers in Marine Science*, 6, 2019.

H. F. Kaiser. The varimax criterion for analytic rotation in factor analysis. *Psychometrika*, 23(3): 187–200, 1958.

S. Kalatha, M. Perraki, M. Economou-Eliopoulos, and I. Mitsis. On the Origin of Bastnaesite-(La,Nd,Y) in the Nissi (Patitira) Bauxite Laterite Deposit, Lokris, Greece. *Minerals*, 7(3):45, 2017.

J. W. Kamphuis. Influence of sand or gravel on the erosion of cohesive sediment. *Journal of Hydraulic Research*, 28(1):43–53, 1990.

J. Karstensen, L. Stramma, and M. Visbeck. Oxygen minimum zones in the eastern tropical Atlantic and Pacific oceans. *Progress in Oceanography*, 77(4):331–350, 2008.

T. Kashiwabara, Y. Takahashi, M. A. Marcus, T. Uruga, H. Tanida, Y. Terada, and A. Usui. Tungsten species in natural ferromanganese oxides related to its different behavior from molybdenum in oxic ocean. *Geochimica Et Cosmochimica Acta*, 106:364–378, 2013.

T. Kashiwabara, Y. Oishi, A. Sakaguchi, T. Sugiyama, A. Usui, and Y. Takahashi. Chemical processes for the extreme enrichment of tellurium into marine ferromanganese oxides. *Geochimica Et Cosmochimica Acta*, 131:150–163, 2014.

A. Kassambara and F. Mundt. Factoextra: Extract and Visualize the Results of Multivariate Data Analyses. R package version 1.0.7. Technical report, 2020.

V. Klemm, M. Frank, S. Levasseur, A. N. Halliday, and J. R. Hein. Seawater osmium isotope evidence for a middle Miocene flood basalt event in ferromanganese crust records. *Earth and Planetary Science Letters*, 273(1-2):175–183, 2008.

G. P. Klinkhammer and M. L. Bender. The distribution of manganese in the Pacific Ocean. *Earth and Planetary Science Letters*, 46(3):361–384, 1980.

M. Knoll, A. Hernández-Guerra, B. Lenz, F. L. Laatzen, F. Machın, T. J. Müller, and G. Siedler. The eastern boundary current system between the Canary Islands and the African coast. *Deep Sea Research Part II: Topical Studies in Oceanography*, 49(17):3427–3440, 2002.

D. Koeppenkastrop and E. H. De Carlo. Sorption of rare-earth elements from seawater onto synthetic mineral particles: An experimental approach. *Chemical Geology*, 95(3):251–263, 1992.

A. Koschinsky and P. Halbach. Sequential leaching of marine ferromanganese precipitates: Genetic implications. *Geochimica Et Cosmochimica Acta*, 59(24):5113–5132, 1995.

A. Koschinsky and J. R. Hein. Uptake of elements from seawater by ferromanganese crusts: Solid-phase associations and seawater speciation. *Marine Geology*, 198(3-4):331–351, 2003.

A. Koschinsky, M. Van Gerven, and P. Halbach. First investigations of massive ferromanganese crusts in the NE Atlantic in comparison with hydrogenetic Pacific occurrences. *Marine Georesources & Geotechnology*, 13(4):375–391, 1995.

A. Koschinsky, P. Halbach, J. R. Hein, and A. Mangini. Ferromanganese crusts as indicators for paleoceanographic events in the NE Atlantic. *Geologische Rundschau*, 85(3):567–576, 1996.

A. Koschinsky, A. Stascheit, M. Bau, and P. Halbach. Effects of phosphatization on the geochemical and mineralogical composition of marine ferromanganese crusts. *Geochimica Et Cosmochimica Acta*, 61(19):4079–4094, 1997.

A. Koschinsky, C. Borowski, and P. Halbach. Reactions of the heavy metal cycle to industrial activities in the deep sea: An ecological assessment. *International Review of Hydrobiology*, 88 (1):102–127, 2003.

M. Kuhn. Caret: Classification and Regression Training. R package version, 6, 0–85 https://CRAN. *R-project. org/package= caret*, 2020.

T. Kuhn, M. Bau, N. Blum, and P. Halbach. Origin of negative Ce anomalies in mixed hydrothermal–hydrogenetic Fe–Mn crusts from the Central Indian Ridge. *Earth and Planetary Science Letters*, 163(1):207–220, 1998.

W. M. Landing and K. W. Bruland. Manganese in the North Pacific. *Earth and Planetary Science Letters*, 49(1):45–56, 1980.

W. M. Landing and K. W. Bruland. The contrasting biogeochemistry of iron and manganese in the Pacific Ocean. *Geochimica et Cosmochimica Acta*, 51(1):29–43, 1997.

D. C. Lee, A. N. Halliday, J. R. Hein, K. W. Burton, J. N. Christensen, and D. Gunther. Hafnium isotope stratigraphy of ferromanganese crusts. *Science*, 285(5430):1052–1054, 1999.

D. Li, Y. Fu, X. Sun, and Z. Wei. Critical metal enrichment mechanism of deep-sea hydrogenetic nodules: Insights from mineralogy and element mobility. *Ore Geology Reviews*, 118:103371, 2020.

J. Li, M. Tran, and J. Siwabessy. Selecting Optimal Random Forest Predictive Models: A Case Study on Predicting the Spatial Distribution of Seabed Hardness. *PLOS ONE*, 11(2):e0149089, 2016.

M. Li and J. Lu. Cobalt in lithium-ion batteries. *Science*, 367(6481):979–980, 2020.

A. Liaw and M. Wiener. Classification and regression by randomForest. *R news*, 2(3):18–22, 2002.

H. F. Ling, K. W. Burton, R. K. O'Nions, B. S. Kamber, F. von Blanckenburg, A. J. Gibb, and J. R. Hein. Evolution of Nd and Pb isotopes in Central Pacific seawater from ferromanganese crusts. *Earth and Planetary Science Letters*, 146(1-2):1–12, 1997.

J. M. Lobo, A. Jiménez-Valverde, and Raimundo Real. AUC: A misleading measure of the performance of predictive distribution models. *Global Ecology and Biogeography*, 17(2):145–151, 2008.

M. W. Lodge and P. A. Verlaan. Deep-Sea Mining: International Regulatory Challenges and Responses. *Elements*, 14(5):331–336, 2018.

P. A. J. Lusty, J. R. Hein, and P. Josso. Formation and occurrence of Ferromanganese Crusts: Earth's Storehouse for Critical Metals. *Elements*, 14(5):313–318, 2018.

F. Machin and J. L. Pelegri. Effect of the Canary Islands in the blockage and mixing of the North Atlantic eastern water masses. *Geophysical Research Letters*, 33(4), 2006.

A. Manceau, A. I. Gorshkov, and V. A. Drits. Structural Chemistry of Mn, Fe, Co, and Ni in Manganese Hydrous Oxides .1. Information from Xanes Spectroscopy. *American Mineralogist*, 77(11-12):1133–1143, 1992.

F. T. Manheim. Marine cobalt resources. *Science*, 232(4750):600–608, 1986.

F. T. Manheim and C. M. Lanebostwick. Cobalt in Ferromanganese Crusts as a Monitor of Hydrothermal Discharge on the Pacific Sea-Floor. *Nature*, 335(6185):59–62, 1988.

F. T. Manheim, P. Popenoe, W. Siapno, and C. Lane. Manganese-phosphorite deposits of the Blake Plateau. 1982.

E. Marino, F. J. Gonzalez, L. Somoza, R. Lunar, L. Ortega, J. T. Vazquez, J. Reyes, and E. Bellido. Strategic and rare elements in Cretaceous-Cenozoic cobalt-rich ferromanganese crusts from seamounts in the Canary Island Seamount Province (northeastern tropical Atlantic). *Ore Geology Reviews*, 87:41–61, 2017.

E. Marino, F. J. Gonzalez, T. Kuhn, P. Madureira, A. V. Wegorzewski, J. Mirao, T. Medialdea, M. Oeser, C. Miguel, J. Reyes, L. Somoza, and R. Lunar. Hydrogenetic, Diagenetic and Hydrothermal Processes Forming Ferromanganese Crusts in the Canary Island Seamounts and Their Influence in the Metal Recovery Rate with Hydrometallurgical Methods. *Minerals*, 9(7), 2019.

M. Marmion, M. Parviainen, M. Luoto, R. K. Heikkinen, and W. Thuiller. Evaluation of consensus methods in predictive species distribution modelling. *Diversity and Distributions*, 15(1): 59–69, 2009.

S. M. McLennan. Relationships between the trace element composition of sedimentary rocks and upper continental crust. *Geochemistry, Geophysics, Geosystems*, 2(4), 2001.

M. Melguen and J. Thiede. Facies Distribution and Dissolution Depths of Surface Sediment Components from Vema Channel and Rio-Grande Rise (Southwest Atlantic Ocean). *Marine Geology*, 17(5):341–353, 1974.

J. L. Mero. *The Mineral Resources of the Sea*. Elsevier Oceanography Series ;. Elsevier Publishing Company, Amsterdam, 1965.

A. Michard and F. Albarede. The REE Content of Some Hydrothermal Fluids. *Chemical Geology*, 55(1-2):51–60, 1986.

K. A. Miller, K. F. Thompson, P. Johnston, and D. Santillo. An Overview of Seabed Mining Including the Current State of Development, Environmental Impacts, and Knowledge Gaps. *Frontiers in Marine Science*, 4, 2018.

R. A. Mills, D. M. Wells, and S. Roberts. Genesis of ferromanganese crusts from the TAG hydrothermal field. *Chemical Geology*, 176(1):283–293, 2001.

K. Mizell, J. R. Hein, P. J. Lam, A. A. P. Koppers, and H. Staudigel. Geographic and Oceanographic Influences on Ferromanganese Crust Composition Along a Pacific Ocean Meridional Transect, 14 N to 14S. *Geochemistry Geophysics Geosystems*, 21(2), 2020.

C. Mohn, M. White, I. Bashmachnikov, F. Jose, and J. L. Pelegrí. Dynamics at an elongated, intermediate depth seamount in the North Atlantic (Sedlo Seamount, 40°20′N, 26°40′W). *Deep Sea Research Part II: Topical Studies in Oceanography*, 56(25):2582–2592, 2009.

D. Mohwinkel, C. Kleint, and A. Koschinsky. Phase associations and potential selective extraction methods for selected high-tech metals from ferromanganese nodules and crusts with siderophores. *Applied Geochemistry*, 43:13–21, 2014.

N. H. Morley, P. J. Statham, and J. D. Burton. Dissolved trace metals in the southwestern Indian Ocean. *Deep Sea Research Part I: Oceanographic Research Papers*, 40(5):1043–1062, 1993.

G. M. Mudd, S. M. Jowitt, and T. T. Werner. The world's by-product and critical metal resources part I: Uncertainties, current reporting practices, implications and grounds for optimism. *Ore Geology Reviews*, 86:924–938, 2017.

S. B. Muinos, M. Frank, C. Maden, J. R. Hein, T. van de Flierdt, S. M. Lebreiro, L. Gaspar, J. H. Monteiro, and A. N. Halliday. New constraints on the Pb and Nd isotopic evolution of NE Atlantic water masses. *Geochemistry Geophysics Geosystems*, 9, 2008.

S. B. Muinos, J. R. Hein, M. Frank, J. H. Monteiro, L. Gaspar, T. Conrad, H. G. Pereira, and F. Abrantes. Deep-sea Fe-Mn Crusts from the Northeast Atlantic Ocean: Composition and Resource Considerations. *Marine Georesources & Geotechnology*, 31(1):40–70, 2013.

J. Murray and A. F. Renard. *Report on Deep-Sea Deposits Based on the Specimens Collected during the Voyage of HMS Challenger in the Years 1872 to 1876*. 1891.

J. W. Murray and J. G. Dillard. Oxidation of Cobalt(II) Adsorbed on Manganese-Dioxide. *Geochimica Et Cosmochimica Acta*, 43(5):781–787, 1979.

B. J. Murton and shipboard scientific party. JC142 Cruise Report, MarineE-Tech Project to map the cobalt-rich Ferromanganese crusts of Tropic Seamount, NE Atlantic Ocean, RSS James Cook. Cruise Report, 2016.

B. J. Murton, P. Lusty, J. Spearman, and M. V. Zubkov. TELEMAC-3D numerical model results used for plume dispersion experiments during cruise JC142 to Tropic Seamount, Northeast Atlantic, as part of the MarineE-tech project (October-December 2016). Technical report, British Oceanographic Data Centre, National Oceanography Centre, NERC, UK, 2020.

N. T. Nassar, R. Barr, M. Browning, Z. W. Diao, E. Friedlander, E. M. Harper, C. Henly, G. Kavlak, S. Kwatra, C. Jun, S. Warren, M. Y. Yang, and T. E. Graedel. Criticality of the Geological Copper Family. *Environmental Science & Technology*, 46(2):1071–1078, 2012.

B. N. Nath, V. Balaram, M. Sudhakar, and W. L. Pluger. Rare-Earth Element Geochemistry of Ferromanganese Deposits from the Indian-Ocean. *Marine Chemistry*, 38(3-4):185–208, 1992.

U. Neettiyath, B. Thornton, M. Sangekar, Y. Nishida, K. Ishii, A. Bodenmann, T. Sato, T. Ura, and A. Asada. Deep-Sea Robotic Survey and Data Processing Methods for Regional-Scale Estimation of Manganese Crust Distribution. *IEEE Journal of Oceanic Engineering*, 46(1):102–114, 2021.

Y. Nishida, K. Nagahashi, T. Sato, A. Bodenmann, B. Thornton, A. Asada, and T. Ura. Development of an autonomous underwater vehicle for survey of cobalt-rich manganese crust. In *OCEANS 2015 - MTS/IEEE Washington*, pages 1–5, 2015.

A. Noguchi, Y. Yamamoto, K. Nishi, A. Usui, and H. Oda. Paleomagnetic study of ferromanganese crusts recovered from the northWest Pacific - Testing the applicability of the magnetostratigraphic method to estimate growth rate. *Ore Geology Reviews*, 87:16–24, 2017.

T. Nozaki, Y. Takaya, T. Toyofuku, A. Tokumaru, K. T. Goto, Q. Chang, J. Kimura, Y. Kato, K. Suzuki, A. H. Augustin, and H. Kitazato. Depositional Age of a Fossil Whale Bone from Sao Paulo Ridge, South Atlantic Ocean, Based on Os Isotope Stratigraphy of a Ferromanganese Crust. *Resource Geology*, 67(4):442–450, 2017.

H. Oda, A. Usui, I. Miyagi, M. Joshima, B. P. Weiss, C. Shantz, L. E. Fong, K. K. McBride, R. Harder, and F. J. Baudenbacher. Ultrafine-scale magnetostratigraphy of marine ferromanganese crust. *Geology*, 39(3):227–230, 2011.

D. Palomino, J. T. Vazquez, L. Somoza, R. Leon, N. Lopez-Gonzalez, T. Medialdea, L. M. Fernandez-Salas, F. J. Gonzalez, and J. A. Rengel. Geomorphological features in the southern Canary Island. Volcanic Province: The importance of volcanic processes and massive slope instabilities associated with seamounts. *Geomorphology*, 255:125–139, 2016.

C. Paton, J. Hellstrom, B. Paul, J. Woodhead, and J. Hergt. Iolite: Freeware for the visualisation and processing of mass spectrometric data. *Journal of Analytical Atomic Spectrometry*, 26(12): 2508–2518, 2011.

M. Patriat and C. Labails. Linking the Canary and Cape-Verde hot-spots, northwest Africa. *Marine Geophysical Researches*, 27(3):201–215, 2006.

C. L. Peacock and E. M. Moon. Oxidative scavenging of thallium by birnessite: Explanation for thallium enrichment and stable isotope fractionation in marine ferromanganese precipitates. *Geochimica Et Cosmochimica Acta*, 84:297–313, 2012.

P. N. Pearson. Planktonic foraminifer biostratigraphy and the development of pelagic caps on guyots in the Marshall Islands group. In *Proceedings of the Ocean Drilling Program. Scientific Results*, volume 144, pages 21–59.

E. Pebesma. Multivariable geostatistics in S: The gstat package. *Computers & Geosciences*, 30(7): 683–691, 2004.

E. Pebesma. Simple Features for R: Standardized Support for Spatial Vector Data. *The R Journal*, 10(1):439–446, 2018.

S. Petersen, A. Kraschell, N. Augustin, J. Jamieson, J. R. Hein, and M. D. Hannington. News from the seabed - Geological characteristics and resource potential of deep-sea mineral resources. *Marine Policy*, 70:175–187, 2016.

S. J. Phillips. Maxnet: Fitting 'Maxent' Species Distribution Models with 'glmnet'. R package version 0.1.2. Technical report, 2017.

S. J. Phillips and M. Dudík. Modeling of species distributions with Maxent: New extensions and a comprehensive evaluation. *Ecography*, 31(2):161–175, 2008.

S. J. Phillips, R. P. Anderson, M. Dudík, R. E. Schapire, and M. E. Blair. Opening the black box: An open-source release of Maxent. *Ecography*, 40(7):887–893, 2017.

D. Z. Piper. Rare-Earth Elements in Ferromanganese Nodules and Other Marine Phases. *Geochimica Et Cosmochimica Acta*, 38(7):1007–1022, 1974.

S. Poehle and A. Koschinsky. Depth distribution of Zr and Nb in seawater: The potential role of colloids or organic complexation to explain non-scavenging-type behavior. *Marine Chemistry*, 188:18–32, 2017.

J. E. Post. Manganese oxide minerals: Crystal structures and economic and environmental significance. *Proceedings of the National Academy of Sciences of the United States of America*, 96 (7):3447–3454, 1999.

L. S. Prakash, D. Ray, A. L. Paropkari, A. V. Mudholkar, M. Satyanarayanan, B. Sreenivas, D. Chandrasekharam, D. Kota, K. A. K. Raju, S. Kaisary, V. Balaram, and T. Gurav. Distribution of REEs and yttrium among major geochemical phases of marine Fe-Mn-Oxides: Comparative study between hydrogenous and hydrothermal deposits. *Chemical Geology*, 312: 127–137, 2012.

D. Puteanus and P. Halbach. Correlation of Co concentration and growth rate—A method for age determination of ferromanganese crusts. *Chemical Geology*, 69(1-2):73–85, 1988.

R Core Team. R: A language and environment for statistical computing. R Foundation for Statistical Computing, Vienna, Austria., 2020.

K. V. Ragnarsdottir. Rare metals getting rarer. *Nature Geoscience*, 1(11):720–721, 2008.

R. P. Rajani, V. K. Banakar, C. Parthiban, A. V. Mudholkar, and A. R. Chodankar. Compositional variation and genesis of ferromanganese crusts of the Afanasiy-Nikitin Seamount, Equatorial Indian Ocean. *Journal of Earth System Science*, 114(1):51–61, 2005.

B. Ramiro-Sánchez, J. M. González-Irusta, L.-A. Henry, J. Cleland, I. A. Yeo, J. R. Xavier, M. Carreiro-Silva, I. Sampaio, J. Spearman, L. Victorero, C. G. Messing, G. Kazanidis, J. M. Roberts, and B. J. Murton. Characterization and Mapping of a Deep-Sea Sponge Ground on the Tropic Seamount (Northeast Tropical Atlantic): Implications for Spatial Management in the High Seas. *Frontiers in Marine Science*, 6, 2019.

W. Revelle. Psych: Procedures for Personality and Psychological Research, v. 2.1.3. Technical report, Northwestern University, Evanston, Illinois, USA,, 2020.

B. C. Reynolds, Martin Frank, and R. K. O'Nions. Nd-and Pb-Isotope time series from Atlantic ferromanganese crusts: Implications for changes in provenance and paleocirculation over the last 8 Myr. *Earth and Planetary Science Letters*, 173(4):381–396, 1999.

J. L. Reyss, V. Marchig, and T. L. Ku. Rapid growth of a deep-sea manganese nodule. *Nature*, 295(5848):401–403, 1982.

R. Rihm, C. L. Jacobs, H.-U. Krastel, H.-U. Schmincke, and B. Alibes. Las Hijas Seamounts—the next Canary Island? *Terra Nova*, 10(3):121–125, 1998.

G. I. Roden. Effect of seamounts and seamount chains on ocean circulation and thermohaline structure. *Seamounts, islands, and atolls*, 43:335–354, 1987.

G. I. Roden. Effects of the Fieberling seamount group upon flow and thermohaline structure in the spring of 1991. *Journal of Geophysical Research: Oceans*, 99(C5):9941–9961, 1994.

P. A. Rona. The changing vision of marine minerals. *Ore Geology Reviews*, 33(3-4):618–666, 2008.

T. C. Royer. Ocean Eddies Generated by Seamounts in the North Pacific. *Science*, 199(4333): 1063–1064, 1978.

P. M. Saager, J. W. De Baar, and P. H. Burkill. Manganese and iron in Indian Ocean waters. *Geochimica et Cosmochimica Acta*, 53(9):2259–2267, 1989.

H. Sato and A. Usui. Metal flux as an alternative parameter in evaluating the resource potential for co-rich ferromanganese crusts. *Marine Georesources & Geotechnology*, 36(7):768–780, 2018.

T. A. Schlacher, A. R. Baco, A. A. Rowden, T. D. O'Hara, M. R. Clark, C. Kelley, and J. F. Dower. Seamount benthos in a cobalt-rich crust region of the central Pacific: Conservation challenges for future seabed mining. *Diversity and Distributions*, 20(5):491–502, 2014.

K. Schmidt, M. Bau, J. R. Hein, and A. Koschinsky. Fractionation of the geochemical twins Zr-Hf and Nb-Ta during scavenging from seawater by hydrogenetic ferromanganese crusts. *Geochimica Et Cosmochimica Acta*, 140:468–487, 2014.

H. U. Schmincke, S. Krastel, T. Hansteen, and M. Sumita. Preliminary Results, Leg M43/1, Rock Sampling and Description. *DECOS/OMEX II, Cruise*, (43):99, 2000.

J. C. Scholten, S. D. Scott, D. Garbe-Schönberg, Jan Fietzke, T. Blanz, and C. B. Kennedy. Hydrothermal iron and manganese crusts from the Pitcairn hotspot region. In *Oceanic Hotspots*, pages 375–405. Springer, 2004.

R. L. Soulsby. Chapter 5 The Bottom Boundary Layer of Shelf Seas. In B. Johns, editor, *Elsevier Oceanography Series*, volume 35 of *Physical Oceanography of Coastal and Shelf Seas*, pages 189–266. Elsevier, 1983.

J. Spearman, J. Taylor, N. Crossouard, A. Cooper, M. Turnbull, A. Manning, M. Lee, and B. J. Murton. Measurement and modelling of deep sea sediment plumes and implications for deep sea mining. *Scientific Reports*, 10(1):5075, 2020.

P. J. Statham, P. A. Yeats, and W. M. Landing. Manganese in the eastern Atlantic Ocean: Processes influencing deep and surface water distributions. *Marine Chemistry*, 61(1):55–68, 1998.

L. Stramma, S. Hüttl, and J. Schafstall. Water masses and currents in the upper tropical northeast Atlantic off northwest Africa. *Journal of Geophysical Research: Oceans*, 110(C12), 2005.

Y. Takahashi, H. Shimizu, A. Usui, H. Kagi, and M. Nomura. Direct observation of tetravalent cerium in ferromanganese nodules and crusts by X-Ray-Absorption near-Edge structure (XANES). *Geochimica Et Cosmochimica Acta*, 64(17):2929–2935, 2000.

Y. Takahashi, A. Manceau, N. Geoffroy, M. A. Marcus, and A. Usui. Chemical and structural control of the partitioning of Co, Ce, and Pb in marine ferromanganese oxides. *Geochimica Et Cosmochimica Acta*, 71(4):984–1008, 2007.

J. Teague, M. J. Allen, and T. B. Scott. The potential of low-cost ROV for use in deep-sea mineral, ore prospecting and monitoring. *Ocean Engineering*, 147:333–339, 2018.

A. S. Templeton, E. J. Knowles, D. L. Eldridge, B. W. Arey, A. C. Dohnalkova, S. M. Webb, B. E. Bailey, B. M. Tebo, and H. Staudigel. A seafloor microbial biome hosted within incipient ferromanganese crusts. *Nature Geoscience*, 2(12):872–876, 2009.

S. Terashima, A. Usui, S. Nakao, and N. Mita. Platinum Abundance in Ocean-Floor Ferromanganese Crusts and Nodules. *Marine Mining*, 7(3):209–218, 1988.

C. E. L. Thompson and C. L. Amos. Effect of Sand Movement on a Cohesive Substrate. *Journal of Hydraulic Engineering*, 130(11):1123–1125, 2004.

B. Thornton, A. Asada, A. Bodenmann, M. Sangekar, and T. Ura. Instruments and Methods for Acoustic and Visual Survey of Manganese Crusts. *IEEE Journal of Oceanic Engineering*, 38(1): 186–203, 2013.

W. Thuiller, B. Lafourcade, R. Engler, and M. B. Araújo. BIOMOD- a platform for ensemble forecasting of species distributions. *Ecography*, 32(3):369–373, 2009.

W. Thuiller, D. Georges, M. Gueguen, R. Engler, and F. Breiner. Biomod2: Ensemble Platform for Species Distribution Modeling. R package version 3.4.13. Technical report, 2020.

A. Usui and N. Okamoto. Geophysical and Geological Exploration of Cobalt-Rich Ferromanganese Crusts: An Attempt of Small-Scale Mapping on a Micronesian Seamount. *Marine Georesources & Geotechnology*, 28(3):192–206, 2010.

A. Usui, M. Yuasa, S. Yokota, M. Nohara, A. Nishimura, and F. Murakami. Submarine Hydrothermal Manganese Deposits from the Ogasawara (Bonin) Arc, Off the Japan Islands. *Marine Geology*, 73(3-4):311–322, 1986.

A. Usui, M. Tanaka, B. Thornton, A. Tokumaru, and T. Urabe. Small-scale ROV Mapping of the Ferromanganese Crusts over the Seamounts in the NW Pacific. *Oceans 2011*, 2011.

A. Usui, H. Sato, K. Nishi, I. Graham, B. Thornton, N. Okamoto, and T. Uraba. Geological Characterization of Co-Rich Ferromaganese Crusts over the Northwestern Pacific Seamounts. *2013 Oceans - San Diego*, 2013.

A. Usui, K. Nishi, H. Sato, Y. Nakasato, B. Thornton, T. Kashiwabara, A. Tokumaru, A. Sakaguchi, K. Yamaoka, S. Kato, S. Nitahara, K. Suzuki, K. Iijima, and T. Urabe. Continuous growth of hydrogenetic ferromanganese crusts since 17 Myr ago on Takuyo-Daigo Seamount, NW Pacific, at water depths of 800-5500 m. *Ore Geology Reviews*, 87:71–87, 2017.

T. van de Flierdt, M. Frank, D. C. Lee, and A. N. Halliday. Glacial weathering and the hafnium isotope composition of seawater (vol 198, pg 167, 2002). *Earth and Planetary Science Letters*, 201(3-4):639–647, 2002.

P. Van Den Bogaard. The origin of the Canary Island Seamount Province-New ages of old seamounts. *Scientific Reports*, 3:2107, 2013.

C. H. Van Der Weijden and E. C. Kruissink. Some geochemical controls on lead and barium concentrations in ferromanganese deposits. *Marine Chemistry*, 5(2):93–112, 1977.

I. M. Varentsov, V. A. Drits, A. I. Gorshkov, A. V. Sivtsov, and B. A. Sakharov. Mn-Fe Oxyhydroxide Crusts from Krylov Seamount (Eastern Atlantic) - Mineralogy, Geochemistry and Genesis. *Marine Geology*, 96(1-2):53–70, 1991.

P. A. Verlaan and D. S. Cronan. Origin and variability of resource-grade marine ferromanganese nodules and crusts in the Pacific Ocean: A review of biogeochemical and physical controls. *Geochemistry*, page 125741, 2021.

L. Victorero, K. Robert, L. F. Robinson, M. L. Taylor, and V. A. I. Huvenne. Species replacement dominates megabenthos beta diversity in a remote seamount setting. *Scientific Reports*, 8(1): 4152, 2018.

A. H. L. Voelker, A. Colman, G. Olack, J. J. Waniek, and D. Hodell. Oxygen and hydrogen isotope signatures of Northeast Atlantic water masses. *Deep Sea Research Part II: Topical Studies in Oceanography*, 116:89–106, 2015.

S. Walbridge, N. Slocum, N. Pobuda, and D. J. Wright. Benthic Terrain Modeler (BTM) 3.0, tools for understanding and classifying the benthic environment. Esri, 2018.

L. Watling and P. J. Auster. Seamounts on the High Seas Should Be Managed as Vulnerable Marine Ecosystems. *Frontiers in Marine Science*, 4, 2017.

A. V. Wegorzewski and T. Kuhn. The influence of suboxic diagenesis on the formation of manganese nodules in the Clarion Clipperton nodule belt of the Pacific Ocean. *Marine Geology*, 357:123–138, 2014.

T. Wei and V. Simko. R package "corrplot": Visualization of a Correlation Matrix (Version 0.84). Available from https://github.com/taiyun/corrplot. Technical report, 2017.

T. Wei, V. Simko, M. Levy, Y. Xie, Y. Jin, and J. Zemla. Package 'corrplot'. *Statistician*, 56(316), 2017.

X. Wen, E. H. De Carlo, and Y. H. Li. Interelement relationships in ferromanganese crusts from the central Pacific ocean: Their implications for crust genesis. *Marine Geology*, 136(3):277–297, 1997.

Z. H. Weng, S. M. Jowitt, G. M. Mudd, and N. Haque. A Detailed Assessment of Global Rare Earth Element Resources: Opportunities and Challenges. *Economic Geology*, 110(8):1925–1952, 2015.

P. Wessel, D. T. Sandwell, and S. S. Kim. The Global Seamount Census. *Oceanography*, 23(1): 24–33, 2010.

H. L. Windom, W. S. Moore, L. F. H. Niencheski, and R. A. Jahrike. Submarine groundwater discharge: A large, previously unrecognized source of dissolved iron to the South Atlantic Ocean. *Marine Chemistry*, 102(3-4):252–266, 2006.

S. N. Wood. Package 'mgcv'. *R package version*, 1:29, 2015.

S. N. Wood. *Generalized Additive Models: An Introduction with R, Second Edition*. CRC Press, 2017.

J. Wu, S. Roshan, and G. Chen. The distribution of dissolved manganese in the tropical–subtropical North Atlantic during US GEOTRACES 2010 and 2011 cruises. *Marine Chemistry*, 166:9–24, 2014.

T. Yamazaki and R. Sharma. Distribution characteristics of co-rich manganese deposits on a seamount in the central Pacific Ocean. *Marine Georesources & Geotechnology*, 16(4):283–305, 1998.

I. A. Yeo, K. Dobson, P. Josso, R. B. Pearce, S. A. Howarth, P. A. J. Lusty, T. P. Le Bas, and B. J. Murton. Assessment of the Mineral Resource Potential of Atlantic Ferromanganese Crusts Based on Their Growth History, Microstructure, and Texture. *Minerals*, 8(8), 2018a.

I. A. Yeo, T. P. Le Bas, and B. J. Murton. Marine geophysical and camera stills data from JC142 cruise to Tropic Seamount as part of the MarineE-tech project (October-December 2016). Technical report, British Oceanographic Data Centre - Natural Environment Research Council, UK, 2018b.

I. A. Yeo, S. A. Howarth, J. Spearman, A. Cooper, N. Crossouard, J. Taylor, M. Turnbull, and B. J. Murton. Distribution of and hydrographic controls on ferromanganese crusts: Tropic Seamount, Atlantic. *Ore Geology Reviews*, 114, 2019.

C. Yesson, M. R. Clark, M. L. Taylor, and A. D. Rogers. The global distribution of seamounts based on 30 arc seconds bathymetry data. *Deep-Sea Research Part I-Oceanographic Research Papers*, 58(4):442–453, 2011.

D. Zawadzki, L. Maciag, R. A. Kotlinski, G. A. Kozub-Budzyn, A. Piestrzynski, and R. Wrobel. Geochemistry of cobalt-rich ferromanganese crusts from the Perth Abyssal Plain (E Indian Ocean). *Ore Geology Reviews*, 101:520–531, 2018.

J. Zhang and Y. Nozaki. Rare earth elements and yttrium in seawater: ICP-MS determinations in the East Caroline, Coral Sea, and South Fiji basins of the western South Pacific Ocean. *Geochimica et Cosmochimica Acta*, 60(23):4631–4644, 1996.

M. Zieringer, M. Frank, R. Stumpf, and E. C. Hathorne. The distribution of neodymium isotopes and concentrations in the eastern tropical North Atlantic. *Chemical Geology*, 511:265–278, 2019.

A. F. Zuur, E. N. Ieno, and C. S. Elphick. A protocol for data exploration to avoid common statistical problems. *Methods in ecology and evolution*, 1(1):3–14, 2010.

K. Zweibel. The Impact of Tellurium Supply on Cadmium Telluride Photovoltaics. *Science*, 328 (5979):699–701, 2010.